The non-Newtonian and non-isothermal spreading of liquid domes using mathematical and numerical methods

Mr Ghanim Mohammed Salih A ALGWAUISH

Submitted in partial fulfilment of the requirements of the degree of

Doctor of Philosophy

June 2019

Keele University

School of Computing and Mathematics

Abstract

This thesis is concerned with the spreading of a large mass of fluid under the influence of gravity and viscous forces, referred to as a viscous-gravity current. The focus is on a particular class of viscous-gravity currents which involve the spreading of a hot fluid undergoing cooling as it flows. The flow of lava is a primary example and is what motivates this work. The flow and cooling are strongly coupled. The fluid properties, such as the viscosity, are temperature-dependent and flows also exhibit non-Newtonian behaviour due to compositional changes as a result of cooling, such as an apparent viscosity and a yield stress. Conversely, the flow convects the heat causing cooling. A consequence of this is the development of dynamic flow patterns, such as fingering-type instabilities, e.g., toe-shaped protrusions at an advancing lava flow front. These behaviours have motivated theoreticians to understand the interplay between flow and cooling and the mechanisms behind these instabilities.

This work develops a theoretical model of a planar liquid dome spreading down an inclined substrate due to gravity. This model incorporates non-Newtonian and viscoplastic behaviour, a temperature-dependent viscosity and heat transfer boundary conditions at the dome's free surface and the underlying substrate. A power-law and Carreau constitutive law is used to describe the non-Newtonian behaviour and a Herschel-Bulkley constitutive law to model the viscoplastic behaviour. Two viscosity-temperature relationships, an exponential and a bi-viscosity model, are considered.

We combine numerical simulations and similarity solutions to perform a parameter study on the influence of key parameters on the free surface shapes and spreading behaviour, such as the apparent viscosity, yield stress, Péclet number (compares conductive and convective heat transport), temperature-viscosity coupling constant and the surface and substrate heat transfer coefficients. Our one-dimensional results reveal a variety of free surface shape profiles, such as symmetric domes, slumped domes, pancake domes and overriding fluid humps. A two-dimensional numerical linear stability analysis reveals the stability characteristics of the above one-dimensional shapes to a small-amplitude transverse perturbation. We have identified a fingering instability based on a thermo-viscous mechanism. The viscosity-temperature coupling is identified as the key parameter that controls the growth rate of the instability and the band of unstable wavenumbers. We provide the necessary conditions on the base state for the onset of the instability. The preliminary work undertaken here provides the basis for doing a thorough theoretical analysis of the instability and for exploring the nonlinear stability of the flow.

Acknowledgements

I would like to express my profound appreciation and sincere gratitude to my supervisor, Dr. Shailesh Naire for his invaluable guidance. I have been extremely lucky to have a supervisor who cared so much about my research and his encouragement and positive criticism have been mainly responsible for the success of this project. I must express my thanks to Dr. Nigel Cassady, Prof. Victor Shrira and Dr. Ralph Gertisser for their guidance and suggestions. I take this opportunity to express my deep gratitude to my parents, and their moral and personal support, and for their encouragement in every step of my life. I especially thank my wife and children, for all the sacrifices, encouragement and support which I received from them. All the thanks to my brothers, sisters for their love and constant support during tough times. I would also like to thank my colleagues in my research group for the knowledge I gained through some interesting discussions with them. In addition, I would like to thank my friends who helped me all the times. I would like to thank Keele University for giving me the opportunity to pursue a PhD degree at a prestigious institution. Many thanks to those who provided me with all the facilities which have been very helpful for my simulations. Finally, I would like to thank the Ministry of Higher Education and Scientific Research and Mosul University in Iraq for providing me with the funding, encouragement, and the support which allowed me to undertake this research.

Contents

List of Figures

Chapter 1

Introduction

1.1 Motivation

The spreading of a mass of liquid, such as a drop or a liquid layer, is ubiquitous in a wide range of problems (see Oron, Davis & Bankoff [67] and Matar & Craster [27] for a nice review of these). It has many important applications in industry, such as in coating flows (e.g., coating a wall with paint) [62], in the spreading of radioactive material in nuclear reactors [33], to name a few. It also occurs frequently in many geophysical and environmental scenarios, such as in lava [40] and glacier [65, 71] flows and mudslides [51]. In these large-scale geophysical and environmental flows, spreading is mainly driven by the force due to gravity causing the liquid to flow down the underlying surface (commonly referred to as a gravity current [49]). In small-scale flows, physical effects such as surface tension (associated with the curvature of the liquid-air interface)

and surface tension variations (e.g., due to chemicals such as surfactants which modify the surface tension at the air-liquid interface) can also drive spreading flows [27, 62]. External forces due to, for example, an electric or magnetic field can also be applied to control spreading which is useful in many industrial applications [27]. Lava and glacier flows, mudslides and landslides can endanger life, even causing death in most cases, and can damage or destroy infrastructure and buildings. Understanding the flow behaviour is therefore important in order to develop strategies on how to control their spreading and mitigate potential future disasters.

The main motivation of this thesis is to understand the variety of features associated with the flow of lava. During a volcanic eruption the magma (molten or partial molten rock) that is extruded through a vent is referred to as lava. The lava spreads on the surface as a gravity current, forming a lava flow. They undergo cooling by transferring their heat to the colder surrounding atmosphere or the underlying solid surface gradually solidifying until they come to rest. There are many observed forms of lava flow which depend on its composition, the effusion rate out of the vent, eruption temperature, cooling rate and the ground topography over which the lava flows [40]. When lava is highly viscous and the extrusion from the vent slow, it does not spread very far but expands itself into a mound around the vent as more and more magma is extruded into the dome's interior. This roughly circular mound is referred to as a *lava dome* (United States Geological Survey, Glossary - Dome; http://volcanoes.usgs.gov/vsc/glossary/dome.html). Figure 1.1(a) shows a side view photograph of a lava dome in August 1981 which was

formed within the crater of the volcano Mount St Helens after its final eruption in October 1980. They can reach heights of several hundred metres and can grow steadily for years. For example, the final explosive eruption of Mount St. Helens on October 1980 formed a lava dome within 30 minutes after the explosion and within a few days, it was about 900 feet wide and 130 feet high. This dome grew intermittently for several years between 1980 and 1987. It reached a height of approximately 800 feet and grew to a diameter of 3,000 feet. Lava flows could also be more fluid-like if the viscosity of

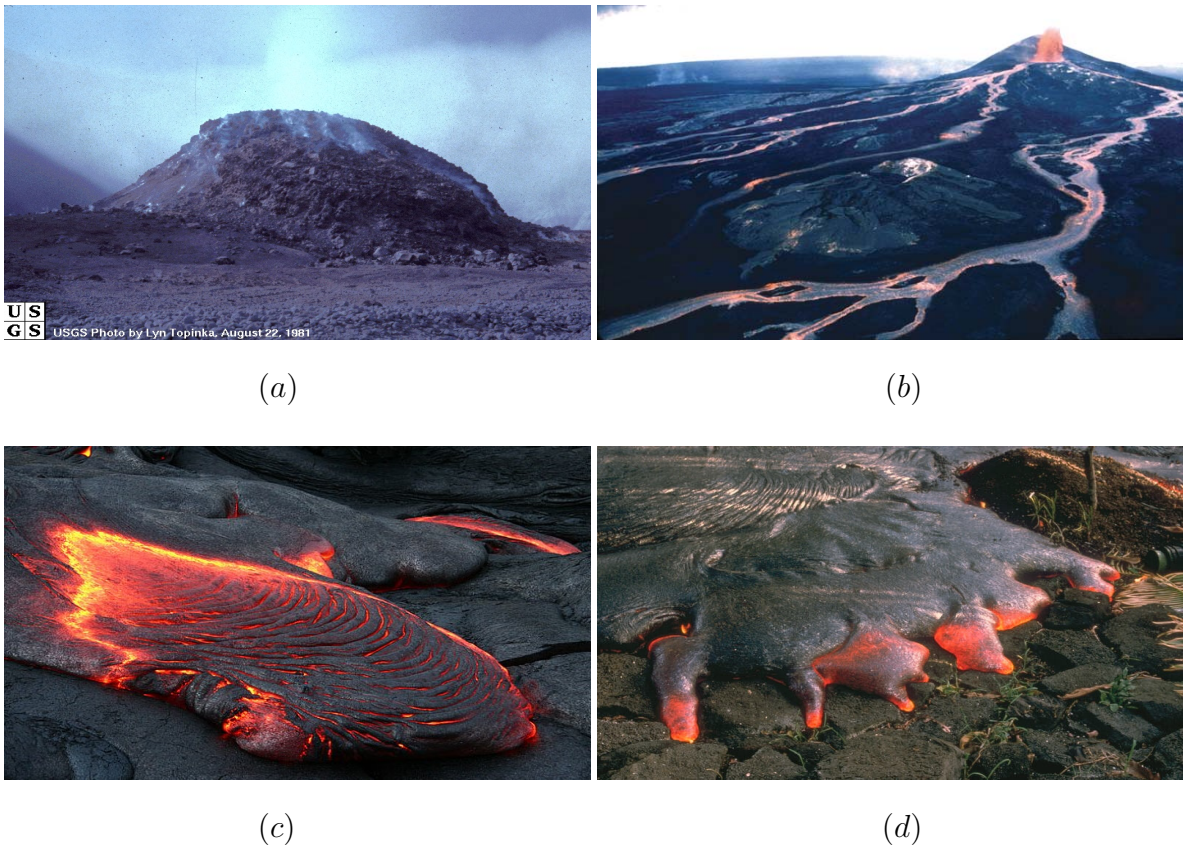

(a) (b)

(c) (d)

Figure 1.1: Examples of some observed forms of lava flow. (a) Side view photograph of Mount St. Helens' lava dome in August 1981 which was over 500 feet high and nearly 1300 feet wide; (b) lava channels formed between levées of solidified lava; (c) and (d) *ropy* and *toey* pahoehoe lava flow. Photographs courtesy of the United States Geological Survey.

the magma feeding the eruption vent is very low [40]. If the effusion rate is large, they produce rapid flows that can travel for long distances on the order of several kilometers [24]. The largest of these flows are those observed in Hawaii, which start off as rapid, open-channel *pahoehoe* flows. These flows are observed to produce their own channel by constructing levées of solidified lava [45] (see Fig. 1.1(b)). The channel flows can also form *lava tubes*, which are roofed channels in which the lava flow is completely surrounded by solidified lava and therefore well insulated against any heat loss at the surface [52]. Instabilities, usually associated with cooling, can lead to branching of the channel flows or the advancing flow front into shallower flows with thin glassy surfaces, referred to as *pahoehoe* lava [40]. Surface features such as a *ropy* appearance are observed in some of these advancing flows (see Fig. 1.1(c)), in others, the advancing flow front has *toe-like* protrusions (see Fig. 1.1(d)).

The rheology of lava is quite complex. It is not a pure liquid but is generally a multi-phase and chemically heterogeneous system, comprising of a melt component, a crystal component, gas bubbles and volatiles [30, 40]. The crystal and bubble volume fractions are time and temperature dependent. The transition from liquid to solidified lava occurs within a temperature interval determined by the liquidus (temperature above which the material is completely liquid) and solidus (temperature below which material is completely solid) temperatures. Lavas usually erupt above their liquidus temperature undergoing cooling (and possibly solidification) as they flow. Hence, the temperature of lava flows is usually in the range between their liquidus and solidus

temperatures. Above their liquidus temperature, lava flows are generally Newtonian liquids, e.g., basaltic lava (molten or partial molten basaltic rock) from volcanoes in Hawaii erupt at about 1200^o and have viscosities approximately 10^2-10^3 Pas. Below the liquidus temperature, lava flows exhibit non-Newtonian characteristics such as a shear-rate dependent viscosity (the apparent viscosity of the lava mixture) and a yield stress. Its rheology can be described as a viscoplastic material which typically behave on the macroscale as a single-phase liquid with no deformation when the applied stress is below the yield stress and the material behaves as a rigid solid, but when the yield stress is exceeded it begins to flow as a viscous liquid [3, 8, 30, 40]. This non-Newtonian behaviour is due to the presence of crystals below the liquidus temperature. The apparent viscosity and the yield stress of lava are a function of the temperature and volume fraction of crystals [40]. The rheological properties of lava such as the apparent viscosity and the yield stress play an important role in the dynamics and flow features of lava flows. The phase transition associated with the solidification of lava due to surface cooling can also play an important role. Solidification occurs by crystallisation if the cooling rate is slow and by the formation of glass if the cooling rate is rapid. The influence of solidification on the lava rheology is to increase the viscosity and the yield stress. The formation of a solid crust (also referred to as talus or carapace) at the lava surface, levées in channelised flows and tunnels in lava tubes are due to solidification of lava by surface cooling.

1.2 Laboratory and theoretical models related to lava flow

Laboratory and theoretical models have complemented field studies in developing the current understanding of lava flows and geological flow problems, in general. This has resulted in the creation of the field of *geological fluid mechanics*, reviewed by Huppert in 1986 [48].

We first consider the laboratory analogues of lava flow.

1.2.1 Laboratory analogue models

Most laboratory experiments of lava flows have focussed on their rheology using analogue materials. The experimental flow configuration involves extruding the lava analogue material from a small vent onto a horizontal or inclined substrate. These flows have then been studied under isothermal and non-isothermal conditions to investigate the morphology and dynamics of lava flows and their dependence on the three main effects associated with lava flows: non-Newtonian effects of shear-rate dependent viscosity and yield stress, temperature-dependent viscosity and yield stress and phase transition due to solidification.

Huppert [46] used Newtonian liquids, such as silicone oils and glycerine, to model the spreading of viscous gravity currents down an inclined plane. By following the

motion, he was able to determine the speed of the advancing liquid front and its depth before the current loses stability to a series of small amplitude rivulets which begin to grow across the slope at critical distances down the inclined plane. The wavelength of these patterns were shown to be controlled by the surface tension of the liquid and independent of its viscosity. Lister [54] performed similar experiments as Huppert using silicone oil, glycerol and sugar syrup to compare long-time theoretical predictions for point liquid release on an inclined plane from a constant flux and constant volume source with experiments (theoretical results discussed in §1.2.2).

Stasiuk *et al.* [80] performed experiments with warm glucose syrup to determine the effects of cooling on the flow behaviour with strongly temperature-dependent viscosity. Viscous-gravity currents of warm glucose syrup were released at constant rate into a tank filled with cold water. Their results show that cooling is preferential near the advancing flow front with the majority of the spreading fluid at a constant higher temperature. In certain cases, the cooling produces a nearly horizontal free surface profile and a steep flow front (like a *pancake*), rather than dome-shaped profile characteristic of spreading on a horizontal plane.

Hulme [45] hypothesised that lavas are non-Newtonian liquids with a yield stress. Laboratory measurements on flows of suspensions of kaolin slurries (materials that exhibit viscoplastic behaviour) were conducted. The occurrence of structures similar to levées on lava flows was predicted. He developed a theory for flows of Bingham liquids (see §1.3.1) for the description of a Bingham material) on inclined planes (dis-

cussed in §1.2.2). Blake [19] used Kaolin slurries to examine the effect of yield stress on the spreading rate and shape of lava domes. His experiments show that a growing dome maintains a state of static equilibrium and provided a scaling law for the dome height, H, as a function of its radius, R, density, ρ, and yield stress, τ_0, related by $H \sim (\tau_0 R/\rho g)^{1/2}$, and is independent of the effusion rate. Liu & Mei [55] perform experiments to study the dynamics of fluid mud using a mixture of Kalonite (clay material) and tap water to simulate mud. Balmforth *et al.* [5] considered the slow extrusion of a Kaolin-water-slurry mixture on a horizontal plane to study the experimental analogue of a slowly cooling lava dome. Osmond & Griffiths [70] obtained static lava dome shapes from laboratory experiments in which slurries of kaolin in polyethylene glycol (PEG) wax were extruded from a small source on an inclined plane. These shapes are compared with those obtained from a theoretical solution of a static three-dimensional shape of a fluid with a finite yield stress using their experimental configuration.

Bagdassarov & Pinkerton [4] investigate the effects of bubbles on the time-dependent, non-Newtonian properties of vesicular melts experimentally using analogue materials such as golden syrup and gum rosin. The shear-thinning behaviour of bubbly liquids is shown to be dependent on the previous shearing history. This behaviour, referred to as *Thixotropy*, is postulated to be caused by delayed bubble deformation and recovery when subjected to changes in shear stress.

To investigate the effects of phase transition due to solidification, laboratory experiments have used polyethylene glycol wax (PEG) or PEG-kaolin slurries, which cool

and solidify as they flow under cold water. These are used to model the growth of a surface crust on a spreading lava flow. These experiments have successfully reproduced a variety of lava flow features observed in field studies by varying the flow rate, the cooling rate and the inclination angle of the plane.

Fink & Griffiths [34] reproduced a variety of lava flow structures including levées, surface *wrinkling* oriented normal to the flow direction, surface fractures, and *pillows*. These are shown to be related to the growth rate of the surface crust. Their experiments showed that when the ambient temperature was low enough, solid crust developed on the surface of the spreading flow. Subsequent compression, extension and shear of the flow surface resulted in a range of morphologic features similar to that seen on natural lava flows. In Fink and Griffiths [35], laboratory simulations together with comparisons of lava dome growth, lead to a classification of various lava dome growth regimes in terms of their morphology. A sequence of four main types of dome were identified in laboratory analogue experiments with a Bingham viscoplastic flow. They represented an estimate of the yield strengths of the magma forming active domes based on data for the effusion rate and composition.

Lava analogue experiments by Griffiths, Kerr & Cashman [41] using polyethylene glycol (PEG) wax flowing down an inclined, open channel of rectangular cross-section under cold water. Two distinct styles of solid crust distribution are observed: "tube" in which there was a rigid solid roof over the flow for much of the length of the channel, with the flow proceeding through an encased tube beneath and a "mobile crust" in

which the flow surface along the centre of the channel was covered with solid, but remained mobile (solid raft). The crust was carried freely downstream. Transitional flow behaviour showed some elements of both the above regimes and was dependent on time and distance down the channel.

Experiments have also explored transitions between the various dynamical flow regimes. Blake & Bruno [20] have shown that the morphological transition from a uniform lava flow to a compound lava flow corresponds to the dynamical transition from the viscous flow regime to the surface crust controlled flow regime. Lyman *et al.* [57, 58, 59] investigated fixed volume releases in a horizontal channel and found that solidifying flows with no internal yield strength can initially spread in an inertial slumping regime and a viscous flow regime, before a final regime where the yield strength of the growing surface crust stops the flow. They also demonstrated that solidifying flows with an internal yield strength can be stopped by either the internal yield strength or the growing surface crust.

Garel *et al.* [38] investigate the coupling between the spreading of a solidifying flow and its surface thermal signal through analogue experiments using PEG wax that solidifies abruptly during cooling. They observe that the flow advance is discontinuous when the effusion rate is low resulting in compound lava flows. At high effusion rates, flows are less sensitive to solidification and exhibit a spreading behaviour similar to that of viscous gravity currents. They conclude that the effusion rate of lava flows can be retrieved from the surface thermal signature of lava flows. However, the prediction of

lava advance as a function of effusion rate is difficult due to the chaotic spreading of solidifying flows.

Robertson & Kerr [74] used polyethylene glycol and kaolin slurries to conduct experiments for isothermal, cooling, and solidifying flows to quantify the effects of the viscoplastic rheology and surface crust formation. An unyielded central plug region was observed to be formed under isothermal and cooling conditions. In the solidifying experiments, a tube regime, in which crust covered the entire flow surface and a shear-controlled regime, with a mobile raft of crust in the channel centre, were identified. Griffiths & Kerr [39] provide a nice overview of almost twenty years of their group's work using laboratory experiments and scaling laws to highlight the coupling between cooling, solidification and flow in generating the variety of features observed in lava flows.

1.2.2 Theoretical models

The general theoretical framework to model lava flows and mudflows is to consider a viscous gravity current generated by either a point or line source spreading down a horizontal or inclined plane (similar to the laboratory experiments). The spreading flow is assumed to be laminar and to have a small aspect ratio, i.e., the characteristic liquid thickness, H is much smaller than the spreading length, L, typical of such flows. This assumption would be valid after the lava has flowed a sufficiently long distance away from the vent. This allows lubrication theory (or a long-wavelength approximation) to

be used to simplify the Navier-Stokes equations (see Acheson [1] and Ockendon [66]).

The leading-order equations in the small aspect ratio, commonly referred to as the *thin-layer* or *thin-film equations* can then be used to determine the evolution of the free surface of the spreading viscous gravity current. The leading-order evolution equation of the free surface using lubrication theory for a Newtonian viscous gravity current spreading on an inclined surface is represented by an advection - diffusion Partial Differential Equation (PDE). The advection term corresponds to the horizontal component of gravity with a characteristic speed proportional to the second power of the free surface height (see Acheson [1] and Ockendon [66]). The diffusion term corresponds to the vertical component of gravity and the diffusion coefficient is proportional to the third power of the free surface height.

This framework has been used by several researchers to investigate various aspects of viscous gravity currents, particularly, their rheology under both isothermal and non-isothermal conditions, e.g., in glacier flows (Fowler [36, 37]), muds (Liu and Mei [55, 56], [26]) and debris flows (Davies [28]). The main physical mechanism in these flows is the balance between viscous forces and gravity and other effects such as surface tension are negligible. This is in contrast to drop spreading problems in which surface tension, surface tension gradients and intermolecular forces could also be important [27, 67].

Huppert [47] derived similarity solutions for the spreading of a viscous Newtonian fluid over a rigid horizontal plane of volume proportional to t^{α}, ($\alpha \geq 0$), in both axisymmetric and planar geometries. The solution predicts that for the axisymmetric

case, $R \sim t^{(3\alpha+1)/8}$ and $h \sim t^{(2\alpha-1)/4}$. For the planar case $L \sim t^{(3\alpha+1)/5}$ and $h \sim t^{(2\alpha-1)/5}$, where R is the radial distance, L is the spreading length and h is the thickness. For example, if $\alpha = 0$ (representing spreading of a constant volume of liquid), then $R \sim t^{1/8}$, $h \sim t^{-1/4}$ for the axisymmetric case and $L \sim t^{1/5}$, $h \sim t^{-1/5}$ for the planar case. The solution agrees well with his laboratory experiments for fixed volume and flux release. Lister [54] derived similarity solutions for the spreading of a Newtonian viscous gravity current generated by a point or line source of fluid down an inclined plane in both axisymmetric and planar geometries. The similarity solutions show that at late times a fluid of volume proportional to t^α spreads like $L \sim t^{(4\alpha+3)/9}$ and thins like $h \sim t^{(2\alpha-3)/9}$ from a point source, and $L \sim t^{(2\alpha+1)/3}$ and $h \sim t^{(\alpha-1)/3}$ from a line source. For example, if $\alpha = 0$, then $L \sim t^{1/3}$ and $h \sim t^{-1/3}$ from a line source. The spreading and thinning rates are faster as the volume and flux of fluid increases and angle of inclination of the plane increases. The flows are observed to be unstable across the slope in the experiments similar to those observed by Huppert [47].

More complex non-Newtonian rheologies have also been investigated by several researchers using the above flow configuration. Slow spreading of a Bingham plastic fluid (see §1.3.1) has been investigated by Liu and Mei [55, 56] to model the dynamics of mud flows. Liu & Mei [55] present a theory based on the shallow-water approximation (similar to the lubrication approximation) to derive the evolution equation of the free surface incorporating the yield stress and a yield surface (below the yield surface, the fluid is yielding and is undergoing shearing motion while above the yield

surface, there is plug flow, i.e., the flow speed is independent of depth). They show that by including the yield stress, a variety of static free surface shapes exist which are shown to be the final states of time-dependent motion. Also shown to exist are steady gravity currents which propagate at constant speed without change of form. Liu & Mei [56] use a modified Bingham plastic model based on bi-viscous fluids (fluid with a much larger viscosity above the yield surface and a much lower viscosity fluid in the region below the yield surface) to derive an approximate evolution equation for the free surface. The bi-viscous fluids model removes an inconsistency of using the Bingham plastic model to derive the thin-layer equations. The inconsistency in the thin-layer theory for Bingham materials, e.g., Liu & Mei [55], is that the equations are continued on to be derived at higher orders describing the lateral yielding motion of the layer, even though a rigid plug flow is assumed. The bi-viscous models replace the plug flow by a slowly yielding region. However, such bi-viscous models reduce to a Bingham model on setting a particular parameter to zero which reduces identically to the inconsistent theory above.

Hung and Garcia [44] extend the above theory to a Herschel - Bulkley fluid (see §1.3.1) to model mud flows. Using a matched-asymptotic perturbation method, they derive a uniformly valid solution over the entire spreading length by matching the inner region near the advancing flow front (balancing both the horizontal and vertical components of gravity and assumed quasi-static) and the outer region away from the front (where horizontal gravity dominates the spreading). The results for the spreading and runout

characteristics and the free surface shapes are shown to agree well with experiments of Liu & Mei [55]. Balmforth & Craster [6] derive a self-consistent thin-layer theory for the Bingham model which does not rely on applying any *ad hoc* approximations, such as the bi-viscous models used by Liu & Mei [56]. The authors demonstrated how lubrication theory could be formulated consistently to describe the existence of a *fake* yield surface separating the flow into two layers: the bottom layer, which is referred to as a region of fully plastic flow undergoing shearing motion, and the upper layer, referred to as a *pseudo-plug* flow region, where the shear rate is *nearly* zero. The term pseudo-plug means that the leading-order equations in this region predict a plug flow, but which is weakly yielding at higher order. They also extended this theory to a Herschel - Bulkley viscoplastic fluid model.

Using this theory, Balmforth *et al.* [5] modelled radially symmetric expanding lava domes by treating the lava as a viscoplastic material over a flat horizontal surface extruding from a point source. A variety of non-Newtonian and visoplastic rheological models were considered such as the Power-law, Bingham and Herschel - Bulkley models. Numerical and similarity solutions (based on volume increase in the dome proportional to t^{α}, where $\alpha \geq 0$) were derived that explore the effects of yield stress and shear thinning on the dome evolution. In Balmforth *et al.* [10], the same model was generalized to an inclined plane in $2+1$ dimensions (two-dimensional planar co-ordinates x and y and $z = h(x, y)$ is the free surface. A variety of numerical and similarity solutions are derived for the dome evolution depending on the yield stress and shear-thinning.

These are then used to characterise the domes' spreading and thinning rates. They also derived explicit solutions for the dome evolution in the field-stress dominated case.

Dubash *et al.* [31] constructed the final shape of a two-dimensional viscoelastic slump using two methods based on a small aspect ratio expansion and a slipline method to reconstruct shapes for arbitrary aspect ratios (following the study by Nye [65]). More recently, Hewitt & Balmforth [43] have extended the thin-film theory to model thixotropic gravity currents flowing down an inclined plane. The rheological constitutive law used to describe thixotrophy includes the degree of initial ageing and the spatio-temporal variations of the microstructure during flow. Their results show that a critical inclination angle needs to be exceeded for flow to be initiated that depends on the ageing time. Above this critical angle and for relatively long ageing times, the fluid dramatically avalanches down the plane with a characteristic fluid hump at the advancing front. The flow is prone to a weak interfacial instability that occurs along the border between structured and de-structured fluid. Experiments with bentonite clay show qualitative similar behaviour to that predicted by the model.

Pritchard *et al.* [73] derived a general evolution equation for a shallow layer of generalized Newtonian fluid undergoing unsteady two-dimensional gravity-driven flow on a horizontal or an inclined plane. This procedure offers a means of obtaining shallow-flow solutions for yield-stress fluids without explicitly tracking the yield surface within the fluid. Studies have also investigated the role of variable topography on the spreading characteristics, e.g., Bernabeu [16] and Osiptsov [68, 69], and including partial slip at

the plane (Vedeneeva [79]), instead of the no-slip condition.

While the isothermal (constant temperature) spreading process of a viscous gravity current has been well studied in the literature, comparatively fewer studies have investigated the non-isothermal effects in this context. Non-isothermal effects are important when there exists a strong coupling between the flow and the temperature field due to a strong dependence of the liquid properties on the temperature (e.g., its viscosity, surface tension, yield stress, etc.) and the heat transfer between the bulk liquid and the surroundings at the free surface and the underlying substrate.

Most non-isothermal mathematical models assume that, within the lubrication approximation in which the dome evolves slowly, heat is conducted (or diffused) sufficiently quickly across the thickness of the liquid layer compared to its convection by the flow, the so-called low reduced Péclet number asymptotic limit. (The reduced Péclet number is the product of the square of the aspect ratio and the Péclet number, which is the ratio of the convective to the diffusive heat transport.) This allows simplification of the temperature field depending on the boundary conditions applied at the free surface and the underlying substrate. If the temperature is specified at both boundaries, this limit results in a linear temperature profile vertical to the flow direction. On the other hand, if heat transfer boundary conditions are applied, then the temperature is uniform in vertical cross-sections at leading order in the aspect ratio, referred to as *thermally well mixed*. To the next order, a one-dimensional convection-diffusion equation for the temperature field can be derived.

This framework has been applied in related thin-layer models. Numerous studies have investigated thermocapillary effects (temperature-dependent surface tension). For example, Ehrhard & Davis [32] investigated theoretically the spreading of a liquid over a horizontal substrate subject to capillary, thermocapillary and gravitational forces. Ajaev & Willis [2] investigate the surface tension gradient-driven flow due to non-uniform heating resulting in the rupture of molten films on a horizontal substrate. Studies more relevant to this thesis are those concerned with the effects of cooling on the dynamics of a gravity current with temperature-dependent viscosity. Sakimoto & Zuber [75] considered a cooling gravity current with a viscosity that has a power-law dependence on time. This model was used to describe the plateau features observed in *pancake* domes observed on Venus.

The flow from a point source of material with a more general temperature-dependent viscosity was investigated by Bercovici [13]. He simulated free surface profiles that develop a steep flow front followed by a central plateau. This work was agreement with experiments performed by Stasiuk et al. [80]. Bercovi and Lin [14] discussed the cooling of mantle plume heads using a temperature-dependent viscosity model. Wyli and Lister [84] investigated instabilities in channel flows undergoing cooling at the channel walls using a temperature-dependent viscosity model. This was used to model fissure eruptions. This study was extended by Wall and Wilson [81] to consider a broad range of temperature-dependent viscosity models. Wilson & Duffy [82, 83] investigated the unsteady gravity-driven draining of a thin rivulet of Newtonian fluid

with temperature-dependent viscosity down a substrate that is either uniformly hotter or uniformly colder than the surrounding atmosphere. A general nonlinear evolution equation was derived for a thin film of fluid with an arbitrary dependence of viscosity on temperature. This model was then used to provide a complete description of the steady flow of a slender rivulet. The PhD thesis of Sansom [76] was the first comprehensive study to investigate the non-isothermal spreading of a viscous gravity current on a horizontal substrate using three temperature-dependent viscosity models (linear, exponential and bi-viscosity). This was motivated by the problem of spreading of coolants in nuclear engineering. A nonlinear diffusion equation was derived for the evolution of the free surface with the diffusion coefficient inversely proportional to the temperature-dependent viscosity. Both the low reduced Péclet number asymptotic limit as well as $O(1)$ reduced Péclet number (in this case, convective heat transport is comparable to vertical conduction of heat) are considered with boundary conditions that either prescribe the temperatures or allow transfer of heat at the free surface and the underlying substrate.

The numerical results for the $1 + 1$ dimensional free surface shapes showed a common feature of the development of a steep flow front followed by a central plateau (the pancake-type profile). This is caused by preferential cooling of fluid near the flow front which forms a barrier, forcing the height at the front to grow as hot, less viscous fluid continues to be fed in behind the front. They also showed that introducing perturbations along the flow front, transverse to the flow direction, can cause the

development of fingering behaviour. This occurred when the coupling between the viscosity and temperature fields was strong and sufficient amount of cooling was necessary in order to produce a significant viscosity contrast along the flow front. The author showed that the fingering patterns were caused by the viscosity gradients near the flow front. Aspects of this thesis have been published in King *et al.* [53] and Sansom *et al.* [77]. Balmforth [7] extend their earlier model of the spreading of a viscoplastic dome over a horizontal plane to include non-isothermal effects. They modified the Herschel-Bulkley constitutive law to include a temperature-dependent viscosity and yield stress. Solutions were obtained for the growth of a vertically isothermal lava dome in the asymptotic limit of low reduced Péclet number. They also considered the development of non-axisymmetrical domes and used the thin layer model to explore the possibility of fingering-type instabilities. Balmforth [11] extended their earlier study to allow the reduced Péclet number to be $O(1)$. An efficient computational algorithm is presented for numerically solving the evolution equation of the free surface coupled to the temperature equation, which depends on both the axial and the vertical coordinates. They describe solutions similar to that presented by Sansom *et al.* [53, 76, 77] that illustrate the dynamics of an expanding Bingham fluid with a temperature-dependent viscosity.

A key feature (also noted by Sansom [76]) highlighted in their results is that liquid near the flow front gets chilled and is then overridden as the fluid expands, creating a so-called *collar* of cold liquid. Two simpler models that further approximate the temperature equation: a vertically isothermal theory (similar to Balmforth [7]), and a *skin*

theory are compared to the $O(1)$ reduced Péclet number numerical simulations. Bernabeu [15] generalized their earlier model [16] to include the non-isothermal viscoplastic flow problem with temperature-dependent viscosity and yield stress on a general topography. The governing equations were solved numerically by auto-adaptive finite element methods allowing to track accurately the front position. Diniega et al. [29] investigate the role of large change in viscosity due to small change in temperature in the formation and propagation of preferred pathways in lava flows. they show that these pathways are initiated when the temperature dependence of viscosity is sufficiently strong. They are shown to form and stabilise over a distance depending on the competition between the cooling rate and the low velocity with in the preferred pathway.

Even fewer models, in the context of spreading viscous gravity currents, have considered phase transition associated with solidification. Bunk *et al.* [22] investigated the spreading of melts on a horizontal substrate under the influence of solidification of the underlying substrate. The influence of solidification on the spreading flow is considered for volume proportional to t^α and various regimes are identified for varying α corresponding to complete solidification, retreating contact lines, stagnating contact lines and advancing contact lines. Myers *et al.* [64] investigated the flow of a thin film undergoing basal solidification on an arbitrary three-dimensional substrate. This modelled the flow and accretion of ice on an aircraft wing. Zadrazil *et al.* [85] studied the spreading, imbibition and solidification of a hot droplet on a cooler porous substrate.

Their numerical results capture the essential dynamics which include: spreading and imbibition accompanied by solidification within the pores leading to their blockage, followed by contact line arrest and basal solidification of the droplet. The possibility of solidified crust formation at the air-liquid interface is excluded from the above and related studies. The crust can directly affect the dynamics by contributing additional forces. For example, a solid shell-like crust may exert a tensile restraining force, as considered by Iverson [50]. Bourgouin *et al.* [21] investigate the axisymmetric evolution of a lava dome enclosed by a brittle shell. They adopted Iverson's assumption that the thin boundary layer behaves like an ideal plastic membrane shell [50] which allowed imposing a surface tension-like boundary condition for the normal stress at the free surface. The level set computational method was used to track the evolution of the deforming interface. Hale [42] developed a computational model for the axisymmetric growth and evolution of a lava dome, including a deformable talus or carapace. The dome is modelled as a fluid with a yield stress while the talus deformation is modelled as a granular material. The growth of the talus and core were found to be strongly dependent on the lava extrusion rate, degree of solidification, the friction angle associated with the talus, and lava dome viscosity.

We can conclude from the above literature review that the main emphasis of the research in the spreading of viscous gravity currents has been primarily on the non-Newtonian rheological aspects of these flows under isothermal conditions. Few studies have investigated the coupling between the flow and cooling and the morphological flow

features and spreading characteristics associated with it. Sansom *et al.* [76, 53, 77] and Balmforth *et al.* [7, 11] have made significant contributions in developing the theoretical framework to investigate non-isothermal aspects of these flows. However, these studies have investigated only spreading over a horizontal substrate and their parameter studies have been restricted to a weak coupling between the flow and cooling. Although, thermoviscous effects (via the temperature-dependent viscosity) have been postulated as the mechanism driving the fingering instabilities, these studies have been unsuccessful in simulating them. We believe that the enhanced mobility of the current due to the inclination of the substrate and its strong coupling with cooling will unravel new flow features that may contribute to the finger instabilities not easily observed in the previous studies.

1.3 Preliminary background on fluid rheology and constitutive laws, energy equation and temperature-dependent viscosity models

We provide below an introductory background on fluid rheology of Newtonian and non-Newtonian fluids and their constitutive laws, the energy equation for non-isothermal conditions and temperature-dependent viscosity relationships that are used in this thesis. A table of the relevant parameter values for lava analogue materials and real lava are provided in Table 1.1.

1.3.1 Fluid rheology and constitutive laws

The study of the relationship between flow of viscous liquids in response to applied stress is known as Rheology [18]. This field investigates the flow behaviour of liquids such as foods, biological, polymers, slurries and other compounds. We consider a simple two-dimensional shearing flow which is relevant to lava flows. Consider a thin layer of a liquid placed between two parallel planes of area $A^\star$ as shown in Fig. 1.2. We consider a two-dimensional planar coordinate system, $(x^\star, y^\star)$, horizontal and vertical to the plane, respectively. The top plane is moved with constant velocity, $U^\star$, by the

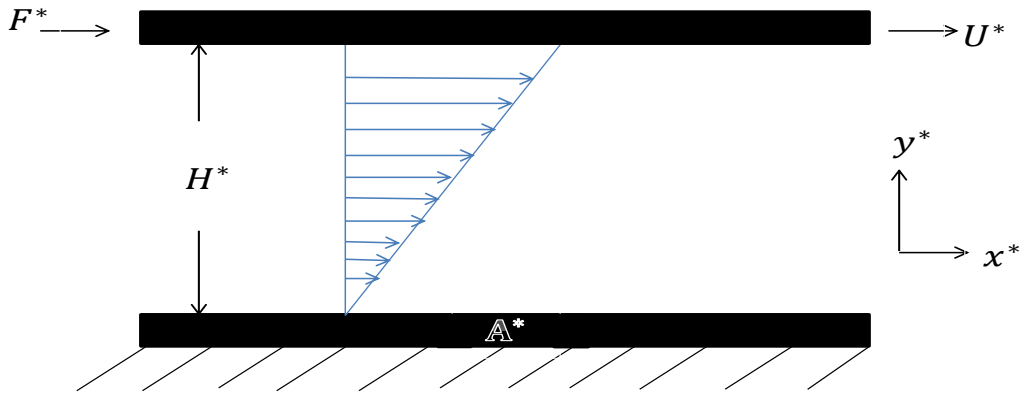

Figure 1.2: Schematic representation of unidirectional two-dimensional shearing flow.

application of a shearing force $F^\star$, while the bottom plane is fixed. Let us assume that a well-developed shearing flow that is parallel to the plane and linear in the vertical direction, $y^\star$, is created due to this shearing force. In this context, the following

definitions apply [25]:

(i) **Shear stress**: The shear stress, $\tau^{\star}_{xy} = F^{\star}/A^{\star}$, is defined by the force per unit area, where the subscript in the shear stress $\tau^{\star}$ represents the stress in the $x^{\star}$ direction acting on a plane whose normal is in the $y^{\star}$ direction .

(ii) **Shear rate:** The shear rate (or rate of strain), $\dot{\gamma}^{\star}$, is the velocity difference between the planes divided by the distance between the two planes, i.e $\dot{\gamma}^{\star} = U^{\star}/H^{\star} = du^{\star}/dy^{\star}$, where $u^{\star}$ is the flow speed in the $x^{\star}$ direction and is assumed to be linear in $y^{\star}$.

A liquid is referred to as a *Newtonian* liquid if the shear rate is proportioned to the applied stress. The constant of proportionality is referred to as the viscosity of the liquid and measures the resistance of the liquid to the shearing force. For the unidirectional two-dimensional shearing flow shown in Fig. 1.2, $\tau^{\star}_{y^{\star}x^{\star}} = \mu^{\star} du^{\star}/dy^{\star}$ for a Newtonian fluid and $\mu^{\star}$ is the fluid viscosity. The above relationship is also referred to as Newton's law of viscosity. The magnitude of the viscosity is not dependent on the shear rate or shear stress and depends only on the material properties, temperature and pressure. This means that when shear stress is plotted versus shear rate, the plot shows a straight line with a constant slope μ passing through the origin (see Fig. 1.3). Table 1.1 shows the wide viscosity range for common materials [25]. For three-dimensional flows in general, we have for a Cartesian coordinate system, $(x^{\star}, y^{\star}, z^{\star})$ the following

stresses applied in the x, y and z direction, respectively [1].

$$\tau^{\star}_{x^{\star}x^{\star}} = 2\mu^{\star}\frac{\partial u^{\star}}{\partial x^{\star}} + \frac{2}{3}\mu^{\star}\Big(\frac{\partial u^{\star}}{\partial x^{\star}} + \frac{\partial v^{\star}}{\partial y^{\star}} + \frac{\partial w^{\star}}{\partial z^{\star}}\Big), \tau^{\star}_{x^{\star}y^{\star}} = \mu^{\star}\Big(\frac{\partial u^{\star}}{\partial y^{\star}} + \frac{\partial v^{\star}}{\partial x^{\star}}\Big), \tau^{*}_{x^{\star}z^{\star}} = \mu^{*}\Big(\frac{\partial u^{\star}}{\partial z^{\star}} + \frac{\partial w^{\star}}{\partial x^{\star}}\Big), \tag{1.1a}$$

$$\tau^{\star}_{y^{\star}y^{\star}} = 2\mu^{\star}\frac{\partial v^{\star}}{\partial y^{\star}} + \frac{2}{3}\mu\Big(\frac{\partial v^{\star}}{\partial y^{\star}} + \frac{\partial u^{\star}}{\partial x^{\star}} + \frac{\partial w^{\star}}{\partial z^{\star}}\Big), \tau^{\star}_{y^{\star}x^{\star}} = \mu^{\star}\Big(\frac{\partial v^{\star}}{\partial x^{\star}} + \frac{\partial u^{\star}}{\partial y^{\star}}\Big), \tau^{\star}_{y^{\star}z^{\star}} = \mu^{\star}\Big(\frac{\partial v^{\star}}{\partial z^{\star}} + \frac{\partial w^{\star}}{\partial y^{\star}}\Big), \tag{1.1b}$$

$$\tau^{\star}_{z^{\star}z^{\star}} = 2\mu^{\star}\frac{\partial w^{\star}}{\partial z^{\star}} + \frac{2}{3}\mu^{\star}\Big(\frac{\partial w^{\star}}{\partial z^{\star}} + \frac{\partial u^{\star}}{\partial x^{\star}} + \frac{\partial v^{\star}}{\partial y^{\star}}\Big), \tau^{\star}_{z^{\star}x^{\star}} = \mu^{\star}\Big(\frac{\partial w^{\star}}{\partial x^{\star}} + \frac{\partial u^{\star}}{\partial z^{\star}}\Big), \tau^{\star}_{z^{\star}y^{\star}} = \mu^{\star}\Big(\frac{\partial w^{\star}}{\partial y^{\star}} + \frac{\partial v^{\star}}{\partial z^{\star}}\Big). \tag{1.1c}$$

Also using symmetry based on the assumption that the fluid is isotropic, [18] we have

$$\tau^{\star}_{y^{\star}x^{\star}} = \tau^{\star}_{x^{\star}y^{\star}}, \tau_{x^{\star}z^{\star}} = \tau^{\star}_{z^{\star}x^{\star}}, \tau^{\star}_{y^{\star}z^{\star}} = \tau^{\star}_{z^{\star}y^{\star}}. \tag{1.2}$$

Any liquid that does not follow Newton's law of viscosity (the proportionality relationship between shear stress and shear rate) is classified as a *non-Newtonian* liquid. The slope of shear stress against shear rate curve is not linear or does not pass through the origin (see Fig. 1.3 for various non-Newtonian liquid behaviours). One then defines an apparent viscosity for such liquids which is dependent on the shear rate. The subject of rheology is devoted to the study of the behavior of such fluids. These fluids can be classified into three categories [25]:

(i) Those fluids for which the rate of shear depends only on the value of the instantaneous shear stress.

(ii) Those fluids for which the relation between shear stress and shear rate depends on both the duration of shearing and their kinematic history. These fluids seem to exhibit a delayed response which fades with time.

(iii) *Viscoelastic* liquids: Viscoelastic fluids are those materials that exhibit both viscous and elastic properties. The rheological properties of such a materials at any moment of time will be a function of the recent history of the material. We cannot describe it by simple relationships between shear stress and shear rate, it also depends on the time derivative of both of these quantities. Examples of viscoelastic fluids are polymer melt, bread dough and egg white.

In our study, we only consider non-Newtonian fluid behaviour classified in (i) above. These fluids are referred as generalized Newtonian fluids (GNF). These fluids, in turn, may be classified into three types:

(i) *Shear thinning* fluids: As the name indicates, the apparent viscosity of these fluids decrease with increasing shear rate. A number of non-Newtonian materials can be described as shear thinning fluids, e.g., grease, molasses, paint and starch.

(ii) *Shear thickening* fluids: The apparent viscosity of this type of fluid increases with the shear rate. They are also called as dilatants fluids. Beach sand mixed with water and peanut butter are common example of dilatants fluids.

(iii) *Viscoplastic* fluids: Viscoplastic materials are type of fluids characterized by a yield stress. When the yield stress is exceeded by externally applied stress, the

material will deform or flow. But if the externally applied stress is smaller than the yield stress, then it behaves like a rigid solid. The common feature of these type of materials is when left alone they simply sit and do not flow, unless they are pushed sufficiently strongly, for example, mud and lava flows, landslides and avalanches and biological materials like mucus are viscoplastic materials [12].

The relationship between the fluid shear stress and shear rate is mathematically described using a constitutive law or equation.

Newtonian constitutive equation:

The Newtonian constitutive equation for compressible fluids is written as [60]

$$\boldsymbol{\tau}^{\star} = \mu^{\star}\dot{\boldsymbol{\gamma}}^{\star} - \frac{2}{3}\mu^{\star}\ (\nabla^{\star}.\mathbf{u}^{\star})\boldsymbol{I}^{\star}, \tag{1.3}$$

where

$$\dot{\boldsymbol{\gamma}}^{\star} = \Big[\nabla^{\star}\mathbf{u}^{\star} + \nabla\mathbf{u}^{\star T}\Big], \tag{1.4}$$

or

$$\dot{\gamma}_{ij}^{\star} = \Big[\frac{\partial u_i^{\star}}{\partial x_j^{\star}} + \frac{\partial u_j^{\star}}{\partial x_i^{\star}}\Big]. \tag{1.5}$$

For an incompressible Newtonian fluid

$$\boldsymbol{\tau}^{*} = \mu^{*}\dot{\boldsymbol{\gamma}}^{*}, \tag{1.6}$$

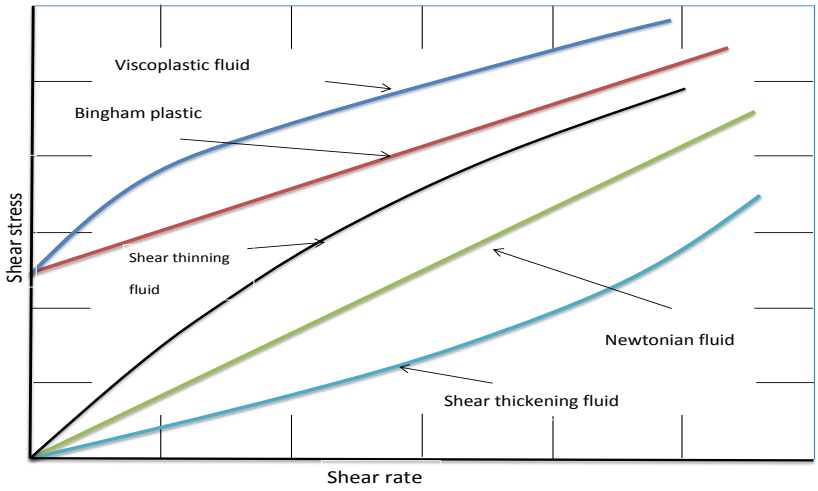

Figure 1.3: Shear stress versus shear rate for a Newtonian and various non-Newtonian fluids. Adapted from Chhabra *et al.* [25].

Generalized Newtonian fluid (GNF) constitutive equations:

The essential shortcoming of the Newtonian constitutive equation is that viscosity is constant, whereas in many fluids the viscosity varies with the flow. In order to improve the applicability of the Newtonian constitutive equation, it requires a development or modification of the linear relationship between the stresses and the strain rates that allow for variable viscosity, such a model is the GNF [8, 25]. We can write the stress versus shear rate relationship as:

$$\boldsymbol{\tau}^* = \mu^*(\dot{\gamma}^*)\dot{\boldsymbol{\gamma}}^*, \tag{1.7}$$

where $\mu^*(\dot{\gamma}^\star)$ is the non- Newtonian viscosity and $\dot{\boldsymbol{\gamma}}^*$ is the rate of strain tensor given by Eq. (1.4). The second invariant of the strain rate tensor, $\dot{\gamma}^*$, is given by

$$\dot{\gamma}^* = |\dot{\boldsymbol{\gamma}}^*| = \sqrt{\frac{1}{2}\dot{\boldsymbol{\gamma}}^* : \dot{\boldsymbol{\gamma}}^*}. \tag{1.8}$$

Power law fluid:

The most widely used form of the GNF constitutive relation is for a power-law fluid and is expressed by [18]

$$\boldsymbol{\tau}^* = k\dot{\boldsymbol{\gamma}}^{*n}, \tag{1.9}$$

where k is the consistency index and n is the power index.

The above model can also be expressed as

$$\boldsymbol{\tau}^* = k^*\dot{\gamma}^{*n-1}\dot{\boldsymbol{\gamma}}^*, \tag{1.10}$$

and the viscosity for the power-law fluid is

$$\mu^*(\dot{\gamma}^*) = k^*\dot{\gamma}^{*n-1}. \tag{1.11}$$

Based on the value of the power-law index the fluids can be classified as shear thinning ($n < 1$; see black curve in Fig. 1.3), Newtonian ($n = 1$; see green curve in Fig. (1.3)) and shear thickening ($n > 1$; see light blue curve in Fig. 1.3). For low shear rates the power law model can give very inaccurate predictions since the apparent viscosity

diverges for a shear thinning fluid and approaches zero for a shear thickening fluid (see Myers [63]). When a fluid is subject to a range of shear rates, including very low values, a different model must be used. Commonly used models include the Carreau and Ellis models which can capture both the low and high shear Newtonian region. We use the Carreau model in this thesis which can be written as:

$$\mu^\star(\dot{\gamma}^\star) = \mu^\star_\infty + \frac{\mu^\star_0 - \mu^\star_\infty}{(1+\lambda^{\star 2}\dot{\gamma}^{\star 2})^{(\frac{1-n}{2})}}, \tag{1.12}$$

where $\mu^\star_0$, $\mu^\star_\infty$ are the limiting viscosities at high and low shear rates.

Herschel-Bulkley fluid:

The Herschel-Bulkley model extends the power-law model to include both shear thinning or thickening and a yield stress [8]. It is written as

$$\begin{aligned} \boldsymbol{\tau}^* &= \left[k^*\dot{\gamma}^{*n-1} + \tfrac{\tau^*_p}{\dot{\gamma}^*}\right]\dot{\boldsymbol{\gamma}}^* \qquad \text{for} \quad \tau^* \geq \tau^*_p, \\ \dot{\boldsymbol{\gamma}}^* &= 0 \qquad\qquad\qquad\qquad\quad \text{for} \quad \tau^* < \tau^*_p, \end{aligned} \tag{1.13}$$

where $\tau^* = |\boldsymbol{\tau}^*| = \sqrt{\frac{1}{2}\boldsymbol{\tau}^* : \boldsymbol{\tau}^*}$ and τ^*_p is the yield stress (see dark blue curve for $\tau^*_p \neq 0$ and $n < 1$ in Fig. 1.3). If $\tau^*_p = 0$, then it reduces to a Power-law fluid, and if $\tau^*_p \neq 0$ and $n = 1$, it reduces to a Bingham fluid; see red curve in Fig. 1.3). The Bingham model does not have the ability to deal with shear-thinning (or thickening) properties. The Herschel-Bulkley model is more realistic since viscoplastic fluids usually exhibit both

a yield stress and a non-linear viscosity [12], and are also commonly used to describe many biological fluids, mud, clay, water slurries, etc.. There are many studies including the Herschel-Bulkley rheological model (see [8, 16, 72]).

1.3.2 The energy equation

The general equation for the rate of change of heat energy per unit volume, $\rho^\star c_p^\star T^\star$, in a material with density, $\rho^\star$, specific heat, $c_p^\star$, thermal conductivity, $\kappa^\star$, thermal diffusivity, $\kappa_d^\star = \kappa^\star/(\rho^\star c_p^\star)$ and temperature $T^\star$ is given by (see Carslaw & Jaeger [23]):

$$(\rho^\star c_p^\star T^\star)_{t^\star} + (\mathbf{u}^\star.\nabla^\star)(\rho^\star c_p^\star T^\star) = \nabla^\star.[\kappa_d^\star \nabla^\star(\rho^\star c_p^\star T^\star)] + \mu^\star \dot{\gamma}_{ij}^{\star 2}, \tag{1.14}$$

where the last term represents heat energy generated through viscous dissipation or friction. We will assume that both the density and specific heat are constant (see Table 1.1), so Eq. (1.14) can be simplified to

$$\rho^\star c_p^\star [T_{t^\star}^\star + (\mathbf{u}^\star.\nabla^\star)T^\star] = \nabla^\star.[\kappa^\star \nabla^\star T^\star] + \mu^\star \dot{\gamma}_{ij}^{\star 2}, \tag{1.15}$$

This equation is supplemented by boundary conditions. In this thesis, we consider heat transfer boundary conditions of the form:

$$-\kappa^\star(\mathbf{n}^\star \cdot \nabla^\star T^\star) = F^\star(T^\star), \tag{1.16}$$

where $\mathbf{n}^\star$ is the outward pointing normal and $F^\star$ is the heat flux at the boundaries. Depending on the physical conditions, various forms are possible, e.g., thermal radiation, convection by wind, convection and conduction in overlying water. We use a simple form based on Newton's law of cooling, so

$$F^\star(T^\star) = a_m^\star(T^\star - T_a^\star), \tag{1.17}$$

where $a_m^\star$ is a heat transfer coefficient and $T_a^\star$ is the ambient temperature. Such a form of the flux function has been used by Balmforth *et al.* [5, 11].

1.3.3 Temperature-dependent viscosity constitutive relationships

As observed in Table 1.1, viscosity variations in temperature could be quite significant in lava flows. Viscosity increases as temperature decreases and this relationship is important in modelling the cooling of liquids, such as in lava flows. Figure 1.4 shows a graph of viscosity versus temperature for various types of lava obtained from Diniega et al. [29]. We observe that the viscosity variations are largest for lava with a high silica content (e.g., Dacite and Rhyolite) and the viscosity contrast decreases for lava with less silica content (e.g., Andesite and Basalt). The simplest viscosity relationship

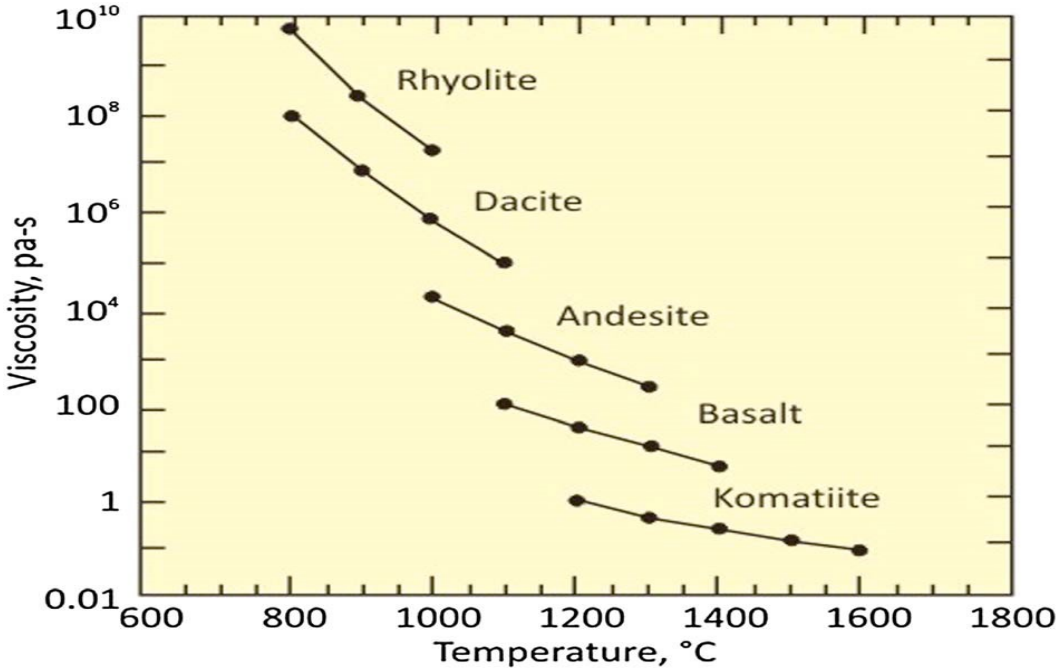

Figure 1.4: Measurements of viscosity versus temperature (solid dots) obtained from Diniega et al. [29] for various types of lava. The solid lines are correlations using the Arrhenius law given in Eq.(1.18).

based on the Arrhenius law is:

$$\mu^\star(T^\star) = \mu_0^\star e^{-\alpha^\star(T^\star - T_a^\star)}, \tag{1.18}$$

where $T^\star$ is the temperature, $T_a^\star$ is a reference temperature, e.g., the ambient temperature), $\mu_0^\star$ is the viscosity at the reference temperature and $\alpha^\star$ is the decay constant. This relationship has been used by Wall & Wilson [81] and Balmforth *et al.* [5, 11] and Sansom *et al.* [53, 76, 77], in related problems. Another temperature-viscosity relationship considered in this thesis is a bi-viscosity model This relationship was proposed by Wylie & Lister [84] and also used by Sansom *et al.* [53, 76, 77]. It can be written

as:

$$\mu^\star = \begin{cases} \mu_e^\star & \text{if } T^\star > T_m^\star, \\ \mu_a^\star & \text{if } T^\star < T_m^\star, \end{cases} \tag{1.19}$$

where $\mu_a^\star = \mu^\star(T_a^\star)$, $\mu_e^\star = \mu^\star(T_e^\star)$ (with $\mu_a^\star > \mu_e^\star$), $T_a^\star$ and $T_e^\star$ are an ambient and eruption temperature, respectively, and $T_m^\star$ ($T_a^\star < T_m^\star \leq T_e^\star$) is a fixed temperature in the solidus-liquidus transition.This relationship is a proxy of a nearly solidified layer characterised by a higher viscosity.

1.3.4 Physical parameters values

In Table 1.1, we provide estimates for the parameters (in some cases at different temperatures) and references they have been obtained from relevant to lava flows. These include: the viscosity, $\mu^\star$, density, $\rho^\star$, yield stress, $\tau_{p^\star}^\star$, specific, $c_p^\star$, and the thermal conductivity, $\kappa^\star$. We observe that the most significant change is in the viscosity with temperature compared to any of the other parameters. We will assume that all the other parameters are constant and independent of temperature. Note that the yield stress could also be strongly dependent on the temperature [40], but will not be considered here.

Liquid	θ (^{o}C)	$\mu^\star$ (Pa s)	$\rho^\star$ (kg/m^3)	$\tau^\star_{p^\star}$ (Pa)	$c^\star_p$ (J/(kg(^{o}C))	$\kappa^\star$ (J/(m s(^{o}C))
Water	20	9×10^{-4}	998	0	4183	0.598
	80	3×10^{-4}	970	0	4200	0.667
Glucose syrup	21	1.3×10^2	1438	0		
(Stasiuk *et al.* [80])	-13	3.2×10^5		0	2059	0.358
PEG	18	0.18	1126	0	2500	0.218
(Fink & Griffiths [35])	25		1122	0		
Kaolin-PEG wax		0.78	1450	84	1800	0.365
(Fink & Griffiths [35])						
Kaolin-water		20	1360	44		
1:1 by weight						
Basaltic lava	1150	$O(10^2)$	2800	$O(10^2)$	1200	1.26
(Fink & Griffiths [35],	1400	$O(10)$				
Diniega et al. [29])						
Silicic lava (e.g., Dacite)	800	$O(10^8)$	2600	$O(10^5)$	1150	1.26
(Fink & Griffiths [35],	1150	$O(10^5)$				
Diniega et al. [29])						

Table 1.1: Physical properties of various liquids.

1.4 Thesis Aims and Objectives

The main aim of this thesis is to theoretically investigate the coupling between the fluid flow and cooling on the flow features and spreading characteristics of liquid domes. We extend the previous modelling studies by Sansom *et al.* [76, 53, 77] and Balmforth *et al.* [7, 11] to consider the spreading of a viscous gravity current over an inclined substrate. We incorporate non-isothermal effects, such as a temperature-dependent viscosity and heat transfer conditions at the boundaries, to investigate the flow features and the spreading behaviour, and the linear stability of these flow features to transverse perturbations. We extend the previous modelling studies by Sansom et al. [74, 51, 75] and Balmforth et al. [7, 11] to consider the spreading of a viscous gravity current over

an inclined substrate. We believe that the additional flow mobility due to the downslope of the inclined substrate coupled with the cooling could result in new flow features, such as the piling-up of fluid near the advancing front, which is not observed in the above studies. Moreover, they could also strongly influence the stability of the front transverse to the flow direction. The absence of such flow features for spreading on a horizontal substrate, in our opinion, is the reason why these studies cannot predict sustained fingering instability. Furthermore, the current work aims to perform a systematic parameter study to identify the necessary conditions based on the observed flow features to fully characterise the existence of the fingering instability. We emphasis here that the results presented in this thesis are purely theoretical; the validation with experiments and field studies will be considered in the future.

1.5 Thesis outline

In this thesis, we extend the theoretical framework developed by Sansom *et al.* [76, 53, 77] and Balmforth *et al.* [7, 11] to investigate the spreading behaviour of a liquid dome down an inclined substrate under isothermal and non-isothermal conditions. The thesis outline is as follows.

In Chapter 2, we explore the one-dimensional spreading of an isothermal and Newtonian planar liquid dome over an inclined substrate with a prescribed flowrate coming through a source or vent on the underlying substrate. We reproduce the early and late-time

similarity solutions by Huppert [47] and Lister [54] which are also validated with the corresponding numerical simulations. In Chapter 3, the one-dimensional Newtonian liquid model is extended to incorporate non-Newtonian effects of apparent viscosity and yield stress. We reproduce early and late-time similarity solutions by Balmforth *et al.* [5, 9] and also identify some new similarity solutions depending on the parameter space, which are also validated with the corresponding numerical simulations. We also discuss the effect of variations of the key parameters on the dome's evolution. Chapter 4 extends the model to incorporate non-isothermal effects and a temperature-dependent viscosity. We focus on the asymptotic limit of a low reduced Péclet number which enables the temperature field to be simplified to vary only in x and t, coupled to an evolution equation for the dome's free surface. We use numerical simulations to determine the evolution of the spreading dome and temperature field. A thorough parametric study is conducted to determine the influence of key parameters, such as the Peclet number, heat transfer coefficients at the free surface and substrate, and the decay constant, $\alpha^\star$, in the exponential viscosity model, with and without a source using two different type of temperature-dependent viscosity relationships, such as the exponential and bi-viscosity models. We identify some new free surface shape profiles which include a fluid hump overriding the front at the dome's leading edge. In Chapter 5, we consider the reduced Péclet number, $Pe_r = O(1)$. The one-dimensional evolution equation for the dome's free surface is coupled to a two-dimensional (both vertical and in the flow direction) advection-diffusion equation for the temperature. We use numerical simulation to describe a variety of dome spreading shapes in different parameter

regimes. We recover the $Pe_r \ll 1$ asymptotic limit solutions of Chapter 4. In fact, we are able to show that the one-dimensional temperature solutions from Chapter 4 for low Pe_r are in good agreement with their corresponding parameter values in Chapter 5. Chapter 6 considers the transverse stability of the one-dimensional solutions determined numerically in Chapters 4 and 5 (assumed *frozen* in time) to small-amplitude perturbations imposed near the leading edge of the dome. Numerical results reveal the existence of a new fingering instability. A thorough investigation of the parameters are done to determine the mechanism behind this instability and to characterise and classify its growth rate and dominant wavenumbers. Finally, in Chapter 7 we draw some general conclusions and briefly describe the future work.

Chapter 2

The isothermal and Newtonian spreading of a liquid dome down an inclined plane

2.1 Introduction

This chapter investigates the evolution of an isothermal and Newtonian liquid dome spreading down an inclined and pre-wetted plane. This problem is the simplest model of a spreading gravity current under isothermal conditions. We extend this model to include an influx flowrate coming from a source on the substrate to mimic lava flow from a vent. We use similarity and numerical solutions to characterise the evolution of the free surface for a range of parameter values corresponding to the source flowrate

and the inclination angle.

The outline of this chapter is as follows. We formulate the one-dimensional mathematical problem in a Cartesian co-ordinate system in §2.2 which provides the governing equations and boundary conditions for the flow. The lubrication approximation allows simplification of the governing equations and boundary conditions to an advection-diffusion PDE for the evolution of the one-dimensional free surface shape. In §2.3 we derive late-time similarity solutions for the evolution of the free surface such that the volume of liquid in the dome is proportional to t^α, ($\alpha \geq 0$). These solutions are then matched against those previously derived by Huppert [47] and Lister [54]. In §2.4, we perform numerical simulations of the evolution equation to determine the free surface shapes for a variety of parameter values. The numerical solutions are validated against the similarity solutions. In §2.5 we discuss the main results.

2.2 Mathematical Formulation

Consider a liquid dome spreading under the influence of gravity down an inclined and pre-wetted plane (see Fig. 2.1). Liquid is introduced into the dome through a source at a fixed location on the plane. We introduce a Cartesian coordinate system $(x^\star, z^\star)$ with the $x^\star$-axis along the plane and the $z^\star$-axis normal to the plane. We denote the free surface of the dome (the air-liquid interface) as $z^\star = h^\star(x^\star, t^\star)$, $(u^\star, w^\star)$ denote the components of the liquid velocity in the x and z directions, respectively and $p^\star$ is

the pressure in the liquid. The liquid in the dome is assumed to be Newtonian with viscosity $\mu^\star$ and its density is $\rho^\star$.

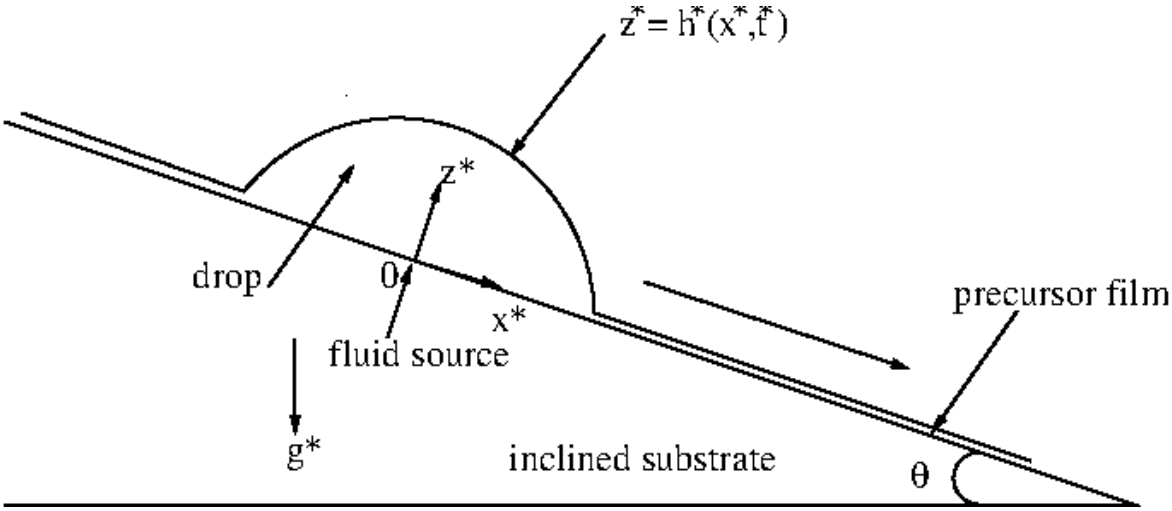

Figure 2.1: Sketch of a dome spreading down on an inclined plane.

2.2.1 Governing Equations

The two-dimensional governing equations are given by the conservation of mass and momentum (see Acheson [1] and Ockendon [66]),

$$u^\star_{x^\star} + w^\star_{z^\star} = 0, \tag{2.1a}$$

$$u^\star_{t^\star} + u^\star u^\star_{x^\star} + w^\star u^\star_{z^\star} = -\frac{1}{\rho^\star} p^\star_{x^\star} + g^\star \sin\theta + \frac{1}{\rho^\star}[\partial^\star_x \tau^\star_{x^\star x^\star} + \partial^\star_z \tau^\star_{x^\star z^\star}], \tag{2.1b}$$

$$w^\star_{t^\star} + u^\star w^\star_{x^\star} + w^\star w^\star_{z^\star} = -\frac{1}{\rho^\star} p_{z^\star} - g^\star \cos\theta + \frac{1}{\rho^\star}[\partial^\star_x \tau^\star_{z^\star x^\star} + \partial_{z^\star} \tau^\star_{z^\star z^\star}]. \tag{2.1c}$$

Here $\tau^\star_{ij}$ denote the liquid stresses.

The constitutive relation between the liquid stress and its rate of strain for a Newtonian

liquid is written as:

$$\boldsymbol{\tau}^\star = \mu^\star \dot{\boldsymbol{\gamma}}^\star, \tag{2.2}$$

where $\mu^\star$ is the liquid viscosity which is a constant and $\dot{\boldsymbol{\gamma}}^\star$ is the rate of strain tensor.

$$\dot{\boldsymbol{\gamma}}^\star = \left[\nabla \mathbf{u}^\star + \nabla \mathbf{u}^{\star T}\right] = \begin{pmatrix} 2u^\star_{x^\star} & u^\star_{z^\star} + w^\star_{x^\star} \\ u^\star_{z^\star} + w^\star_{x^\star} & 2w^\star_{z^\star} \end{pmatrix}. \tag{2.3}$$

2.2.2 Boundary conditions

At the surface of the plane, $z = 0$, we impose the no-slip boundary condition for the velocity field. To model the source of fluid we specify a vertical velocity $w^\star_s(x^\star, t^\star)$ at the location of this source. Hence

$$u^\star = 0, \quad w^\star = w^\star_s(x^\star, t^\star) \text{ at } z^\star = 0. \tag{2.4}$$

Similar to lava extrusions from vents on to inclined planes the source is assumed to be a circular source with $x^\star_0$ is the vent radius. Assuming Poiseuille flow through this vent with liquid flux (per unit width), $Q^\star_s$, $w^\star_s$ can be written as:

$$w^\star_s(x^\star, t^\star) = \frac{3Q^\star_s(t^\star)}{4x^\star_0}\left[1 - \left(\frac{x^\star}{x^\star_0}\right)^2\right]\mathcal{H}(x^{\star 2}_0 - x^{\star 2}). \tag{2.5}$$

Here, $\mathcal{H}(x^\star)$ is the Heaviside function.

The free surface $z^\star = h^\star(x^\star, t^\star)$ is a material surface and is assumed to be stress free.

Taking the pressure of the liquid in the dome relative to the air pressure and neglecting surface tension, the normal stress at the air-liquid interface is written as:

$$(-p^\star \boldsymbol{I} + \boldsymbol{\tau}^\star) \cdot \mathbf{n}^\star = 0, \quad \text{at} \;\; z^\star = h^\star(x^\star, t^\star), \tag{2.6}$$

where, $\mathbf{n}^\star$, the unit outward normal to the free surface $z^\star = h^\star(x^\star, t^\star)$ is given by

$$\mathbf{n}^\star = \frac{\nabla^\star \left(z^\star - h^\star(x^\star, t^\star)\right)}{|\nabla^\star \left(z^\star - h^\star(x^\star, t^\star)\right)|} = \frac{1}{\sqrt{1 + h_{x^\star}^{\star 2}}} \left(-h_{x^\star}^\star, 1\right). \tag{2.7}$$

The corresponding tangent vector to the free surface is given by

$$\mathbf{n}^\star \cdot \mathbf{t}^\star = 0, \;\Rightarrow\; \mathbf{t}^\star = \frac{1}{\sqrt{1 + h_{x^\star}^{\star 2}}} \left(1, h_{x^\star}^\star\right). \tag{2.8}$$

We can write the normal and tangential component of Eq. (2.6) as

$$\mathbf{n}^\star \cdot (-p^\star \boldsymbol{I} + \boldsymbol{\tau}^\star) \cdot \mathbf{n}^\star = 0, \;\Rightarrow\; -h_x \tau_{zx} + \tau_{zz} - p = 0, \tag{2.9a}$$

$$\mathbf{t}^\star \cdot (-p^\star \boldsymbol{I} + \boldsymbol{\tau}^\star) \cdot \mathbf{n}^\star = 0, \;\Rightarrow\; -h_x(\tau_{xx} - p) + \tau_{xz} = 0. \tag{2.9b}$$

The kinematic condition at the free surface $z^\star = h^\star(x^\star, t^\star)$ is based on this being a material surface so that fluid particles which lie on the surface must always remain on the surface. This implies that $\frac{D}{Dt}[z^\star - h^\star(x^\star, t^\star)] = 0$ or

$$\frac{\partial}{\partial t^\star} \left(z^\star - h^\star(x^\star, t^\star)\right) + \mathbf{u} \cdot \nabla^\star \left(z^\star - h^\star(x^\star, t^\star)\right) = 0. \tag{2.10}$$

This can be written as:

$$h^\star_{t^\star} + u^\star h^\star_{x^\star} = w^\star. \tag{2.11}$$

2.2.3 Nondimensionalisation and the lubrication (or long-wavelength) approximation

Nondimensionalisation

To nondimensionalise the equations, we first need to select characteristic quantities that describe the flow problem. We use a dome height $H^\star$ to measure the length scale in the $z^\star$ direction and $L^\star$, for the dome length in the $x^\star$ direction. The characteristic length scale of the extruded dome, $L^\star$, is much greater than the characteristic height, $H^\star$, so $\epsilon = H^\star/L^\star \ll 1$ is the aspect ratio and is a small parameter. We measure the velocities, $u^\star$ and $w^\star$, by $U^\star$ and $\epsilon U^\star$ (scaled with ϵ to satisfy the continuity equation), respectively, where $U^\star$ is a characteristic speed of spreading which is determined below. We measure pressure using a characteristic scale $P^\star$ which is also determined below. We nondimensionalise time by $L^\star/U^\star$. We nondimensionalise the variables as follows:

$$\begin{aligned} &x^\star = L^\star x, \;\; (z^\star, h^\star) = H^\star(z, h), \;\; (u^\star, w^\star) = (U^\star, \epsilon U^\star)(u, w), \;\; p^\star = P^\star p, \\ &\tau^\star = \mu^\star \left(\frac{U^\star}{H^\star}\right) \tau, \;\; \dot{\gamma}^\star = \left(\frac{U^\star}{H^\star}\right) \dot{\gamma}, \;\; t^\star = (L^\star/U^\star) t. \end{aligned} \tag{2.12}$$

The characteristic pressure $P^\star$ is chosen so as to balance the vertical liquid pressure gradient and the vertical component of gravity. This gives $P^\star = \rho^\star g^\star H^\star \cos\theta$ (the hydro-

static pressure). The characteristic speed $U^\star$ is chosen to balance the horizontal liquid pressure gradient and the liquid shear stress. This gives $U^\star = (\rho^\star g^\star {H^\star}^3)/(\mu^\star L^\star)\cos\theta$. For lava domes, the dome length, $L^\star = 100$m, and height, $H^\star = 10$m and effusion rate is $0.1 - 10\text{m}^3/\text{s}$ (Fink & Griffiths [35]). Using the density and viscosity from Table 1.1, we obtain $U^\star \approx 10^{-4}$m/s. For lava analogues such as Kaolin-Water, experiments (Balmforth *et al.* [5]) have used the dome length, $L^\star = 0.1$m, and height, $H^\star = 0.01$m and effusion rate is $10^{-6}\text{m}^3/\text{s}$. Using the density and viscosity from Table 1.1, we obtain $U^\star \approx 10^{-3}$m/s.

On substituting the above into the governing equations, Eqs. (2.1), the nondimensionalised governing equations are:

$$u_x + w_z = 0, \tag{2.13a}$$

$$\epsilon^2 R_e(u_t + uu_x + wu_z) = -p_x + \epsilon\partial_x\tau_{xx} + \partial_z\tau_{xz} + S, \tag{2.13b}$$

$$\epsilon^4 R_e(w_t + uw_x + ww_z) = -p_z + \epsilon^2\partial_x\tau_{zx} + \epsilon\partial_z\tau_{zz} - 1, \tag{2.13c}$$

The nondimensional parameters $S = \tan\theta/\epsilon$ is a measure of the downslope and the Reynold's number $Re = (U^\star L^\star)/\mu^\star \equiv (g^\star {H^\star}^3/{\mu^\star}^2)\cos\theta$, which compares inertial and viscous effects and is assumed to be much less than one so that inertial effects are negligible. The non-dimensional parameter estimates are (based on the above estimates of the physical quantities): $\epsilon = 0.1$, $Re \approx 10^{-5}$ and $Q_s \approx 10^5$ for lava and $\epsilon = 0.1$, $Re \approx 10^{-5}$ and $Q_s \approx 10^5$ for Kaolin-Water experiments.

The dimensionless strain rate tensor becomes

$$\dot{\gamma}_{ij} = \begin{pmatrix} 2\epsilon u_x & u_z + \epsilon^2 w_x \\ u_z + \epsilon^2 w_x & 2\epsilon w_z \end{pmatrix}. \tag{2.14}$$

The nondimensional boundary conditions can be written as:

$$u = 0 \ \text{ and } \ w(x,t) = w_s(x,t), \ \text{ at } \ z = 0. \tag{2.15}$$

Here $w_s(x,t) = [3Q_sQ_s(t)(1-(x/x_0)^2)/4]\mathcal{H}(x^2 - x_0^2)$, where Q_s is a dimensionless parameter, $Q_s = Q_s^\star/(x_0^\star \epsilon U)$ and $Q_s^\star$ is a characteristic source flow rate (per unit width) $Q_s(t)$ is a dimensionless time-dependent flux term. The dimensionless vent width is $x_0 = x_0^\star/L^\star$.

The nondimensional boundary conditions at $z = h(x,t)$ are given by

$$h_t + uh_x = w \ , \tag{2.16a}$$

$$p = \epsilon^2(\tau_{zz} - \epsilon h_x \tau_{xz}), \tag{2.16b}$$

$$\tau_{xz} + ph_x = \epsilon^2 h_x \tau_{xx}. \tag{2.16c}$$

The lubrication approximation

In order to reduce the governing equations we exploit the small aspect ratio ($\epsilon \ll 1$) [6], with Reynolds number of order unity at most. We pose an asymptotic expansion of the variables in powers of ϵ: $(u, w, p, h) = u(, w, p, h)_0 + \epsilon(u, w, p, h)_1 + \ldots$. Substituting these into the governing equations and boundary conditions, Eqs. (2.13,2.15,2.16) and collecting terms of the same order in ϵ, we obtain of leading order:

$$u_{0_x} + w_{0_z} = 0, \tag{2.17a}$$

$$-p_{0_x} + \partial_z \tau_{xz_0} + S = 0, \tag{2.17b}$$

$$-p_{0_z} - 1 = 0, \tag{2.17c}$$

$$\tau_{xz_0} = p_0 = 0,\ h_{0_t} + u_0 h_{0_x} = w_0, \ \text{ at } \ z = h_0(x,t), \tag{2.17d}$$

$$u_0 = 0,\ w_0 = w_s(x,t), \ \text{ at } \ z = 0. \tag{2.17e}$$

Integrating Eq. (2.17c) and using the boundary condition for p_0 in Eq. (2.17d) gives $p_0 = h_0(x,t) - z$. Integrating Eq. (2.17b)and using the boundary condition for τ_{xz_0} in Eq. (2.17d) and p_0 above gives $\tau_{xz_0}(x,z) = (S - h_{0_x})(h_0 - z)$. Using the shear stress τ_{xz_0}, we obtain the leading order shear rate, $u_{0_z} = \tau_{xz_0} = (S - h_{0_x})(h_0 - z)$. Now, the leading order liquid flux through a cross-section can be written as:

$$Q_0(x,t) = \int_0^{h_0} u_0(x,z,t)dz = (z - h_0)u_0|_0^{h_0} - \int_0^{h_0} (z - h_0)u_{0_z}dz = \int_0^{h_0} (h_0 - z)u_{0_z}dz. \tag{2.18}$$

Using the expression for u_{0_z} above and the boundary condition for u_0 in Eq. (2.17e), we obtain $Q_0(x,t) = \frac{1}{3}h_0^3(S - h_{0_x})$. Integrating the continuity equation Eq. (2.17a) using the boundary conditions in Eq. (2.17e) and substituting into the kinematic boundary condition in Eq. (2.17d), one obtains the evolution equation for h_0:

$$h_{0_t} + Q_{0_x} = w_s. \tag{2.19}$$

Using the expressions for Q_0 and w_s from above, we can write the evolution equation for h_0 as:

$$h_{0_t} + \frac{1}{3}[h_0^3(S - h_{0_x})]_x = w_s, \quad \text{where} \quad w_s = \frac{3}{4}Q_{s_0}Q_s(t)\left[1 - (x/x_0)^2\right]\mathcal{H}(x^2 - x_0^2). \tag{2.20}$$

The second term on the left-hand side represent the contribution to the liquid flux in the dome due to the horizontal component of gravity (convective term) and the vertical component of gravity (nonlinear diffusion term).

Integrating Eq. (2.20) over the length of the liquid dome provides the total mass conservation,

$$\frac{d}{dt}\int_{X_T}^{X_N} h_0(x,t)\, dx = \int_{X_T}^{X_N} w_s(x,t)\, dx = Q_{s_0}Q_s(t), \tag{2.21}$$

where the liquid dome lies in the region $X_T < x < X_N$, where X_N is its leading edge and X_T its trailing edge. $Q_{s_0} = 0$ corresponds to the spreading of a constant volume of liquid in the dome. In §2.3, we consider self-similar evolution of dome shapes based on power-law time-dependent behaviour of $Q_s(t) = \alpha t^{(\alpha-1)}$, with $\alpha = 0$ (constant volume),

$\alpha = 1$ (constant source flux), etc.

2.3 Late-time similarity solutions for power-law time-dependent $Q_s(t)$

We seek late-time similarity solutions of Eq. (2.20) such that the volume of liquid released by the source onto the plane is proportional to $t^\alpha (t \geq 0)$, where $\alpha \geq 0$ (or $Q_s(t) = \alpha t^{(\alpha-1)}$). This volume constraint (representing conservation of volume of liquid in the dome) is written as:

$$\int_{X_T}^{X_N} h \; dx = Q_{s_0} t^\alpha + V_0, \tag{2.22}$$

where the flow lies in $X_T(t) < x < X_N(t)$ and V_0 is an initial volume of liquid in the dome. It is convenient, when seeking similarity solutions, to consider the following form of the evolution equation (equivalent to Eqs. (2.20, 2.21)),

$$h_{0_t} + \frac{1}{3}[h_0^3(S - h_{0_x})]_x = 0, \tag{2.23a}$$

$$\int_{X_T}^{X_N} h \; dx = Q_{s_0} t^\alpha + V_0. \tag{2.23b}$$

There is no similarity solution to Eq. (2.23a) when both the convection and diffusion terms contribute equally. However, as we show below, similarity solutions exist at early times when diffusion dominates convection, at late time for the case $S = 0$ for

spreading on a horizontal plane and at late time when convection dominates diffusion (for the case $S \neq 0$ for spreading down an inclined plane). Below we derive similarity solutions for these two cases for any value of α.

Late-time similarity solution for $S = 0$

We define the similarity variables

$$\xi = \frac{x}{t^b \left(\frac{Q_{s_0}^3}{3}\right)^{1/5}}, \quad h(x,t) = (3Q_{s_0}^2)^{1/5} t^a \phi(\xi), \tag{2.24}$$

where the exponents a and b need to be determined. Substituting in Eq. (2.23a), the evolution equation can be written in the form

$$t^{a-1}\left(a\phi - b\xi\phi_\xi\right) = t^{4a-2b}\left(\phi^3\phi_\xi\right)_\xi. \tag{2.25}$$

Setting

$$a - 1 = 4a - 2b \Rightarrow 3a - 2b + 1 = 0. \tag{2.26}$$

Substituting the similarity transformation in Eq. (2.23b) gives

$$t^{a+b}\int_0^{\xi_N} \phi \, d\xi = t^\alpha + \frac{V_0}{Q_{s_0}}. \tag{2.27}$$

We choose $a + b = \alpha$ so that

$$\int_0^{\xi_N} \phi \, d\xi = 1 + O(t^{-\alpha}). \tag{2.28}$$

We anticipate $b > 0$ since it is a spreading problem. Solving for a and b, we obtain $a = \frac{2\alpha-1}{5}$, $b = \frac{3\alpha+1}{5}$. Therefore, the similarity variables can be written as:

$$h(x,t) = \left(3Q_{s_0}^2\right)^{1/5} t^{\frac{2\alpha-1}{5}} \phi(\xi), \quad \xi = \frac{x}{t^{\frac{3\alpha+1}{5}} \left(\frac{Q_{s_0}^3}{3}\right)^{1/5}}. \tag{2.29}$$

For $t \gg 1$, the above equation shows that the maximum dome height (which for $S = 0$ is $h(\xi = 0)$), $h \sim t^{\frac{2\alpha-1}{5}}$ and the location of its front $X_N \sim t^{\frac{3\alpha+1}{5}}$. We also note that for $0 < \alpha < 1/2$, the maximum dome height decreases with time and increases otherwise. Thus, Eqs. (2.25, 2.28) can be written as:

$$\frac{2\alpha-1}{5}\phi - \frac{3\alpha+1}{5}\xi\phi_\xi = \left(\phi^3\phi_\xi\right)_\xi, \tag{2.30a}$$

$$\int_0^{\xi_N} \phi \, d\xi = 1 + O(t^{-\alpha}). \tag{2.30b}$$

Define $z = \xi/\xi_N$ and $\phi(z) = \xi_N^\beta \tilde{\phi}(z)$, where the constant β will be determined below. Substituting this into Eq. (2.30a), we obtain

$$\xi_N^\beta \left(\frac{2\alpha-1}{5}\tilde{\phi} - \frac{3\alpha+1}{5} z\tilde{\phi}_z\right) = \xi_N^{4\beta-2}\left(\tilde{\phi}^3\tilde{\phi}_z\right)_z. \tag{2.31}$$

Choose $\beta = \frac{2}{3}$, this implies

$$\left(\tilde{\phi}^3\tilde{\phi}_z\right)_z + \frac{3\alpha+1}{5}z\tilde{\phi}_z - \frac{2\alpha-1}{5}\tilde{\phi} = 0. \tag{2.32}$$

Substituting the above change of variables into Eq. (2.30b), we obtain

$$\xi_N = \left(\int_0^1 z\tilde{\phi}\ dz\right)^{-3/5}. \tag{2.33}$$

Therefore

$$z = \frac{x}{\xi_N\left(\frac{Q_{s_0}^3}{3}\right)^{1/5}t^{\frac{3\alpha+1}{5}}}, \quad h(x,t) = \xi_N^{2/3}(3Q_{s_0}^2)^{1/5}t^{\frac{(2\alpha-1)}{5}}\tilde{\phi}(z), \tag{2.34a}$$

$$\left(\tilde{\phi}^3\tilde{\phi}_z\right)_z + \frac{1}{5}(3\alpha+1)z\tilde{\phi}_z - \frac{1}{5}(2\alpha-1)\tilde{\phi} = 0, \tag{2.34b}$$

$$\xi_N = \left(\int_0^1 \tilde{\phi}\ dz\right)^{-3/5}. \tag{2.34c}$$

Eq. (2.34b) is solved numerically for any value of $\alpha > 0$. The boundary condition at $z = 0$ is given by $\tilde{\phi}_z = 0$ (from symmetry at $x = 0$). We can apply the Frobenius method to determine a solution of Eq. (2.34b) in the neighbourhood of the point $z = 1$. We seek a solution of the form $\tilde{\phi}(z) = \sum_{m=0}^{\infty} a_m(1-z)^{r+m}$, where r is a constant to be determined. Substituting this in Eq. (2.34b), we can show that the solution is given by (for details see Appendix 1)

$$\tilde{\phi}(z) = \left[\frac{3}{5}(3\alpha+1)\right]^{1/3}(1-z)^{1/3}\left[1-\frac{3\alpha-4}{24(3\alpha+1)}(1-z)+O(1-z)^2\right], \text{ for } z = 1^-. \tag{2.35}$$

In practice, we choose $z = 1 - \delta$, for $\delta \ll 1$ specified. For arbitrary α, and using Eq. (2.34b) with boundary conditions $\tilde{\phi}_z = 0$ at $z = 0$ and Eq. (2.35) at $z = 1 - \delta$, the solution can be obtained by numerically integrating Eq. (2.34b) by using FSOLVE module in MATLAB (Release 2013a, The MathWorks, Inc., Natick, Massachusetts, United States). The similarity solution is represented by the boundary-value problem in Eq. (2.34b) along with the boundary conditions given by $\tilde{\phi}_z = 0$ at $z = 0$ and Eq. (2.35) at $z = 1 - \delta$.

For $\alpha = 0$ the solution of Eq. (2.30a) can be obtained analytically, where this equation reduces to

$$-\frac{1}{5}\left(\phi + \xi\phi_\xi\right) = \left(\phi^3\phi_\xi\right)_\xi . \tag{2.36}$$

Integrating and using the boundary condition $\phi_\xi = 0$, at $\xi = 0$ gives

$$-\frac{1}{5}\left(\xi\phi\right) = \left(\phi^3\phi_\xi\right) . \tag{2.37}$$

Integrating again and using $\phi = 0$ at $\xi = \xi_N$, we obtain

$$\phi = \begin{cases} (\frac{3}{10})^{1/3}(\xi_N^2 - \xi^2)^{1/3}, & \xi < \xi_N, \\ 0, & \xi > \xi_N, \end{cases} \tag{2.38}$$

where ξ_N is given by

$$\left(\frac{3}{10}\right)^{1/3} \int_0^{\xi_N} \left(\xi_N^2 - \xi^2\right)^{1/3} \, d\xi = \left(\frac{3}{10}\right)^{1/3} \xi_N^{5/3} \int_0^{\pi/2} \sin^{5/3}(\theta) \, d\theta = 1. \tag{2.39}$$

In the above, we have used the substitution $\xi = \xi_N \cos\theta$. This simplifies to

$$\xi_N = \left(\frac{3}{10}\right)^{-1/5} \left(\frac{1}{\int_0^{\pi/2} \sin^{5/3}(\theta)\ d\theta}\right)^{3/5}. \tag{2.40}$$

Using Mathematica, we obtain

$$\xi_N = \left(\frac{3}{10}\right)^{-1/5} \left(\frac{1}{0.841309}\right)^{3/5}. \tag{2.41}$$

The solution, $\phi(\xi)$, as a function of ξ is shown in Fig. 2.2 for various values of α. We observe that as α increases, although the free surface shapes look similar, the length over which they have spread, ξ_N decreases and the maximum height, $\phi(\xi = 0)$, increases. This is consistent with the fact that as α increases, the additional volume of liquid from the source contributes more to inflating the dome rather than its spreading.

Late-time similarity solution for $S > 0$

Now, we describe the late-time solution for any α with $S > 0$. We define the similarity variables

$$\xi = \frac{x}{t^b \left(\frac{Q_{s_0}^2}{3}\right)^{(1/3)}}, \quad h(x,t) = (3Q_{s_0})^{(1/3)}\, t^a \phi(\xi). \tag{2.42}$$

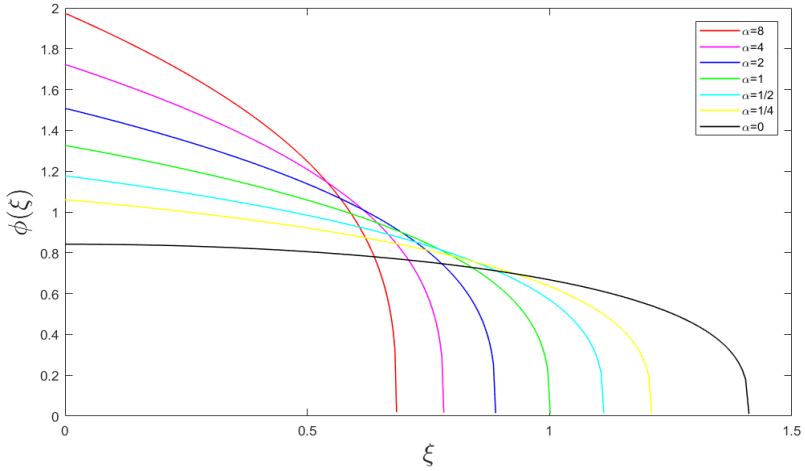

Figure 2.2: The late-time similarity solution, ϕ, as a function of ξ for $S = 0$ and varying α obtained from the numerical solution of Eq. (2.34b) using boundary conditions $\tilde{\phi}_z = 0$ at $z = 0$ and Eq. (2.35) at $z = 1 - \delta$.

where the exponents a and b need to be determined. Substituting in Eq. (2.23a), the evolution equation can be written in the form

$$t^{a-1}\left(a\phi - b\xi\phi_\xi\right) + \left[t^{3a-b}\left(S - \left(\frac{3^2}{Q_{s_0}}\right)^{1/3} t^{a-b}\phi_\xi\right)\phi^3\right]_\xi = 0. \tag{2.43}$$

To obtain a sensible balance for $t \gg 1$, we require a balance between the unsteady and convective terms. Hence, $t^{a-1} \sim t^{3a-b}$. Therefore, we require $-2a + b = 1$. Eq. (2.27) will also hold,

$$t^{a+b}\int_{\xi_T}^{\xi_N} \phi d\xi = t^\alpha + + \frac{V_0}{Q_{s_0}}. \tag{2.44}$$

We choose $a + b = \alpha$ so that

$$\int_{\xi_T}^{\xi_N} \phi \; d\xi = 1 + O(t^{-\alpha}). \tag{2.45}$$

We anticipate $b > 0$ since it is a spreading problem. Solving for a and b, we obtain $a = \frac{\alpha-1}{3}$ and $b = \frac{2\alpha+1}{3}$. Therefore, the similarity variables can be written as:

$$\xi = \frac{x}{t^{\frac{2\alpha+1}{3}} \left(\frac{Q_{s_0}^2}{3}\right)^{1/3}}, \quad h(x,t) = (3Q_{s_0})^{1/3}\, t^{\frac{\alpha-1}{3}} \phi(\xi). \tag{2.46}$$

For $t \gg 1$, the above equation shows that the maximum dome height $h \sim t^{\frac{\alpha-1}{3}}$ and the location of its front $X_N \sim t^{\frac{2\alpha+1}{3}}$. We also note that for $0 < \alpha < 1$, the maximun dome height decreases with time and increases otherwise. Thus, Eqs. (2.43, 2.45) can be written as:

$$\left(\frac{1-\alpha}{3}\phi + \frac{2\alpha+1}{3}\xi\phi_\xi\right) = \left[\left(S - \left(\frac{3^2}{Q_{s_0}}\right)^{1/3} t^{-(\alpha+2)/3}\phi_\xi\right)\phi^3\right]_\xi, \tag{2.47a}$$

$$\int_{\xi_T}^{\xi_N} \phi \; d\xi = 1 + O(t^{-\alpha}). \tag{2.47b}$$

Note that $\alpha > 0$ so the last term in Eq. (2.47a) is much smaller compared to the first two terms when $t \gg 1$. The late-time similarity solution satisfies

$$\left(\frac{1-\alpha}{3}\phi + \frac{2\alpha+1}{3}\xi\phi_\xi\right) = \left(S\phi^3\right)_\xi + O(t^{-(\alpha+2)/3}). \tag{2.48}$$

Using the integrating factor $\phi^{3\alpha/(1-\alpha)}$ to multiply both sides of the above equation, we obtain

$$\frac{1}{3}\left((1-\alpha)\xi\phi^{\frac{2\alpha+1}{(1-\alpha)}}\right)_\xi = \left(S(1-\alpha)\phi^{\frac{3}{(1-\alpha)}}\right)_\xi + O(t^{-(\alpha+2)/3}). \tag{2.49}$$

Integrating this equation with respect to ξ and applying the boundary condition $\phi(\xi = \xi_T) = \phi_0$ (determined below), we obtain the solution in implicit form,

$$\xi - \xi_T = 3S \left(\frac{\phi^{3/(1-\alpha)} - \phi_0^{3/(1-\alpha)}}{\phi^{\frac{2\alpha+1}{(1-\alpha)}}} \right). \tag{2.50}$$

We can show that $\phi_0(\xi_T) = (\frac{\alpha}{S})^{1/3}$ (for details see Appendix 2). From our numerical simulations, $\xi_T \approx 0$ for $t \gg 1$, hence for our purposes we can take $\xi_T \approx 0$, Using Eq. (2.47b), the location of the leading edge of the front $\xi = \xi_N$, and the height there $\phi = \phi_N$, can be written as (for detail see Appendix 2):

$$\xi_N = \frac{3}{2\phi_0} \left(\frac{2\alpha}{1+2\alpha} \right)^{\frac{(1+2\alpha)}{3}}, \quad \phi_N = \left(\frac{1+2\alpha}{2\alpha} \right)^{\frac{(1-\alpha)}{3}} \phi_0. \tag{2.51}$$

The similarity solution is represented by the implicit relationship between ϕ and ξ given in Eq. (2.50), the solution can be obtained numerically using FSOLVE module in MATLAB. Setting $\alpha = 1$ (constant source flow rate) we can show that

$$\phi(\xi) = 1, \;\; \xi_N = 1, \;\; \phi_N = 1. \tag{2.52}$$

For $\alpha = 0$, we obtain

$$\frac{1}{3}(\phi + \xi\phi_\xi) = \left[\left(S - \left(\frac{3^2}{q} \right)^{1/3} t^{-2/3} \phi_\xi \right) \phi^3 \right]_\xi. \tag{2.53}$$

For $t \gg 1$, Eq. (2.53) becomes

$$\frac{1}{3}\left(\phi + \xi\phi_\xi\right) = \left(S\phi^3\right)_\xi . \tag{2.54}$$

Integrating and using $\phi(\xi = 0) = 0$ yields

$$\phi = \left(\frac{1}{3S}\xi\right)^{1/2}, \quad \xi_N = \frac{3}{2^{2/3}}S^{1/3}, \quad \phi_N = (2S)^{-1/3}. \tag{2.55}$$

The solution for this is shown in Fig. 2.3 for $S = 1$ and various values of α. We observe a similar trend as that shown in Fig. 2.2 for $S = 0$; the length over which the dome spreads, ξ_N, decreases and the height at the leading edge, ϕ_N, increases. We note that ξ_N is larger than that for $S = 0$ due to the additional contribution from the inclination of the plane. Similar to the $S = 0$ case, as α increases, the additional volume of liquid from the source contributes more to inflating the dome rather than its spreading. The

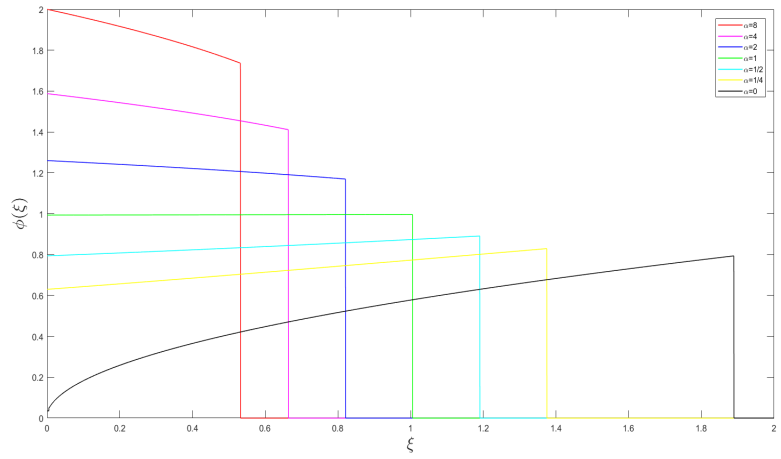

Figure 2.3: The late-time similarity solution, ϕ, as a function of ξ for $S = 1$ and varying α obtained from Eq. (2.50).

location of the leading edge of the dome, ξ_N, and the height there, ϕ_N as a function of α are shown in Fig. 2.4. This is consistent with our earlier observations.

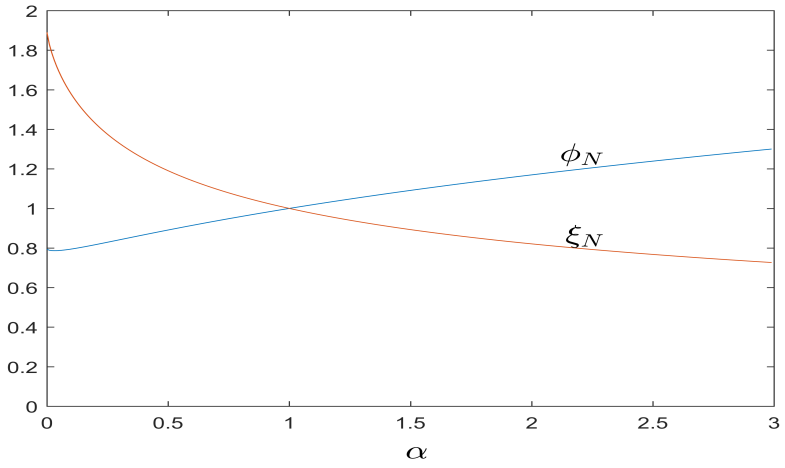

Figure 2.4: The location of the leading edge of the dome, ξ_N, and the height there, ϕ_N as a function of α for $S = 1$.

Early-time similarity solution for $S > 0$

It is also worth considering the possibility of early-time similarity solutions for $S > 0$. The main balance at early-time is between the unsteady and diffusion terms described by the evolution equation in Eq. (2.25) for $S = 0$. For $S > 0$, this evolution equation takes the form:

$$t^{a-1}\left(a\phi - b\xi\phi_\xi\right) = t^{4a-2b}\left(\phi^3\phi_\xi\right)_\xi + O(t^{3a-b}). \tag{2.56}$$

The $O(t^{3a-b})$ term corresponds to the convection due to the horizontal component of gravity. The volume conservation is given by Eq. (2.23b). At very early-time, we anticipate the contribution to the change in volume from the source to be small. Hence,

the volume conservation at these times is given by

$$t^{a+b}\int_0^{\xi_N}\phi\ d\xi = Q_{s_0}t^{\alpha}+1. \tag{2.57}$$

For $t \ll 1$, this is equivalent to the constant volume (or $\alpha = 0$) case. Note that to derive the above we have replaced the Q_{s_0} with V_0 in the similarity variables given in Eq. (2.24). Hence, we require that $3a-2b+1=0$ (as for the case $S=0$) and $a+b=0$ to remove the time dependence in Eq. (2.57). This gives $a=-1/5$ and $b=1/5$. This is analogous to the case $\alpha = 0$ when $S = 0$. We note that the convective term neglected in Eq. (2.56) is $O(t^{-a+b}) = O(t^{2/5})$ which is small for $t \ll 1$.

At early time when the volume contribution from the source now exceeds the initial volume, the appropriate volume conservation is given by Eq. (2.23b). The similarity solution is now identical to that derived for the case when $S = 0$ for any α. The convective term neglected in Eq. (2.56) is now $O(t^{(\alpha+2)/5})$ which is still small for $t \ll 1$. As t increases, the contribution from this term also increases and eventually the similarity solution is identical to the late-time similarity solution for $S > 0$.

2.4 Numerical results

In this section, we seek the numerical solution of Eq. (2.20) for $x \in [-L, L]$, where L is the length of the computational domain. We assume that the plane is pre-wetted with a precursor layer of thickness b. The boundary conditions specified are: $h = b$ at

$x = \pm L$. We choose the initial condition to mimic a one-dimensional dome as follows:

$$h(x,t) = (1-x^2)H(1-x^2) + b, \quad x \in \quad [-L, L]. \tag{2.58}$$

Our focus is in investigating the evolution of the dome height h varying the parameters: the inclination angle, $S = \tan(\theta)/\epsilon$, the source flow rate Q_{s_0} and the source flux power-law parameter α. In particular, we consider two cases corresponding to $\alpha = 0$ (constant volume or zero source flowrate, so $Q_{s_0} = 0$) and $\alpha = 1$ (constant flow rate). In all the results shown below, we fix the source vent width $x_0 = 0.15$ and the precursor thickness $b = 10^{-6}$ for horizontal plane and $b = 10^{-3}$ for inclined plane. The length of the computational domains L is chosen sufficiently large so that the boundary condition $h \to b$ as $x \to \infty$ is satisfied numerically.

The evolution equation, Eq. (2.20), is solved numerically using the Method of lines [78, 61]. This is done as follows. We discretise the domain, $[-L, L]$, into $N+1$ points $x_i = -L + (i-1)\Delta x, \ i = 1, \ldots, N+1$, where $\Delta x = 2L/N$. Note that for $S = 0$ (horizontal plane), we use symmetry about $x = 0$ to only consider the domain $[0, L]$. We define a forward and backward finite difference for the spatial derivative as:

$$h_{x,i} = \frac{h_{i+1} - h_i}{\Delta x}, \quad h_{\bar{x},i} = \frac{h_i - h_{i-1}}{\Delta x}, \tag{2.59}$$

respectively. The spatial derivatives in Eq. (2.20) are then discretized as follows:

$$\begin{aligned}[(h^3)_i(S-h_{\tilde{x},i})]_x &= \frac{1}{\Delta x}\Big[(h^3)_{i+\frac{1}{2}}(S-h_{x,i+1}) - (h^3)_{i-\frac{1}{2}}(S-h_{x,i})\Big], \\ &= \frac{1}{\Delta x}\Big[(h^3)_{i+\frac{1}{2}}(S-\frac{h_{i+1}-h_i}{\Delta x}) - (h^3)_{i-\frac{1}{2}}(S-\frac{h_i-h_{i-1}}{\Delta x})\Big],\end{aligned} \tag{2.60}$$

where $(h^3)_{i+\frac{1}{2}} = \frac{(h^3)_{i+1}+(h^3)_i}{2}$, $(h^3)_{i-\frac{1}{2}} = \frac{(h^3)_i+(h^3)_{i-1}}{2}$. Using this, the discretised form of Eq. (2.20), keeping the time derivative continuous, can be written as:

$$h_{t,i} + \frac{1}{3\Delta x}\Big[(h^3)_{i+\frac{1}{2}}\Big(S-\frac{h_{i+1}-h_i}{\Delta x}\Big) - (h^3)_{i-\frac{1}{2}}\Big(S-\frac{h_i-h_{i-1}}{\Delta x}\Big)\Big] = w_{s,i}, \;\; i=2,\ldots,N, \tag{2.61}$$

where $w_{s,i} = \frac{3}{4}Q_{s_0}Q_s(t)\left[1-(x_i/x_0)^2\right]\mathcal{H}(x_i^2-x_0^2)$. We use the boundary condition at the end points, $h_1 = h_{N+1} = b$. For $S=0$ (horizontal plane), we impose the symmetry boundary condition $h_x = 0$ at $x=0$. The evolution equation for h_1 can then written as:

$$h_{t,1} - \frac{1}{3\Delta x}\Big[(h^3)_{1+\frac{1}{2}}(h_{\tilde{x},2}) - (h^3)_{1-\frac{1}{2}}(h_{\tilde{x},1})\Big] = w_{s,1}, \tag{2.62}$$

where $(h^3)_{1+\frac{1}{2}} = \frac{(h^3)_2+(h^3)_1}{2}$ and $(h^3)_{1-\frac{1}{2}} = \frac{(h^3)_1+(h^3)_0}{2}$. The symmetry boundary condition, $h_x = 0$, when discretised using a centered finite difference scheme gives $h_0 = h_2$ and $(h^3)_0 = (h^3)_2$, where the subscript "0" corresponds to a fictitious point outside the domain. Using this, Eq. (2.62), can be written as:

$$h_{t,1} = \frac{1}{3\Delta x^2}\Big[\frac{(h^3)_2+(h^3)_1}{2}\Big(h_2-h_1\Big) - \frac{(h^3)_2+(h^3)_1}{2}\Big(h_1-h_2\Big)\Big], \tag{2.63}$$

Hence,

$$h_{t,1} = \frac{1}{3\Delta x^2}\Big[((h^3)_2 + (h^3)_1)\Big(h_2 - h_1\Big)\Big]. \tag{2.64}$$

The resulting system of ordinary differential equations given by Eq. (2.61) are then solved in MATLAB (Release 2013a, The MathWorks, Inc., Natick, Massachusetts, United States) using the stiff ODE solver *ode15i*. We also compare the late-time behaviour of these solution with the corresponding similarity solutions derived in §2.3.

In Fig. 2.5, we show the evolution of $h(x,t)$ at different times varying from $t = 0 - 10^3$. The parameter values are $S = 1$ (corresponding to $\theta \approx 6^o$) and $Q_{s_0} = 0$ (constant volume). We observe the *s*lumping of the dome as it spreads down the inclined plane with a front developing at its leading edge. Fig. 2.6 show the evolution of $h(x,t)$

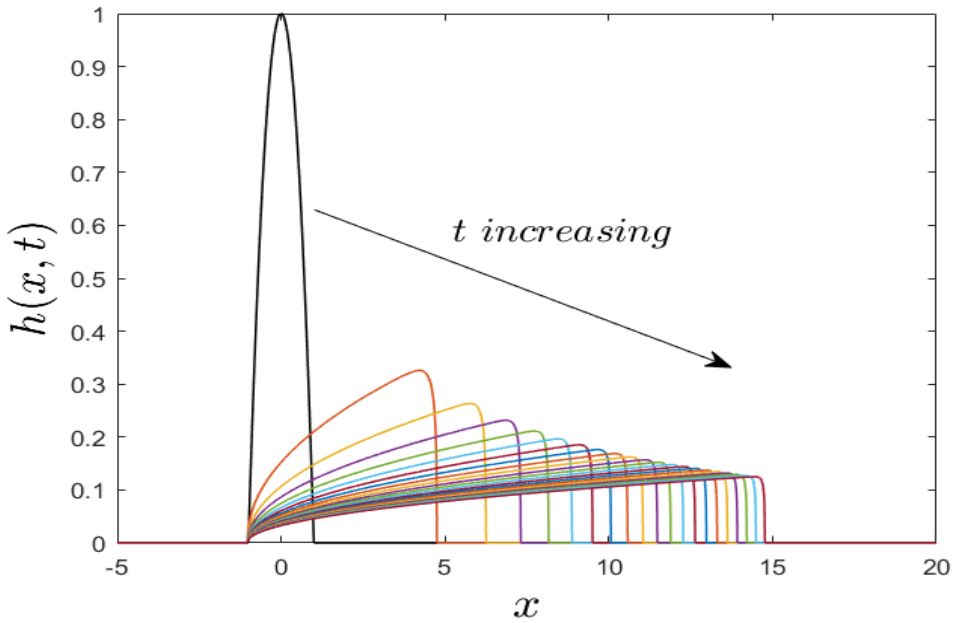

Figure 2.5: The evolution of $h(x,t)$ for t varying from $t = 0 - 10^3$. The parameter values are $S = 1$ (corresponding to $\theta \approx 6^o$) and $Q_{s_0} = 0$ (constant volume).

at times varying between $t = 0$ and $t = 0 - 10^3$. The parameter values are $S = 0$ (horizontal plane) and $Q_{s_0} = 0$ (constant volume). The spreading for this case is symmetric about $x = 0$. We also observe that the spreading of the dome is much slower compared to that shown in Fig 2.5. Fig. 2.7 shows the late-time similarity

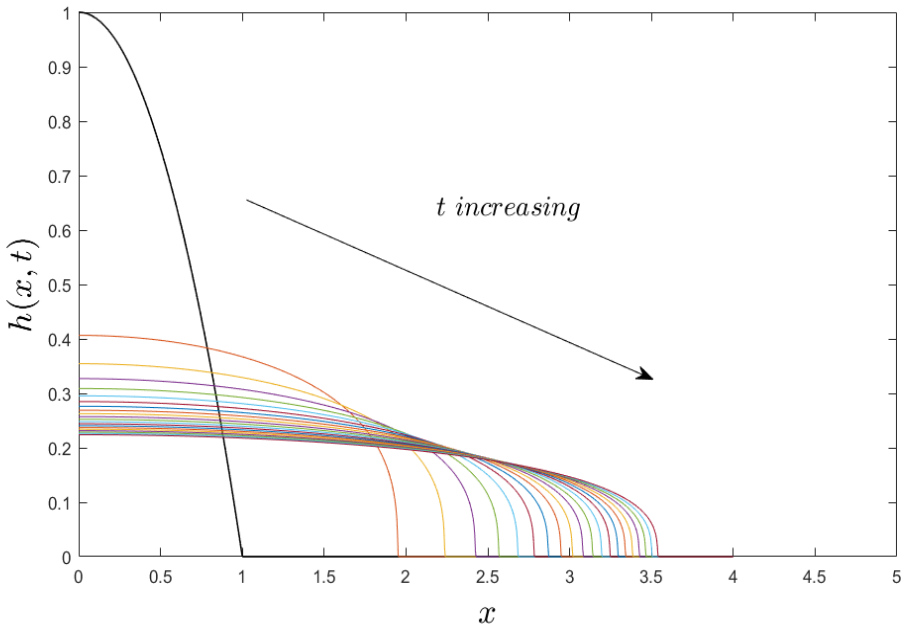

Figure 2.6: The evolution of $h(x,t)$ for t varying from $t = 0$ to $t = 10^3$. The parameter values are $S = 0$ (horizontal plane) and $Q_{s_0} = 0$ (constant volume).

solution for the evolution shown in Fig. 2.5 using the similarity variables $\xi = x/t^{1/3}$ and $\phi = t^{-1/3}h(x,t)$. The dashed line is the corresponding similarity solution, $\phi = [\xi/(3S)]^{1/2}$. The agreement is good. Figure 2.8 shows that the late-time numerical solution shown in Fig. 2.6 collapses to a single curve under the similarity scaling, $\xi = x/t^{1/5}$ and $\phi = t^{-1/5}h(x,t)$. The dashed line in Fig. 2.8 shows the corresponding similarity solution given by Eq. (2.38). This matches the numerical solution very well. Figure 2.9(a,b) plot the leading edge of the dome (or location of the liquid front at the

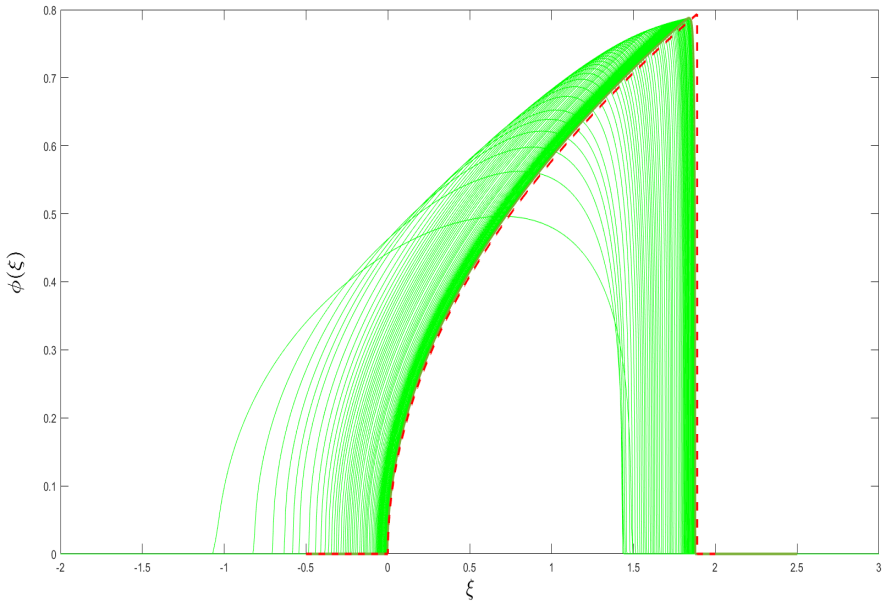

Figure 2.7: The evolution of $h(x,t)$ shown in Fig. 2.5 using the similarity scaling $\xi = x/t^{1/3}$ and $\phi = t^{-1/3}h(x,t)$. The dashed line is the similarity solution for this case, $\phi = [\xi/(3S)]^{1/2}$.

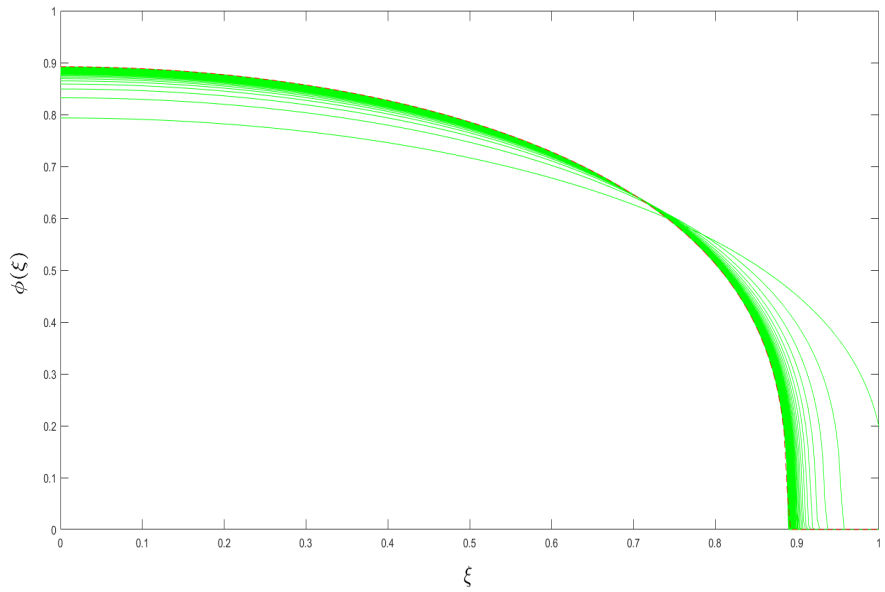

Figure 2.8: The evolution of $h(x,t)$ shown in Fig. 2.6 using similarity scaling , $\xi = x/t^{1/5}$ and $\phi = t^{-1/5}h(x,t)$. The dashed line shows the corresponding similarity solution given by Eq. (2.38).

dome's leading edge), x_N, and the dome height, h_N, at $x = x_N$, respectively, versus time, t. These are calculated from the dome evolution shown in Fig. 2.5 for $S = 1$ and $Q_{s_0} = 0$ (constant volume). The maximum dome height, h_N, is determined at the leading edge of the dome from the numerical solution. The location of the leading edge, x_N, is the value of x at which this maximum height is attained. Figure 2.9(a,b) also show the slopes which confirm that $x_N \sim t^{1/3}$ and $h_N \sim t^{-1/3}$ as derived in §2.3. Figure 2.10 (a,b) plot the leading edge of the dome, x_N, and the maximum dome

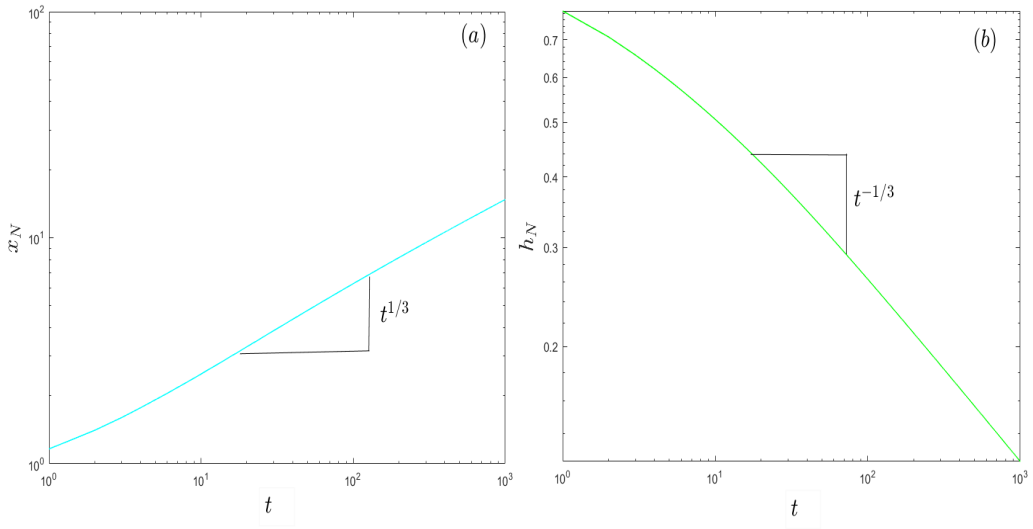

Figure 2.9: (a) Log-Log plot of the leading edge of the dome, x_N, and (b) Semi-Log plot of the dome height, h_N, at $x = x_N$, versus time, t using data shown in Fig. 2.5 for $S = 1$ and $Q_{s_0} = 0$ (constant volume). The slopes show that $x_N \sim t^{1/3}$ and $h_N \sim t^{-1/3}$.

height, $h(x = 0)$, respectively, versus time, t. These are calculated from the dome evolution shown in Fig. 2.6 for $S = 0$ and $Q_{s_0} = 0$ (constant volume). The location of the leading edge of the dome is calculated by the value of x where the dome height first becomes less than a prescribed value (10^{-5} in the case shown). Figure 2.10(a,b)

also show the slopes which confirm that $x_N \sim t^{1/5}$ and $h_N \sim t^{-1/5}$ as derived in §2.3. Figure 2.11 shows the dome height $h(x, t = 5 \times 10^2)$ for different values of inclination

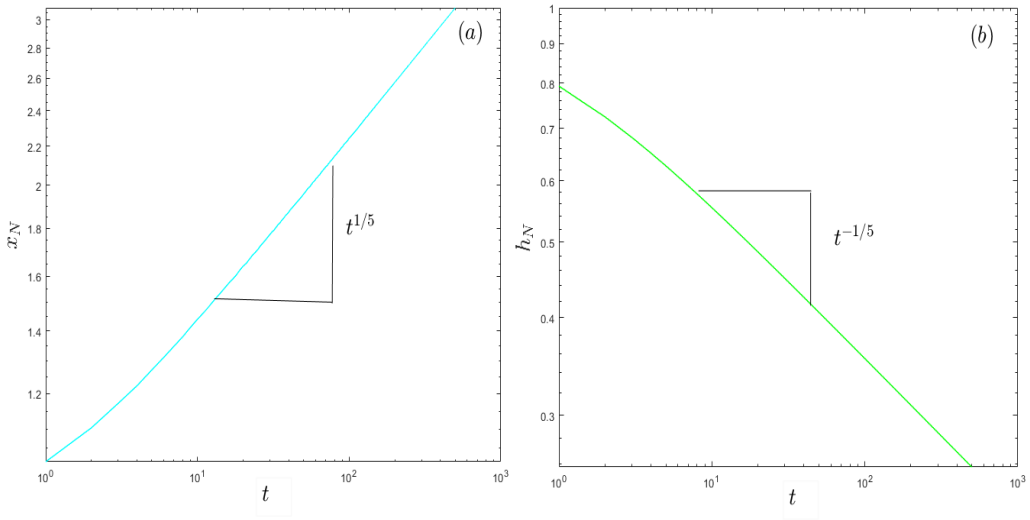

Figure 2.10: (a) Log-Log plot of the leading edge of the dome, x_N, and (b) Semi-Log plot of the maximum dome height, $h(x = 0)$, versus time, t using the data shown in Fig. 2.6 for $S = 0$ and $Q_{s_0} = 0$ (constant volume). The slopes show that $x_N \sim t^{1/5}$ and $h_N \sim t^{-1/5}$.

angles $S = 0.7\ (4^o), 1\ (6^o), 2.145\ (12^o), 3.732\ (18^o)$ and $Q_{s_0} = 0$ (constant volume). We observe that the dome has spread over a longer distance and also thinned more as S increases.

We now consider the case where $\alpha = 1$. Fig. 2.12 shows the evolution of $h(x, t)$ for varying $t = 0 - 2 \times 10^2$. The parameter values are $S = 1$, $Q_{s_0} = 4$ and $\alpha = 1$. At early time, the strength of the source is sufficiently high and the build-up of fluid at the source results in the dome height increasing near $x = 0$ without any spreading. At later times, we observe the dome to spread down the incline with almost uniform height

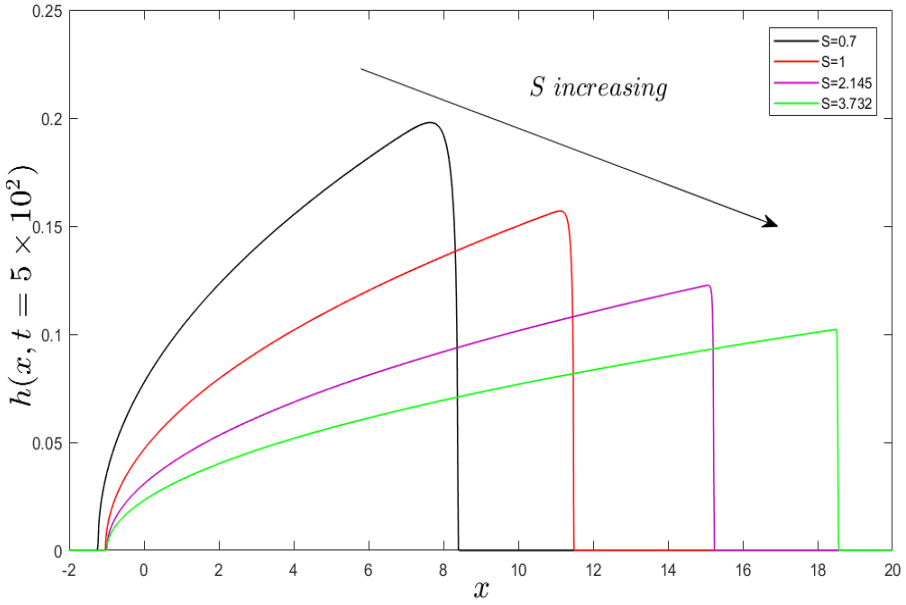

Figure 2.11: The thickness of spreading dome for varying inclination angles, $S = 0.7\ (4^o), 1\ (6^o), 2.145\ (12^o), 3.732\ (18^o)$, with $Q_{s_0} = 0$ (constant volume).

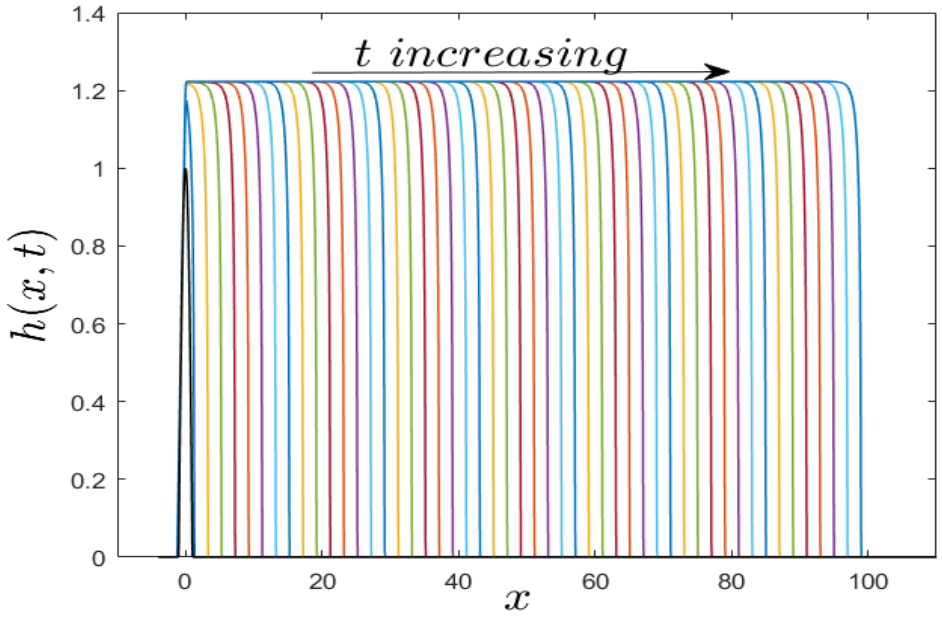

Figure 2.12: The evolution of $h(x, t)$ with $S = 1$, $Q_{s_0} = 4$ and $\alpha = 1$ for varying $t = 0 - 2 \times 10^2$.

behind its leading edge. This is due to the source being strong enough to constantly supply liquid which replaces that due to spreading down the incline. Figure 2.13 shows the evolution of $h(x,t)$ shown in Fig. 2.12 using the similarity scaling given in Eqs. (2.46) with $\alpha = 1$ and $Q_{s_0} = 4$ (so the exponents $a = 0$ and $b = 1$). The dashed

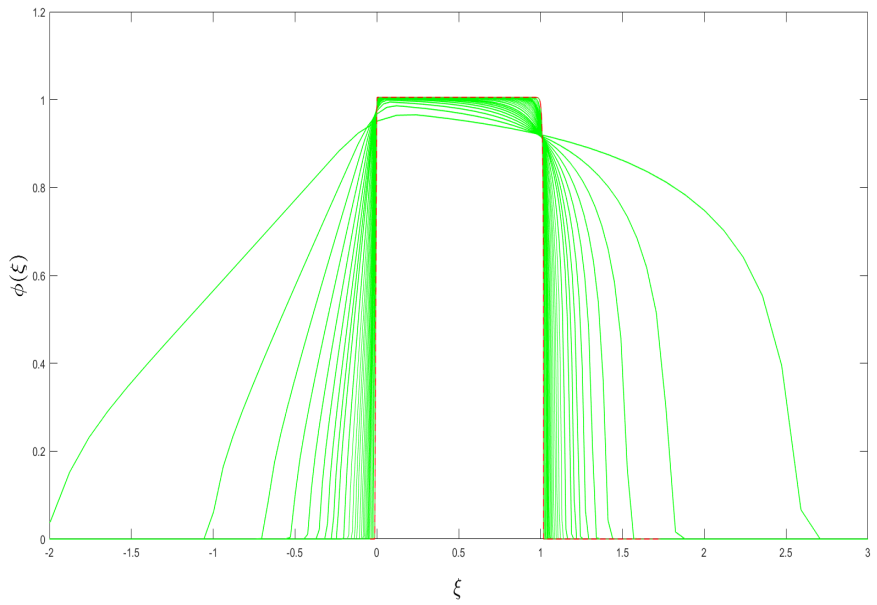

Figure 2.13: The evolution of $h(x,t)$ shown in Fig. 2.12 using similarity scaling given in Eqs. (2.46) with $\alpha = 1$ and $Q_{s_0} = 4$ (so the exponents $a = 0$ and $b = 1$). The dashed line shows the similarity solution given by Eq. (2.50).

line shows the corresponding similarity solution given by Eq. (2.50). We observe that the curves collapse onto the similarity solution under this scaling. Fig. 2.14(a,b) plot the leading edge of the dome, x_N, and the dome height, h_N, respectively, versus time, t. These are calculated from the dome evolution shown in Fig. 2.12 for $S = 1$ and $Q_{s_0} = 4$ and $\alpha = 1$ (constant source flow rate). Figure 2.14(a,b) also show the slopes which confirm that $x_N \sim t$ and h_N tends to a constant (≈ 1.21) as derived in §2.3.

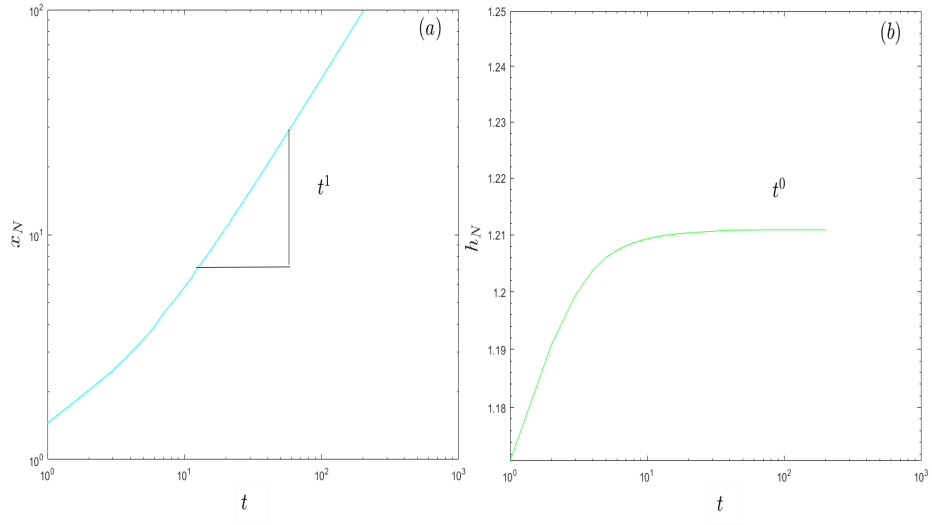

Figure 2.14: (a) Log-Log plot of the leading edge of the dome, x_N, and (b) Semi-Log plot of the dome height, h_N, versus time, t using the data shown in Fig. 2.12 for $S = 1$ and $Q_{s_0} = 4$ and $\alpha = 1$ (constant source flow rate). The slopes show that $x_N \sim t^1$ and $h_N \sim t^0$.

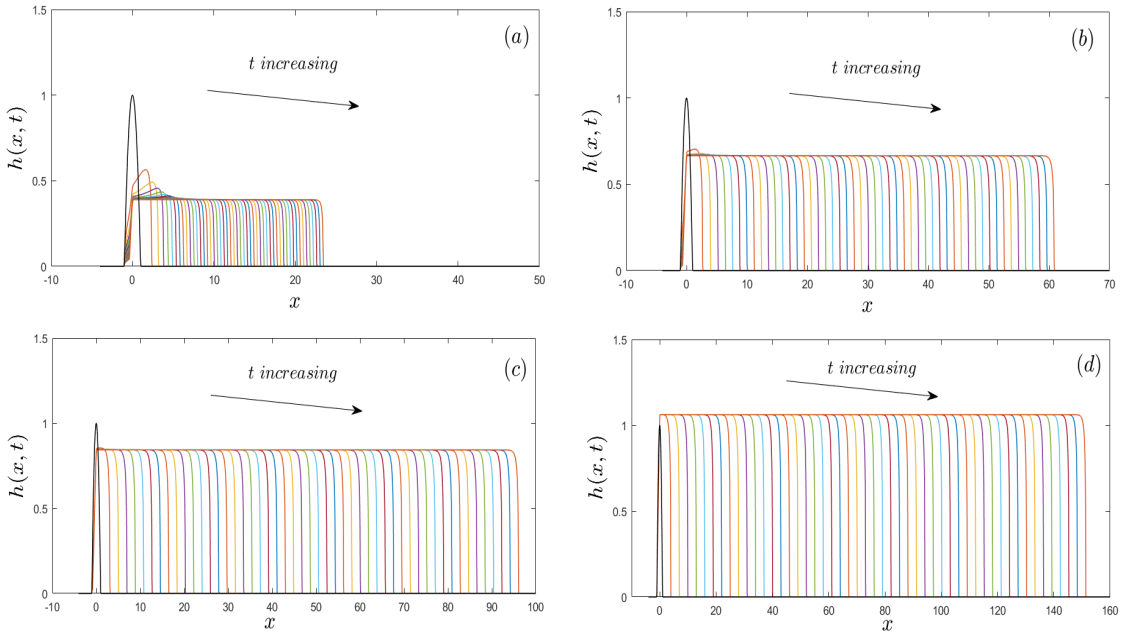

Figure 2.15: The evolution of $h(x,t)$ between $t = 0 - 2 \times 10^2$ for varying $Q_{s_0} = 0.13, 0.17, 1.3, 2.7$, and $S = 1$ and $\alpha = 1$.

We now consider the influence of the flow rate $Q_{s,0}$ on the evolution for $S = 1$ and $S = 0$. In Figure 2.15(a,b,c,d), we display the evolution of $h(x,t)$ between $t = 0-2\times10^2$ for different values of $Q_{s_0} = 0.13, 0.17, 1.3, 2.7$, respectively, for $S = 1$ and $\alpha = 1$. For low values of Q_{s_0}, the dome height near the source initially decreases in time as the dome spreads over the incline plane. At later time, the flow rate from the source is sufficiently large to sustain a constant height dome as it spreads down the plane (see Fig. 2.15(a)). For higher values of Q_{s_0}, the flow rate from the source is sufficiently large to sustain a constant height from early time (see Fig. 2.15(b,c,d)).

Fig. 2.16(a,b,c,d) show the evolution of $h(x,t)$ for t varying between $t = 0$ to $t = 200$ for various values of the source strength $Q_{s_0} = 0.01(a), 0.06(b), 0.13(c), 0.16(d)$, respectively. The parameter values are $S = 0$ and $\alpha = 1$. For low values of Q_{s_0}, the dome height near the source decreases in times as the dome spreads over the horizontal plane (see Fig. 2.16(a)). For slightly higher values of Q_{s_0}, we observe the dome height to decrease near the source. However, at later times the accumulation of liquid near the source results in the dome height increasing there as it spreads over the horizontal plane (see Fig. 2.16(b,c,d)). We observe that for the above values of Q_{s_0} the source is not strong enough to overcome the spreading due to gravity and the dome does not grow significantly. In Fig. 2.17(a,b,c,d), we display results for the dome height $h(x,t)$ for t varying between $t = 0$ to $t = 5 \times 10^2$ with a stronger source $Q_{s_0} = 1.33, 2.67, 4, 5.33$, respectively. In this case, we observe that the dome height grows significantly near the source and overcomes the spreading down the plane. It

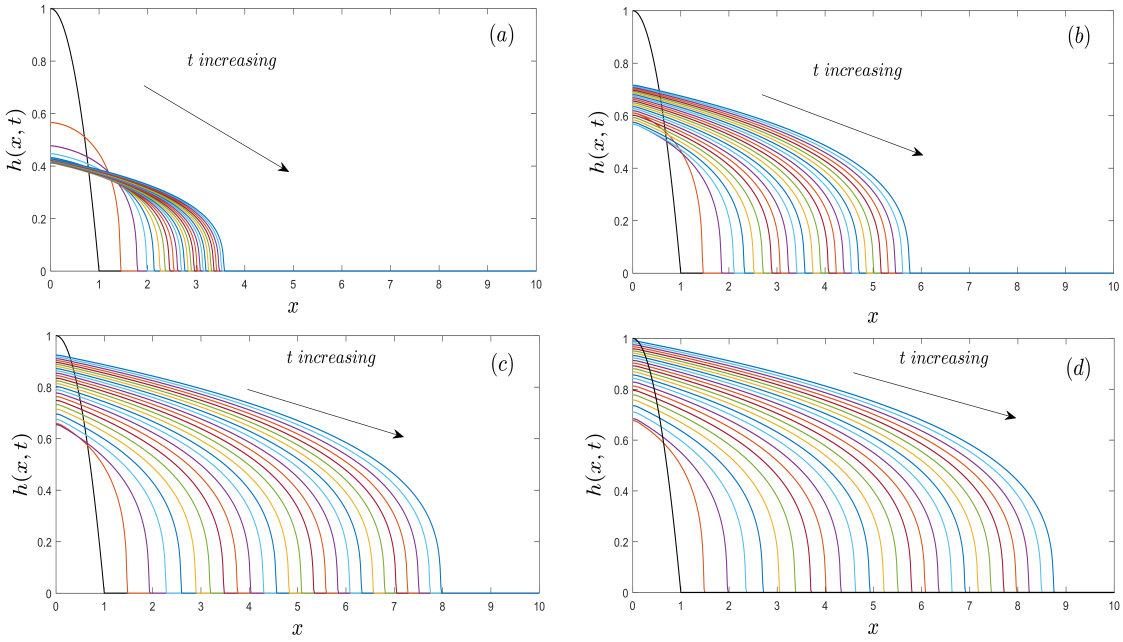

Figure 2.16: The evolution of $h(x,t)$ for t varying between $t = 0$ to $t = 5{\times}10^2$ for various values of the source strength $Q_{s_0} = 0.01(a), 0.06(b), 0.13(c), 0.16(d)$, respectively. The parameter values are $S = 0$ and $\alpha = 1$.

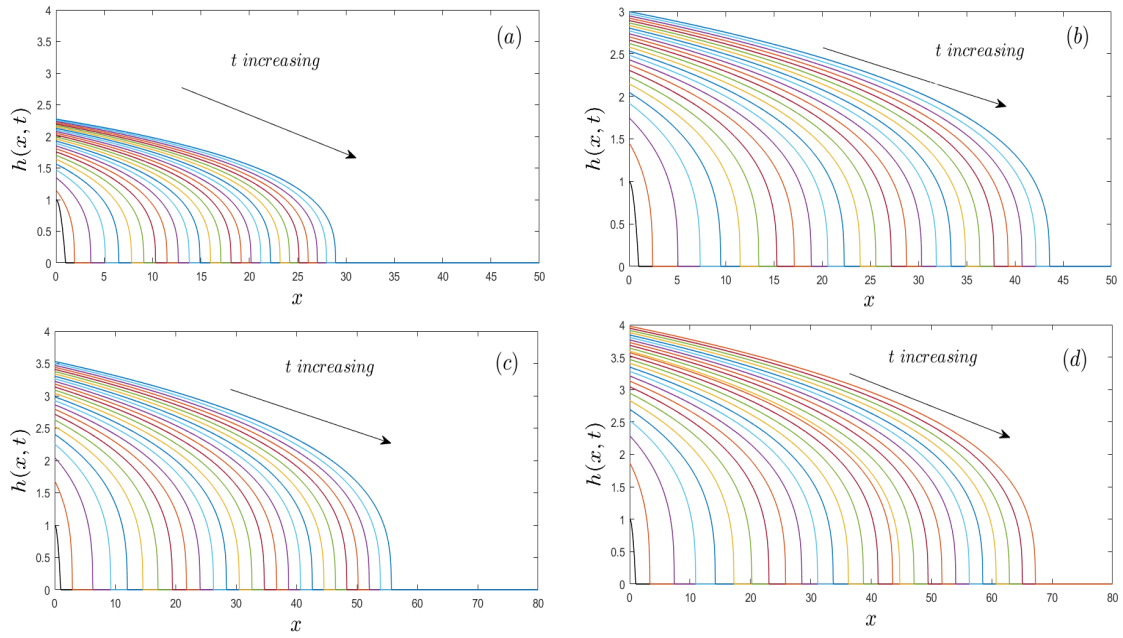

Figure 2.17: The evolution of $h(x,t)$ for t varying between $t = 0$ to $t = 5 \times 10^2$ with $Q_{s_0} = 1.33(a), 2.67(b), 4(c), 5.33(d)$, respectively. The parameter values are $S = 0$ and $\alpha = 1$.

is clear from Fig. 2.18, for example, that the dynamics of the dome, related to its continued growth and expansion, depends on the strength of the source parameter Q_{s_0} (in the case shown in Fig. 2.18, $Q_{s_0} = 4$, $S = 0$, $\alpha = 1$ and time varies between $t = 0$ to $t = 5 \times 10^2$. There appears to exist threshold value of Q_{s_0} where the fluid supplied by the source is sufficiently large. This influences the growth and expansion of the dome. Figure 2.19 shows that the numerical solution shown in figure 2.18 collapses to

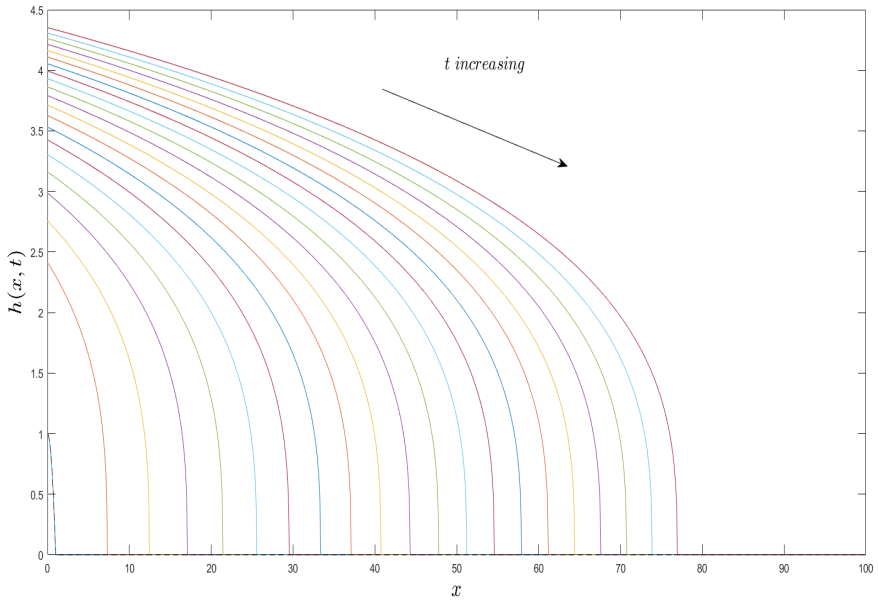

Figure 2.18: The evolution of $h(x,t)$ with $Q_{s_0} = 7$, $S = 0$ and $\alpha = 1$ for varying times between $t = 0$ to $t = 5 \times 10^2$.

a single curve under the similarity scaling, $x \sim t^{4/5}$ and $h \sim t^{1/5}$, described in §2.3, with $\alpha = 1$. Figure 2.20 shows the variation of the position of the leading edge, x_N and the maximum height, $h(x = 0)$, as a function of time for $\alpha = 1$. The two graphs confirm that $x_N \sim t^{4/5}$ and $h(x = 0) \sim t^{1/5}$ for $t \gg 1$.

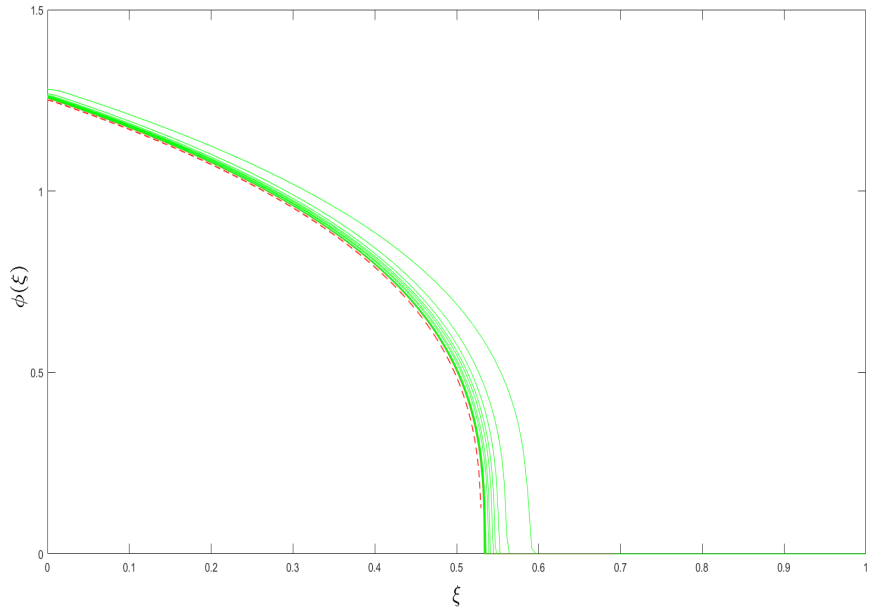

Figure 2.19: The evolution of $h(x,t)$ shown in Fig. 2.18 using the similarity scaling, $x \sim t^{4/5}$ and $h \sim t^{1/5}$. The dashed line shows the similarity solution given by Eq. (2.34b).

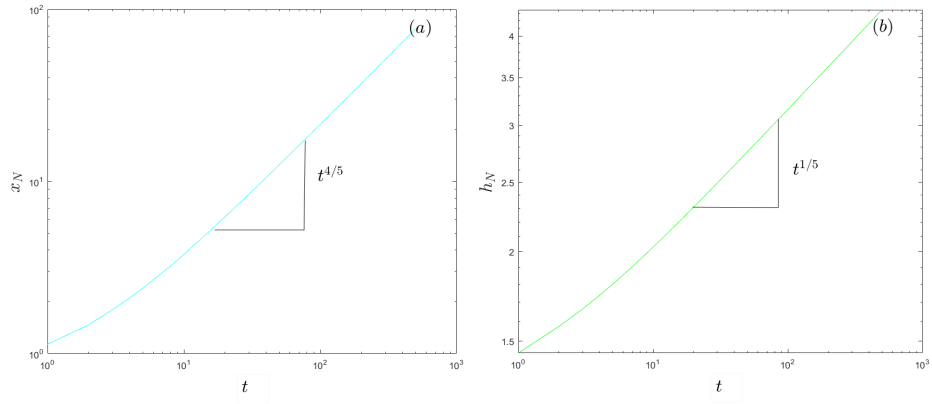

Figure 2.20: (a) Log-Log plot of the leading edge of the dome, x_N, and (b) Semi-Log plot of the maximum dome height, $h(x=0)$, versus time, t using the data shown in Fig. 2.18 for $S=0$, $Q_{s_0}=4$ and $\alpha=1$ (constant source flow rate). The slopes show that $x_N \sim t^{4/5}$ and $h(x=0) \sim t^{1/5}$.

2.5 Conclusions

In this chapter we investigate the spreading of a planar Newtonian liquid dome down a pre-wetted and inclined substrate as a simple model for the spreading of viscous-gravity currents. We assume isothermal conditions, so the liquid properties, particularly, the viscosity are constant. A parameter study, particularly, the substrate inclination angle ($S = 0$ corresponding to a horizontal plane and $S > 0$ for an inclined plane), source flowrate parameter, α ($\alpha = 0$ for constant volume and $\alpha = 1$ for constant flowrate) and the "strength" of the source, Q_{s_0}, reveal their influence on the evolution of free surface and the spreading characteristics.

Late-time similarity solutions of the evolution equation for the free surface provide scaling relationships for the maximum dome height, h_N, and the spreading distance, x_N. These similarity solutions are characterised by a volume of liquid proportional to t^α, ($\alpha \geq 0$), of liquid released by the source onto the plane. For $S = 0$, $h_N = h(x = 0, t) \sim t^{(2\alpha-1)/5}$ and $x_N \sim t^{(3\alpha+1)/5}$. For $0 < \alpha < 1/2$, h_N decreases with time and increases otherwise. For $S > 0$, $h_N = h(x = x_N, t) \sim t^{(\alpha-1)/3}$ and $x_N \sim t^{(2\alpha+1)/3}$. For $0 < \alpha < 1$, h_N decreases with time and increases otherwise. While these similarity solutions have been derived previously by Huppert [47] for $S = 0$ and Lister [54] for $S > 0$, we have validated them with corresponding numerical solutions. Our numerical solutions when scaled by the appropriate similarity variables collapse to the corresponding similarity solution at late times.

Our numerical solutions reveal the dynamics of the dome evolution. Two distinct free

surface shapes were identified from the numerical solutions and similarity solutions. For spreading of a dome with constant volume (so $\alpha = 0$), we observe

(i) a dome-shaped profile which thins and spreads in time for $S = 0$, and

(ii) a slumping dome with a steep front at its leading edge which also thins and spreads in time observed for $S > 0$.

For spreading of a dome with constant flowrate (so $\alpha = 1$), we observe

(i) for $S = 0$, a dome-shaped profile which grows in time depending on the source strength parameter, Q_{s_0}. There exists a critical value of Q_{s_0} beyond which significant dome growth in the dome height occurs, and

(ii) for $S > 0$, the dome height grows to a constant height balanced by the spreading length.

The model and results presented in this chapter are theoretical and at best describe qualitatively the dynamics associated with real spreading of viscous gravity currents, such as lava flows. Nevertheless results such as the significant growth in the dome height past a critical value of Q_{s_0} predicted by the model could be linked to catastrophic events related to dome collapse.

Chapter 3

The isothermal and non-Newtonian spreading of a liquid dome down an inclined plane

3.1 Introduction

In this chapter, we extend the one-dimensional Newtonian liquid model to incorporate non-Newtonian effects, such as apparent or shear rate-dependent viscosity and yield stress. The constitutive relations between the liquid stress and its shear rate for a general non-Newtonian and viscoplastic liquid described in §1.3.1, Chapter 1 are considered. We use similarity and numerical solutions to characterise the evolution of the free surface for a range of parameter values associated with non-Newtonian and

viscoplastic effects along with the source flowrate and the inclination angle.

The outline of this chapter is as follows. In §3.2, we extend the one-dimensional mathematical formulation for a Newtonian liquid to include non-Newtonian and viscoplastic constitutive relations for a Power-law, Bingham, Herschel-Bulkley and Carreau fluid. The lubrication approximation is used again to reduce the governing equations to a single PDE for the evolution of the one-dimensional free surface shape. In §3.3 we derive late-time similarity solutions for the evolution of the free surface such that the volume of liquid in the dome is proportional to t^α, ($\alpha \geq 0$). Previously, Balmforth *et al.* [5, 9] have identified similarity solutions for Power-law and Herschel Bulkley models for constant volume spreading. We generalise these to general α and also explicitly compute the similarity solutions. In §3.4, we perform numerical simulations of the evolution equation to determine the free surface shapes for a variety of parameter values, in particular, the power-law index and the yield stress. The numerical solutions are validated against the similarity solutions. In §3.5 we discuss the main results.

3.2 Mathematical Formulation

We consider a similar problem set-up as described in §2.2 of a liquid dome spreading under the influence of gravity down an inclined and pre-wetted plane (see Fig. 2.1 for a schematic). The liquid in the dome is assumed to be non-Newtonian.

3.2.1 Governing Equations

The one-dimensional governing equations are given by the conservation of mass and momentum, Eqs. (2.1). The constitutive relation between the liquid stress and its rate of strain for a generalised non-Newtonian liquid is written as:

$$\boldsymbol{\tau}^\star = \mu^\star(\dot{\gamma}^\star)\dot{\boldsymbol{\gamma}}^\star, \tag{3.1}$$

where the function $\mu^\star(\dot{\gamma}^\star)$ is the non-Newtonian liquid viscosity, $\dot{\boldsymbol{\gamma}}^\star$ is the rate of strain tensor given by Eq. (2.3) and $\dot{\gamma}^\star$ is the second invariant of the rate of strain tensor given by $\dot{\gamma}^\star = \sqrt{\frac{1}{2}\dot{\gamma}^\star_{ij}\dot{\gamma}^\star_{ij}}$. We also require the second invariant of the stress tensor, $\tau^\star = \sqrt{\frac{1}{2}\tau^\star_{ij}\tau^\star_{ij}}$.

The boundary conditions are given by Eqs. (2.4-2.11).

This problem is also nondimensionalised in the same way as in Chapter 2. We use a constant reference viscosity, $\mu^\star_R$, in the nondimensionalisations used. The nondimensional form of Eq. (3.1) is given by

$$\boldsymbol{\tau} = \mu(\dot{\gamma})\dot{\boldsymbol{\gamma}}, \tag{3.2}$$

where $\dot{\boldsymbol{\gamma}}$ is given by Eq. (2.14) and the dimensionless second invariants of the rate of

strain and stress tensors are given by

$$\dot{\gamma} = \sqrt{(u_z + \epsilon^2 w_x)^2 + 4\epsilon^2 {u_x}^2}, \;\; \tau = \sqrt{\tau_{xz}^2 + \frac{1}{2}\epsilon^2(\tau_{xx}^2 + \tau_{zz}^2)}. \tag{3.3}$$

We proceed in the same way as described in Chapter 2 in performing the lubrication approximation for the leading order problem in ϵ. We follow the same sequence of steps in solving the leading order problem until the expression for the leading order shear stress, $\tau_{xz_0}(x,z) = (S - h_{0_x})(h_0 - z)$. Using Eq. (3.2) and $\dot{\gamma}_0 = \sqrt{u_{0_z}^2} = |u_{0_z}|$, we obtain the leading order relationship between the shear stress and the shear rate as $\tau_{xz_0} = f(|u_{0_z}|)u_{0_z}$. Using the expression for τ_{xz_0}, we obtain

$$f(|u_{0_z}|)u_{0_z} = (S - h_{0_x})(h_0 - z). \tag{3.4}$$

This equation needs to be solved for a given function $f(|u_{0_z}|)$ to obtain the leading order shear rate, u_{0_z}. Proceeding in the same way as described in Chapter 2, we can write the evolution equation as:

$$h_{0_t} + Q_{0_x} = w_s, \;\; Q_0(x,t) = \int_0^{h_0} (h_0 - z)u_{0_z} dz. \tag{3.5}$$

The evolution equation is coupled with Eq. (3.4) for u_{0_z}.

We now consider different forms of the function $f(|u_{0_z}|)$ in Eq. (3.4) corresponding to constitutive relationships for a Power-law, Herschel-Bulkley and Carreau liquid.

Power-law model

For a Power-law model, we have

$$f(|u_{0_z}|) = K|u_{0_z}|^{n-1}, \tag{3.6}$$

where $K = (K^\star/\mu_R^\star)(U^\star/H^\star)^{n-1}$, is a dimensionless liquid consistency index and n is the power-law index. Eq. (3.4) becomes

$$K|u_{0_z}|^{n-1}u_{0_z} = (S - h_{0_x})(h_0 - z). \tag{3.7}$$

Hence,

$$u_{0_z} = \frac{1}{K}[|S - h_{0_x}|(h_0 - z)]^{\frac{1}{n}} sgn(S - h_{0_x}), \tag{3.8}$$

The flux, Q_0 is then given by

$$Q_0(x,t) = \frac{1}{K}\frac{n}{2n+1}\left[|S - h_{0_x}|^{(\frac{1}{n}-1)}h_0^{\frac{2n+1}{n}}\right](S - h_{0_x}). \tag{3.9}$$

Thus, the evolution equation, Eq. (3.5) can be written as

$$h_{0_t} + \frac{1}{K}\frac{n}{2n+1}\left[|S - h_{0_x}|^{(\frac{1}{n}-1)}(S - h_{0_x})h_0^{\frac{2n+1}{n}}\right]_x = w_s. \tag{3.10}$$

Herschel-Bulkley Model

For a Herschel-Bulkley constitutive law,

$$f(|u_{0_z}|) = K|u_{0_z}|^{n-1} + \frac{B}{|u_{0_z}|}, \tag{3.11}$$

where $B = \frac{\tau_y^\star H^\star}{\mu_R^\star U^\star} = \frac{\tau_y^\star L^\star}{\rho^\star g^\star H^{\star 2}\cos\theta}$ is the Bingham number which compares the liquid yield stress to the viscous stress. Eq. (3.4) becomes

$$\begin{aligned} \left[K|u_{0_z}|^{n-1} + \tfrac{B}{|u_{0_z}|}\right] u_{0_z} &= (S - h_{0_x})(h_0 - z), \quad \text{for } \tau_0 = |\tau_{xz_0}| = |S - h_{0_x}|(h_0 - z) \geq B, \\ u_{0_z} &= 0, \quad \text{for } \tau_0 = |\tau_{xz_0}| = |S - h_{0_x}|(h_0 - z) < B, \end{aligned} \tag{3.12}$$

where τ_0 is the leading order second invariant of the stress tensor (Eq. (3.3)). We define a yield surface, $z = \mathcal{Y}(x,t)$, such that $|\tau_{xz_0}| = B$ and $u_{0_z} = 0$ there. This implies that $|S - h_{0_x}|(h_0 - \mathcal{Y}) = B$ at $z = \mathcal{Y}(x,t)$. Hence, $\mathcal{Y} = \max(h_0 - \frac{B}{|S - h_{0_x}|}, 0)$. Using the definition of the yield surface, we can write Eq. (3.12) as:

$$\begin{aligned} \left[K|u_{0_z}|^{n-1} + \tfrac{B}{|u_{0_z}|}\right] u_{0_z} &= (S - h_{0_x})(h_0 - z), \quad \text{for } z \leq \mathcal{Y}, \\ u_{0_z} &= 0, \quad \text{for } z > \mathcal{Y}. \end{aligned} \tag{3.13}$$

One can solve the above for u_{0_z} to obtain:

$$u_{0_z} = \begin{cases} \frac{1}{K}|S - h_{0_x}|^{1/n}\left(\mathcal{Y} - z\right)^{1/n} sgn(S - h_{0_x}), & \text{for } z \leq \mathcal{Y}, \\ 0, & \text{for } z > \mathcal{Y}. \end{cases} \tag{3.14}$$

The flux, Q_0 is then given by

$$Q_0(x,t) = \frac{1}{K}\frac{n}{(n+1)(2n+1)}|S-h_{0_x}|^{\frac{1}{n}-1}\mathcal{Y}^{\frac{1}{n}+1}[(2n+1)h_0 - n\mathcal{Y}](S-h_{0_x}). \quad (3.15)$$

Thus, the evolution equation, Eq. (3.5) can be written as

$$h_{0_t} + \frac{1}{K}\frac{n}{(n+1)(2n+1)}\left[|S-h_{0_x}|^{\frac{1}{n}-1}\mathcal{Y}^{\frac{1}{n}+1}[(2n+1)h_0 - n\mathcal{Y}](S-h_{0_x})\right]_x = w_s, \quad (3.16)$$

where the yield surface, $\mathcal{Y}(x,t) = \max(h_0 - \frac{B}{|S-h_{0_x}|}, 0)$.

Carreau Model

For the Carreau model, the constitutive law,

$$f(|u_{0_z}|) = \mu_\infty + \frac{\mu_0 - \mu_\infty}{[1+(\lambda|u_{0_z}|)^2]^{(\frac{1-n}{2})}}, \quad (3.17)$$

where $\mu_\infty = \mu_\infty^\star/\mu_R^\star$, $\mu_0 = \mu_0^\star/\mu_R^\star$ and $\lambda = \lambda^\star H^\star/U^\star$. Eq. (3.4) becomes

$$\left[\mu_\infty + \frac{\mu_0 - \mu_\infty}{[1+(\lambda|u_{0_z}|)^2]^{(\frac{1-n}{2})}}\right] u_{0_z} = (S-h_{0_x})(h_0 - z). \quad (3.18)$$

Define $q = u_{0_z}$ and assume $u_{0_z} \geq 0$. Then we can write Eq. (3.18) as:

$$f(q)q = |S-h_{0_x}|(h_0 - z). \quad (3.19)$$

Taking the derivative with respect to z implies: $|S - h_{0_x}|dz = -\frac{d(f(q)q)}{dq}dq$. Now, $(h_0 - z) = \frac{f(q)q}{|S-h_{0_x}|}$, so $q = 0$ when $z = h_0$ and $q = q_0$, when $z = 0$ with $f(q_0)q_0 = |S - h_{0_x}|h_0$. Substituting these in Eq. (3.5), we obtain

$$Q_0(x,t) = \int_0^{q_0} \frac{f(q)q^2}{|S-h_x|^2}\left(\frac{d[f(q)q)]}{dq}dq\right). \tag{3.20}$$

The above equation can be written in the form:

$$Q(x,t) = \frac{F(q_0)}{|S-h_x|^2}, \quad F(q_0) = \int_0^{q_0} f(q)q^2\frac{d[f(q)q)]}{dq}dq, \tag{3.21}$$

where $q_0 = q|_{z=0}$ is the shear rate at the substrate given by $f(q_0)q_0 = |S - h_{0_x}|h_0$. Substituting Eq(3.21) in Eq(3.5) we obtain the evolution equation

$$h_t + \left[\frac{F(q_0)}{|S-h_{0_x}|^2}\right]_x = w_s, \tag{3.22a}$$

$$F(q_0) = \int_0^{q_0} f(q)q^2\frac{d[f(q)q)]}{dq}dq, \tag{3.22b}$$

$$f(q_0)q_0 = |S - h_{0_x}|h_0. \tag{3.22c}$$

3.3 Late-time similarity solutions for Herschel-Bulkley time-dependent $Q_s(t)$

Similar to §2.3 in Chapter 2, here we seek similarity solutions of the liquid dome height evolution, Eqs. (3.10, 3.16), for the Power-law and Herschel-Bulkley constitutive models, respectively. This is subject to the volume constraint (a total conservation of mass)

$$\int_{X_T}^{X_N} h \, dx = Q_{s_0} t^{\alpha} + V_0, \tag{3.23}$$

where the flow lies in $X_T(t) < x < X_N(t)$ and V_0 is an initial volume of liquid in the dome.

We seek similarity solutions for the evolution equation representing the Herschel-Bulkley constitutive model:

$$h_{0_t} + \frac{1}{K} \frac{n}{(n+1)(2n+1} \left[|S - h_{0_x}|^{\frac{1}{n}-1} \mathcal{Y}^{\frac{1}{n}+1} [(2n+1)h_0 - n\mathcal{Y}](S - h_{0_x}) \right]_x = 0, \tag{3.24a}$$

$$\int_{X_T}^{X_N} h \, dx = Q_{s_0} t^{\alpha} + V_0. \tag{3.24b}$$

Special cases corresponding to $B = 0$ (Power-law liquid), $\alpha = 0$ (constant volume) and $\alpha = 1$ (constant source flow rate) will be considered separately, if necessary.

Late-time similarity solution for $S = 0$

We define the similarity variables

$$\xi = \frac{x}{t^b \left(\frac{Q_{s_0}^{n+2}}{(\frac{2n+1}{n})^n}\right)^{1/(2n+3)}}, \quad h(x,t) = \left[\left(\frac{2n+1}{n}\right)^n Q_{s_0}^{n+1}\right]^{1/(2n+3)} t^a \phi(\xi), \tag{3.25}$$

where the exponents a and b need to be determined. Substituting in Eq. (3.24a), the evolution equation can be written in the form

$$t^{a-1}\left(a\phi - b\xi\phi_\xi\right) - t^{a-b}\frac{1}{n+1}\left[(t^{a-b}|\phi_\xi|)^{\frac{1}{n}-1}(t^a)^{\frac{1}{n}+1}\mathcal{Y}^{\frac{1}{n}+1}\left[(2n+1)\phi - n\mathcal{Y}\right](t^{a-b}\phi_\xi)\right]_\xi = 0, \tag{3.26a}$$

$$\text{where} \quad \mathcal{Y} = \max\left(\phi - B\frac{t^{-2a+b}}{|\phi_\xi|\left[\left(\frac{2n+1}{n}\right)^3 Q_{s_0}\right]^{n/(2n+3)}}, 0\right). \tag{3.26b}$$

Setting

$$a\left(1+\frac{2}{n}\right) - b\left(1+\frac{1}{n}\right) = -1, \tag{3.27}$$

removes any time dependence in Eq. (3.26a). For $t \gg 1$, Eq. (3.26b) has error $O(t^{-2a+b})$. Hence, we require $b < 2a$ for the error to be sub-dominant for $t \gg 1$. Now, $a + b = \alpha$ from the conservation of volume. Hence, we obtain $a = \frac{\alpha(n+1)-n}{2n+3}$, $b = \frac{\alpha(n+2)+n}{2n+3}$. To satisfy the condition $b < 2a$, we require $\alpha > 3$.

Therefore, the similarity variables can be written as:

$$h(x,t) = \left[\left(\frac{2n+1}{n}\right)^n Q_{s_0}^{n+1}\right]^{1/(2n+3)} t^{\frac{\alpha(n+1)-n}{2n+3}}\phi(\xi), \;\; \xi = \frac{x}{t^{\frac{\alpha(n+2)+n}{2n+3}}}\left(\frac{(\frac{2n+1}{n})^n}{Q_{s_0}^{n+2}}\right)^{1/(2n+3)}. \tag{3.28}$$

For $t \gg 1$, the above equation shows that the maximum dome height for $S = 0$ is $h(\xi = 0))$ $h \sim t^{\frac{\alpha(n+1)-n}{2n+3}}$ and the location of its front $x_N \sim t^{\frac{\alpha(n+2)+n}{2n+3}}$. Therefore, for $\alpha > 3$, the late-time behaviour of Eq. (3.26) can be written as:

$$\left[\frac{\alpha(n+1)-n}{2n+3}\phi - \frac{\alpha(n+2)+n}{2n+3}\xi\phi_\xi\right] - \frac{1}{n+1}\left[|\phi_\xi|^{\frac{1}{n}-1}\phi^{\frac{2n+1}{n}}\phi_\xi\right]_\xi = O(t^{\frac{n(3-\alpha)}{2n+3}}), \tag{3.29a}$$

$$\int_0^{\xi_N} \phi \; d\xi = 1 + O(t^{-\alpha}). \tag{3.29b}$$

For $\alpha = 3$, the late-time behaviour of Eq. (3.26) can be written as:

$$\left[\frac{\alpha(n+1)-n}{2n+3}\phi - \frac{\alpha(n+2)+n}{2n+3}\xi\phi_\xi\right] - \frac{1}{n+1}\left[|\phi_\xi|^{\frac{1}{n}-1}\mathcal{Y}^{\frac{1}{n}+1}\left[(2n+1)\phi - n\mathcal{Y}\right]\phi_\xi\right]_\xi = 0, \tag{3.30a}$$

$$\mathcal{Y} = \max\left(\phi - \frac{\tilde{B}}{|\phi_\xi|}, 0\right), \;\; \text{where} \;\; \tilde{B} = \frac{B}{\left[\left(\frac{2n+1}{n}\right)^3 Q_{s_0}\right]^{n/(2n+3)}}, \tag{3.30b}$$

$$\int_0^{\xi_N} \phi \; d\xi = 1 + O(t^{-\alpha}). \tag{3.30c}$$

For $\alpha < 3$, there does not exist a late-time similarity solution for $B \neq 0$. However, for $B = 0$ (or $\mathcal{Y} = \phi$), there exist a similarity solution for all $\alpha > 0$. This late time behaviour is also described by Eq. (3.29) with the error term in Eq. (3.29a) now exactly zero. This is precisely the similarity solution for the Power-law model in Eq. (3.10). Eq. (3.29a) can also be written as:

$$\left[|\phi_\xi|^{\frac{1}{n}-1}\phi^{\frac{2n+1}{n}}\phi_\xi\right]_\xi + \left[\frac{\alpha(n+2)+n}{2n+3}\right]\xi\phi_\xi - \left[\frac{\alpha(n+1)-n}{2n+3}\right]\phi = 0, \tag{3.31}$$

Define $z = \xi/\xi_N$ and $\phi(z) = \xi_N^{\frac{n+1}{n+2}}\tilde{\phi}(z)$. Substituting this into Eq. (3.31), we obtain

$$\left[|\tilde{\phi}_z|^{\frac{1}{n}-1}\tilde{\phi}^{\frac{2n+1}{n}}\tilde{\phi}_z\right]_z + \left[\frac{\alpha(n+2)+n}{2n+3}z\tilde{\phi}_z - \frac{\alpha(n+1)-n}{2n+3}\tilde{\phi}\right] = 0, \tag{3.32}$$

Also substituting the above into Eq. (3.29b), we obtain

$$\xi_N = \left(\int_0^1 z\tilde{\phi}dz\right)^{-(n+2)/(2n+3)}. \tag{3.33}$$

Therefore

$$z = \frac{x}{\xi_N t^{\frac{\alpha(n+2)+n}{2n+3}}}\left(\frac{(\frac{2n+1}{n})^n}{Q_{s_0}^{n+2}}\right)^{1/(2n+3)}, \quad h(x,t) = \xi_N^{\frac{n+1}{n+2}}\left[\left(\frac{2n+1}{n}\right)^n Q_{s_0}^{n+1}\right]^{1/(2n+3)} t^{\frac{\alpha(n+1)-n}{2n+3}}\tilde{\phi}(z), \tag{3.34a}$$

$$\left[|\tilde{\phi}_z|^{\frac{1}{n}-1}\tilde{\phi}^{\frac{2n+1}{n}}\tilde{\phi}_z\right]_z + \left[\frac{\alpha(n+2)+n}{2n+3}z\tilde{\phi}_z - \frac{\alpha(n+1)-n}{2n+3}\tilde{\phi}\right] = 0, \tag{3.34b}$$

$$\xi_N = \left(\int_0^1 z\tilde{\phi}dz\right)^{-(n+2)/(2n+3)}. \tag{3.34c}$$

Eq. (3.34b) is solved numerically for any value of $\alpha > 0$. The boundary condition at $z = 0$ is given by $\tilde{\phi}_z = 0$ (from symmetry at $x = 0$). We can apply the Frobenius method to determine a solution of Eq. (3.34b) in the neighbourhood of the point $z = 1$. We seek a solution of the form $\tilde{\phi}(z) = \sum_{m=0}^{\infty} a_m (1-z)^{r+m}$, where r is a constant to be determined. Substituting this in Eq. (3.34b), we can show that the solution is given by

$$\tilde{\phi}(z) = (n+2)^{1/n+2} \Big[\frac{\alpha(n+2)+n}{2n+3} \Big]^{n/(n+2)} (1-z)^{1/(n+2)} + \text{h.o.t, for } z = 1^{-}. \quad (3.35)$$

In practice, we chose $z = 1 - \delta$, for $\delta \ll 1$ specified. For arbitrary α, and using Eq. (3.34b) with boundary conditions $\tilde{\phi}_z = 0$ at $z = 0$ and Eq. (3.35) at $z = 1 - \delta$, the solution can be obtained by numerically integrating Eq. (3.34b) using FSOLVE module in MATLAB (Release 2013a, The MathWorks, Inc., Natick, Massachusetts, United States). The similarity solution is represented by the boundary-value problem in Eq. (3.34b) along with the boundary conditions given by $\tilde{\phi}_z = 0$ at $z = 0$ and Eq. (3.35) at $z = 1 - \delta$.

For $\alpha = 0$ the solution of Eq. (3.34b) can be obtained analytically, where this equation reduces to

$$-\frac{n}{2n+3} (\phi - \xi\phi_\xi) - \Big[|\phi_\xi|^{\frac{1}{n}-1} \phi^{\frac{2n+1}{n}} \phi_\xi \Big]_\xi = 0. \quad (3.36)$$

Integrating and using the boundary condition $\phi_\xi = 0$, at $\xi = 0$ gives

$$-\frac{n}{2n+3} (\xi\phi_\xi) = \Big(|\phi_\xi|^{\frac{1}{n}} \phi^{\frac{2n+1}{n}} \Big). \quad (3.37)$$

Integrating again and using $\phi = 0$ at $\xi = \xi_N$, we obtain

$$\phi = \begin{cases} \left[(\frac{n}{2n+3})^n (\frac{n+2}{n+1})(\xi^{n+1} - \xi_N^{n+1}) \right]^{1/(n+2)}, & \xi < \xi_N, \\ 0, & \xi > \xi_N, \end{cases} \tag{3.38}$$

where ξ_N is given by

$$\left[\left(\frac{n}{2n+3} \right) \left(\frac{n+2}{n+1} \right) \right]^{1/(n+2)} \int_0^{\xi_N} \left(\xi_N^{n+1} - \xi^{n+1} \right)^{1/(n+2)} \, d\xi = 1. \tag{3.39}$$

Using the substitution $\xi = \xi_N \cos^{\left(\frac{2}{n+1}\right)}(\theta)$, this simplifies to

$$\left[\left(\frac{n}{2n+3} \right) \left(\frac{n+2}{n+1} \right) \right]^{1/(n+2)} \xi_N^{\left(\frac{2n+3}{n+2}\right)} \int_0^{\pi/2} \sin^{\left(\frac{2n+3}{n+2}\right)}(\theta) d\theta = 1. \tag{3.40}$$

$$\xi_N \equiv \left[\left(\frac{n}{2n+3} \right) \left(\frac{n+2}{n+1} \right) \right]^{-1/(2n+3)} \left(\frac{1}{\int_0^{\pi/2} \sin^{\left(\frac{2n+3}{(n+2)}\right)}(\theta) d\theta} \right)^{\left(\frac{n+2}{2n+3}\right)}. \tag{3.41}$$

The solution, $\phi(\xi)$, as a function of ξ is shown in Fig. 3.1 for various values of α with $n = 0.6$. We observe that as α increases, although the free surface shapes look similar, the length over which they have spread, ξ_N decreases and the maximum height, $\phi(\xi = 0)$, increases. This is consistent with the fact that as α increases, the additional volume of liquid from the source contributes more to inflating the dome rather than its spreading. The results in Fig. 3.1 are similar to the results in Chapter 2 for a Newtonian fluid, except for $\alpha > 1$, the dome decreases in height and increases in length compared to the Newtonian fluid. The opposite happens for $\alpha < 1$. This is due to the shear thinning for $n = 0.6$. In Fig. 3.2 we show the solution, $\phi(\xi)$, as a function

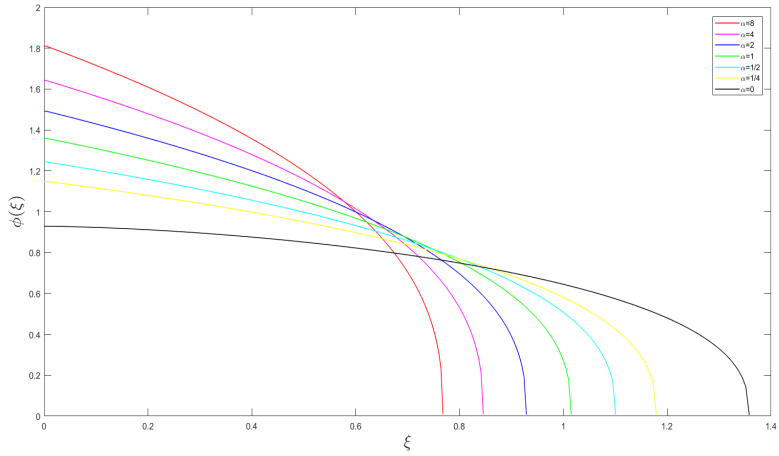

Figure 3.1: The late-time similarity solution, ϕ, as a function of ξ for $S = 0$ with $n = 0.6$ and varying α obtained from the numerical solution of Eq.(3.34b) using boundary conditions $\tilde{\phi}_z = 0$ at $z = 0$ and Eq.(3.35) at $z = 1 - \delta$.

of ξ for various values of n with $\alpha = 0$. We observe that as n decreases, the dome spreads less in comparison to a Newtonian dome. This is because the flow shear rate is much less than one, so the viscosity increases as n decreases slowing the spreading.

Late-time similarity solution for $S > 0$

We define the similarity variables

$$\xi = \frac{x}{t^b \left(\frac{Q_{s_0}^{n+1}}{(\frac{2n+1}{n})^n} \right)^{1/(2n+1)}}, \quad h(x,t) = \left[\left(\frac{2n+1}{n} \right) Q_{s_0} \right]^{n/(2n+1)} t^a \phi(\xi), \tag{3.42}$$

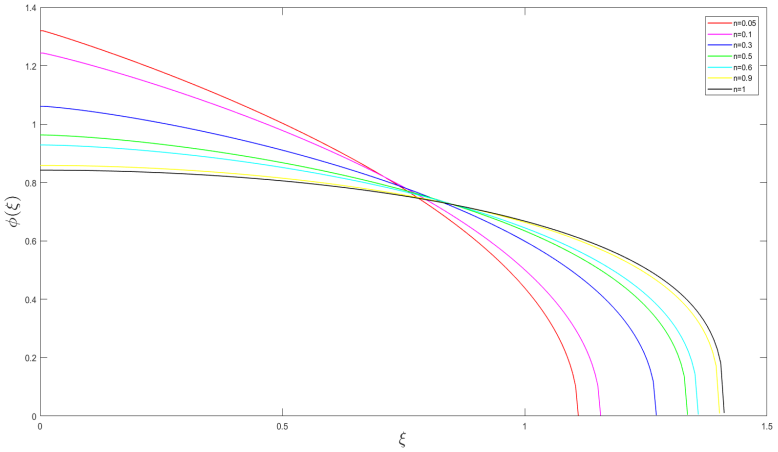

Figure 3.2: The late-time similarity solution, ϕ, as a function of ξ for $S = 0$ with $\alpha = 0$ and varying n obtained from the numerical solution of Eq.(3.34b) using boundary conditions $\tilde{\phi}_z = 0$ at $z = 0$ and Eq.(3.35) at $z = 1 - \delta$.

where the exponents a and b need to be determined. Substituting in Eq. (3.24a), the evolution equation can be written in the form

$$(a\phi - b\xi\phi_\xi)t^{a-1} + t^{a-b}\frac{1}{n+1}\left[|\zeta|^{\frac{1}{n}-1}t^{a(\frac{1}{n}+1)}\mathcal{Y}^{\frac{1}{n}+1}\left[(2n+1)\phi - n\mathcal{Y}\right]\zeta\right]_\xi = 0, \tag{3.43a}$$

$$\text{where} \quad \mathcal{Y} = \max\left(\phi - B\frac{t^{-a}}{|\zeta|\left(\frac{2n+1}{n}Q_{s_0}\right)^{n/(2n+1)}}, 0\right), \quad \zeta = \left[S - \left(\frac{(\frac{2n+1}{n})^2}{Q_{s_0}^{1/n}}\right)^{n/(2n+1)} t^{a-b}\phi_\xi\right]. \tag{3.43b}$$

We set

$$a\left(1 + \frac{1}{n}\right) - b = -1. \tag{3.44}$$

For $t \gg 1$, Eq. (3.26b) has error $O(t^{a-b}, t^{-a}, t^{-b}, t^{2a-2b})$. Hence, we require $a - b < 0$, $a > 0$ and $b < 0$ for the error to be sub-dominant for $t \gg 1$. Now, $a + b = \alpha$ from the conservation of volume. Hence, we obtain $a = \frac{n(\alpha-1)}{2n+1}$, $b = \frac{\alpha(n+1)+n}{2n+1}$. The condition

$a-b<0$ and $b>0$ are staisfied for all α and n. For $a>0$, we require $\alpha>1$.

Therefore, the similarity variables can be written as:

$$h(x,t)=\left[\left(\frac{2n+1}{n}\right)Q_{s_0}\right]^{n/(2n+1)}t^{\frac{n(\alpha-1)}{2n+1}}\phi(\xi),\ \ \xi=\frac{x}{t^{\frac{\alpha(n+1)+n}{2n+1}}}\left(\frac{(\frac{2n+1}{n})^n}{Q_{s_0}^{n+1}}\right)^{1/(2n+1)}. \tag{3.45}$$

For $t\gg 1$, the above equation shows that the maximum dome height for $S>0$ is $h(\xi=0))$ $h\sim t^{\frac{n(\alpha-1)}{2n+1}}$ and the location of its front $x_N\sim t^{\frac{\alpha(n+1)+n}{2n+1}}$. Therefore, for $\alpha>1$, the late-time behaviour of Eq. (3.43) can be written as:

$$\left[\frac{n(\alpha-1)}{2n+1}\phi-\frac{\alpha(n+1)+n}{2n+1}\xi\phi_\xi\right]+\frac{1}{n+1}\left[S^{\frac{1}{n}}\mathcal{Y}^{\frac{1}{n}+1}\left[(2n+1)\phi-n\mathcal{Y}\right]\right]_\xi= \tag{3.46a}$$

$$O(t^{\frac{-(\alpha+2n)}{2n+1}},t^{-\frac{n(\alpha-1)}{2n+1}},t^{-\frac{\alpha(n+1)+n}{2n+1}}),$$

$$\text{where}\quad \mathcal{Y}=\max\left(\phi-B\frac{t^{-\frac{n(\alpha-1)}{2n+1}}}{|\zeta|\left(\frac{2n+1}{n}Q_{s_0}\right)^{n/(2n+1)}},0\right),\ \ \zeta=\left[S-\left(\frac{(\frac{2n+1}{n})^2}{Q_{s_0}^{1/n}}\right)^{n/(2n+1)}t^{\frac{-(\alpha+2n)}{2n+1}}\phi_\xi\right], \tag{3.46b}$$

$$\int_{\xi_T}^{\xi_N}\phi\ d\xi=1+O(t^{-\alpha}). \tag{3.46c}$$

For $\alpha=1$, the late-time behaviour of Eq. (3.43) can be written as:

$$[\xi\phi_\xi]=\frac{1}{n+1}\left[S^{\frac{1}{n}}\mathcal{Y}^{\frac{1}{n}+1}\left[(2n+1)\phi-n\mathcal{Y}\right]\right]_\xi+O(t^{-1}), \tag{3.47a}$$

$$\mathcal{Y}=\max\left(\phi-\tilde{B},0\right),\ \ \zeta=S+O(t^{-1})\ \ \text{where}\ \ \tilde{B}=\frac{B}{S\left(\frac{2n+1}{n}Q_{s_0}\right)^{n/(2n+1)}}, \tag{3.47b}$$

$$\int_{\xi_T}^{\xi_N}\phi\ d\xi=1+O(t^{-\alpha}). \tag{3.47c}$$

Eq. (3.47a) reduces to

$$[\xi\phi_\xi] = \frac{1}{n+1}\left[S^{\frac{1}{n}}(\phi-\tilde{B})^{\frac{1}{n}+1}\left[(n+1)\phi+n\tilde{B}\right]\right]_\xi \tag{3.48}$$

For $\alpha < 1$, there does not exist a late-time similarity solution for $B \neq 0$. However, for $B = 0$ (or $\mathcal{Y} = \phi$), there exist a similarity solution for all $\alpha > 0$. This late time behaviour is also described by Eq. (3.46). This is precisely the similarity solution for the Power-law model in Eq. (3.10) and is written as:

$$\left[\frac{n(\alpha-1)}{2n+1}\phi - \frac{\alpha(n+1)+n}{2n+1}\xi\phi_\xi\right] + \left[S^{\frac{1}{n}}\phi^{\frac{1}{n}+2}\right]_\xi = O(t^{\frac{-(\alpha+2n)}{2n+1}}, t^{-\frac{\alpha(n+1)+n}{2n+1}}), \tag{3.49a}$$

$$\int_{\xi_T}^{\xi_N} \phi \; d\xi = 1 + O(t^{-\alpha}). \tag{3.49b}$$

Using the integrating factor $\phi^{\frac{\alpha(2n+1)}{(1-\alpha)n}}$ to multiply both sides of Eq. (3.49a), we obtain

$$\frac{n}{2n+1}\left[(1-\alpha)\xi\phi^{\frac{\alpha(n+1)+n}{(1-\alpha)n}}\right]_\xi = S^{\frac{1}{n}}\left[(1-\alpha)\phi^{\frac{(2n+1)}{(1-\alpha)n}}\right]_\xi + O(t^{\frac{-(\alpha+2n)}{2n+1}}) = 0. \tag{3.50}$$

Integrating this equation with respect to ξ and applying the boundary condition $\phi(\xi = \xi_T) = \phi_0$ (determined below), we obtain the solution in implicit form,

$$\xi - \xi_T = \left(\frac{2n+1}{n}\right) S^{1/n}\left(\frac{\phi^{(2n+1)/(1-\alpha)n} - \phi_0^{(2n+1)/(1-\alpha)n}}{\phi^{\frac{\alpha(n+1)+n}{(1-\alpha)n}}}\right). \tag{3.51}$$

We can show that $\phi_0(\xi_T) = (\frac{\alpha}{S^{1/n}})^{\frac{2n+1}{n}}$ (for detail see Appendix 2). From our numerical simulations, $\xi_T \approx 0$ for $t \gg 1$, hence for our purposes we can take $\xi_T \approx 0$, Using Eq.

(3.49b), the location of the leading edge of the front $\xi = \xi_N$, and the height there $\phi = \phi_N$, can be written as:(for detail see Appendix 2)

$$\xi_N = \frac{(2n+1)}{(n+1)\phi_0}\left(\frac{\alpha(n+1)}{\alpha((n+1))+n}\right)^{\frac{\alpha(n+1)+n}{(2n+n)}}, \quad \phi_N = \left(\frac{\alpha(n+1)+n}{\alpha(n+1)}\right)^{\frac{n(1-\alpha)}{(2n+1)}}, \tag{3.52}$$

The similarity solution is represented by the implicit relationship between ϕ and ξ given in Eq. (3.51).

For $\alpha = 0$, we have using Eq. (3.51) and $\phi(0) = 0$ that

$$\phi = \left[\frac{n\xi}{(2n+1)S^{1/n}}\right]^{n/(n+1)}, \quad \xi_N = \left[\left(\frac{2n+1}{n+1}\right)\left(\frac{2n+1}{n}\right)^{n/(n+1)} S^{1/(n+1)}\right]^{\frac{n+1}{(2n+1})}, \tag{3.53}$$

$$\phi_N = \left(\frac{n+1}{n}S\right)^{-n/(2n+1)}.$$

For $\alpha = 1$ (constant source flow rate), we have (by setting $\tilde{B} = 0$ in Eq. (3.48)

$$[\xi\phi_\xi] = \left[S^{\frac{1}{n}}\phi^{\frac{1}{n}+2}\right]_\xi \tag{3.54}$$

This has solution $\phi(\xi) = 1$, so $\xi_N = \phi_N = 1$.

The solution for this is shown in Fig. 3.3 for $S = 1$ and $n = 0.6$, and for various values of α. We observe a similar trend as that shown in Fig. 3.1 for $S = 0$; the length over which the dome spreads, ξ_N, decreases and the height at the leading edge, ϕ_N, increases. We note that ξ_N is larger than that for $S = 0$ due to the additional

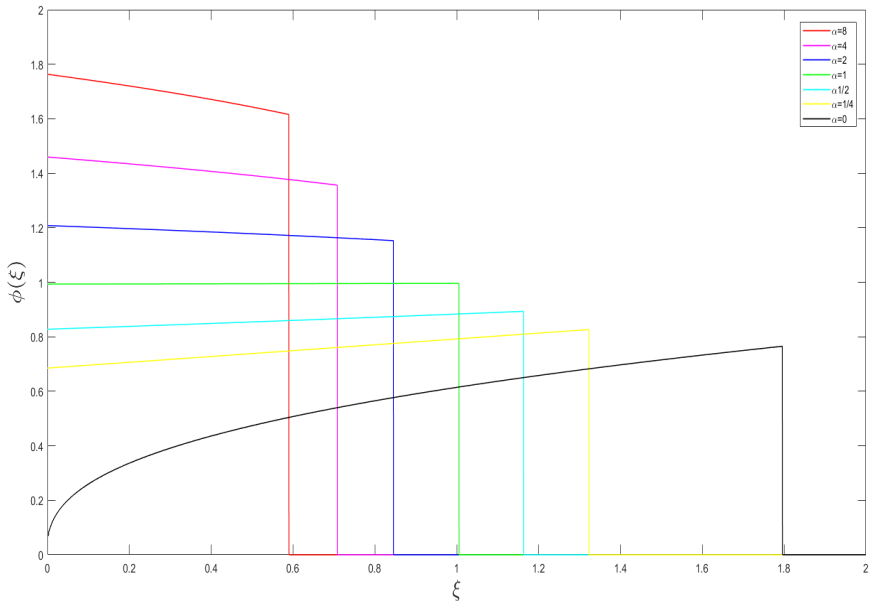

Figure 3.3: The late-time similarity solution, ϕ, as a function of ξ for $S = 1$ and $n = 0.6$ varying α obtained from Eq. (3.51).

contribution from the inclination of the plane. Similar to the $S = 0$ case, as α increases, the additional volume of liquid from the source contributes more to inflating the dome rather than its spreading. The results in Fig. 3.3 are similar to the results in Chapter 2 for a Newtonian fluid, except for $\alpha > 1$, the dome decreases in height and increases in length compared to the Newtonian fluid. The opposite happens for $\alpha < 1$. This is due to the shear thinning for $n = 0.6$. The location of the leading edge of the dome, ξ_N, and the height there, ϕ_N as a function of α are shown in Fig. 3.4. This is consistent with our earlier observations. In Fig. 3.5 we show the solution, $\phi(\xi)$, as a function of ξ for various values of n with $\alpha = 0$. As in the case with $S = 0$, we observe that as n decreases, the dome spreads less in comparison to a Newtonian dome. This is because the flow shear rate is much less than one, so the viscosity increases as n decreases

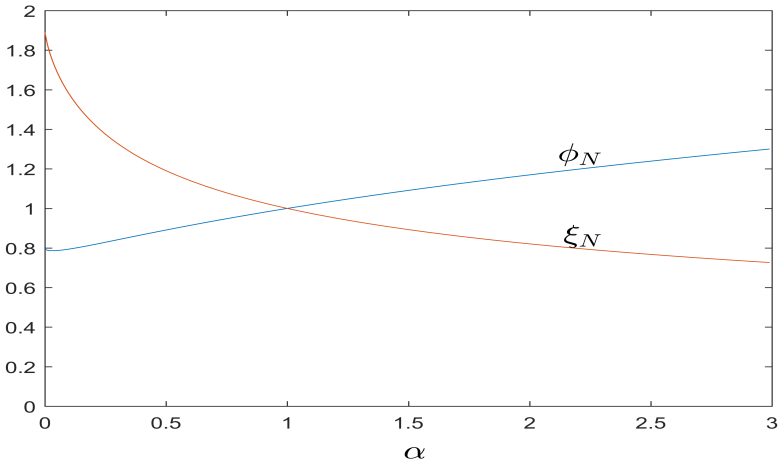

Figure 3.4: The location of the leading edge of the dome, ξ_N, and the height there, ϕ_N as a function of α for $S = 1$.

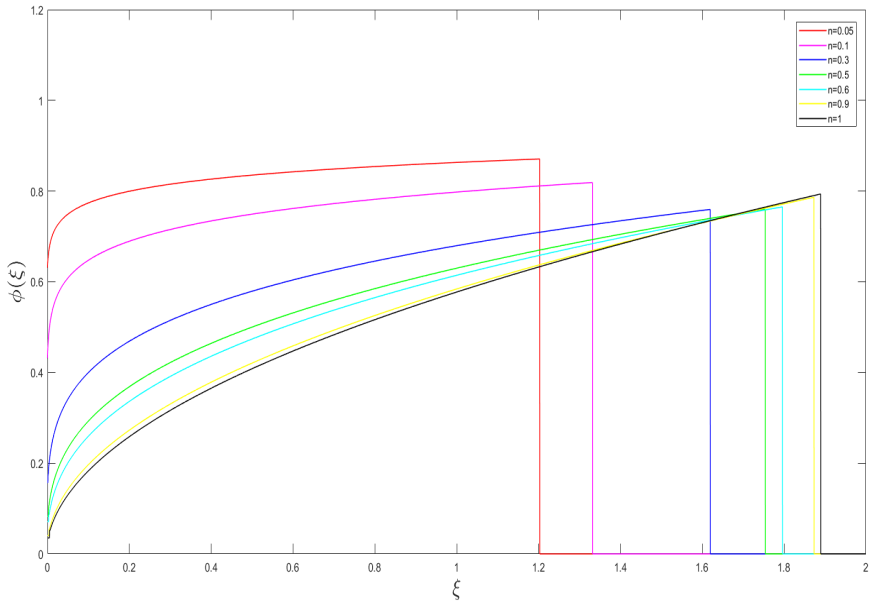

Figure 3.5: The late-time similarity solution, ϕ, as a function of ξ for $S = 1$ and $\alpha = 0$ varying n obtained from Eq. (3.51).

slowing the spreading.

3.4 Numerical results

In this section, we seek the numerical solution of Eq. (3.16 for the evolution of the dome height for the Herschel-Bulkley constitutive law. We do not present any numerical solution for the Carreau model, Eq. (3.22). Realistically, =O(1) which combined with the low shear stress associated with this particular spreading flow, makes the Carreau model behave like Newtonian for these values of . For the Carreau model to capture the non-Newtonian behaviour, one would need to increase by several orders of magnitude which may be unrealistic.

For $B = 0$, Eq. (3.16) reduces to the Power-law model given by Eq. (3.10). The computational domain is $x \in [-L, L]$, where L is the length of the domain. We assume that the plane is pre-wetted with a precursor layer of thickness b. The boundary conditions specified are: $h = b$ at $x = \pm L$. We choose the initial condition to mimic a one-dimensional dome as follows:

$$h(x,t) = (1-x^2)H(1-x^2) + b, \quad x \in \quad [-L, L]. \tag{3.55}$$

Our focus is in investigating the evolution of the dome height h varying the parameters: the power-law index, n and the Bingham number, B (comparing the strength of the yield stress). These parameters are varied for two choices of the inclination angle,

$S = 0$ ($\theta = 0^o$) and $S = 1$ ($\theta \approx 6^o$), and two values of α corresponding to $\alpha = 0$ (constant volume) and $\alpha = 1$ (constant source flow rate). In all the results shown below, we fix the source vent width $x_0 = 0.15$ and the precursor thickness $b = 10^{-6}$. The length of the computational domains L is chosen sufficiently large so that the boundary condition $h \to b$ as $x \to \infty$ is satisfied numerically. The evolution equations for the three models, Eqs. (3.10,3.16), are solved numerically using the Method of lines [78, 61]. The numerical scheme is similar as that presented in §2.4. Numerical investigation utilizing the Bingham and Herschel-Bulkley model are complicated by the presence of the discontinuity in the derivative of the stress-strain rate relation, Eq. 3.11, and for ease in computation we use a regularization given by Balmforth *et al.* [5, 9]. The complication arises due to the discontinuity in the derivative of the stress-rate of strain constitutive law for the Herschel-Bulkley model. Following Balmforth *et al.*[5], we regularise the constitutive law, Eq. (3.11) by assuming the fluid to be weakly yielding at low strain rates, of the form, $f(|u_{0_z}|) = K|u_{0_z}^2 + \mu_1^2|^{(n-1)} + \frac{B}{\sqrt{u_{0_z}^2+\mu_1^2}}$, where μ_1 is the regularising parameter.

To illustrate the typical features of the evolution of the free surface, we first present the numerical results for Power-law and Bingham fluid which are compared to the corresponding similarity solutions derived in the previous chapter. In Fig.3.6, we show the numerical solution for a Power-law fluid with index $n = 0.6$ and $S = 1$ (corresponding to $\theta \approx 6^o$), with $Q_{s_0} = 0$. The evolution of $h(x,t)$ are shown for times varying from $t = 0 - 5 \times 10^2$. We observe the dome spreading down the inclined plane with a front

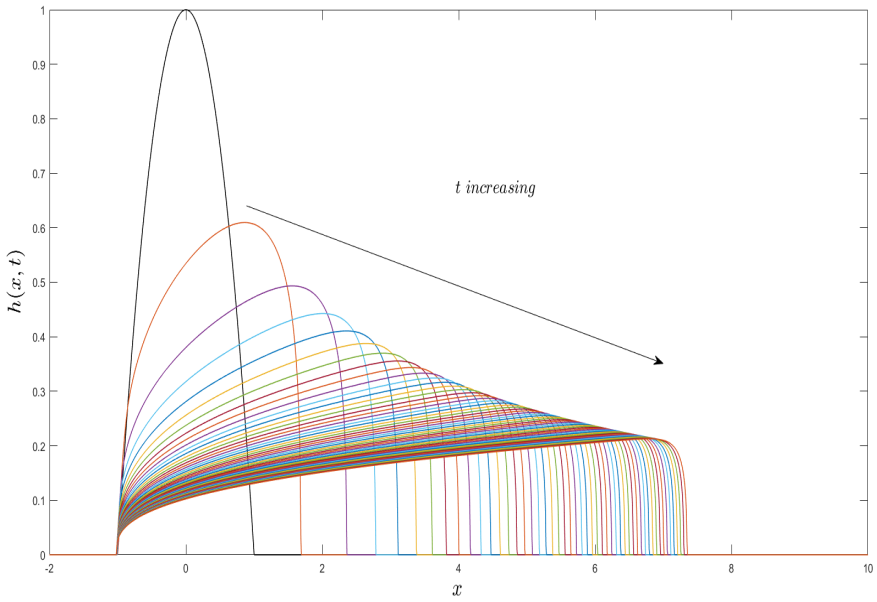

Figure 3.6: Evolution of free surface shapes for $t = 0$ to $t = 5 \times 10^2$ with $n = 0.6$, $S = 1$ (corresponding to $\theta \approx 6^o$) and $Q_{s_0} = 0$ (constant volume).

developing at its leading edge. This free shape profiles are similar to the Newtonian case. The spreading is much slower for this case because the flow shear rate is much less than one, so the viscosity is much larger than that of a Newtonian fluid, hence slowing the spreading. In Fig. 3.7, we show the evolution of $h(x, t)$ for horizontal plane $S = 0$ at times varying between $t = 0$ and $t = 5 \times 10^2$ with power-law index $n = 0.6$. The spreading for this case is symmetric about $x = 0$ with $Q_{s_0} = 0$. We also observe that the spreading of the dome is much slower compared that shown in previous figure. This is again due to the large viscosity at very low shear rates for a Power-law fluid. The results in Fig. 3.8 show the late-time similarity solution for evolution shown in Fig. 3.6 using the similarity variables in Eq. (3.45). The dashed line is the corresponding similarity solution, Eq. (3.54) where the late-time numerical solution collapse to a sin-

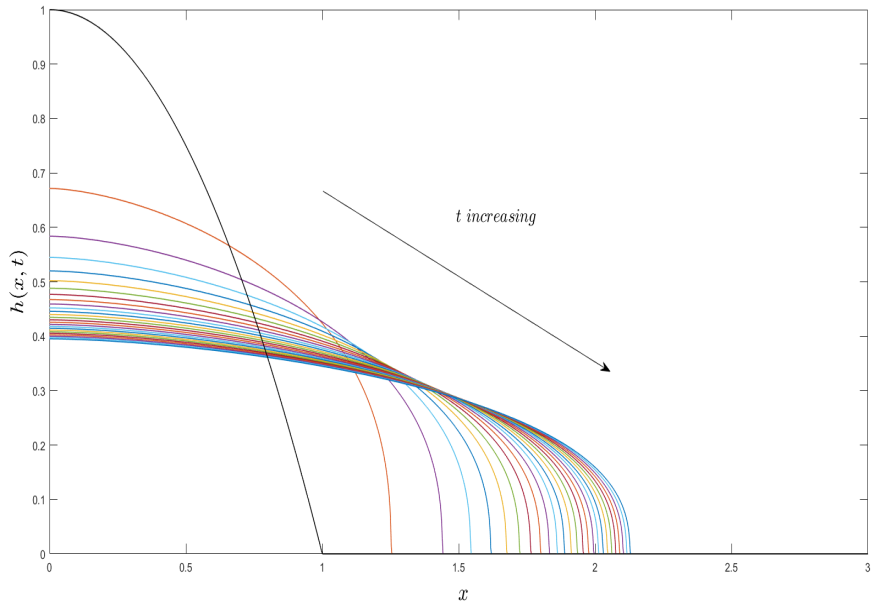

Figure 3.7: Evolution of free surface shapes for $t = 0$ to $t = 5 \times 10^2$ with $n = 0.35$, $S = 0$ and $Q_{s_0} = 0$ (constant volume).

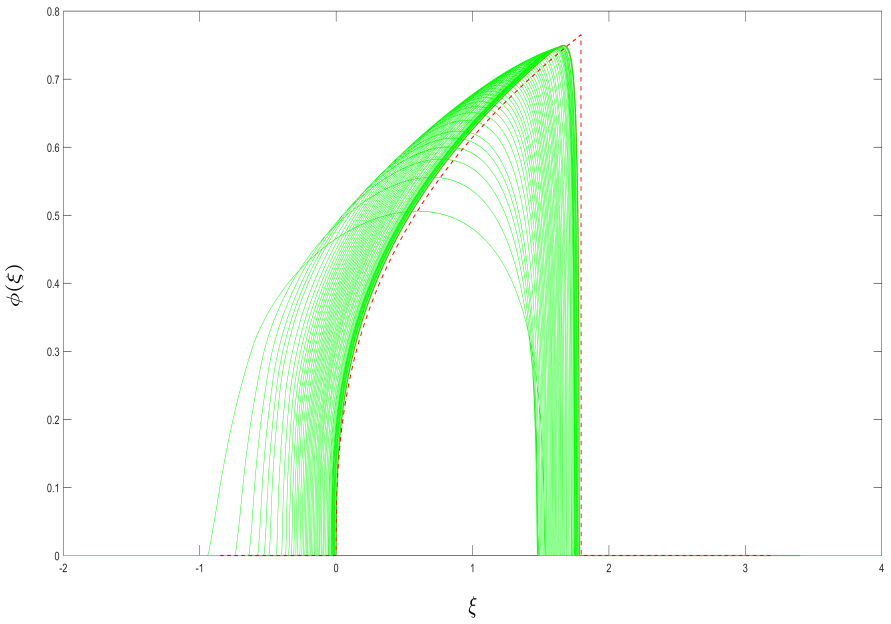

Figure 3.8: The height field of constant mass is plotted using similarity scaling $\xi = x/t^{1/3}$ and $\phi = t^{-1/3}h(x,t)$

gle curve. Figure 3.9 again shows that the late-times numerical solution shown in Fig. 3.7 collapses to a single curve under the similarity scaling, Eq. (3.28). The dashed line

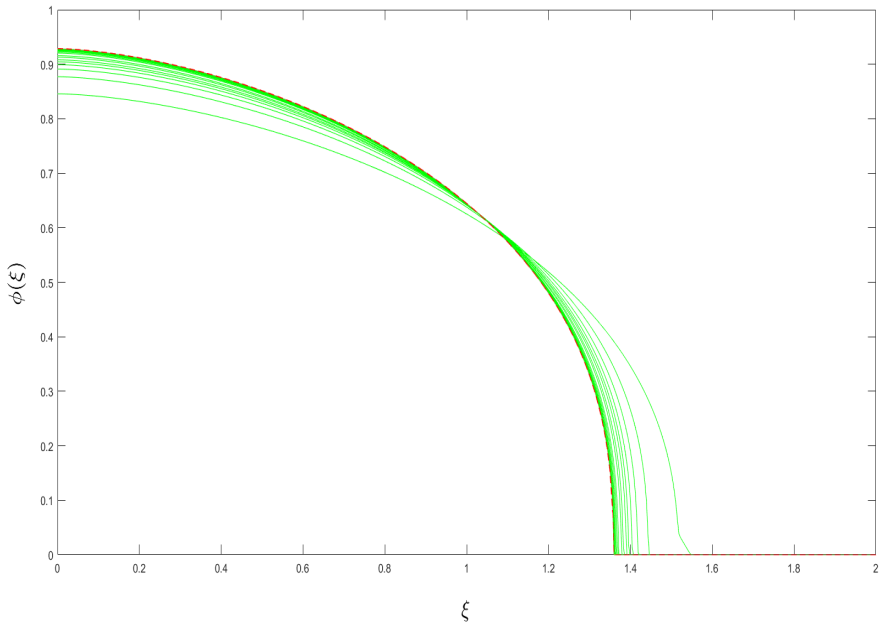

Figure 3.9: The height field is scaled by $\xi = x/t^{1/5}$ and $\phi = t^{1/5}h(x,t)$ which are plotted against the similarity solution.

in Fig. 3.9 shows the corresponding similarity solution given by Eq.(3.38) which is in good agreement. Figure 3.10 plot the location of the liquid front at the domes leading edge, x_N, is determined at the leading edge of the dome numerically, this figure show the slopes which confirm that x_N and h_N. The results in Fig. 3.11 show the leading edge of the dome, x_N, and the maximum dome height $h(x = 0)$, respectively. These are calculated from the dome evolution that shown in Fig. 3.7. similar for previous chapter, the location of the leading edge of the dome is calculated by the value of x,where the dome height first become less than 10^{-5}, in this figure the slope confirms that x_N and h_N. In Figs. 3.12, 3.13, we show the results for the dome height $h(x, t = 5 \times 10^2)$

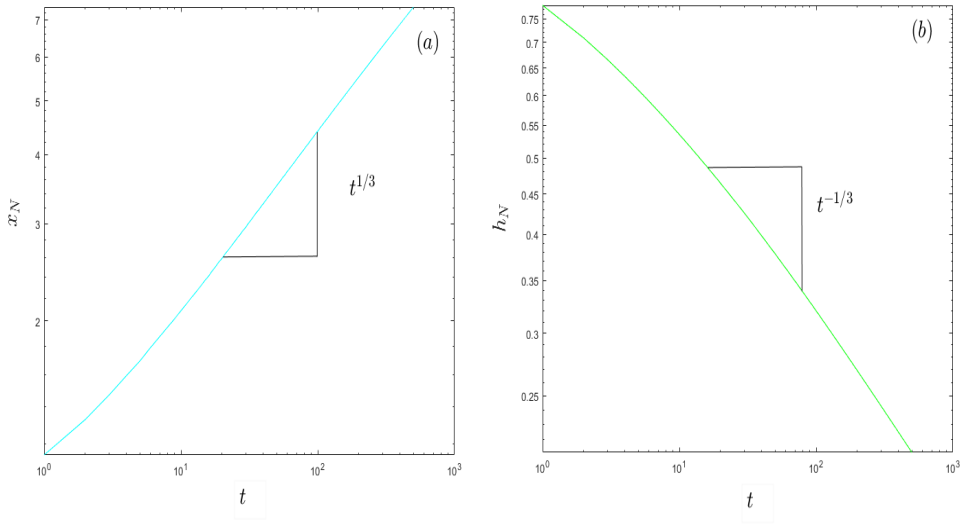

Figure 3.10: The variation in the length $x_N$and height h_N with time for $n = 0.6$ and $S = 1$

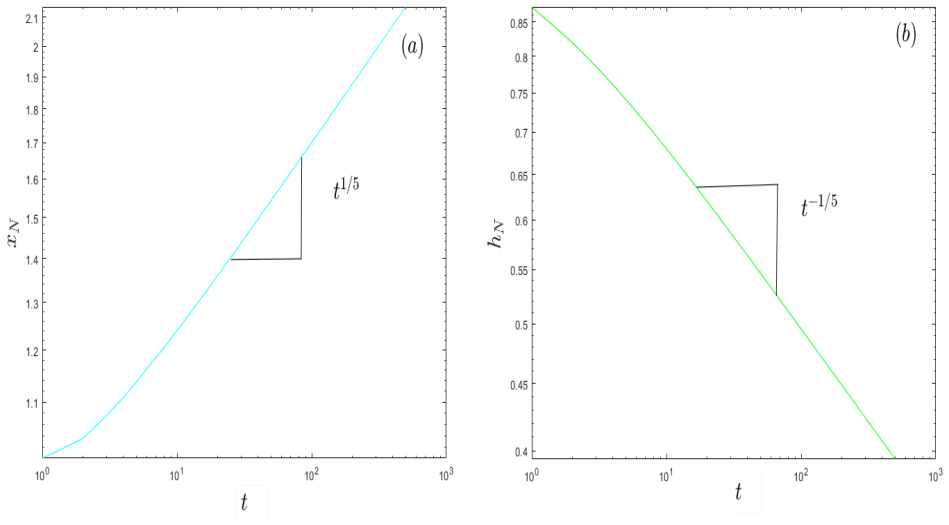

Figure 3.11: Evolution of the dome height h_N and length x_N for $n = 0.35$ with $t = 0 - 5 \times 10^2$

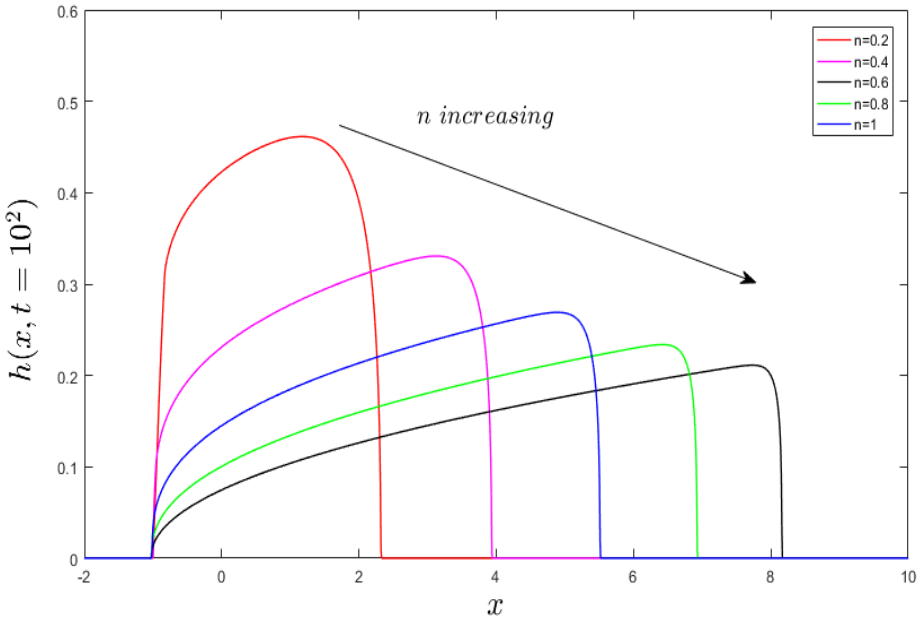

Figure 3.12: The thickness for spreading dome computed numerically using the thin-layer model with $S = 1$. Four snapshots of the domes at time 10^2 for various values of n

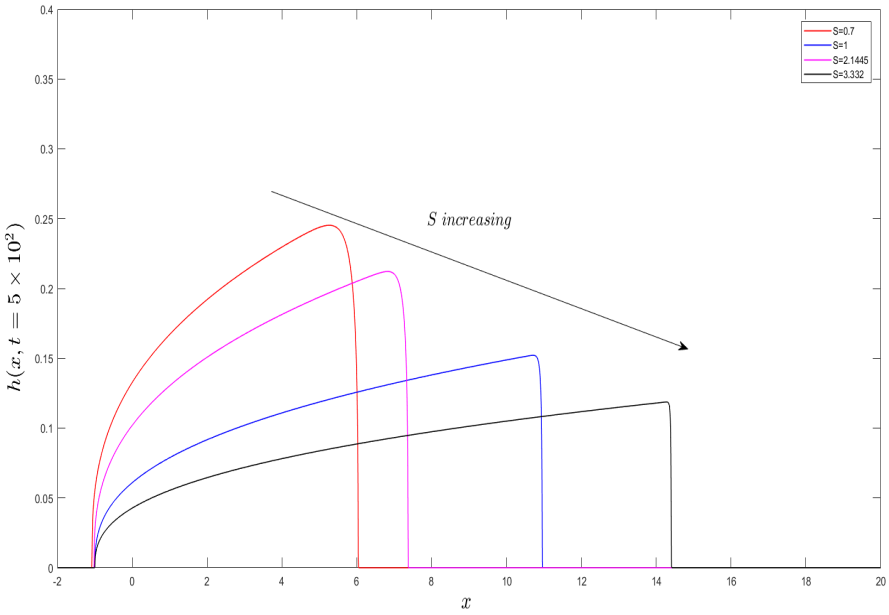

Figure 3.13: The thickness for spreading dome computed numerically using the thin-layer model with $n = 0.6$. Four snapshots of the domes at time $1 - 5 \times 10^2$ for various values of $S = 0.7\ (4^o), 1\ (6^o), 2.145\ (12^o), 3.732\ (18^o)$.

for different values of power index $n = 0.2,\ 0.4,\ 0.6,\ 0.8, 1$, and inclination angles $S = 0.7\ (4^o), 1\ (6^o), 2.145\ (12^o), 3.732\ (18^o)$ for $Q_{s_0} = 0$, respectively. We observe that the dome have spreads over a longer distance and thinned more as n, S increases. Fig-

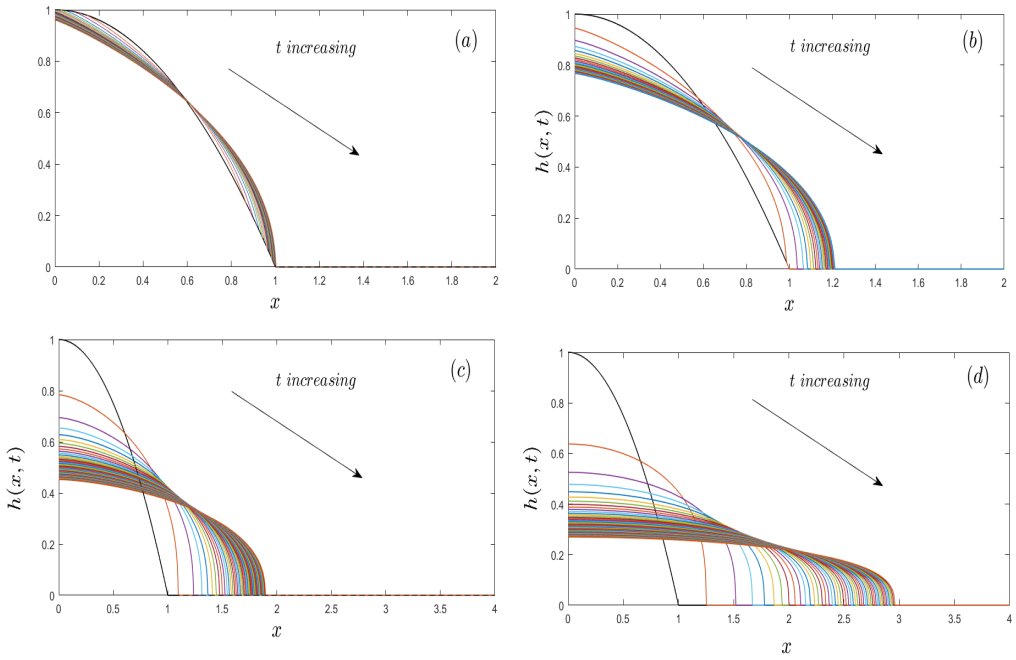

Figure 3.14: The evolution of the dome for four different power index n, $n = 0.1,\ 0.2,\ 0.5,\ 0.95$.

ure 3.14 show the same behaviour in previous figures where the dome has spread over a longer distance as n increase. For the case of $\alpha = 1$, Fig. 3.15 show the evolution of $h(x,t)$ for varying $t = 0 - 2\times10^2$, with $n = 0.1$ and $Q_{s_0} = 4$. The inclination is set to be $S = 1$. The results in this figure illustrate that the upper section of the dome is almost flat surface behind its leading edge. The strength of the source is sufficiently large and the build-up of the fluid at the source results in the dome height increasing near $x = 0$ without any spreading. The results of the scaling numerical solution are presented in Fig. 3.16 for t varying between $t = 0$ to $t = 2 \times 10^2$ with $\alpha = 1$ and $Q_{s_0} = 4$. These

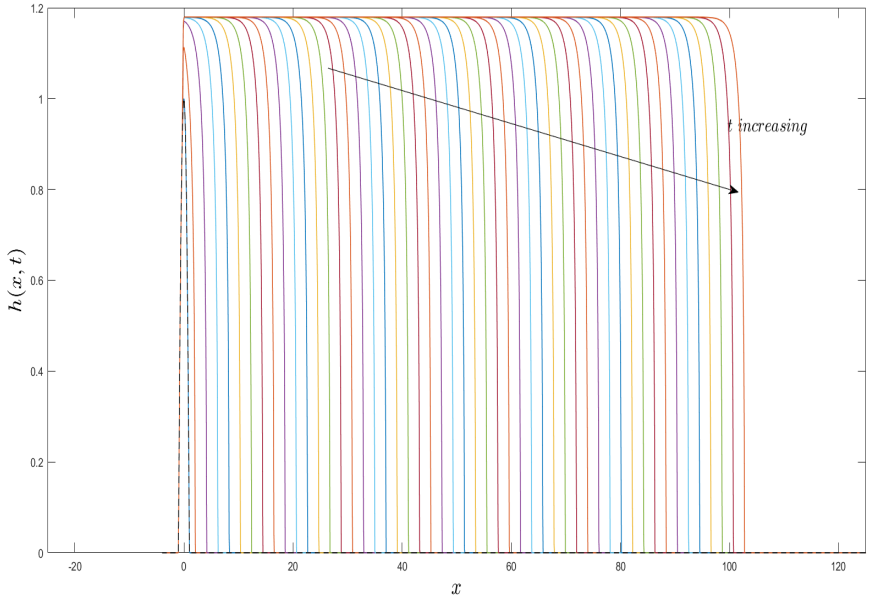

Figure 3.15: Dome evolution for $Q_{s_0} = 4$,n=0.1, $S = 1$ and $t = 0 - 2 \times 10^2$.

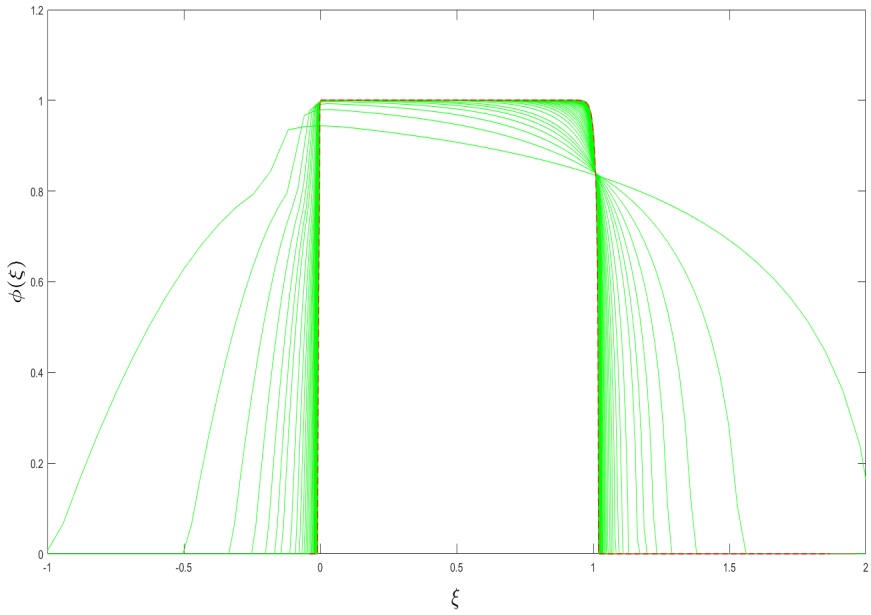

Figure 3.16: The height field is scaled and plotted against the similarity solution.

results show how this scaling converges to the exact similarity solution (dashed line) for $\alpha = 1$ in Fig. 3.3, where the curves collapses onto the similarity solution under scaling variables (3.45). Similar in previous chapter, Fig. 3.17 plot the leading edge

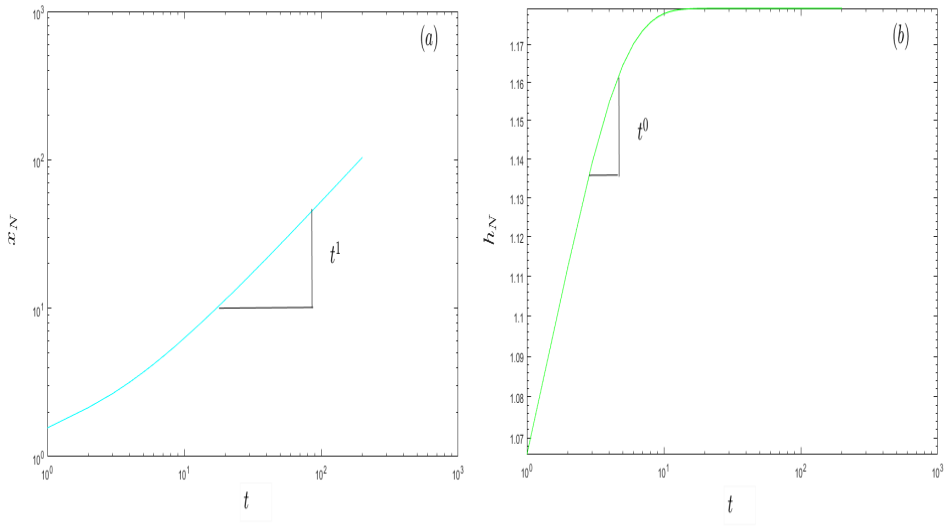

Figure 3.17: Evolution of the dome height h_N and length x_N for $Q_{s_0} = 4$

of the dome, x_N, and the dome height, h_N, respectively for varies time t. Figures 3.18, 3.19 are shows the dome height $h(x, t = 200)$ for different values of power index $n = 0.05, 0.2, 0.5, 0.9$, and inclination, $S = 0.7$ $(4^o), 1$ $(6^o), 2.145$ $(12^o), 3.732$ (18^o) for $Q_{s_0} = 0.5$. This figure illustrated that the dome become more thinner with spreading over longer length as n and S increases. For zero inclination, Fig. 3.20 illustrate the dynamics of the dome which related to its continued growth and expansion depending on the strength of the sources $Q_{s_0} = 6.5$ for t between 0 and 5×10^2. Figure 3.21 shows that the numerical solution shown in figure 3.20 collapse to a single curve under the similarity scaling (3.28) with $\alpha = 1$. The similarity solution for equations (3.34a)

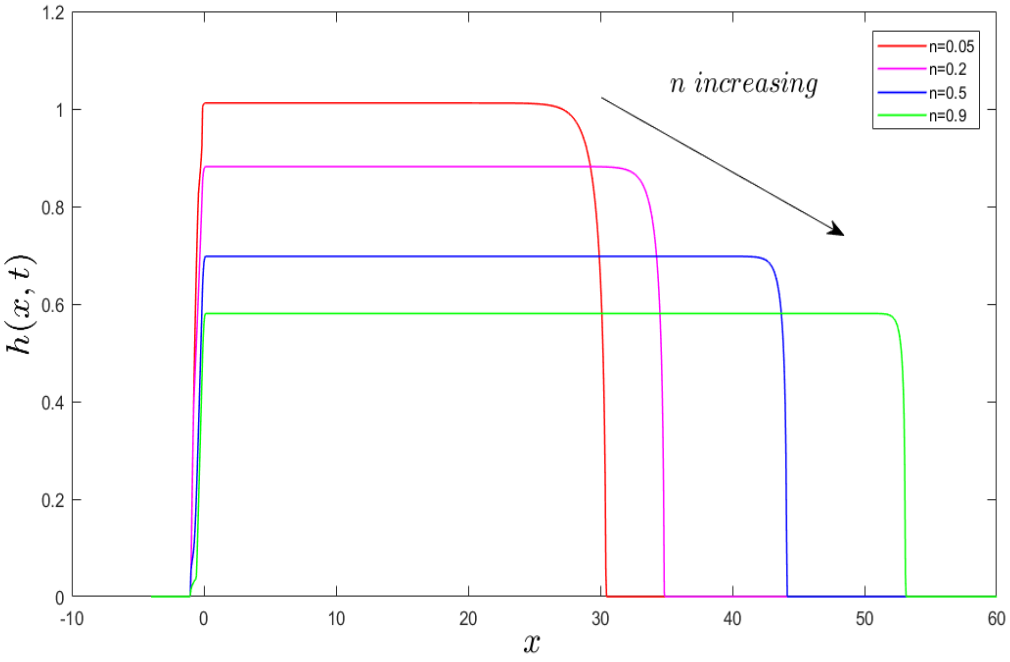

Figure 3.18: The evolution of the dome for four different power-law index $n = 0.05, 0.2, 0.5, 0.9$ for $Q_{s_0} = 0.5$.

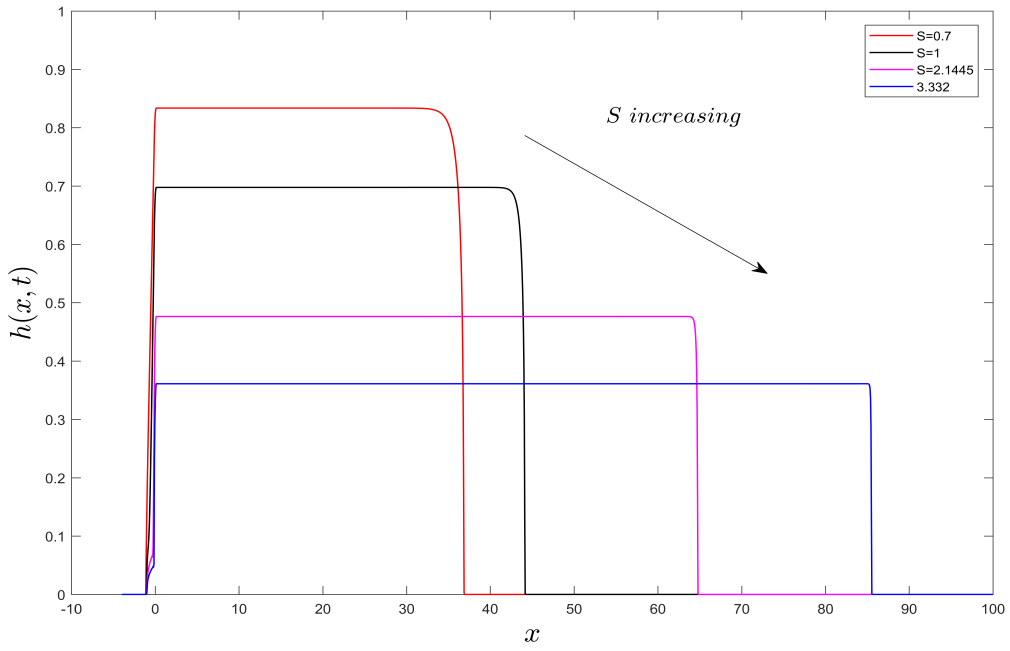

Figure 3.19: The thickness of spreading dome with $Q_{s_0} = 0.5$ and $n = 0.5$ for varying S.

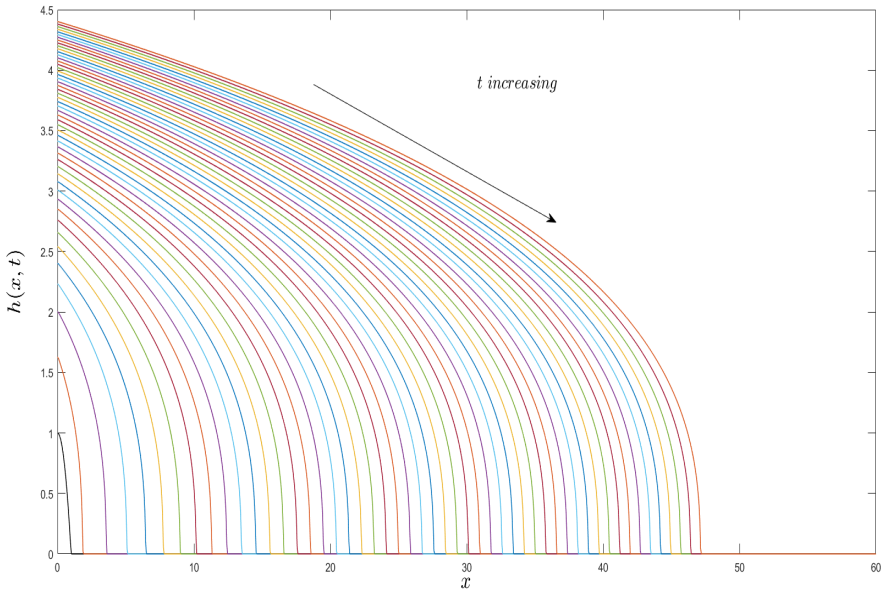

Figure 3.20: The thickness of spreading dome with $Q_{s_0} = 6.5$ and $n = 0.65$ for $t = 0 - 5 \times 10^2$

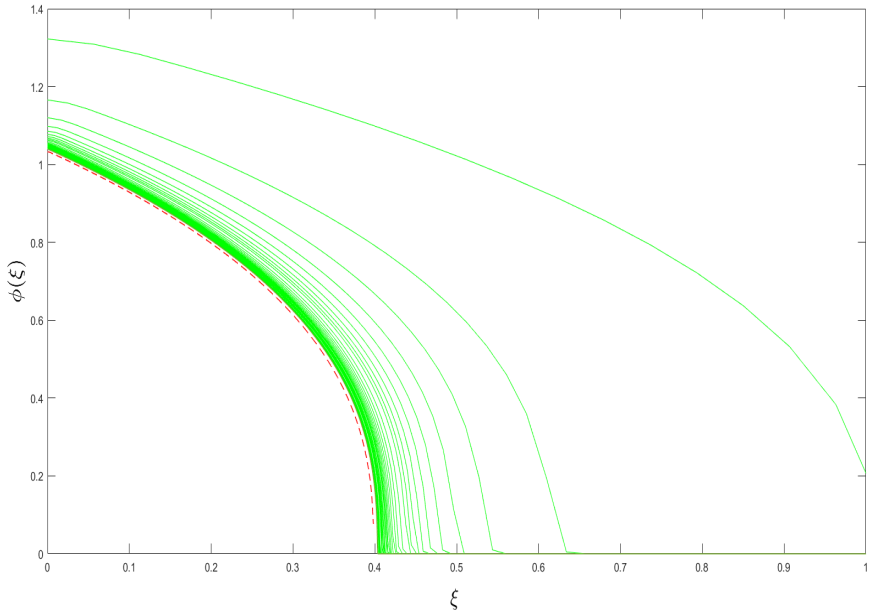

Figure 3.21: The height field is scaled by $\xi = x/t^{4/5}$ and $\phi = t^{1/5}h(x,t)$ which plotted against the similarity solution.

which is solved by the ode45 (Runge Kutta-Fehlberg method) in MATLAB is shown in figure 3.21, where the numerical solution of evolution equation converge to the similarity solution. The red line in figure 3.21 shows the similarity solution which matches the numerical solution very well. Hence, a Non-Newtonian fluid from a constant point source spreads like $t^{1/(2n+3)}$. This again agrees with the similarity solution derived by Huppert [47]. Fig. 3.22(a,b) plot the leading edge of the dome, x_N, and the dome

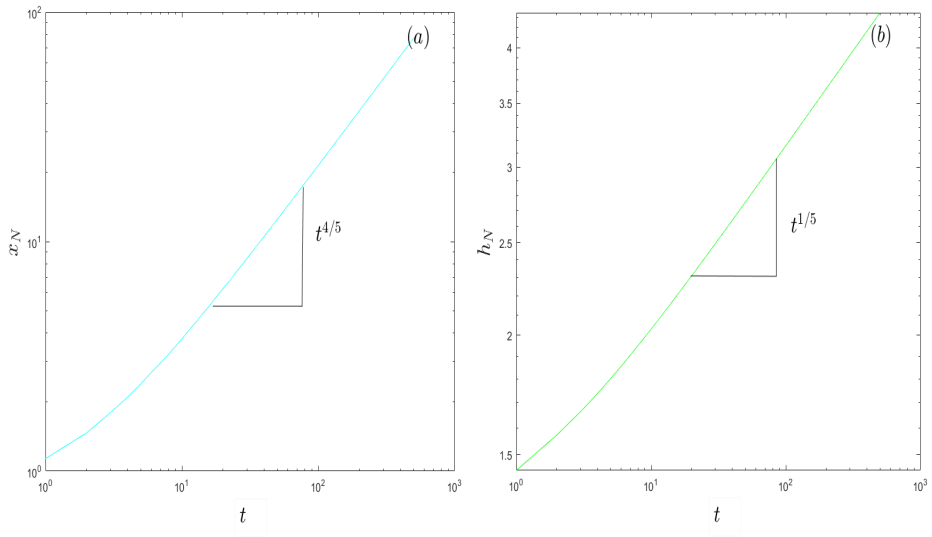

Figure 3.22: The variation in the length x_N and height h_N with time for $n = 0.65$ and $S = 0$.

height, h_N, respectively, versus time, t. These are calculated from the dome evolution shown in Fig. 3.20 for $S = 1$ and $Q_{s_0} = 6.5$ and $\alpha = 1$ (constant source flow rate). We consider in Fig. 3.23 different values of power index $n = 0.2,\ 0.4,\ 0.6,\ 0.8,\ 1$ with $Q_{s_0} = 6.5$.

We now consider the influence of the yield stress and Bingham numbers, B, for con-

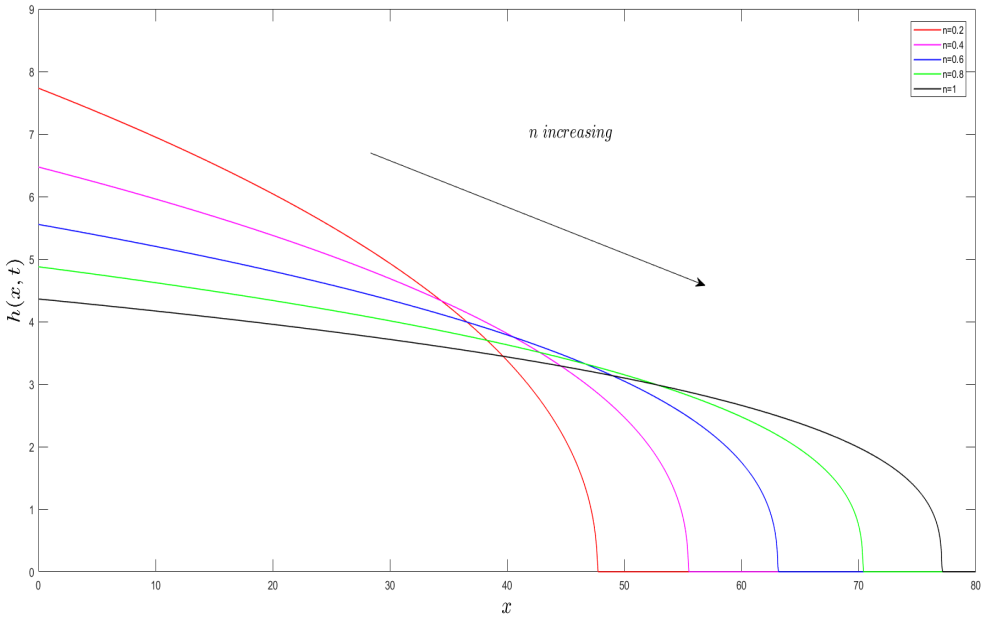

Figure 3.23: The evolution of the dome for four different power index $n, n = 0.05, 0.2, 0.5, 0.9$ with $Q_{s_0} = 6.5$

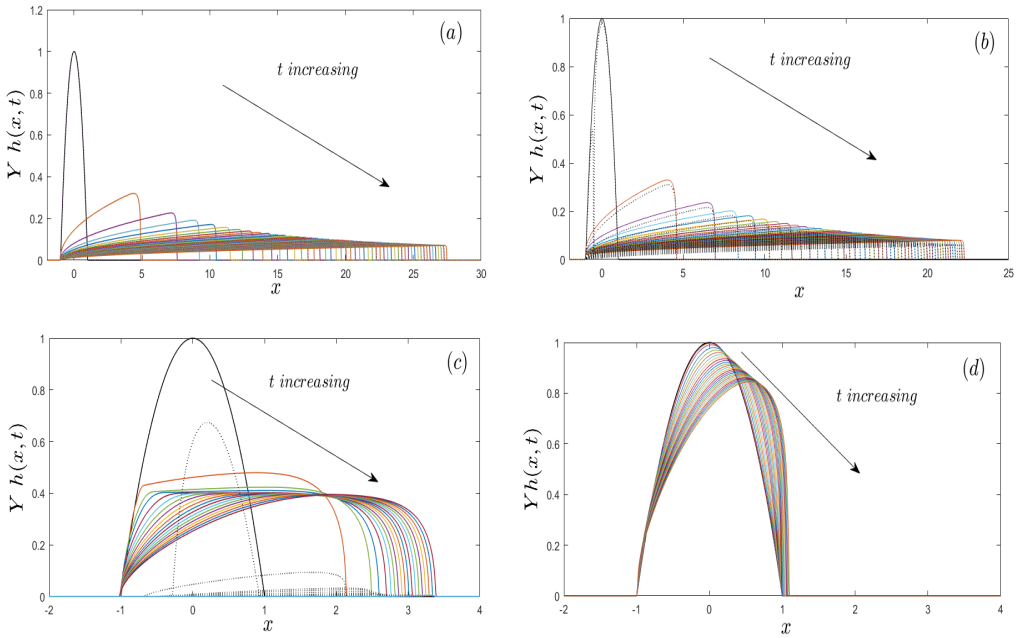

Figure 3.24: Inclined plane for $S = 1$. Shown are height (solid lines),h and the yield surface (dotted lines), $\mathcal{Y}$ for (a) $B = 0.0002$, (b) $B = 0.02$, (c) $B = 0.4$, (d) $B = 4$ with $n = 1$ (Bingham fluid) for constant volume at $t = 0 - 5 \times 10^3$

stant volume, $Q_{s_0} = 0$, in Fig. 3.24 the results are show the effects of yield stress using different values of $B = 0.0002, 0.02, 0.4, 4$ for t varying between $t = 0$ to $t = 5 \times 10^3$. Figure 3.25 shows that the late-time numerical solution shown in Fig. 3.24 collapses

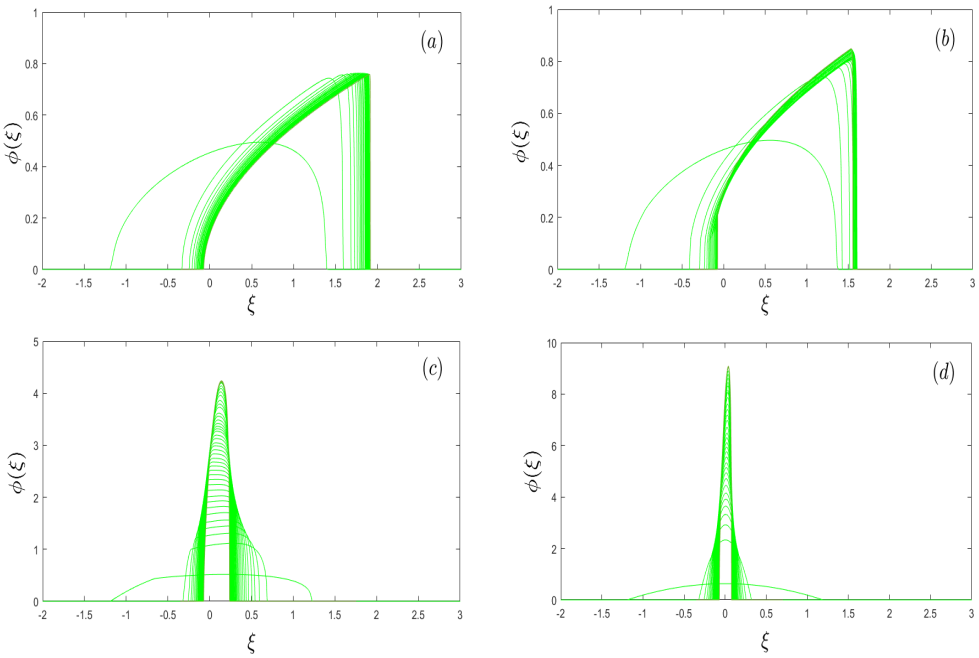

Figure 3.25: The height field is scaled for varying B, (a) $B = 0.0002$, (b) $B = 0.02$, (c) $B = 0.4$,(d) $B = 4$

to a single curve under the similarity scaling when $B \to 0$ and match with similarity solution. In Fig. 3.26 we show the maximum dome height, h_N, which is determined at the leading edge of the dome from the numerical solution with the location of the leading edge, x_N, from this figure we observe that the for small B, the curve is similar for Newtonian. In Figs. 3.27 and 3.28, we display different value of B with $S = 0.7\ (4^o), 1\ (6^o), 2.145\ (12^o), 3.732\ (18^o)$ for $Q_{s_0} = 0$. We observe from these figures as S increases the dome spread over a longer distance depending on Bingham number. In the case of horizontal plane, we illustrate the evolution of an extrusion onto zero

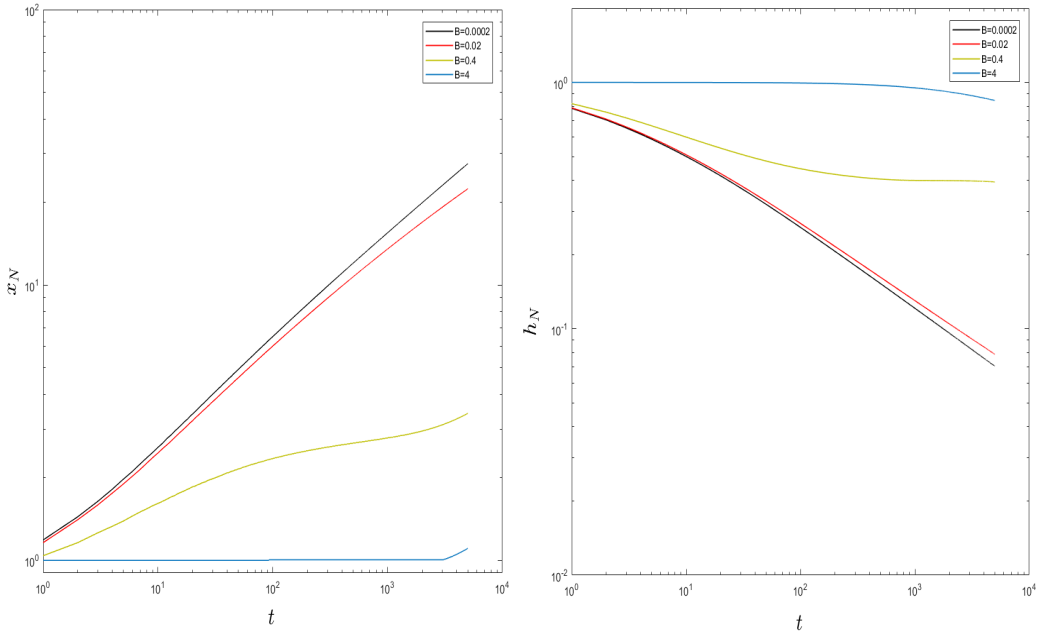

Figure 3.26: Evolution of the domes length x_N and height h_N for various values of B and $n = 1$.

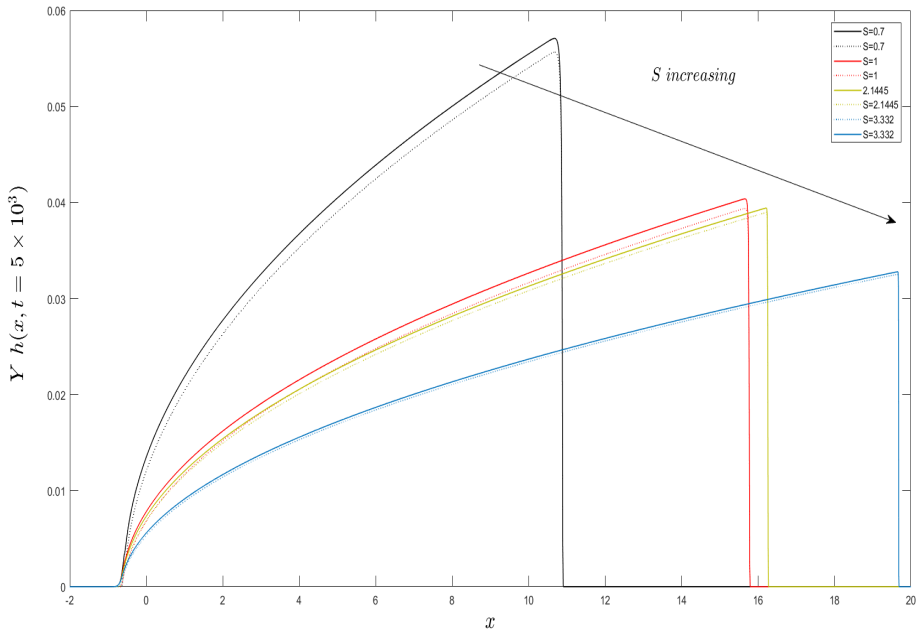

Figure 3.27: Inclined plane for $B = 0.0001$ and $n = 1$. Snapshots of the thickness (solid lines), h, and yield surface (dotted lines), $\mathcal{Y}$, for varying S.

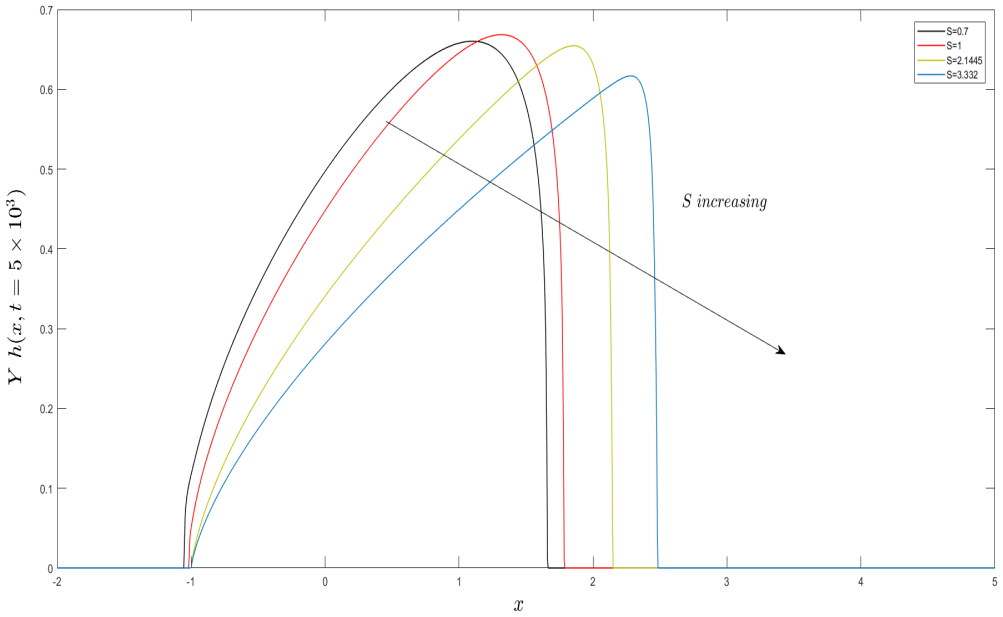

Figure 3.28: Inclined plane for $B = 5$ and $n = 1$. Snapshots of the thickness (solid lines), h, and yield surface (dotted lines), $\mathcal{Y}$, for varying S.

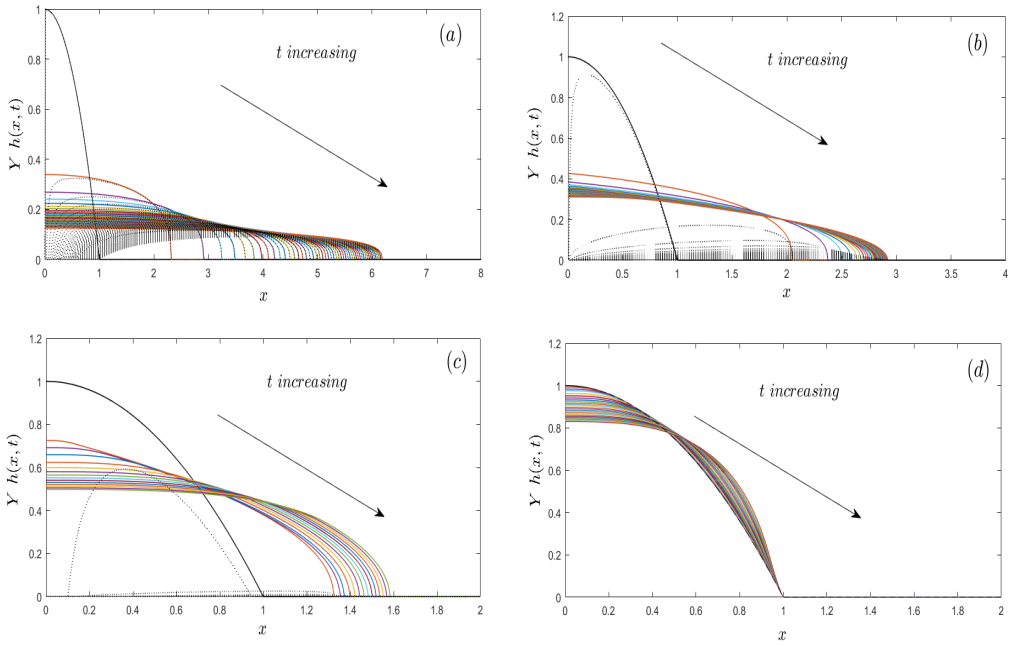

Figure 3.29: Horizontal planar for $n = 1$. Shown are the height (solid lines), h, and yield surface (dotted lines), Y, for (a) $B = 0.1$ (b)$B = 0.5$ (c)$B = 1$ (d) $B = 20$ for constant mass at $t = 0 - 500$.

sloping plane in Fig. 3.29. The dome have $B = 0.0002, 0.02, 0.2, 2$ respectively and $n = 1$ with $x_* = 0.15$ for the vent radius, and $S = 0$. In this figure there are four panel which illustrate that the spreading is decreases with increase the value of B. Here, the 'plug' occupies roughly half of the fluid (Fig. 3.29(a, b)) and most of the fluid in Fig. 3.29(c, d). Figure3.30 shows that the scaling of numerical solution shown in figure 3.29

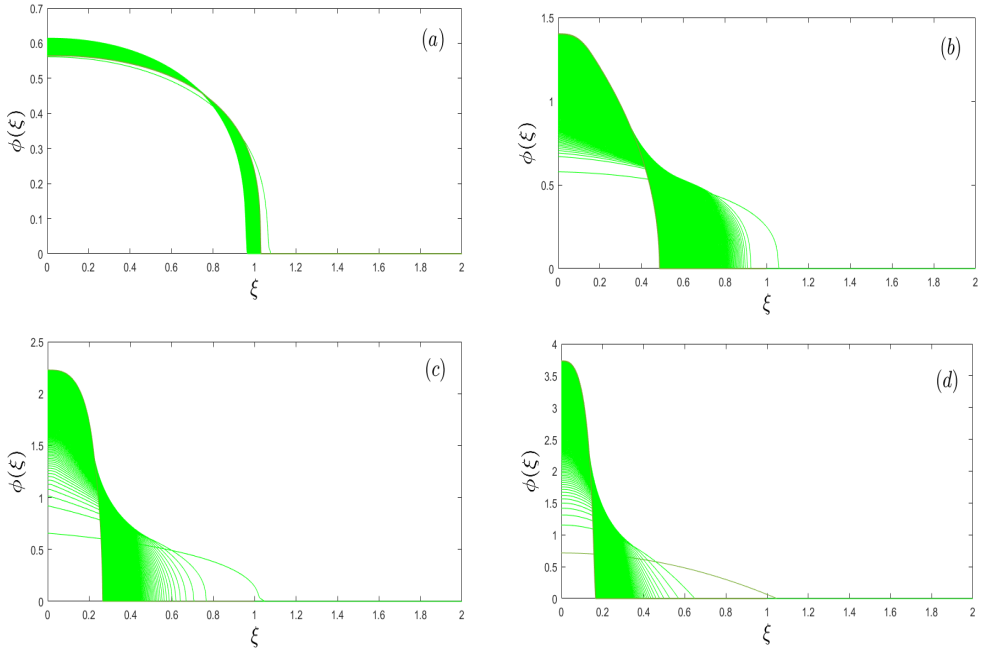

Figure 3.30: The height field is scaled for varying B.

collapse to a single curve with different ship under similarity scaling.

By taking Q_{s_0} the form of a line source, we illustrate the results surface profile and the evolution of length and height for fluids with different values of B. The results for $B = 0.001, B = 0.5, B = 5$, and $B = 20$, are shown in Figs. 3.31-3.37. In inclination planer, for comparison, we show domes with four different values of B in Figs. 3.31,3.34, and 3.35. The first two panel a, b in each figures are almost Newtonian, whereas the second two panel in each figures c, d are dominated by yield stress, which

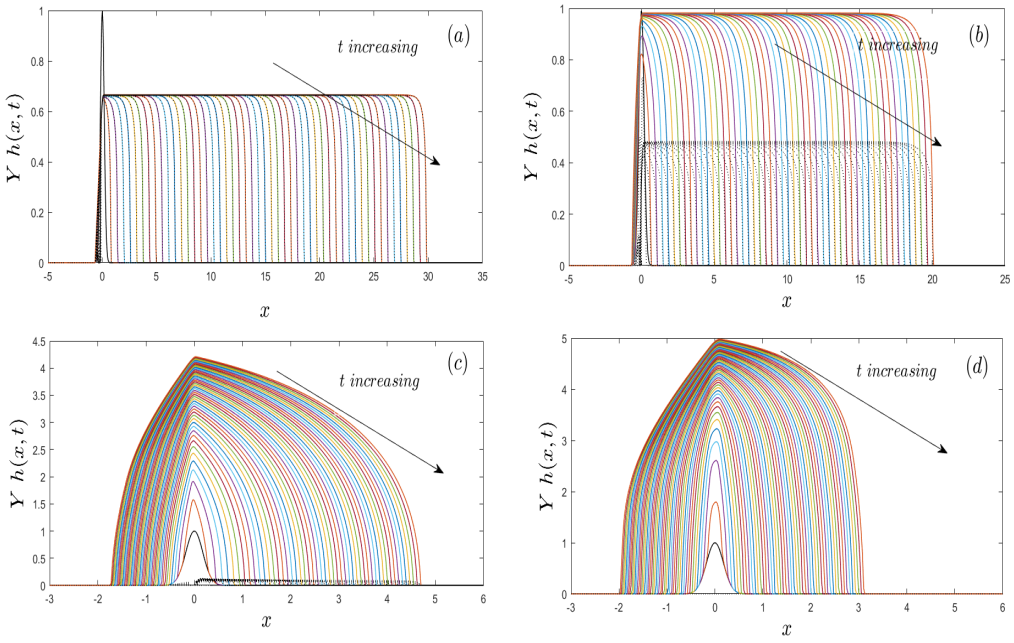

Figure 3.31: Numerical solution showing the inclined of a two- dimensional fluid on an inclined planar for $S = 1$. Snapshots of height (solid lines), h, and yield surface (dotted lines), $\mathcal{Y}$, for (a) $B = 0.001$ (b)$B = 0.5$ (c)$B = 5$ (d)$B = 20$ with a line source $Q_{s_0} = 0.5, x_* = 0.15$ and $n = 1$.

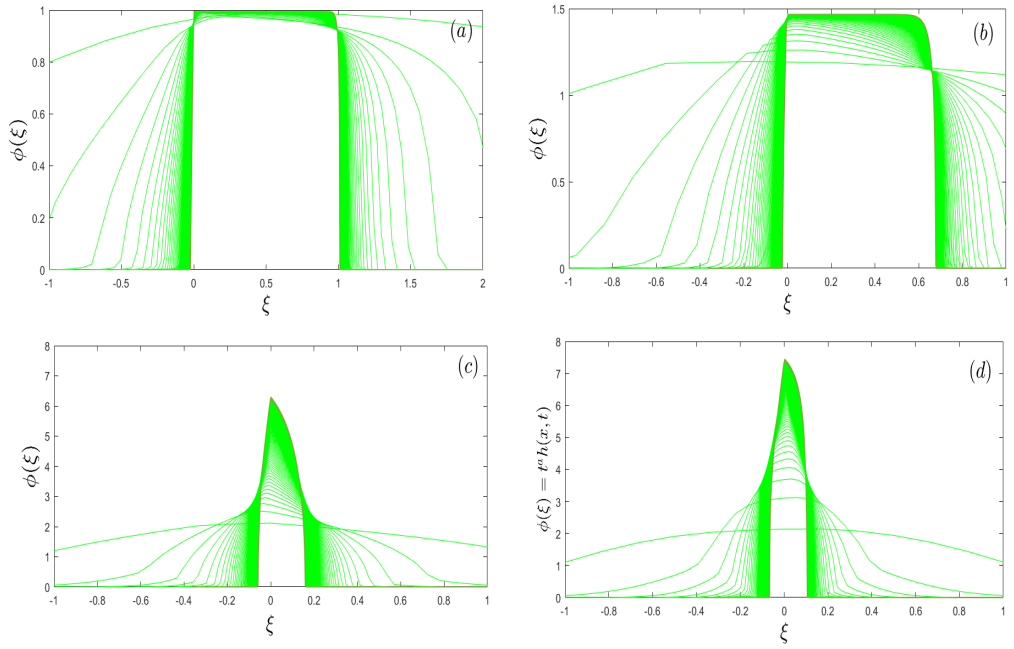

Figure 3.32: The height field is scaled for varying B.

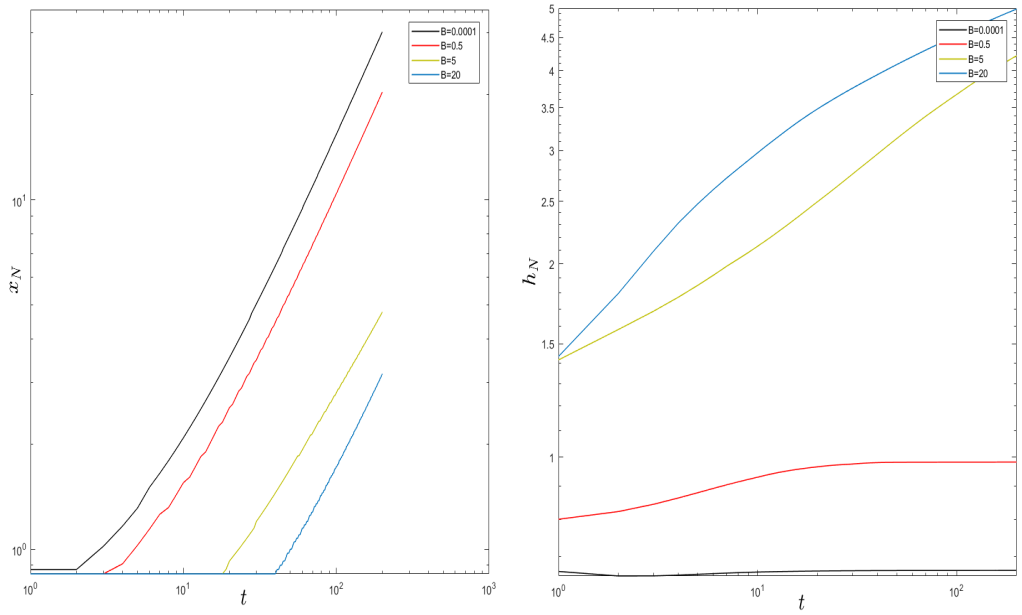

Figure 3.33: Evolution of the domes length x_N and height h_N for various values of B and $n = 1$.

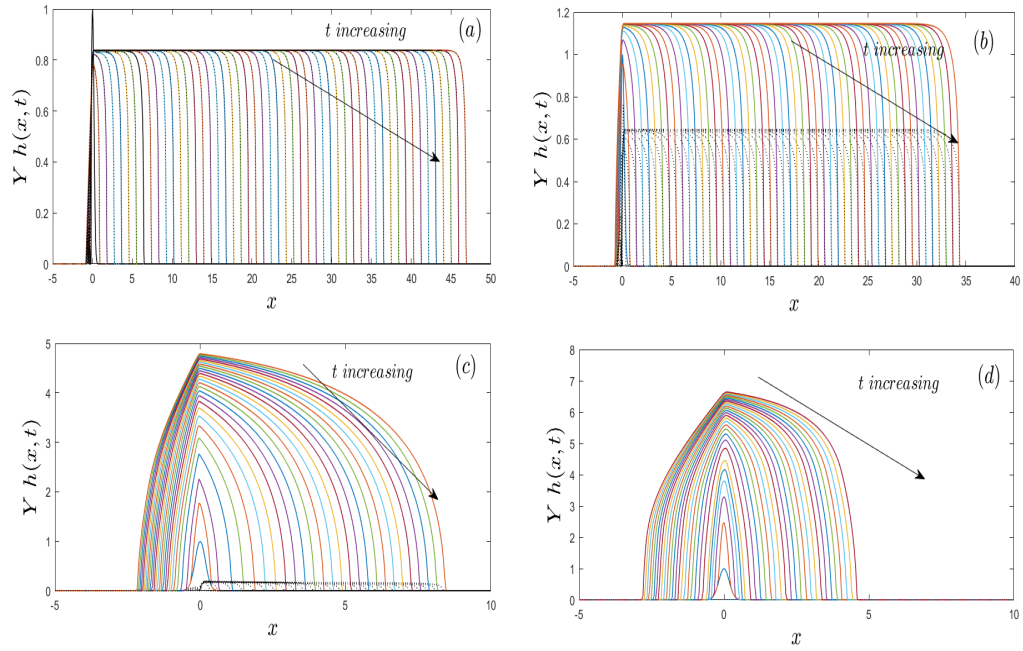

Figure 3.34: A similar picture to Fig. 3.31, but for a dome with $Q_{s_0} = 2$.

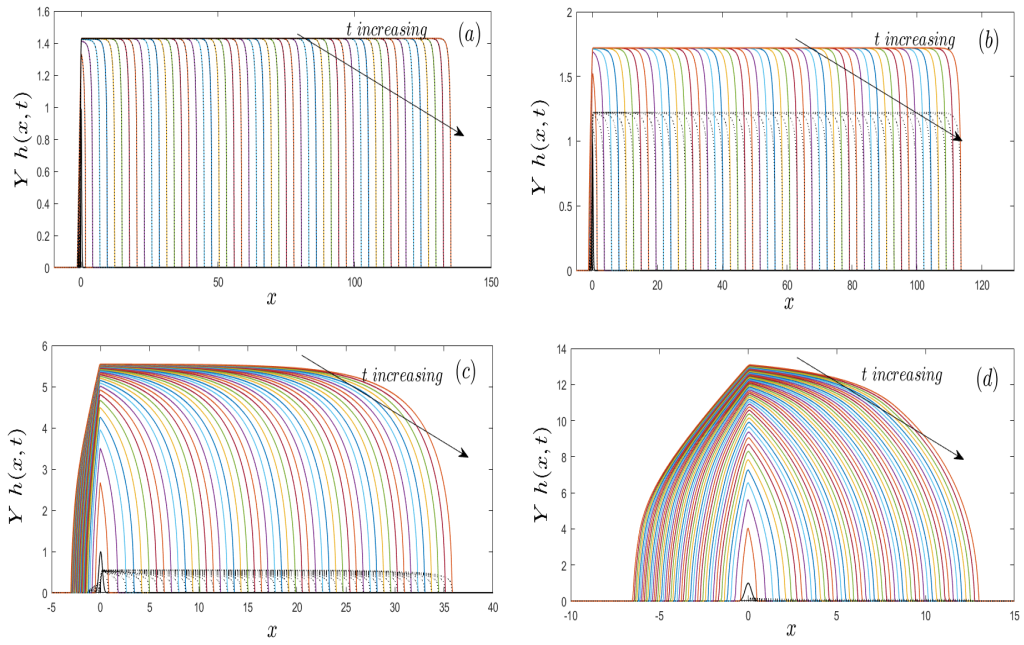

Figure 3.35: A similar picture to Fig. 3.31, but for a dome with $Q_{s_0} = 7$.

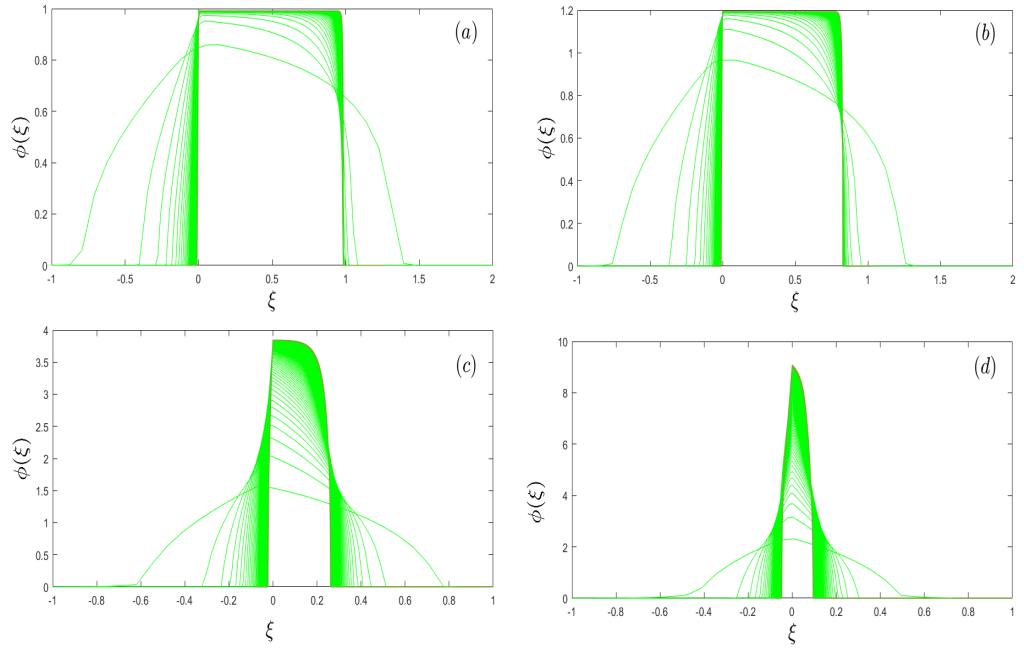

Figure 3.36: The height field is scaled for varying B.

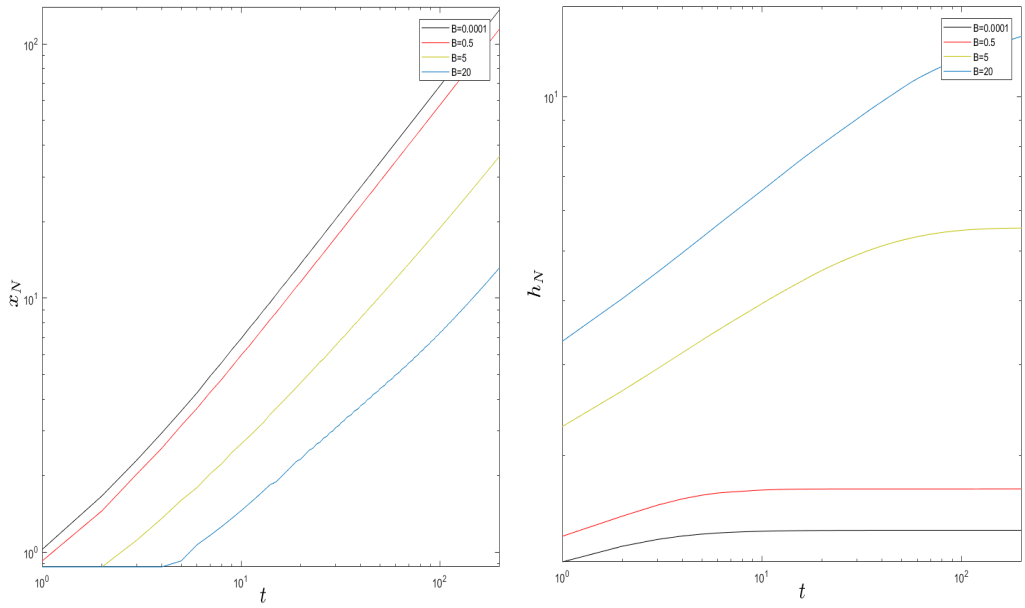

Figure 3.37: Evolution of the domes length x_N and height h_N for various values of B and $n = 1$.

occupies almost the whole dome and $Y << h$. The results of applying the similarity scaling for evolution equation are shown in Figs. 3.32 and 3.36 where all the numerical solution in Figs. 3.31 and 3.35 respectively are collapses to a single curve, we illustrate from this figures, that the for B very small the numerical solution scaling matched with the similarity solution for Newtonian one.

Figure 3.38 display the effect of using different inclination $S = 0.7, 1, 2.145, 3.732$ respectively. Here, the 'plug' occupies roughly half of the fluid for all values of S.

The last three figures presents an illustration of the evolution of an extrusion onto a horizontal plane. The dome have $B = 1$ and $B = 10$ for $Q_{s_0} = 2, 7, 14$. The profiles of the dome together with the corresponding yield surface illustrated how this dome has a pseudo-plug and a yielding region. The similarity scaling of numerical solution

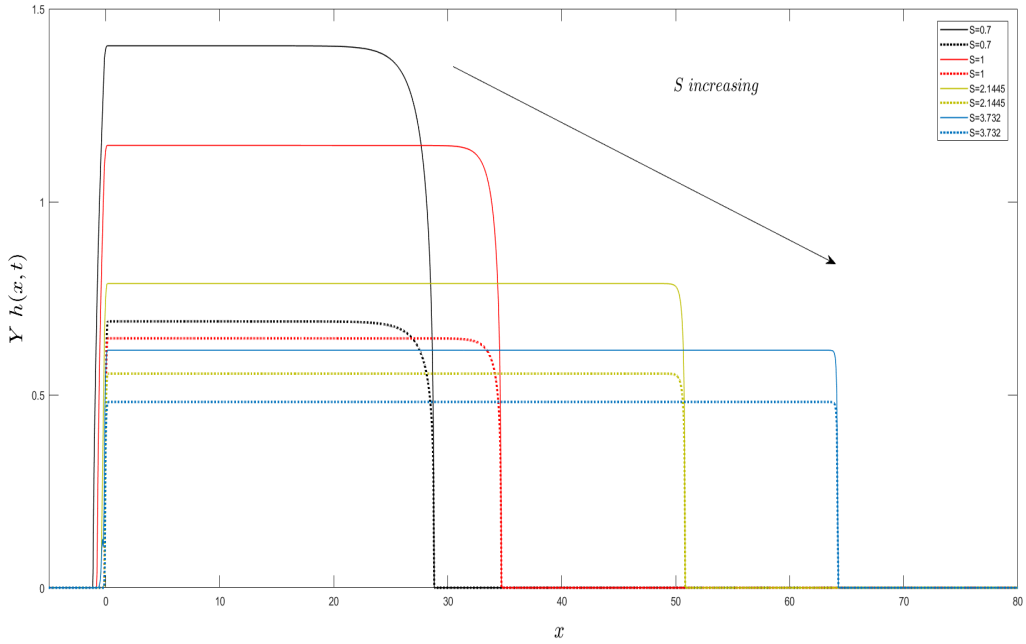

Figure 3.38: Inclined planar for $Q_{s_0} = 2$ and $B = 0.5$. Snapshots of the thickness (solid lines), h, and yield surface (dotted lines), Y, for varying S.

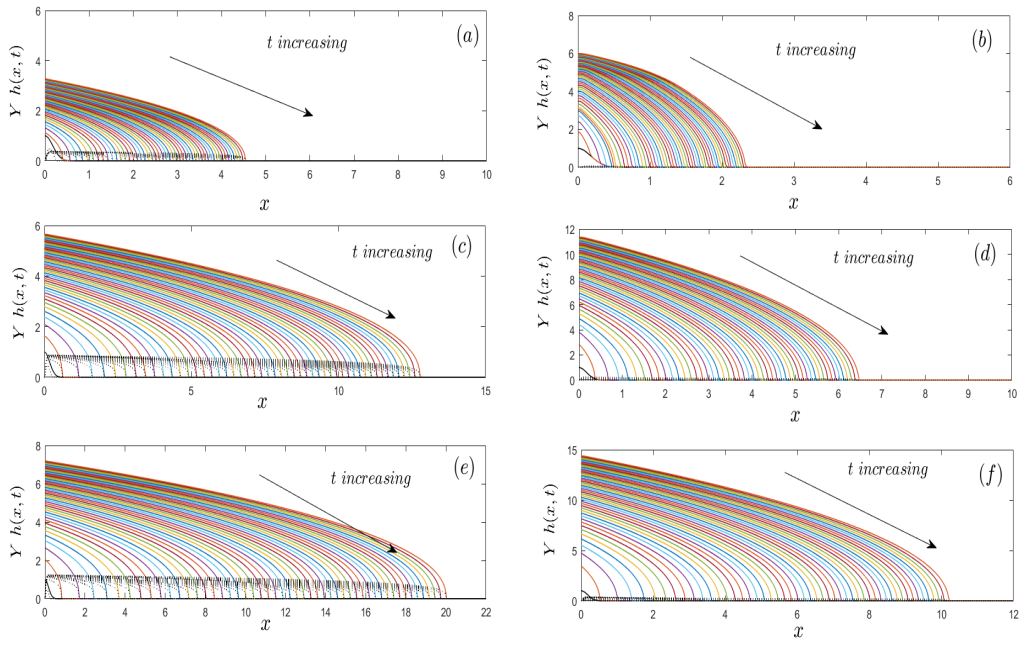

Figure 3.39: Numerical solution showing the height filed of the domes at two-dimensional fluid on an flat planar. Snapshots of height (solid lines), h, and yield surface (dotted lines), Y, for (a) $Q_{s_0} = 2$, $B = 1$ (b) $Q_{s_0} = 2$, $B = 10$ (c) $Q_{s_0} = 7$, $B = 1$ (d) $Q_{s_0} = 7$, $B = 10$,(e) $Q_{s_0} = 14$, $B = 1$,(f) $Q_{s_0} = 14$, $B = 10$,for $n = 1$.

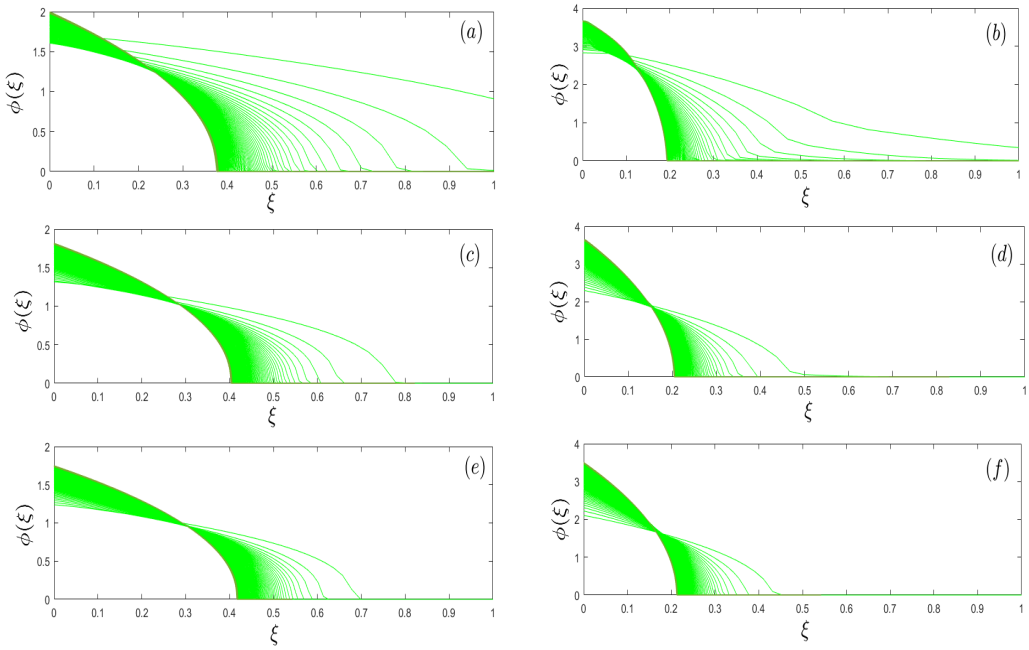

Figure 3.40: The height field is scaled for varying B.

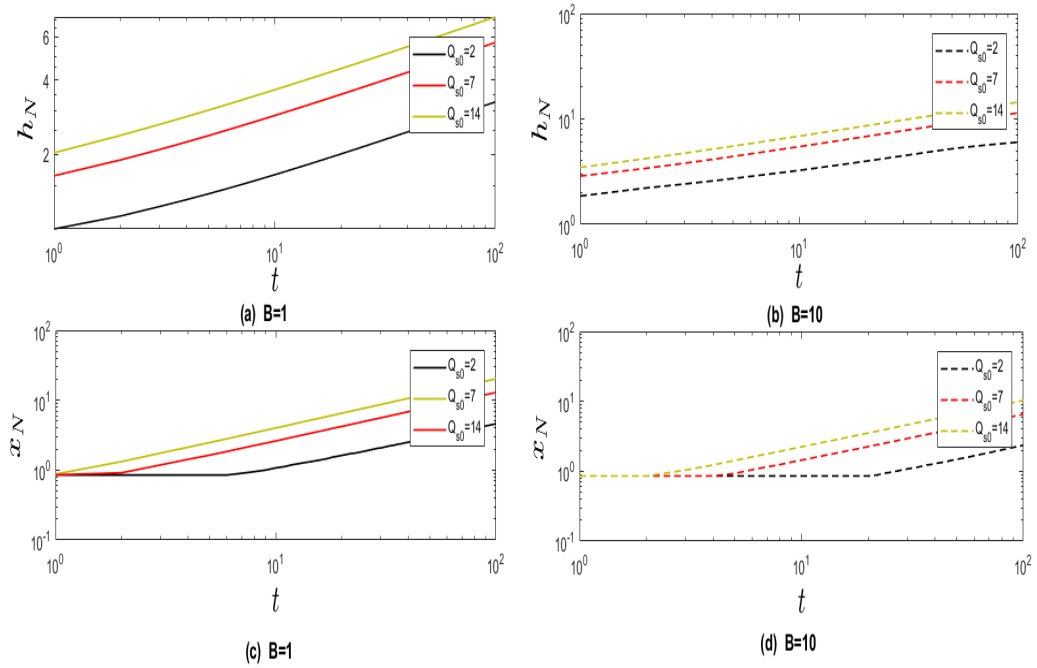

Figure 3.41: Evolution of the domes length x_N and height h_N for various values of B and $n = 1$.

in Fig. 3.39 are illustrate in Fig. 3.40 using scale (3.28). In Fig. 3.41 we show the maximum dome height, h_N, with the location of the leading edge, x_N, corresponding to Fig. 3.39

3.5 Conclusions

In this chapter we investigate the spreading of a planar non-Newtonian liquid dome down a pre-wetted and inclined substrate as a simple model to investigate the influence of non-Newtonian effects, such as the apparent viscosity and yield stress on the spreading of viscous-gravity currents. We assume isothermal conditions, so the liquid properties, particularly, the viscosity are constant. An extensive study of the system parameters, particularly, the power-law index, n, and the Bingham number, B (measures the magnitude of the yield stress), along with S and Q_{s_0}, reveal their influence on the evolution of free surface and the spreading characteristics.

Late-time similarity solutions of the evolution equation for the free surface provide scaling relationships for the maximum dome height, h_N, and the spreading distance, x_N. These similarity solutions are characterised by a volume of liquid proportional to t^α, ($\alpha \geq 0$), of liquid released by the source onto the plane. For $S = 0$, $h_N = h(x = 0, t) \sim t^{(\alpha(n+1)-n)/(2n+3)}$ and $x_N \sim t^{(\alpha(n+2)+n)/(2n+3)}$. For $B \neq 0$, similarity solutions are shown to exist for $\alpha > 3$ with h_N inceasing in time. For, $\alpha < 3$, the yield stress grows in time and eventually the dome attains a static shape in time (depending on B) with the

yield surface, $\mathcal{Y} = 0$, i.e., the entire dome becomes non-yielding. For $B = 0$, similarity solutions exist for all values of α with h_N increasing in time for $\alpha > n/(n+1)$. For $S > 0$, $h_N = h(x = x_N, t) \sim t^{n(\alpha-1)/(2n+1)}$ and $x_N \sim t^{\alpha(n+1)+n/(2n+1)}$. For $0 < \alpha < 1$, h_N decreases with time and increases otherwise. For $B \neq 0$, similarity solutions are shown to exist for $\alpha > 1$ with h_N inceasing in time. For $\alpha < 1$, the dome attains a static shape in time (depending on the value of B) for the same reason as for the $S = 0$ case. For $B = 0$, similarity solutions exist for all values of α with h_N increasing in time for $\alpha > 1$. The similarity scalings have been derived previously by Balmforth *et al.* [5, 9] for Power-law and Herschel Bulkley models for constant volume spreading, $Q_{s0} = 0$. Our work has generalised these to general α. We also explicitly compute these similarity solutions and are validated against corresponding numerical solutions at late times.

Our numerical solutions reveal the dynamics of the dome evolution for variations in parameter values, in particular, the power-law index n and the Bingham number, B. The free surface shapes are similar to those reported in Chapter 2 for a Newtonian liquid. The spreading rates are observed to decrease as the power-law index, n, decreases. This is due to the viscosity becoming very large in the limit of small shear rates, therefore slowing down the spreading. For such low shear rates the power law model might not be appropriate (see Myers [63]) for the reason above. We have formulated the evolution equation for a Carreau model (not shown any simulations here) which would be more applicable for a range of shear rates. We have also investigated

the role of the yield stress via the Bingham number, B. The spreading is close to Newtonian for small values of B; for intermediate values of B, there exists a growing yield surface, $\mathcal{Y}$, above which the fluid is non-yielding; for large B, the dome becomes static in finite time with $\mathcal{Y} = 0$, i.e., the entire dome becomes non-yielding.

In the next Chapter, we investigate the spreading of a liquid dome under non-isothermal conditions.

Chapter 4

The non-isothermal and Newtonian spreading of a hot liquid dome down an inclined plane: the small reduced Péclet number limit

4.1 Introduction

In Chapters 2 and 3, the spreading problem was investigated under isothermal conditions. In this Chapter, we extend this model for a Newtonian liquid to include non-isothermal effects, in particular, a temperature-dependent viscosity, which provides the coupling between the temperature field and the flow, and cooling effects due

to heat transfer at the dome's free surface and the underlying substrate. We follow closely the previous modelling studies by Sansom *et al.* [76, 53, 77] and Balmforth *et al.* [7, 11] for spreading of a viscous gravity current over an horizontal substrate.

The outline of this chapter is as follows. We formulate the one-dimensional mathematical problem in §4.2 which provides the governing equations and boundary conditions for the flow and the temperature field. The lubrication approximation and the assumption of the reduced Péclet number, $Pe_r \ll 1$, allows simplification of the governing equations and boundary conditions to a system of two coupled PDEs for the evolution of the one-dimensional free surface shape and the temperature field. In §4.3, we perform numerical simulations of the evolution equations to determine the free surface shapes and temperature fields for a variety of parameter values and two viscosity-temperature models, the exponential viscosity and the bi-viscosity models. In §4.4 we discuss the main results which include the existence of some new free surface shapes and their parameter regime.

4.2 Mathematical Formulation

The fluid flow problem is the same as that described in §2.2 of a hot liquid dome spreading under the influence of gravity down a colder inclined and pre-wetted substrate (see Fig. 2.1 for a schematic). The liquid in the dome is assumed to be Newtonian with constant properties, except, the liquid viscosity is dependent on the temperature.

The liquid loses its heat via the colder free surface $z^\star = h^\star(x^\star, t^\star)$ and substrate at $z^\star = 0$.

4.2.1 Governing Equations

The governing equations for the flow are given by the conservation of mass and momentum, Eqs. (2.1). The two-dimensional governing equation for the temperature, $T^\star$ in Cartesian coordinates, $(x^\star, z^\star)$ is given by (see Eq. (1.15))

$$\rho^\star c_p^\star (T_{t^\star}^\star + u^\star T_{x^\star}^\star + w^\star T_{z^\star}^\star) = \kappa^\star \left[T_{x^\star x^\star}^\star + T_{z^\star z^\star}^\star\right], \tag{4.1}$$

in a material with density, $\rho^\star$, specific heat, $c_p^\star$, thermal conductivity, $\kappa^\star$ and thermal diffusivity, $\kappa_d^\star = \kappa^\star/(\rho^\star c_p^\star)$. We neglect the contribution from viscous dissipation. $(u^\star, w^\star)$ are the flow speeds in the $x^\star$ and $z^\star$ directions, respectively. The constitutive relation between the liquid stress and its rate of strain for a Newtonian liquid with temperature-dependent viscosity is written as:

$$\boldsymbol{\tau}^\star = \mu^\star(T^\star)\dot{\boldsymbol{\gamma}}^\star, \tag{4.2}$$

where $\mu^\star(T^\star)$ is the temperature-dependent liquid viscosity and $\dot{\boldsymbol{\gamma}}^\star$ is the rate of strain tensor given by Eq. (2.3). The boundary condition for the flow are given by Eqs. (2.4-2.11). The boundary conditions for the temperature, $T^\star$ are as follows. At the

free surface $z^\star = h(x^\star, t^\star)$, we impose a heat flux boundary condition:

$$-\kappa^\star \mathbf{n}^\star \cdot \nabla T^\star = a_m^\star (T^\star - T_a^\star), \tag{4.3}$$

where $a_m^\star$ is a heat transfer coefficient (assumed constant) and $T_a^\star$ is the ambient temperature (assumed constant), and $\mathbf{n}^\star$ is the outward-pointing normal given by Eq. (2.7). This assumes that the heat flux is proportional to the temperature difference across this boundary, referred to as Newton's law of cooling. We can write Eq. (4.3) as:

$$\kappa^\star \left(1 + \left(\frac{\partial h^\star}{\partial x}\right)^2\right)^{-\frac{1}{2}} \left(\frac{\partial T^\star}{\partial z} - \frac{\partial h^\star}{\partial x}\frac{\partial T^\star}{\partial x}\right) = -a_m^\star (T^\star - T_a^\star). \tag{4.4}$$

At $z^\star = 0$, we impose the following heat flux boundary condition (see Balmforth *et al.* [7, 11]):

$$\kappa^\star T_{z^\star}^\star = \rho^\star c_p^\star (T^\star - T_e^\star) w_s^\star + b_s^\star (T^\star - T_s^\star), \tag{4.5}$$

where $T_e^\star$ and $T_s^\star$ are the eruption and substrate temperature, respectively (assumed constant), $b_s^\star$ is a heat transfer coefficient at the substrate and $w_s^\star(x^\star, t^\star)$, given by Eq. (2.5), is the vertical velocity at the location of this source (or vent), i.e., $|x^\star| \leq x_0^\star$, where $x_0^\star$ is the vent radius. The first term on the right-hand-side of Eq. (4.5) models the contribution of the heat flux at the vent which is assumed to be proportional to both the temperature difference across the vent and the flow speed there, whereas Newton's law of cooling is applied away from the vent, as represented by the second term on the right-hand-side of Eq. (4.5).

The non-dimensionalisation of the flow variables are the same as in §2.2.3 in Chapter 2. We define: $T^\star = T_a^\star + \Delta^\star T^\star \theta$ $(0 \leq \theta \leq 1)$, $\Delta^\star T^\star = T_e^\star - T_a^\star$. Note: $\theta = 0$, implies $T^\star = T_a^\star$ and $\theta = 1$, implies $T^\star = T_e^\star$ Using this, Eqs. (4.1,4.3,4.5) in dimensionless form are:

$$\epsilon^2 Pe[\theta_t + u\theta_x + w\theta_z) = [\epsilon^2\theta_{xx} + \theta_{zz}]\,, \tag{4.6a}$$

$$\theta_z = \epsilon^2 Pe(\theta - 1)w_s + b\epsilon^2(\theta - \theta_s), \text{ at } z = 0, \tag{4.6b}$$

$$\theta_z = \epsilon^2 h_x\theta_x - a\epsilon^2\theta\sqrt{1 + \epsilon^2 h_x^2}, \text{ at } z = h(x,t). \tag{4.6c}$$

Here $Pe = (\rho^\star c_p^\star U^\star L^\star)/\kappa^\star = U^\star L^\star/\kappa_d^\star$, is the Péclet number (compares convective to diffusive heat transport; assumed to be $O(1)$), the reduced Péclet number, $Pe_r = \epsilon^2 Pe \ll 1$, $a = a_m^\star H^\star/(\epsilon^2\kappa^\star)$ and $b = b_s^\star H^\star/(\epsilon^2\kappa^\star)$ are the heat transfer coefficients at the free surface and substrate, respectively, and $\theta_s = (T_s^\star - T_a^\star)/(T_e^\star - T_a^\star)$.

Let $\theta(x,z,t) = \theta_0(x,z,t) + \epsilon^2\theta_1(x,z,t) + \ldots$. Substituting into Eq. (4.6) gives to leading order in ϵ:

$$\theta_{0_{zz}} = 0, \tag{4.7a}$$

$$\theta_{0_z} = 0, \text{ at } z = 0, h(x,t). \tag{4.7b}$$

Integrating and applying the boundary conditions gives $\theta_0(x,z,t) = \theta_0(x,t)$. At $O(\epsilon^2)$,

we obtain:

$$\theta_{0_t} + u\theta_{0_x} = \frac{1}{Pe}\left[\theta_{0_{xx}} + \theta_{1_{zz}}\right], \tag{4.8a}$$

$$\theta_{1_z} = Pe(\theta_0 - 1)w_s + b(\theta_0 - \theta_s), \tag{4.8b}$$

$$\theta_{1_z} = h_{0_x}\theta_{0_x} - a\theta_0. \tag{4.8c}$$

After rearranging Eq. (4.8a) and integrating with respect to z from $z = 0$ to h, together with the boundary conditions, Eqs.(4.8b,4.8c), we obtain

$$h_{0x}\theta_{0x} - a\theta - (P_e(\theta_0 - 1)w_s + b(\theta_0 - \theta_{0s})) = P_e(h_0\theta_{0t} + \theta_{0x}Q_0) - h_0\theta_{0xx}, \tag{4.9}$$

where the fluid flux, $Q_0 = \int_{z=0}^{z=h_0(x,t)} u_0\, dz$. Dropping the subscripts, the leading order temperature field is given by

$$\theta_t + \frac{Q_0}{h}\theta_x - \frac{h_x}{hPe}\theta_x = \frac{1}{Pe}\theta_{xx} - \frac{1}{hPe}[a\theta + b(\theta - \theta_s)] - \frac{w_s}{h}(\theta - 1). \tag{4.10}$$

We will determine the flux Q_0 from the flow speed u_0 as shown below. Using the constant reference viscosity, $\mu_R^\star$, the non-dimensional form of Eq. (4.2) is given by

$$\boldsymbol{\tau} = \mu(\theta)\dot{\boldsymbol{\gamma}}, \tag{4.11}$$

where $\dot{\boldsymbol{\gamma}}$ is given by Eq. (2.14).

We proceed in the same way as described in Chapter 2 in performing the lubrication

approximation for the leading order flow problem in ϵ. We follow the same sequence of steps in solving the leading order flow problem until the expression for the leading order shear stress, $\tau_{xz_0}(x,z) = (S - h_{0_x})(h_0 - z)$. Using Eq. (4.11), we obtain the leading order relationship between the shear stress and the shear rate as $\tau_{xz_0} = \mu(\theta_0)u_{0_z}$. Using the expression for τ_{xz_0} and the fact that θ_0 is independent of z, we obtain

$$\mu(\theta_0)u_{0_z} = (S - h_{0_x})(h_0 - z). \tag{4.12}$$

Noting that θ_0 is independent of z, we can integrate the above with respect to z and using the boundary condition $u_0(z=0) = 0$, we obtain

$$u_0 = \frac{(S - h_{0_x})}{\mu(\theta)}(h_0 z - \frac{z^2}{2}), \;\; Q_0 = \int_{z=0}^{z=h_0(x,t)} u_0 \; dz = \frac{(S - h_{0_x})h_0^3}{3\mu(\theta)}. \tag{4.13}$$

Proceeding in the same way as described in Chapter 2, we derive the evolution equation as:

$$h_{0_t} + \frac{1}{3}\left[\frac{h_0^3}{\mu(\theta_0)}(S - h_{0_x})\right]_x = w_s, \tag{4.14}$$

where

$$w_s = \frac{3}{4}Q_{s_0}Q_s(t)\left[1 - (x/x_0)^2\right]\mathcal{H}(x^2 - x_0^2). \tag{4.15}$$

Hence, the coupled flow and thermal problem can be written as (dropping the sub-

script):

$$
\begin{aligned}
h_t &+\frac{1}{3}\left[\frac{h^3}{\mu(\theta)}(S-h_x)\right]_x = w_s, && \text{(4.16a)}\\
\theta_t &+\frac{Q}{h}\theta_x - \frac{h_x}{hPe}\theta_x = \frac{1}{Pe}\theta_{xx} - \frac{1}{hPe}[a\theta + b(\theta-\theta_s)] - \frac{w_s}{h}(\theta-1), && \text{(4.16b)}\\
Q &= \frac{(S-h_x)h^3}{3\mu(\theta)}, && \text{(4.16c)}\\
w_s &= \frac{3}{4}Q_{s_0}Q_s(t)\left[1-(x/x_0)^2\right]\mathcal{H}(x^2-x_0^2). && \text{(4.16d)}
\end{aligned}
$$

The viscosity-temperature relationship, $\mu(\theta)$, is given by the non-dimensionalised form of Eqs. (1.18,1.19) given in §1.3.3 in Chapter 1.

$$
\begin{aligned}
\mu(\theta) &= e^{-\alpha\theta}, \qquad \text{(exponential model)} && \text{(4.17a)}\\
\mu(\theta) &= \begin{cases} \mu_e & \text{if } \theta > \theta_m, \qquad \text{(Bi-viscosity model)} \\ \mu_a & \text{if } \theta < \theta_m. \end{cases} && \text{(4.17b)}
\end{aligned}
$$

Here, $\alpha = \alpha^\star(T_e^\star - T_a^\star)$, $\mu_e = \mu_e^\star/\mu_R^\star$, $\mu_a = \mu_a^\star/\mu_R^\star$ and $\theta_m = (T_m^\star - T_a^\star)/(T_e^\star - T_a^\star)$.

4.3 Numerical Results

In this section, we seek the numerical solution of Eq. (4.16) for $x \in [-L, L]$, where L is the length of the computational domain. We assume that the plane is pre-wetted with a precursor layer of thickness b_1. The boundary conditions specified are: $h = b_1$

and $\theta_x = 0$ at $x = \pm L$. The initial conditions for h and θ are chosen as:

$$h(x,0) = (1-x^2)H(1-x^2) + b_1, \quad \theta(x,0) = 1, \quad x \in \quad [-L, L]. \tag{4.18}$$

Our focus is in investigating the evolution of the dome height h varying the key parameters related to the non-isothermal conditions: the Péclet number, Pe, the heat transfer coefficients, a, b, at the free surface and substrate, respectively, the decay constant, α, in the exponential viscosity-temperature relationship and μ_a and μ_e in the bi-viscosity model. We consider variations in the above parameters for $S = 0$ (horizontal plane) and $S = 1$ (plane inclined at angle of approximately 6^o), and for constant volume or zero source flowrate ($Q_{s_0} = 0$) and constant flow rate. The length of the computational domains L is chosen sufficiently large so that the boundary condition $h \to b_1$ and $\theta_x = 0$ as $x \to \infty$ is satisfied numerically for the range of times considered here. The evolution equations for h and θ, Eqs. (4.16a,4.16b), are solved numerically using the Method of lines [78, 61]. The numerical discretisation scheme for h is described in Chapters 2 and 3. We follow a similar discretisation scheme for θ with an up-winding scheme to discretise the convective term (second and third terms on the left-hand-side of Eq. (4.16b). In all the results shown below, we fix the source vent width $x_0 = 0.15$, the precursor thickness $b_1 = 10^{-3}$ for $S = 1$ and $b_1 = 10^{-5}$ for $S = 0$ and the temperature at the substrate, $\theta_s = 0$ (or $T_s^\star = T_a^\star$).

Strictly speaking, the asymptotic expansion in §4.2.1 takes the limit $\epsilon \geq 0$ with $Pe = O(1)$. However, for this asymptotic theory to work, we require the reduced Péclet

number, $Pe_r = \epsilon^2 Pe \ll 1$. For lava, $\epsilon \sim 0.01 - 0.1$, so $Pe \ll 10^4$. For the results to follow, we choose the Péclet number in the range $0 < Pe < 10^4$. One needs to be cautious when applying the asymptotic theory in the range of the higher Péclet numbers, $Pe = 10^2 - 10^4$. Justification of this is shown in Chapter 5, which considers the theory for $Pe_r = O(1)$. The range of validity of the vertical isothermal theory presented here is shown to be in good agreement for the higher range of Péclet numbers considered here and even beyond, e.g., $Pe = 10^5, 10^6$.

We first consider the results for $S = 0$ (horizontal plane) and $Q_{s_0} = 0$ (constant volume drop) using the exponential decay viscosity model. Figure 4.1 shows the evolution of $h(x,t)$ with $\alpha = 0$ corresponding to the isothermal case with $\mu(\theta) = 1$. This isothermal case is also obtained in the limit of $Pe \to 0$. The time range shown is for $0 \leq t \leq 30$. This case is equivalent to the fluid being at the ambient temperature $\theta = 0$. We observe the characteristic dome-shaped spreading with a steep front at its leading edge as described in Chapter 2. As $Pe \to 0$, the cooling is significant over the entire domain resulting in the temperature quickly dropping to its equilibrium value, $\theta = 0$ (or $T^\star = T_a^\star$) and the evolution of $h(x,t)$ is similar to that of isothermal spreading with $\mu(\theta) = 1$. This can be clearly seen in Fig. 4.2(b) with $P_e = 0.1$, $\alpha = 2$, $a = 0.2$ and $b = 0.3$ where the temperature drops very quickly from its initial condition, $\theta = 1$, to zero due to significant cooling to the surroundings. The corresponding evolution of $h(x,t)$ is shown in Fig. 4.2(a) which is similar to Fig. 4.1. The cooling is much less rapid as the Péclet number is increased (see Fig. 4.3(b) for $Pe = 10^2$). This

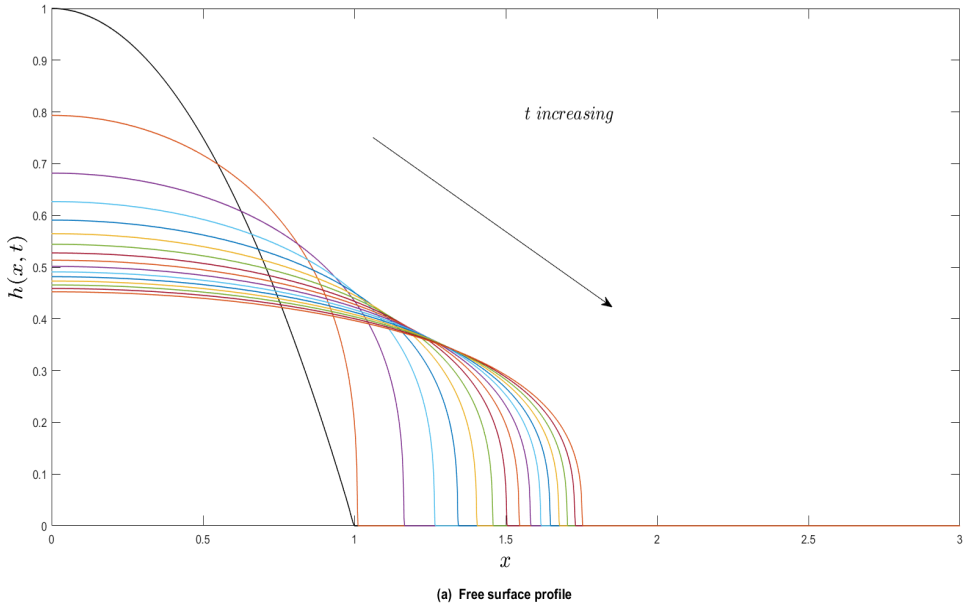

Figure 4.1: The evolution of $h(x,t)$ for t varying between $t = 0 - 30$ corresponding to the isothermal constant volume case with $\mu(\theta) = 1$. The parameter values are: $S = 0$, $\alpha = 0$, $Q_{s_0} = 0$ and $\theta_s = 0$.

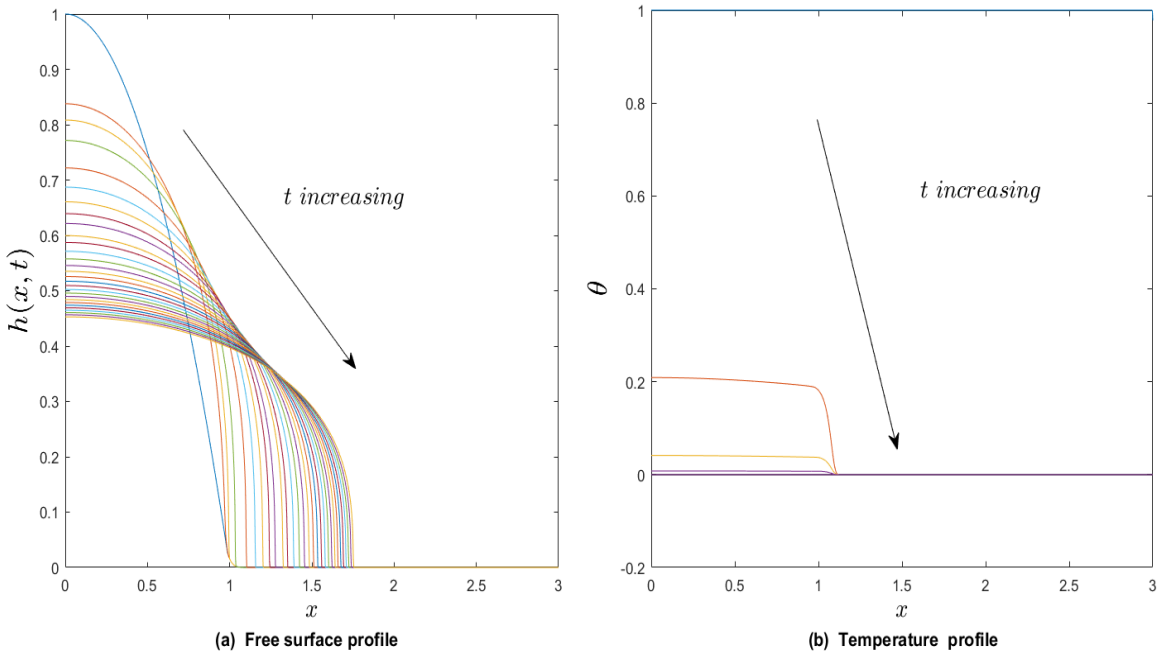

Figure 4.2: The evolution of (a) $h(x,t)$ and (b) $\theta(x,t)$ for t varying between $t = 0 - 30$ with $Pe = 0.1$, $\alpha = 2$, $Q_{s_0} = 0$, $\theta_s = 0$, $a = 0.2$ and $b = 0.3$.

cooling is more pronounced near the leading edge of the advancing front where h is small, compared to elsewhere. This is due to the rate of heat loss being inversely proportional to h (see second term on the right-hand-side of Eq. (4.16b). We note here that the temperature in the precursor film ahead of the advancing front is the same as that near the front which is not shown in Fig. 4.3(b) and the subsequent temperature profiles in the rest of this chapter. Figure 4.3(b) shows the gradual decrease in the temperature to its equilibrium value, $\theta = 0$, over the entire domain. The resulting increase in the liquid viscosity is not as rapid as in the previous case with $Pe = 0.1$, so that the liquid in the dome is more mobile and the spreading is faster than before (see Figure 4.3(a)). Increasing the Péclet number, further reduces the cooling (see

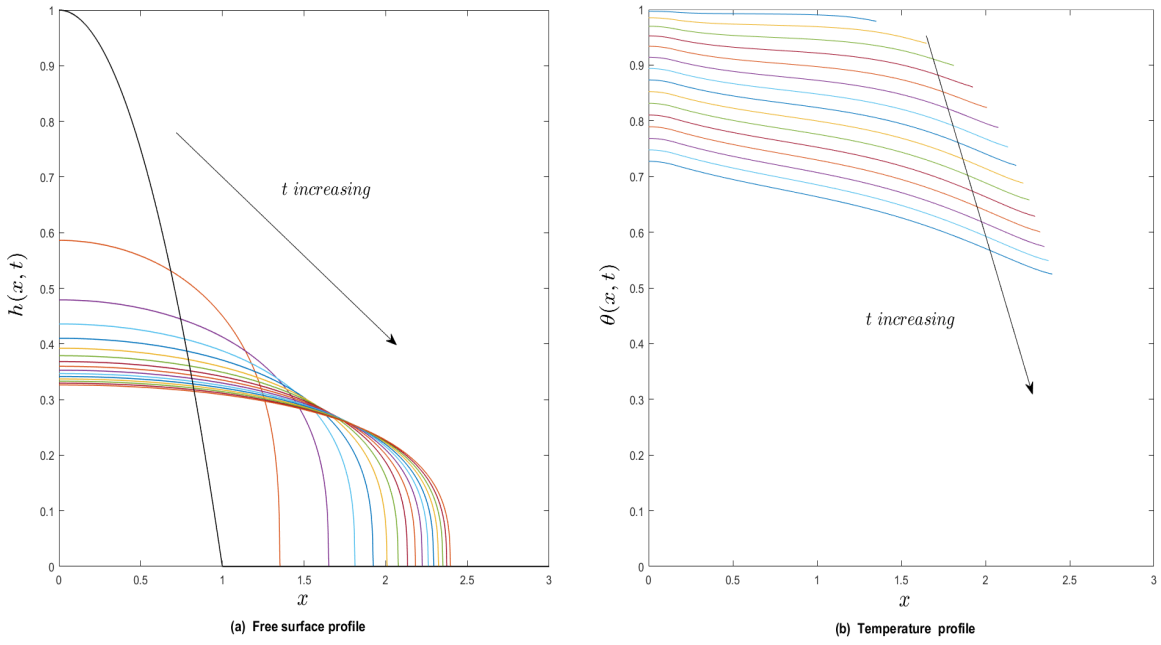

Figure 4.3: The evolution of (a) $h(x,t)$ and (b) $\theta(x,t)$ for t varying between $t = 0 - 30$ with $Pe = 10^2$, $\alpha = 2$, $Q_{s_0} = 0$, $\theta_s = 0$, $a = 0.2$ and $b = 0.3$.

Fig. 4.4(b) for evolution of $\theta(x,t)$ with $Pe = 10^4$) which is now more localised near

the leading edge of the front with the bulk of the drop at the initial temperature, $\theta = 1$ (or $T^\star = T_e^\star$). This in turn decreases the viscosity resulting in faster spreading (see Fig. 4.4(a) for evolution of $h(x,t)$ with $Pe = 10^4$). We also note that due to the increased contribution of convection as the Péclet number increases, the temperature is transported a slightly longer distance by the flow compared to the case with $Pe = 10^2$. In the limit as $Pe \to \infty$, we would expect negligible heat loss and the evolution would

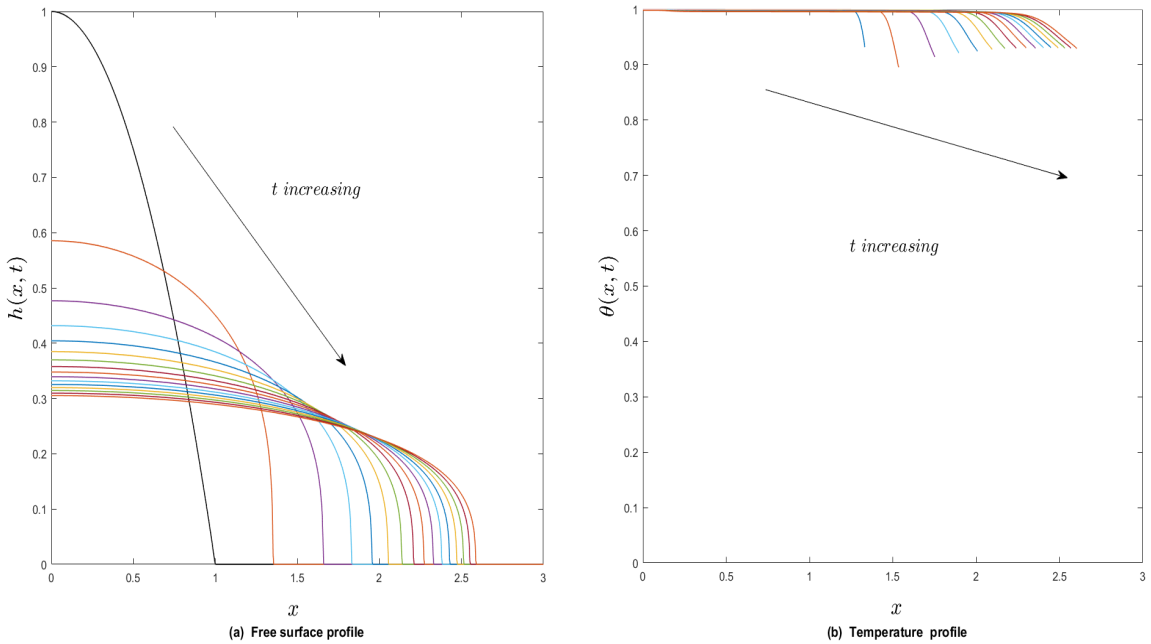

Figure 4.4: The evolution of (a) $h(x,t)$ and (b) $\theta(x,t)$ for t varying between $t = 0 - 30$ with $Pe = 10^4$, $\alpha = 2$, $Q_{s_0} = 0$, $\theta_s = 0$, $a = 0.2$ and $b = 0.3$.

be the same as isothermal spreading except with a smaller viscosity, $\mu = \mu_e = e^{-2}$, corresponding to $\theta = 1$ (or $T^\star = T_e^\star$). In Fig. 4.5, we show the evolution of the location of the leading edge of the dome, x_N (Fig. 4.5(a)) and the dome height at its centre, $h_N = h(0,t)$ (Fig. 4.5(b)), for varying Péclet number Pe between $0.1 \leq Pe \leq 10^4$. We observe that the results are bounded above and below by the two isothermal cases

corresponding to $Pe \to \infty$ and $Pe \to 0$, respectively. For $\mu = e^{-2}$, we can confirm that $x_N \sim t^{1/5}$ and $h_N \sim t^{-1/5}$ which is in agreement with the spreading rates and similarity solution derived in Eq. (2.29) in §2.3 of Chapter 2.

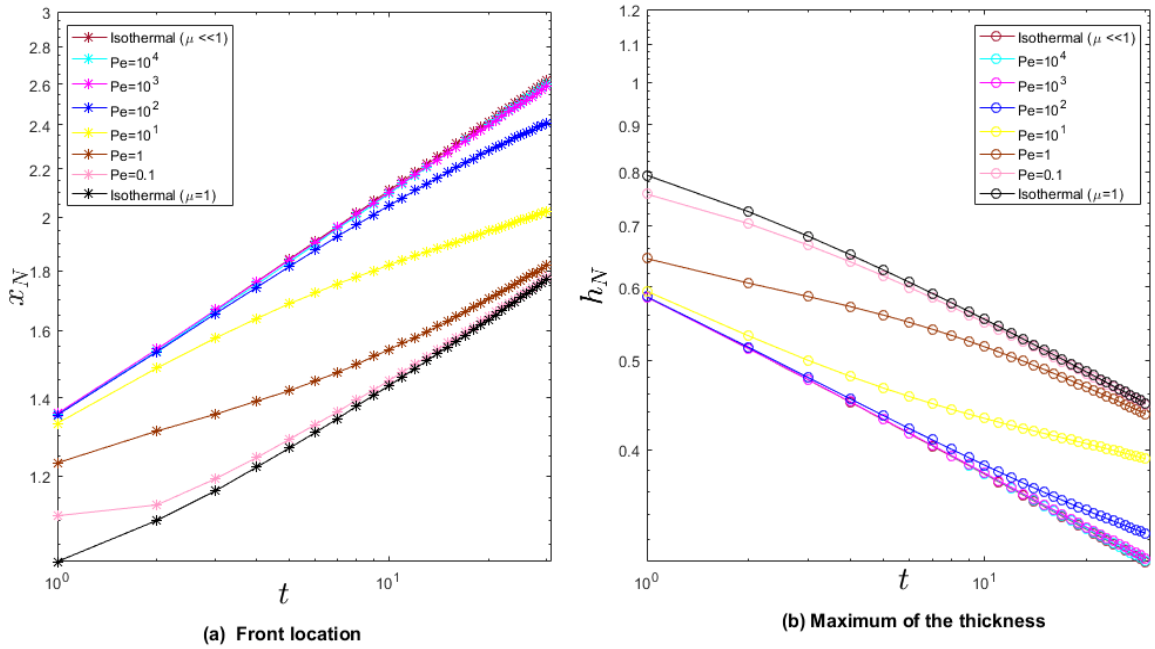

Figure 4.5: The (a) leading edge of the front, x_N, and (b) the maximum in h, $h_N = h(0,t)$, as a function of time, t, for various Péclet number, Pe. The parameter values are: $\alpha = 2$, $Q_{s_0} = 0$, $\theta_s = 0$, $a = 0.2$ and $b = 0.3$.

By increasing α in the exponential viscosity relationship, the coupling between the flow and temperature increases. Figure 4.6(a,b) show the evolution of h and θ for $Pe = 10^4$ and $\alpha = 7$ for $t = 0 - 30$. We observe a change in shape from that of a dome-shaped profile that spreads and thins (see Fig. 4.4(a) for $Pe = 10^4$ and $\alpha = 2$) to a long developing plateau region with a steep front at its leading edge (a pancake-shaped profile; see Fig. 4.6(a)). The temperature profile is similar to that for $Pe = 10^4$ and $\alpha = 2$, except that the cooling is much more significant near the front region

(Fig. 4.6(b)). We also note that the higher value of α would result in much lower viscosities, hence increasing the mobility and the spreading rate of the dome (compare Fig. 4.4(a) for $\alpha = 2$ with Fig. 4.6(a) for $\alpha = 6$ for the same timeframe, $t = (0 - 30)$. Figure 4.7 shows $h(x, t = 30)$ for $\alpha = 6$ and varying Péclet number, Pe. We observe

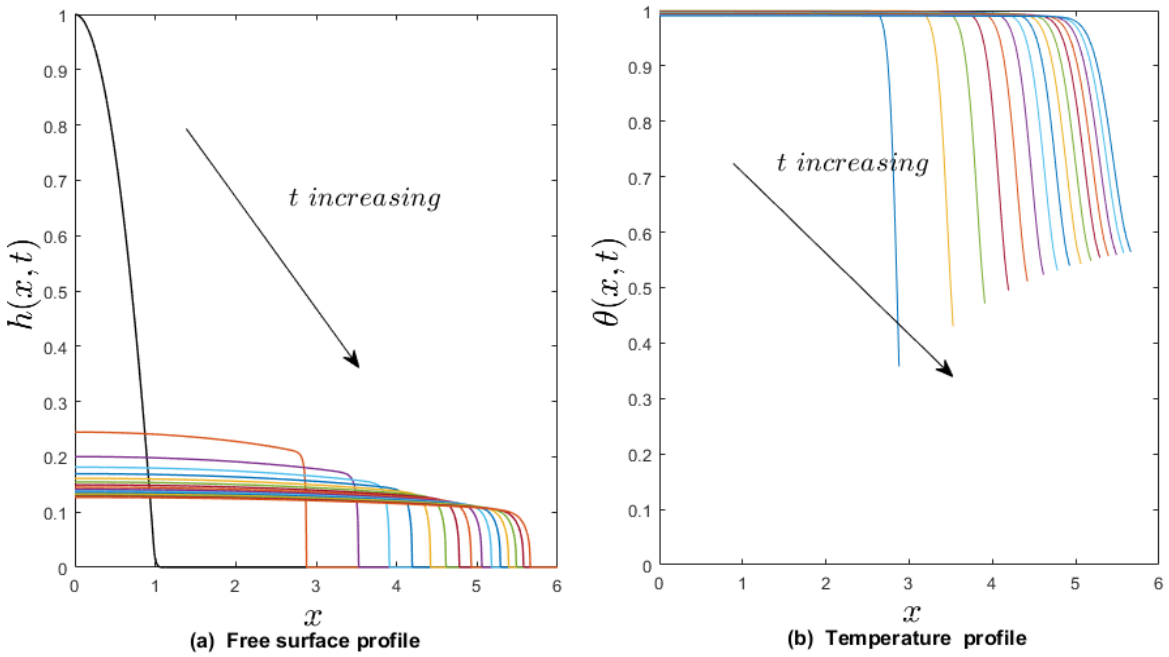

Figure 4.6: The evolution of (a) $h(x, t)$ and (b) $\theta(x, t)$ for t varying between $t = 0 - 30$ with $Pe = 10^4$, $\alpha = 7$, $Q_{s_0} = 0$, $\theta_s = 0$, $a = 0.2$ and $b = 0.3$.

two distinct types of profiles: a pancake-shaped profile with a long plateau middle region and a steep front at its leading edge is observed for Péclet numbers roughly between $10^3 \leq Pe \leq 10^4$. For $Pe < 10^4$, we observe the usual dome-shaped profile spreading and thinning with a steep front at it's leading edge. In Fig. 4.8, we show the evolution of the location of the leading edge of the dome, x_N (Fig. 4.8(a)) and the dome height at its centre, $h_N = h(0, t)$ (Fig. 4.8(b)), for varying Péclet number Pe between $0.1 \leq Pe \leq 10^4$ and $\alpha = 6$. The same trends hold as in Fig. 4.5 for $\alpha = 2$, except that

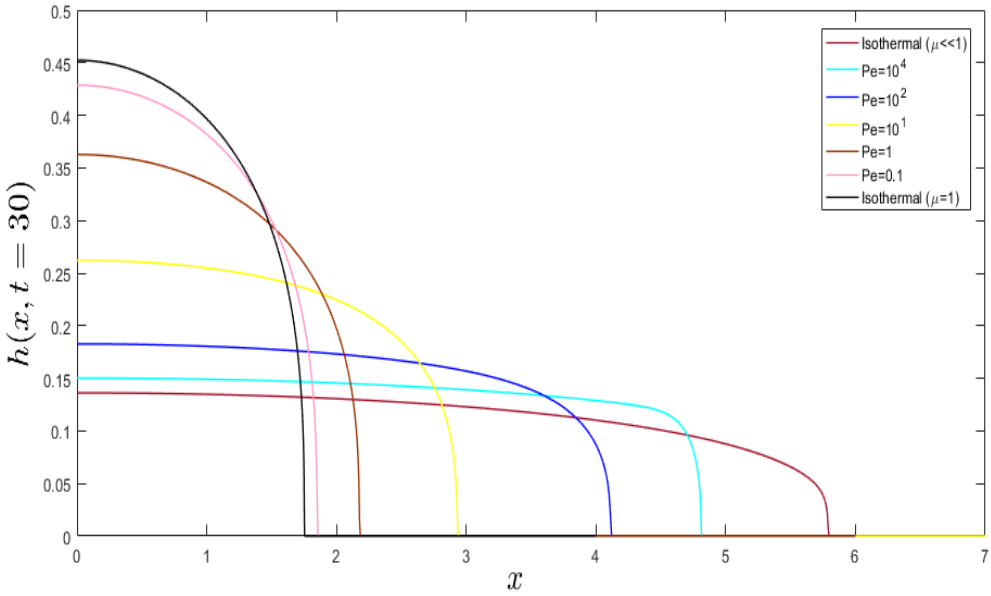

Figure 4.7: The dome height, $h(x, t = 30)$, for $\alpha = 6$ and varying Péclet number, Pe, with $Q_{s_0} = 0$, $\theta_s = 0$, $a = 0.2$ and $b = 0.3$.

the spreading rates are higher for $\alpha = 6$ due to the lower viscosity resulting in the dome spreading over a longer distance compared to $\alpha = 2$, particularly for higher values of Pe. For lower values of Pe, the spreading is largely independent of α. This is due to rapid cooling that occurs at these values of Pe lowering the temperature to $\theta = 0$ over the entire domain. The next set of results show the influence of the heat transfer coefficients, a and b, on the evolution of h and θ. Figure 4.9(a, b) show the evolution of $h(x, t)$ and $\theta(x, t)$, respectively, for $Pe = 10^2$, $\alpha = 2$ and $a = b = 0$ for time varying between $t = 0 - 30$. The temperature $\theta = 1$ for all time since there is no heat loss or cooling and spreading of the dome is isothermal with viscosity, $\mu = e^{-\alpha} = e^{-2}$. Figure 4.10$(a, b)$ show the evolution of $h(x, t)$ and $\theta(x, t)$, respectively, for $Pe = 10^2$, $\alpha = 2$ and $a = 0.02$ and $b = 0.03$ for time varying between $t = 0 - 30$. There is minimal heat loss

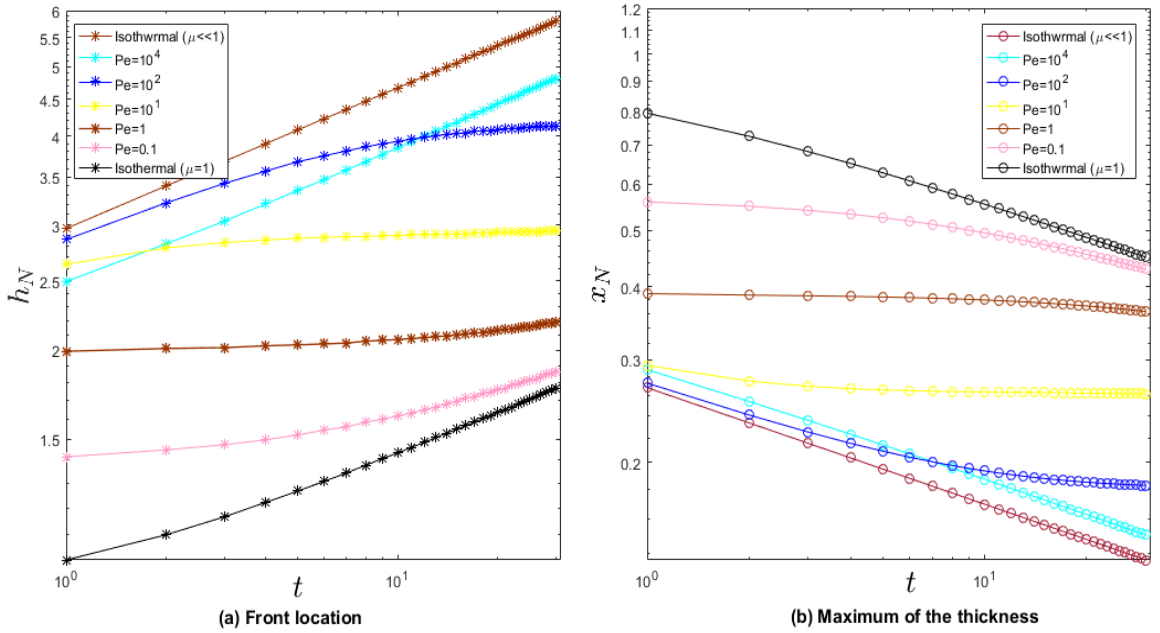

Figure 4.8: The (a) leading edge of the front, x_N, and (b) the maximum in h, $h_N = h(0,t)$, as a function of time, t, for various Péclet number, Pe. The parameter values are: $\alpha = 6$, $Q_{s_0} = 0$, $\theta_s = 0$, $a = 0.2$ and $b = 0.3$.

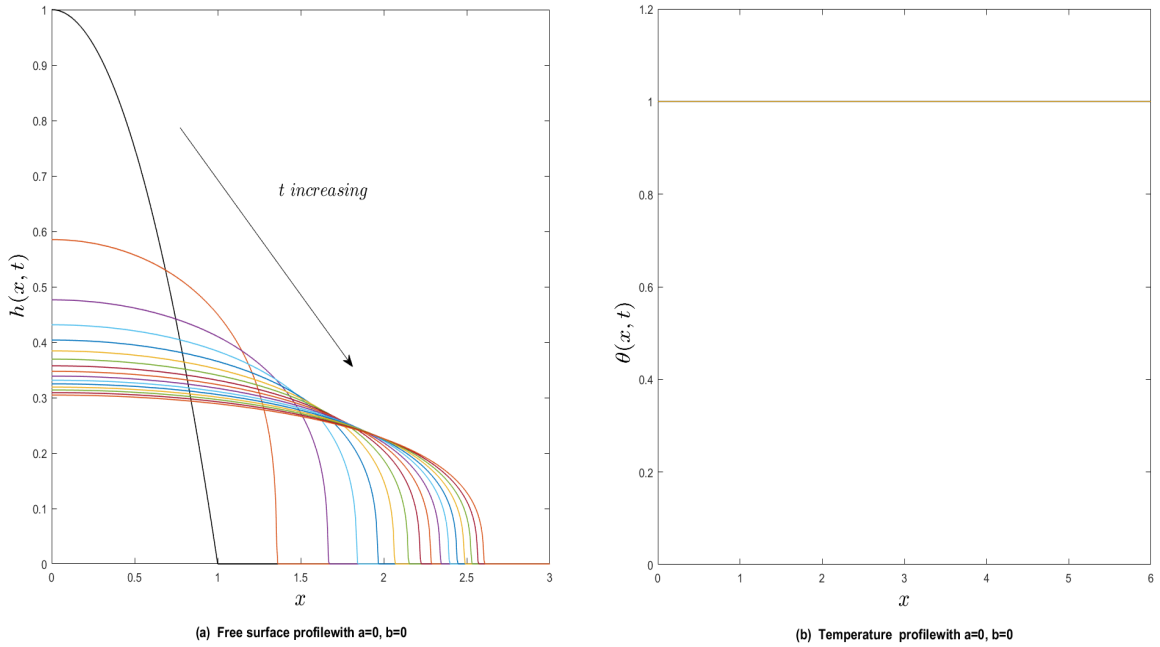

Figure 4.9: The evolution of (a) $h(x,t)$ and (b) $\theta(x,t)$ for t varying between $t = 0 - 30$ with $Pe = 10^2$, $\alpha = 2$, $Q_{s_0} = 0$, $\theta_s = 0$ and $a = b = 0$.

or cooling for the times shown and spreading of the dome is close to isothermal. Figure 4.10(c, d) show the evolution of $h(x,t)$ and $\theta(x,t)$, respectively, for $Pe = 10^2$, $\alpha = 2$ and $a = b = 10$ for time varying between $t = 0 - 30$. The cooling is much more pronounced for these higher values of the heat transfer coefficients resulting in a rapid decrease in temperature to the ambient temperature, $\theta = 0$. The evolution of $h(x,t)$ is similar to the isothermal case with viscosity $\mu = 1$ corresponding to $\theta = 0$. We now consider the

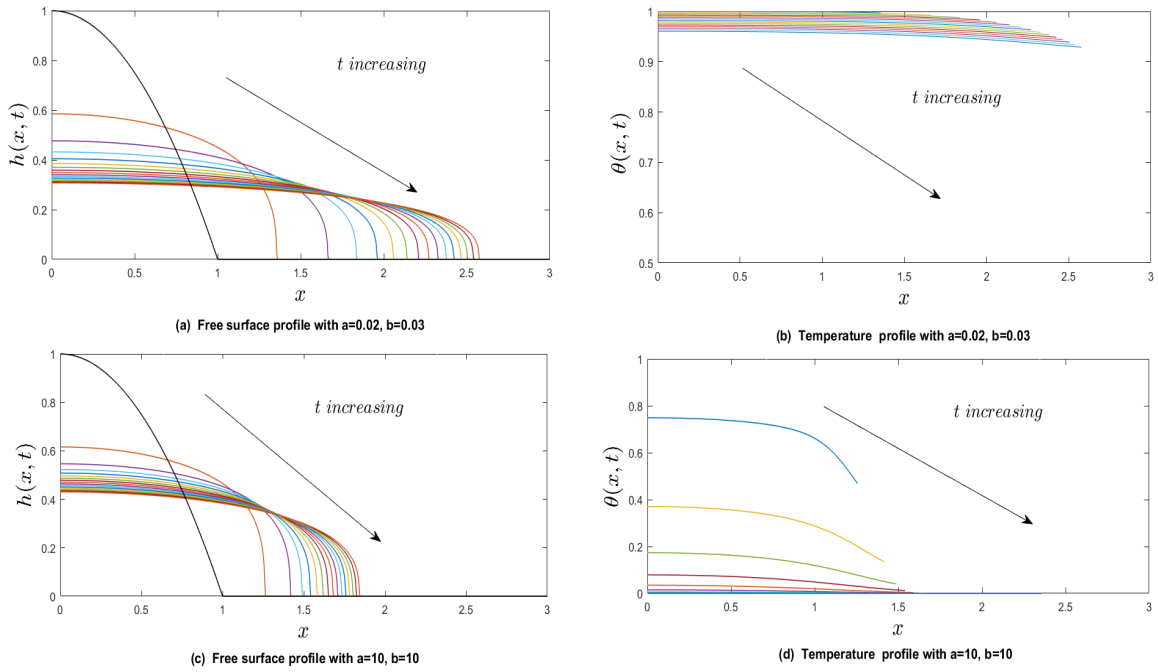

Figure 4.10: The evolution of (a) $h(x,t)$ and (b) $\theta(x,t)$ for t varying between $t = 0 - 30$ with $a = 0.02$ and $b = 0.03$ and (c) $h(x,t)$ and (d) $\theta(x,t)$ with $a = b = 10$. The other parameter values are: $Pe = 10^2$, $\alpha = 2$, $Q_{s_0} = 0$ and $\theta_s = 0$.

effects of an influx of liquid from a source or vent with flowrate, $Q_{s_0} = 7$. Figure 4.11 shows the constant viscosity case, $\mu = 1$ (corresponding to $\alpha = 0$) for $t = 0 - 20$. The strength of the source is sufficiently strong to drive both the spreading of the dome as well as building-up of liquid around the vent. These results show a good agreement with those in Chapter 2. Fig. 4.12(b) shows the temperature profile for $Pe = 10^4$. There is

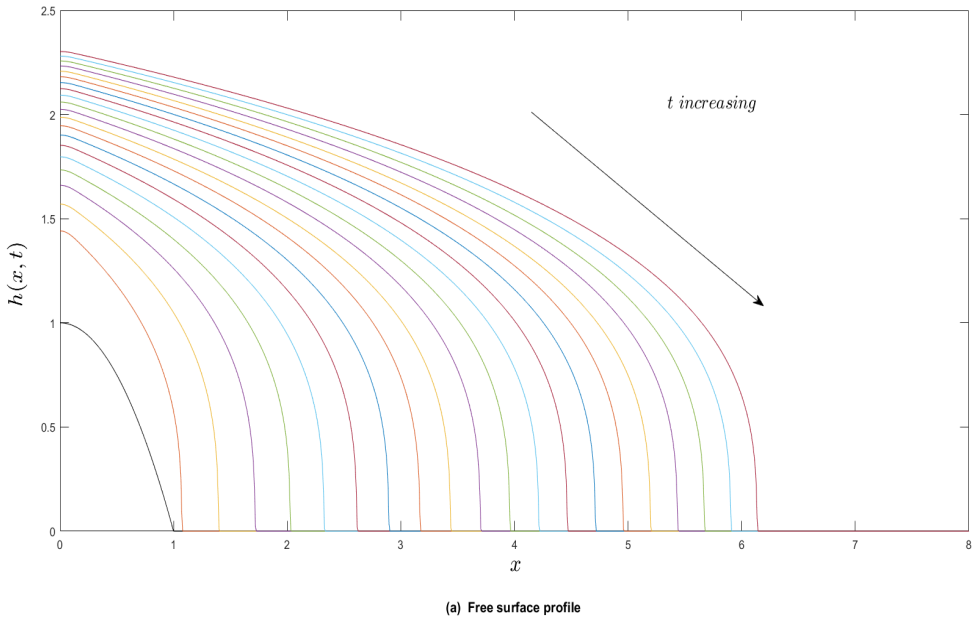

Figure 4.11: The evolution of $h(x,t)$ with an influx flowrate, $Q_{s_0} = 7$, for t varying between $t = 0-20$ corresponding to the isothermal constant volume case with $\mu(\theta) = 1$. The parameter values are: $S = 0$, $\alpha = 0$ and $\theta_s = 0$.

noticeable cooling near the front and We also observe steepening near the front (Fig. 4.12(a)). Decreasing Pe to 10^2, we observe that the cooling is now more distributed over the entire dome length rather than localised at the front (Fig. 4.13(b)). We note that $\theta = 1$ always at the source $x = 0$ since the temperature here is always at the eruption temperature $T_e^\star$. Consequently, the free surface shape now looks more like a dome with not as much pronounced steepening near the front (Fig. 4.13(a)). Lowering Pe further (not shown here) would increase the cooling even further over the length of the dome resulting in the evolution of the dome approaching the isothermal case corresponding to $\mu = 1$ or $\theta = 0$. In Fig. 4.14, we show the evolution of the location of the leading edge of the dome, x_N (Fig. 4.14(a)) and the dome height at its centre, $h_N = h(0,t)$ (Fig. 4.14(b)), for varying Péclet number Pe between $0.1 \leq Pe \leq 10^4$

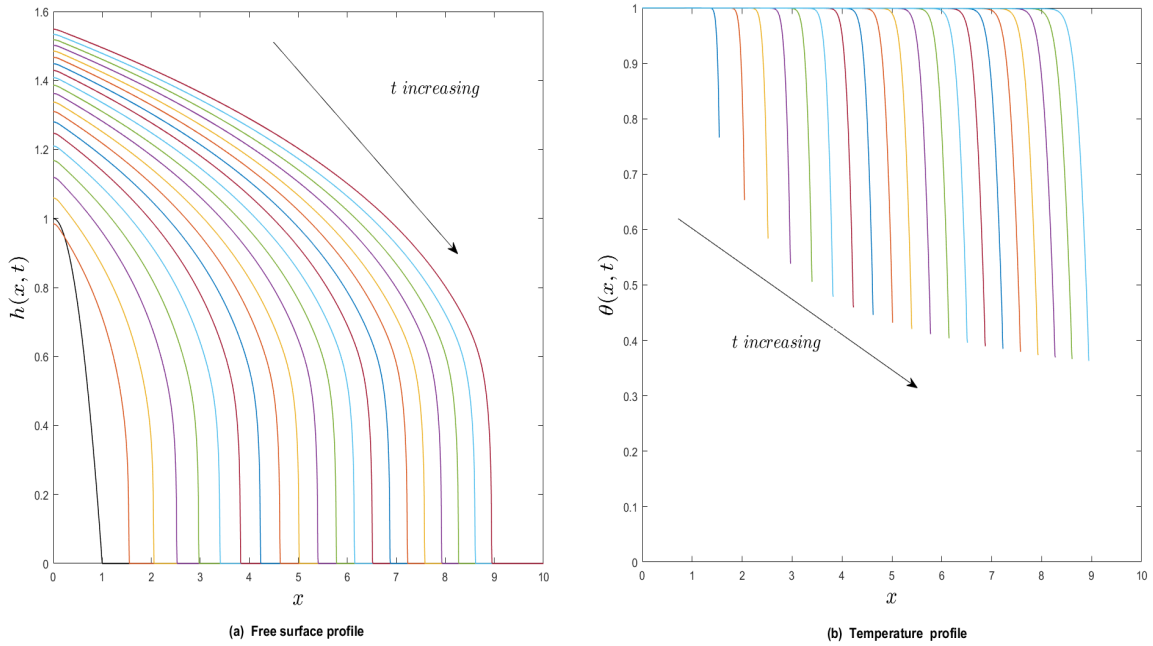

Figure 4.12: The evolution of (a) $h(x,t)$ and (b) $\theta(x,t)$ with an influx flowrate, $Q_{s_0} = 5$, for t varying between $t = 0 - 20$ with $Pe = 10^4$, $\alpha = 2$, $\theta_s = 0$, $a = 1$ and $b = 2$.

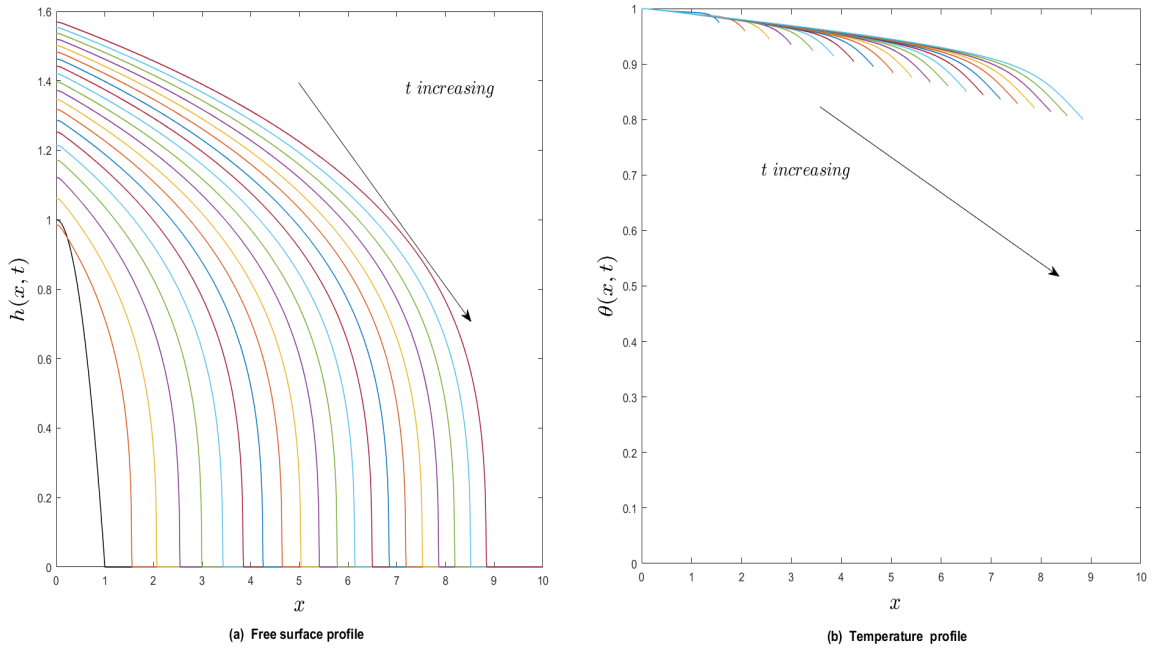

Figure 4.13: The evolution of (a) $h(x,t)$ and (b) $\theta(x,t)$ with an influx flowrate, $Q_{s_0} = 7$, for t varying between $t = 0 - 20$ with $Pe = 10^2$, $\alpha = 2$, $\theta_s = 0$, $a = 1$ and $b = 2$.

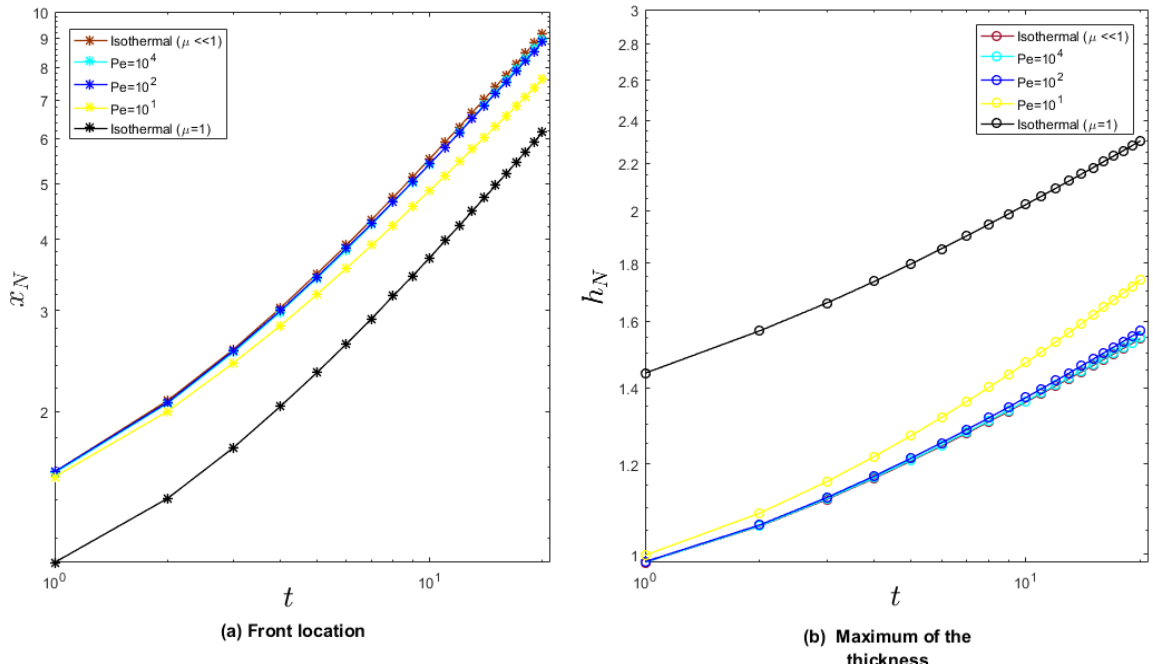

Figure 4.14: The (a) leading edge of the front, x_N, and (b) the maximum in h, $h_N = h(0,t)$, as a function of time, t, for various Péclet number, Pe. The parameter values are: $\alpha = 2$, $Q_{s_0} = 7$, $\theta_s = 0$, $a = 1$ and $b = 2$.

with $Q_{s_0} = 7$, $a = 1$ and $b = 2$ and $\alpha = 2$. The same trends hold as before, except that the spreading rates are much higher due to the additional flowrate from the source and monotonically approach the $Pe \to \infty$ limit as Pe increases (unlike the previous cases). The dome height at the centre also increases due to the flowrate from the source and is now bounded above by the isothermal limit (unlike the previous cases where h_N was bounded below by the isothermal limit). The results also appear to be not sensitive to changes in Pe suggesting that the flow behaviour is primarily driven by the source flowrate, at least for the value of $Q_{s_0} = 5$ used here. Figures 4.15, 4.16 show $h(x,t)$ and $\theta(x,t)$ for a lower source flowrate $Q_{s_0} = 0.65$ for $Pe = 10^4$ and $Pe = 10^2$, respectively, with $\alpha = 6$, $a = 0.2$ and $b = 0.3$ and $t = 0 - 20$. The source flowrate is not strong enough to expand the dome over its initial shape as in the previous case. Fig.

4.15(a) shows the development of a front with a lengthening plateau behind while Fig. 4.16(a)) shows a spreading dome getting steeper at its leading edge. The temperature profiles are similar to the earlier scenarios with more localised cooling for higher Péclet numbers and at low Péclet numbers, the cooling is more distributed over the length of the dome.

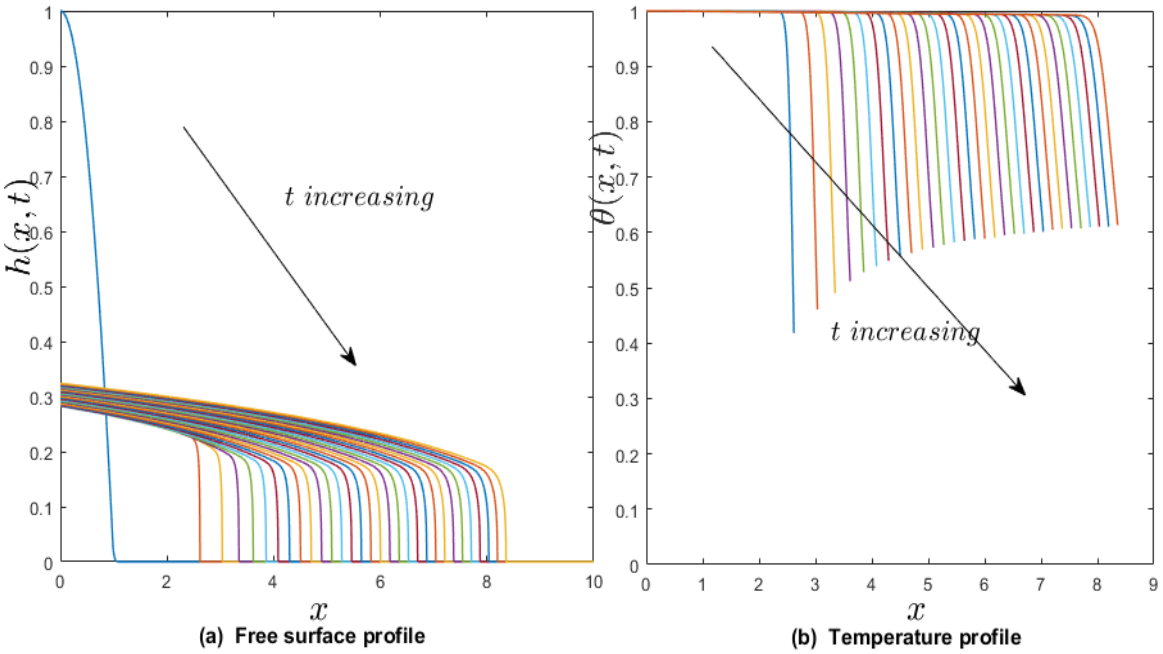

Figure 4.15: The evolution of (a) $h(x,t)$ and (b) $\theta(x,t)$ with an influx flowrate, $Q_{s_0} = 0.65$, for t varying between $t = 0 - 20$ with $Pe = 10^4$, $\alpha = 6$, $\theta_s = 0$, $a = 0.2$ and $b = 0.3$.

We next consider the results for $S = 1$ (plane inclined at angle of approximately 6^o) and $Q_{s_0} = 0$ (constant volume drop) using the exponential decay viscosity model. Figure 4.17 shows the evolution of $h(x,t)$ with $\alpha = 0$ corresponding to the isothermal case with $\mu(\theta) = 1$. This isothermal case is also obtained in the limit of $Pe \to 0$. The time range shown is for $0 \leq t \leq 30$. This case is equivalent to the fluid being at the ambient

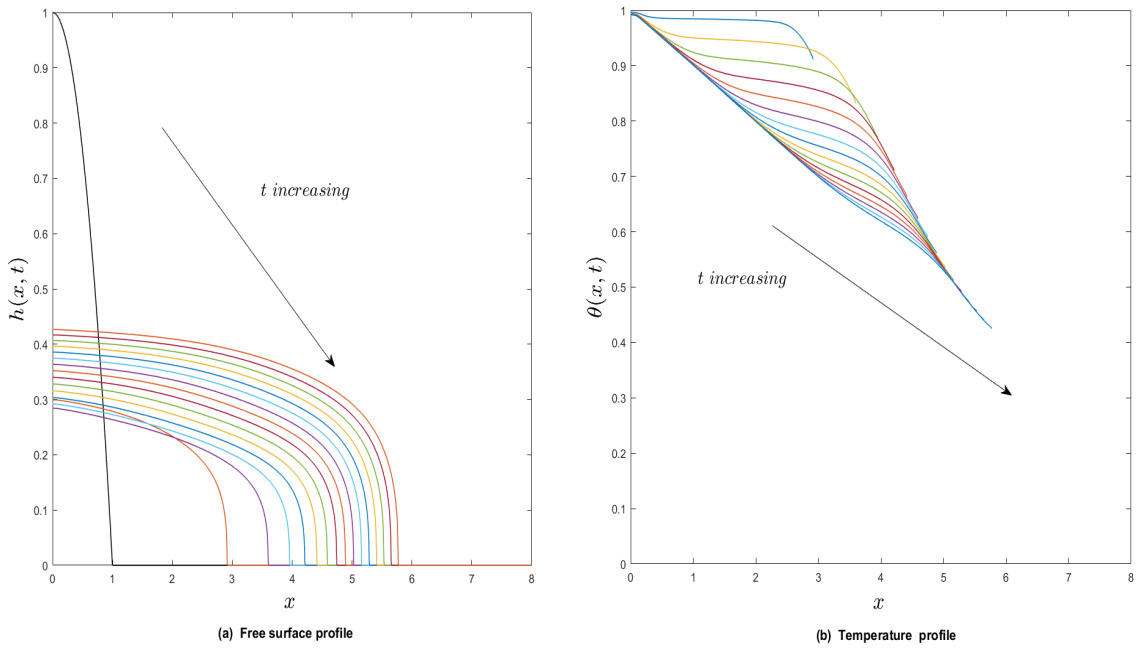

Figure 4.16: The evolution of (a) $h(x,t)$ and (b) $\theta(x,t)$ with an influx flowrate, $Q_{s_0} = 0.65$, for t varying between $t = 0 - 20$ with $Pe = 10^2$, $\alpha = 6$, $\theta_s = 0$, $a = 0.2$ and $b = 0.3$.

temperature $\theta = 0$. We observe that the spreading is non-symmetric about $x = 0$ and the dome slumps as it spreads with a steep front at its leading edge as described in Chapter 2. As $Pe \to 0$, the cooling is significant over the entire domain resulting in the temperature quickly dropping to its equilibrium value, $\theta = 0$ (or $T^\star = T_a^\star$) and the evolution of $h(x,t)$ is similar to that of isothermal spreading with $\mu(\theta) = 1$. This can be clearly seen in Fig. 4.18(b) with $P_e = 1$, $\alpha = 2$, $a = 0.2$ and $b = 0.3$ where the temperature drops very quickly from its initial condition, $\theta = 1$, to zero everywhere due to significant cooling to the surroundings. The corresponding evolution of $h(x,t)$ is shown in Fig. 4.18(a) which is similar to Fig. 4.17. The cooling is much less rapid as the Péclet number is increased (see Fig. 4.19(b) for $Pe = 10$). This cooling is more pronounced near the leading edge of the advancing front and the trailing edge

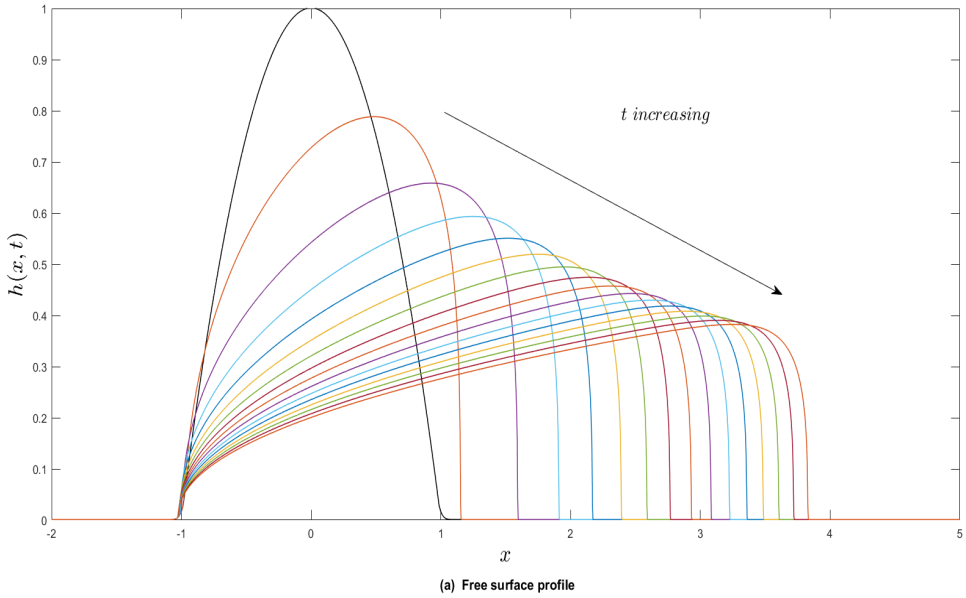

Figure 4.17: The evolution of $h(x,t)$ for t varying between $t = 0 - 30$ corresponding to the isothermal constant volume case with $\mu(\theta) = 1$. The parameter values are: $S = 1$ (approximately 6^o inclination), $\alpha = 0$, $Q_{s_0} = 0$ and $\theta_s = 0$.

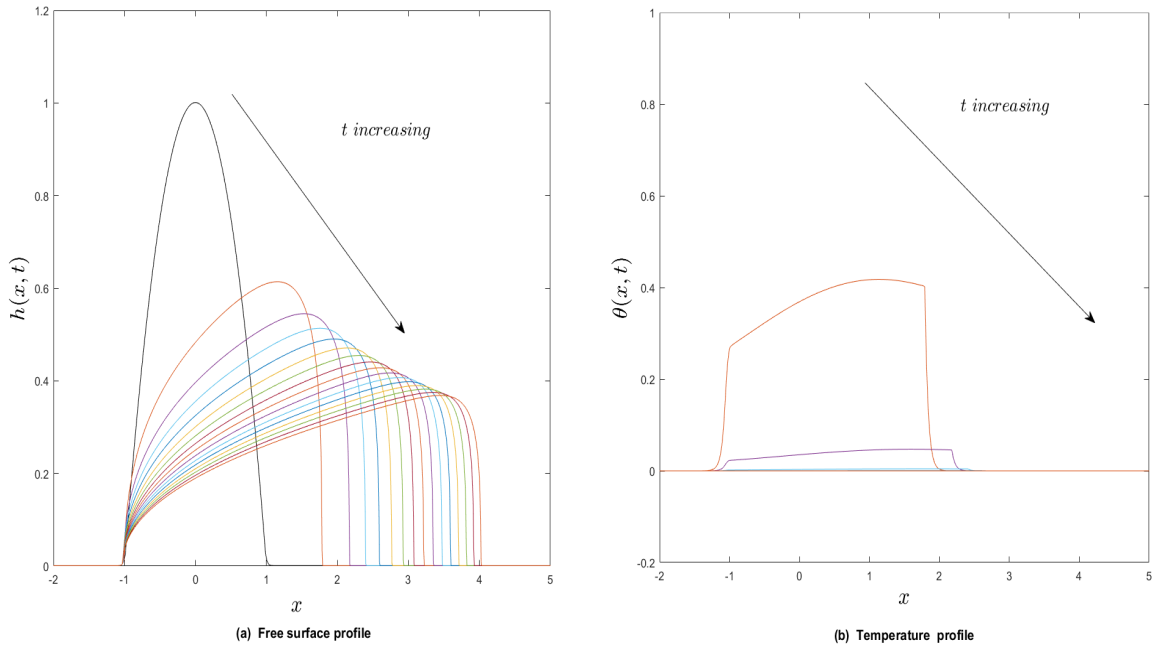

Figure 4.18: The evolution of (a) $h(x,t)$ and (b) $\theta(x,t)$ for t varying between $t = 0 - 30$ with $Pe = 1$, $\alpha = 2$, $Q_{s_0} = 0$, $\theta_s = 0$, $a = 0.2$ and $b = 0.3$.

of the dome where h is small, compared to elsewhere. This is due to the rate of heat loss being inversely proportional to h (see second term on the right-hand-side of Eq. (4.16b). Figure 4.19(b) shows the gradual decrease in the temperature to its equilibrium value, $\theta = 0$, over the entire domain. The resulting increase in the liquid viscosity is not as rapid as in the previous case so that the liquid in the dome is more mobile and the spreading is faster than before (see Figure 4.19(a)). Increasing the Péclet number,

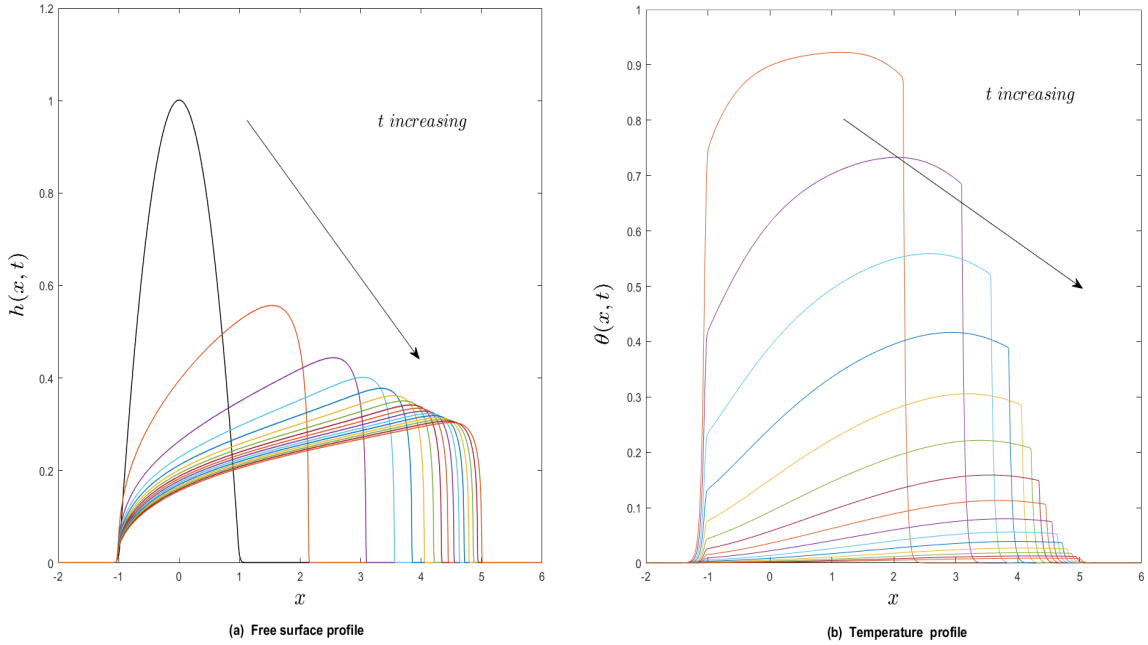

Figure 4.19: The evolution of (a) $h(x,t)$ and (b) $\theta(x,t)$ for t varying between $t = 0-30$ with $Pe = 10$, $\alpha = 2$, $Q_{s_0} = 0$, $\theta_s = 0$, $a = 0.2$ and $b = 0.3$.

further reduces the cooling (see Fig. 4.20(b) for evolution of $\theta(x,t)$ with $Pe = 10^3$). The cooling is now more localised near the dome's edges and in the bulk of the drop the cooling is comparatively much lower. This in turn decreases the viscosity resulting in faster spreading (see Fig. 4.20(a) for evolution of $h(x,t)$ with $Pe = 10^3$). We start to see the formation of a characteristic fluid *hump*-like structure developing near the

dome's leading edge as it spreads over the inclined plane (Fig. 4.20(a)). This is due to the strong temperature contrast near the leading edge during the spreading process (Fig. 4.20(b)). The temperature behind the leading edge is much higher than that ahead; the increase in mobility due to the reduced liquid viscosity results in the hotter liquid piling-up over the relatively colder liquid ahead of it resulting in the development of the hump in the free surface shape near the leading edge. At earlier time, this hump has not yet developed because the temperature contrast is not sufficiently strong for the above mechanism to apply. As time progresses, the temperature contrast starts getting stronger and we observe the gradual development of this fluid hump. Increasing

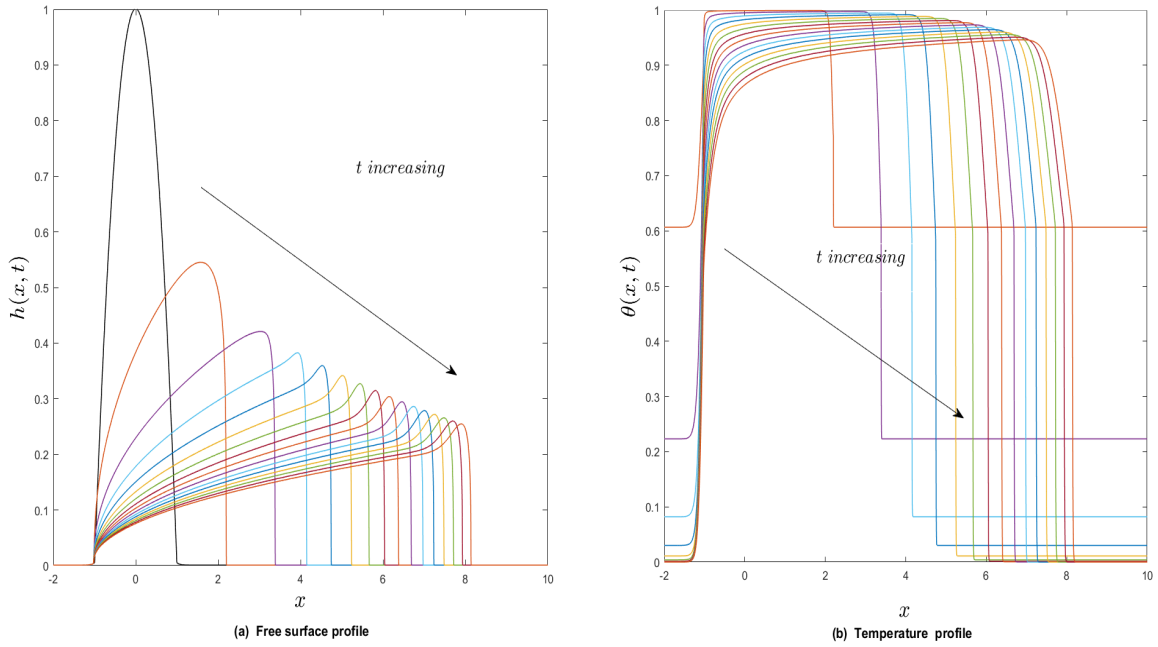

Figure 4.20: The evolution of (a) $h(x,t)$ and (b) $\theta(x,t)$ for t varying between $t = 0-30$ with $Pe = 10^3$, $\alpha = 2$, $Q_{s_0} = 0$, $\theta_s = 0$, $a = 0.2$ and $b = 0.3$.

the Péclet number to $Pe = 10^4$, we still observe the development of the fluid hump (Fig. 4.21(a)) near the leading edge. We note here that it takes much longer for

the temperature contrast there to become sufficiently strong compared to the earlier case, hence the delay in the development of the fluid hump (compare Fig. 4.21(a) for $Pe = 10^4$ with Fig. 4.20(a) for $Pe = 10^3$). We also note that the size of the fluid hump is larger than the earlier case for $Pe = 10^3$. The hot liquid in the hump region is at a higher temperature ($\theta = 1$) compared to the earlier case making its viscosity relatively smaller, hence more mobile which results in a larger hump. In Fig. 4.22, we

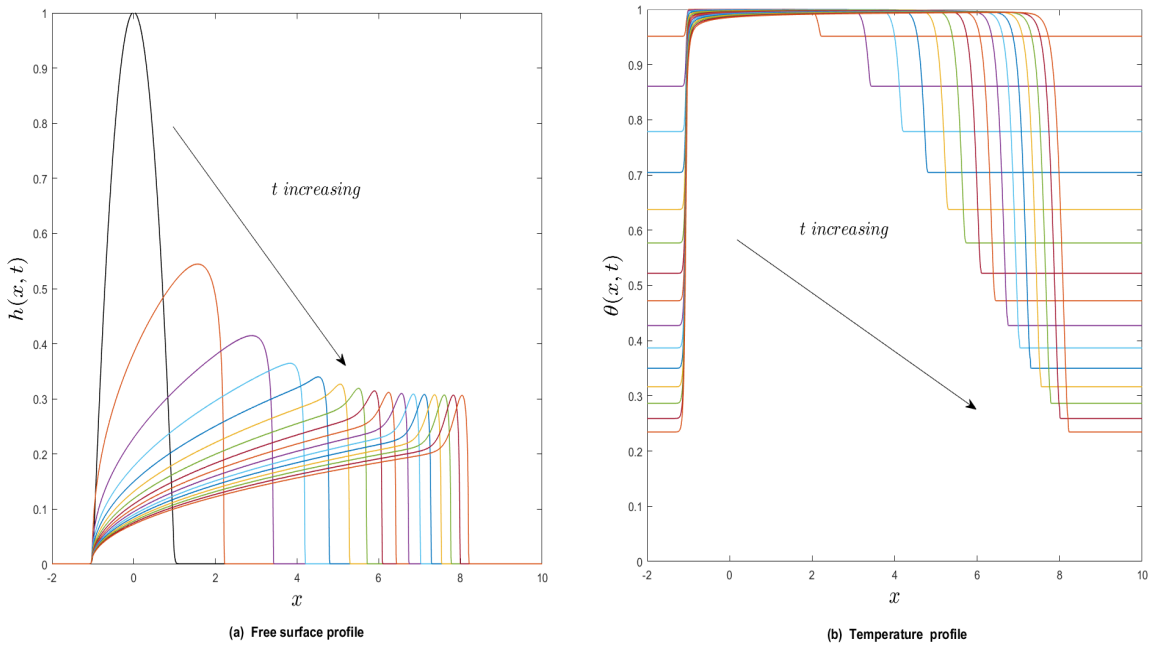

Figure 4.21: The evolution of (a) $h(x,t)$ and (b) $\theta(x,t)$ for t varying between $t = 0-30$ with $Pe = 10^4$, $\alpha = 2$, $Q_{s_0} = 0$, $\theta_s = 0$, $a = 0.2$ and $b = 0.3$.

show the evolution of the location of the leading edge of the dome, x_N (Fig. 4.22(a)) and the dome height at its leading edge, $h_N = h(x_N, t)$ (Fig. 4.22(b)), for varying Péclet number Pe between $0.01 \leq Pe \leq 10^4$. We observe that the results are bounded above and below by the two isothermal cases corresponding to $Pe \to \infty$ and $Pe \to 0$, respectively. For $\mu = e^{-2}$, we can confirm that $x_N \sim t^{1/3}$ and $h_N \sim t^{-1/3}$ which is

in agreement with the spreading rates and similarity solution derived in Eq. (2.46) in §2.3 of Chapter 2.

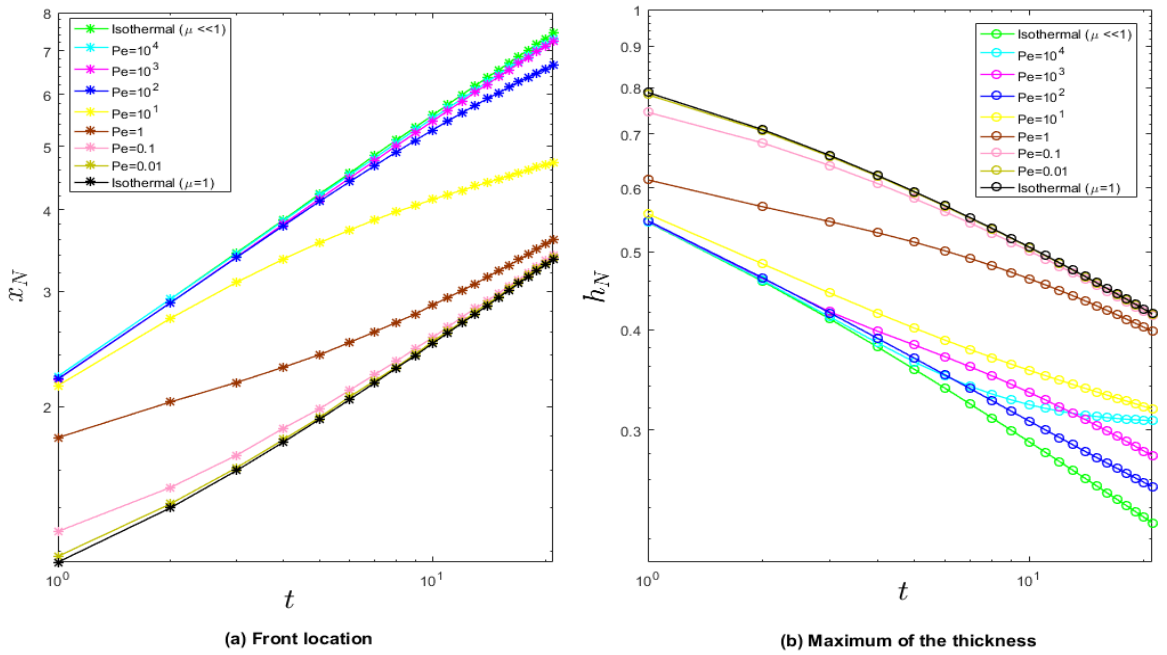

Figure 4.22: The (a) leading edge of the front, x_N, and (b) the maximum in h (i.e., height of the front), $h_N = h(x_N, t)$, as a function of time, t, for various Péclet number, Pe. The parameter values are: $\alpha = 2$, $Q_{s_0} = 0$, $\theta_s = 0$, $a = 0.2$ and $b = 0.3$.

Fig. 4.23 shows the evolution of $h(x,t)$ and $\theta(x,t)$ using the same parameter values as in Fig. 4.20, except α is increased from $\alpha = 2$ to $\alpha = 6.5$ and $Pe = 10^3$. The temperature profile (Fig. 4.23(b)) is similar that shown in Fig. 4.20(b). Although the range in temperature in both cases are similar, the larger α gives a lower viscosity at higher temperatures resulting in more mobility, hence increased spreading rate. For the same reason, we also observe that the fluid hump at the leading edge (Fig. 4.23(a)) is much bigger than that shown in Fig. 4.20(a). This is again due to the much hotter liquid in the hump being more mobile than the colder liquid in front, resulting in the

liquid piling-up behind the front. Figure 4.24(a, b) show the evolution of $h(x, t)$ and

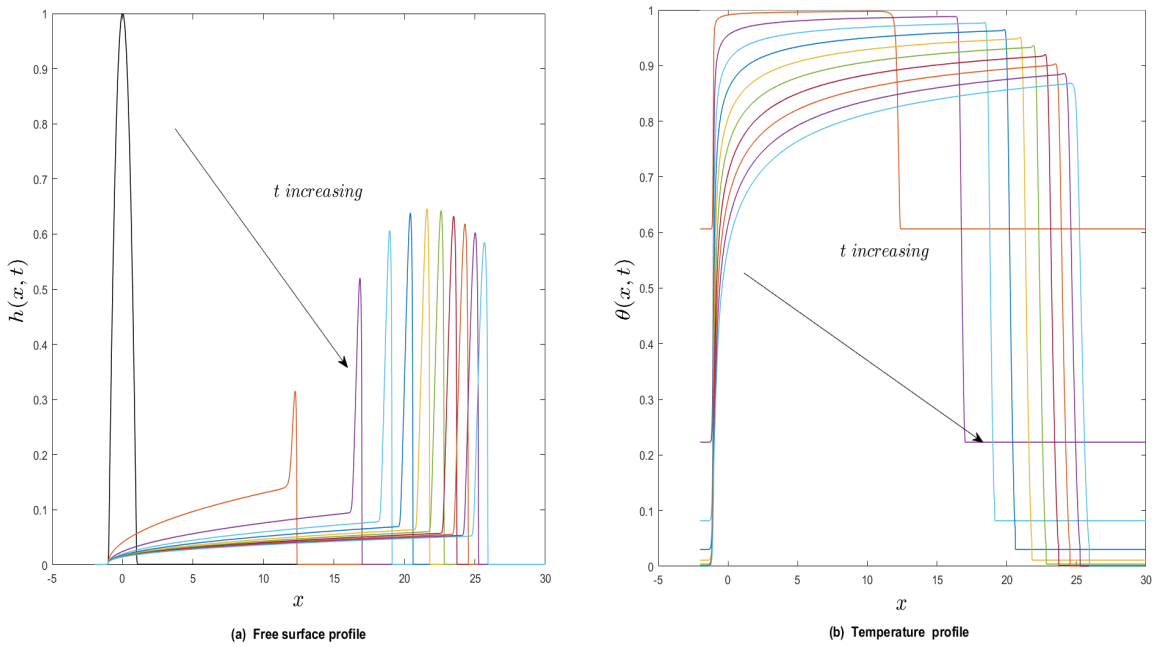

Figure 4.23: The evolution of (a) $h(x, t)$ and (b) $\theta(x, t)$ for t varying between $t = 0 - 30$ with $Pe = 10^3$, $\alpha = 6.5$, $Q_{s_0} = 0$, $\theta_s = 0$, $a = 0.2$ and $b = 0.3$.

$\theta(x, t)$, respectively, for $Pe = 10^4$, $\alpha = 2$ and $a = 0.02$ and $b = 0.03$ for time varying between $t = 0 - 30$. There is minimal heat loss or cooling within the bulk liquid with significant cooling confined to the leading and trailing edges of the spreading dome (Fig. 4.24(b)). The spreading is close to isothermal with $\mu = \mu_e = e^{-2}$ or $\theta = 1$ (Fig. 4.24(a)). Figure 4.24(c, d) show the evolution of $h(x, t)$ and $\theta(x, t)$, respectively, for the same parameters as above, except $a = 5$ and $b = 10$. The cooling is much more pronounced near the edges for these higher values of the heat transfer coefficients while the bulk liquid is at a much higher temperature (Fig. 4.24(c)). This results in a strong temperature gradient leading to the formation and development of a liquid hump near the leading edge (Fig. 4.24(a)) which is very similar to that observed in Fig.

4.21(a). Fig. 4.25 is a parameter survey in $(a = b, Pe)$ space with $\alpha = 2$ and $S = 1$

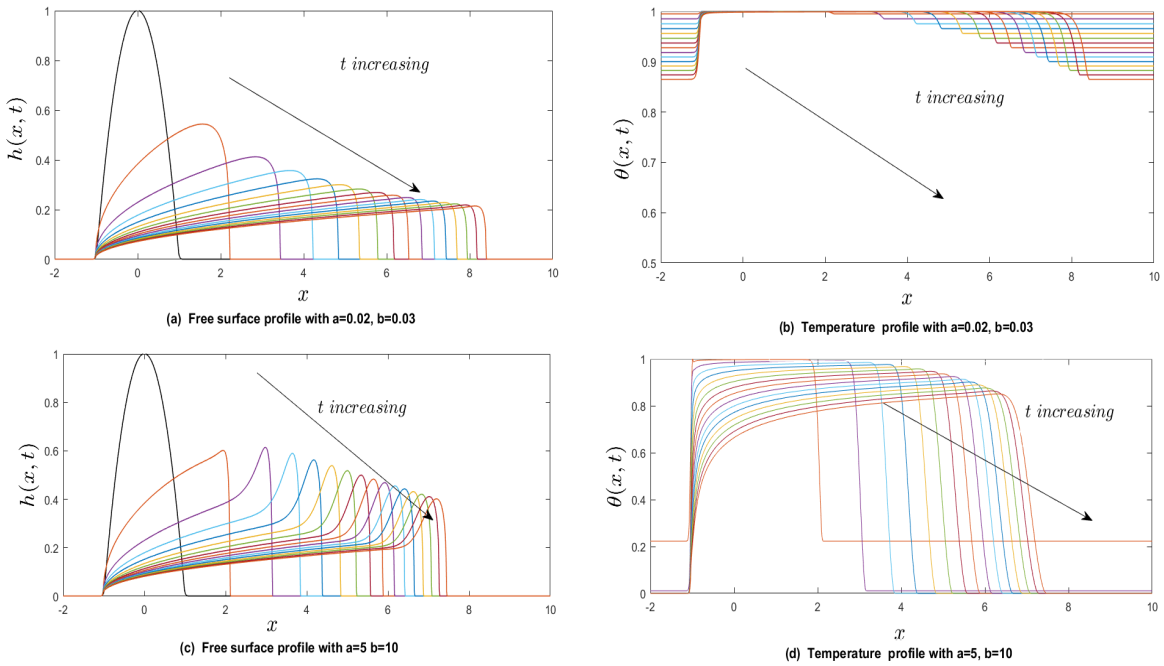

Figure 4.24: The evolution of (a) $h(x,t)$ and (b) $\theta(x,t)$ for t varying between $t = 0-30$ with $a = 0.02$ and $b = 0.03$ and (c) $h(x,t)$ and (d) $\theta(x,t)$ with $a = 5$, $b = 10$. The other parameter values are: $Pe = 10^2$, $\alpha = 2$, $Q_{s_0} = 0$ and $\theta_s = 0$.

(inclination angle approximately 6^o) to show the existence of free surface shapes, $h(x,t)$ with and without a fluid hump near the leading edge. If we were to extend the above investigation in two-dimensional $(a = b, Pe)$ space to three-dimensional $(a = b, Pe, \alpha)$ space, we would speculate that the regions of humps would expand as α increases. We also speculate that the height of the fluid hump would get bigger as α increases (e.g., see Fig. 4.23 for $\alpha = 6.5$). This is due to the liquid viscosity difference between the hotter bulk liquid behind the front and the colder liquid at the front being even more enhanced for larger values of α.

We now consider the effects of an influx of liquid from a source or vent with flowrate,

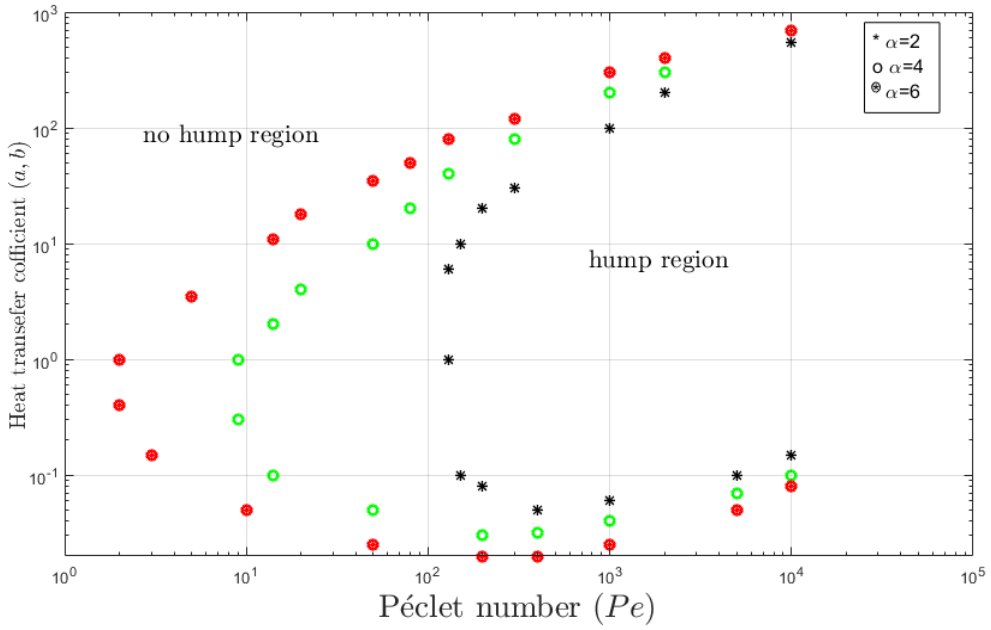

Figure 4.25: Parameter survey in $(Pe, a = b, \alpha)$ space to show existence of free surface shapes, $h(x,t)$ with and without a fluid hump (or ridge). The parameter values are: $\alpha = 2, 4, 6$ and $S = 1$ (inclination angle approximately 6^o).

$Q_{s_0} = 7$. Figure 4.26 shows the constant viscosity case, $\mu = 1$ (corresponding to $\alpha = 0$) for $t = 0 - 20$. The strength of the source is sufficiently strong to drive both the spreading of the dome as well as building-up of liquid around the vent over the initial dome shape. These results show a good agreement with those in Chapter 2. Figure 4.27(a, b) show the evolution of $h(x,t)$ and $\theta(x,t)$ for $Pe = 10^4$. The source flowrate is $Q_{s_0} = 7$ and the heat transfer coefficients are $a = 0.2$ and $b = 0.3$. Localised cooling is observed near the front's leading edge. The strong temperature contrast near the leading edge and the constant flowrate provided by the source results in the free surface profile developing a fluid hump at it's leading edge which increases in size as time progresses (see Fig. 4.27(a)). Figure 4.28(a, b) show the evolution of $h(x,t)$ and $\theta(x,t)$ for $Pe = 10^2$. The source flowrate is $Q_{s_0} = 7$ and the heat transfer coefficients

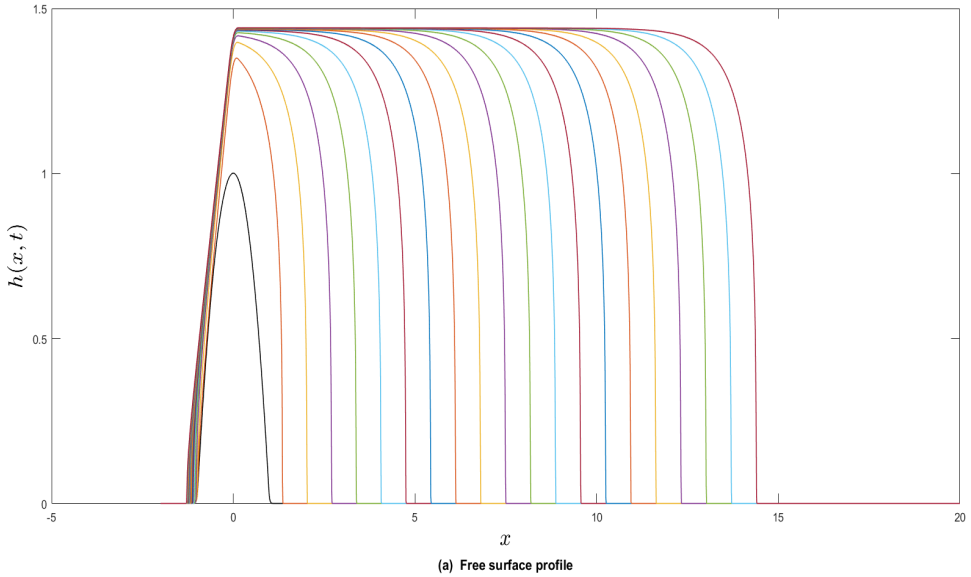

Figure 4.26: The evolution of $h(x,t)$ with an influx flowrate, $Q_{s_0} = 7$, for t varying between $t = 0-20$ corresponding to the isothermal constant volume case with $\mu(\theta) = 1$. The parameter values are: $S = 1$, $\alpha = 0$ and $\theta_s = 0$.

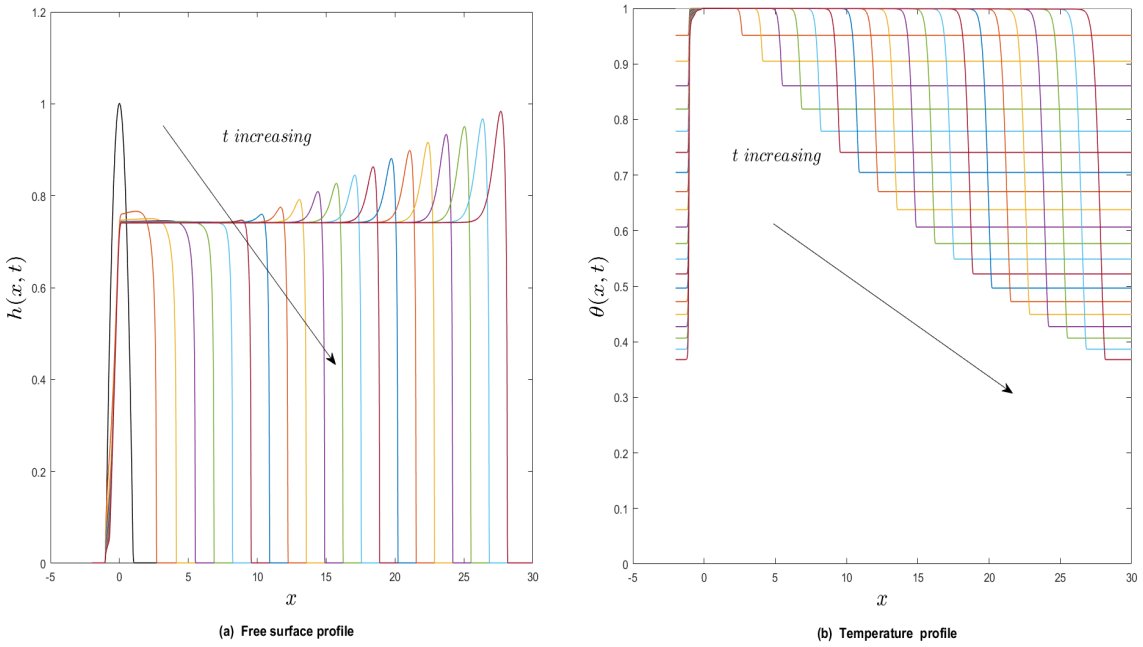

Figure 4.27: The evolution of (a) $h(x,t)$ and (b) $\theta(x,t)$ with an influx flowrate, $Q_{s_0} = 7$, for t varying between $t = 0 - 20$ with $Pe = 10^4$, $\alpha = 2$, $\theta_s = 0$, $a = 0.2$ and $b = 0.3$.

are $a = 0.2$ and $b = 0.3$. There is much more significant localised cooling near the front's leading edge compared to the earlier two cases. There is some cooling observed in the bulk liquid too (Fig. 4.28(b)). The strong temperature gradient results in the development of a fluid hump near the front's leading edge which also grows as time progresses (Fig. 4.28(a)). Figure 4.29(a, b) show the evolution of $h(x,t)$ and $\theta(x,t)$

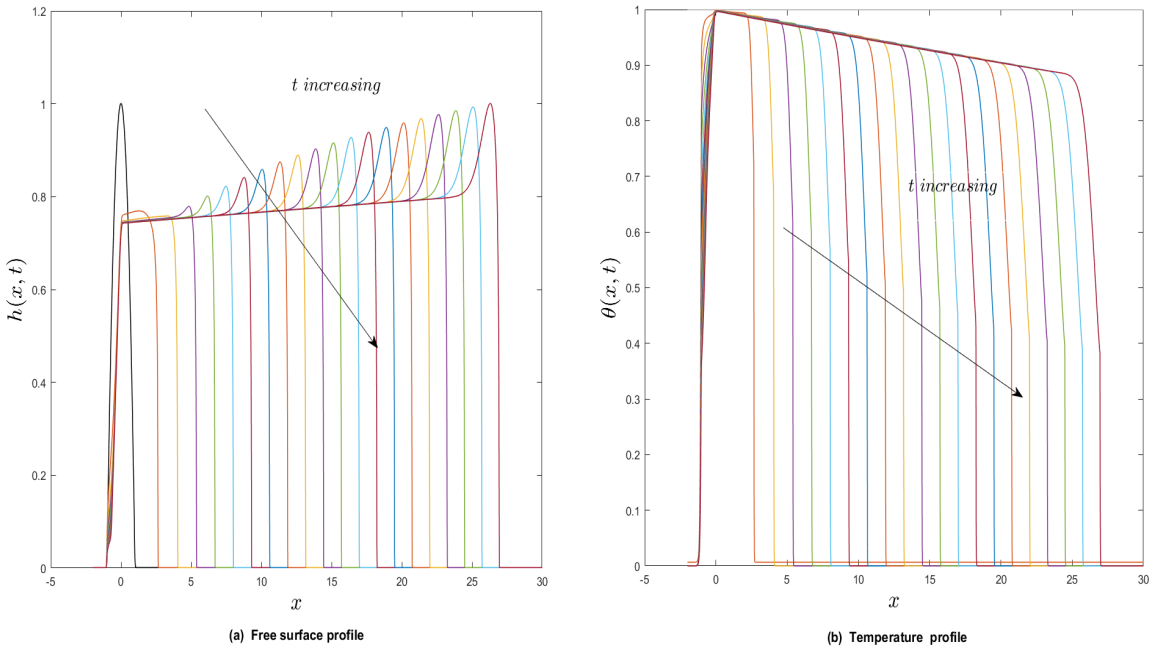

Figure 4.28: The evolution of (a) $h(x,t)$ and (b) $\theta(x,t)$ with an influx flowrate, $Q_{s_0} = 7$, for t varying between $t = 0 - 20$ with $Pe = 10^2$, $\alpha = 2$, $\theta_s = 0$, $a = 0.2$ and $b = 0.3$.

for $Pe = 10$. The source flowrate is $Q_{s_0} = 7$ and the heat transfer coefficients are $a = 0.2$ and $b = 0.3$. Similar to the earlier cases, there is significant cooling localised around the front's leading and trailing edges. The temperature in the bulk liquid is non-uniform decreasing from the vent towards the leading edge (Fig. 4.29(b)). This is unlike the earlier cases where the bulk liquid is almost uniform and at the vent temperature, $\theta = 1$. The resultant difference in viscosity and hence the mobility leads

to an almost linear increase in the front height from the vent to it's leading edge (Fig. 4.29(a)). Decreasing the Péclet number further (results not shown here) would result

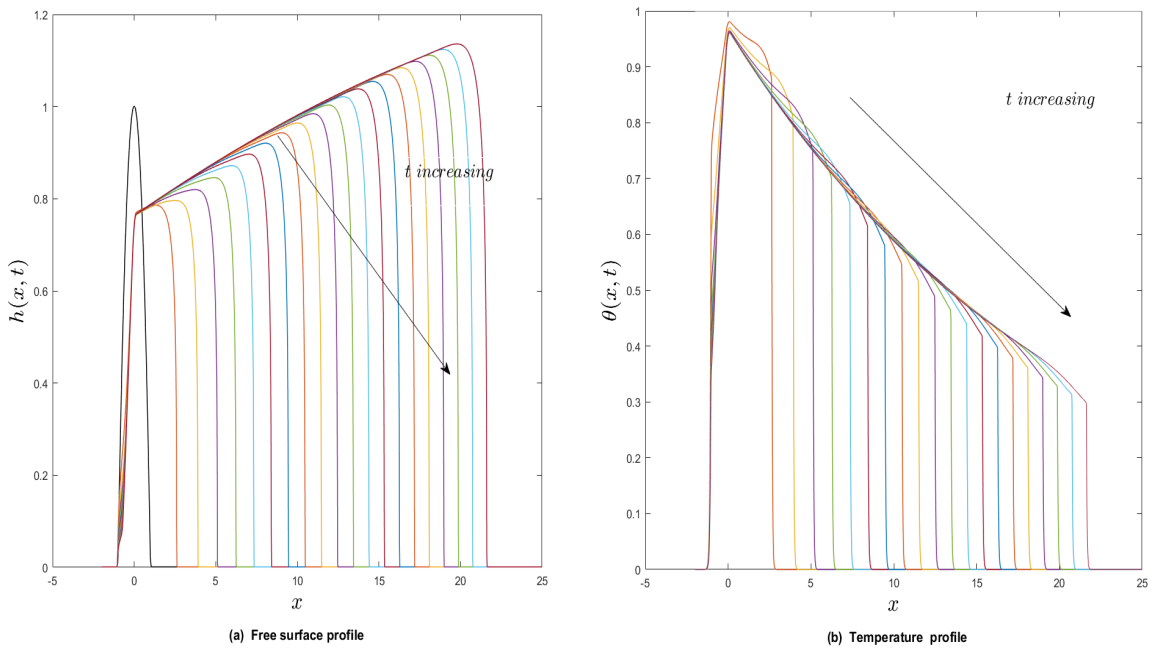

Figure 4.29: The evolution of (a) $h(x,t)$ and (b) $\theta(x,t)$ with an influx flowrate, $Q_{s_0} = 7$, for t varying between $t = 0 - 20$ with $Pe = 10$, $\alpha = 2$, $\theta_s = 0$, $a = 0.2$ and $b = 0.3$.

in the temperature over most of the front to be at the ambient temperature, $\theta = 0$, except around the vent where $\theta = 1$. This would lead to the front having an almost uniform height which would be similar to the isothermal case as $Pe \to 0$ or $\theta = 0$ (see isothermal case in Fig. 4.30(b) for the height at the front, h_N, which stays almost constant over time). Figure 4.30(a, b) show the evolution of the location of the leading edge of the front, x_N (Fig. 4.30(a)) and the maximum height of the front, $h_N = h(x_N, t)$ (Fig. 4.30(b)), for varying Péclet number Pe between $10 \leq Pe \leq 10^4$ with $Q_{s_0} = 7$, $a = 0.2$ and $b = 0.3$ and $\alpha = 2$. The same trends hold as before and the evolution of x_N and h_N is bounded above and below by the isothermal cases corresponding to

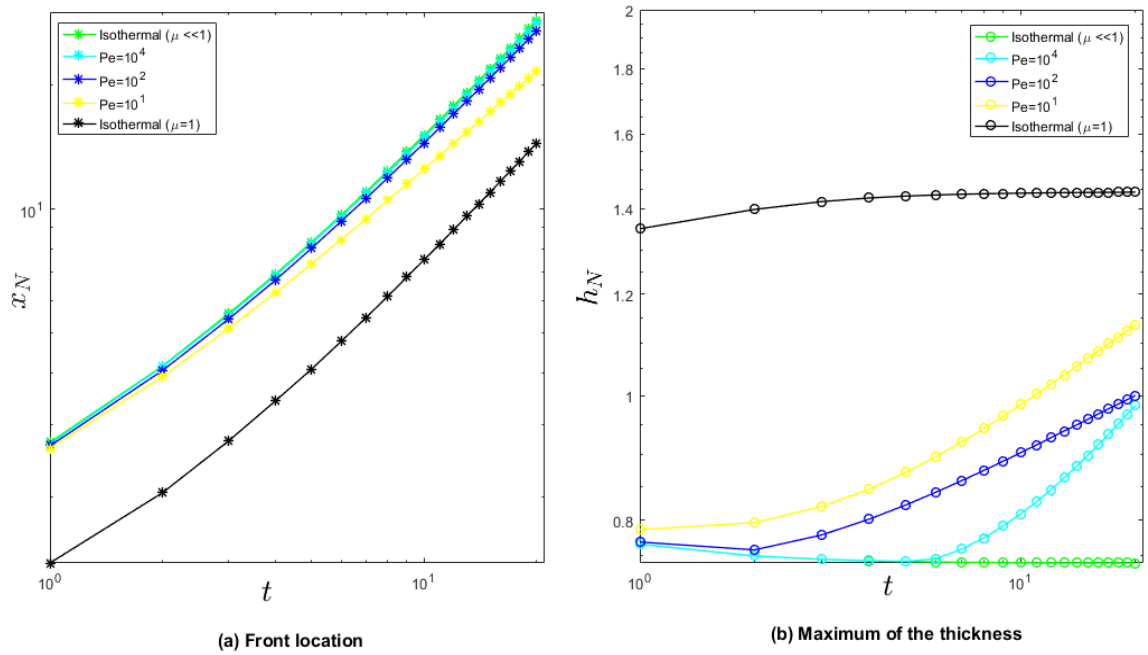

Figure 4.30: The (a) leading edge of the front, x_N, and (b) the maximum in h (i.e., height of the front), $h_N = h(x_N, t)$, as a function of time, t, for various Péclet number, Pe. The parameter values are: $\alpha = 2$, $Q_{s_0} = 7$, $\theta_s = 0$, $a = 0.2$ and $b = 0.3$.

either $Pe \to 0$ or $Pe \to \infty$.

We now present some numerical results using the bi-viscosity model given by Eq. (4.17b). We set μ_a=1, $\mu_e < \mu_a = 10^{-2}$ and $\theta_m = 0.5$ (note: $0 < \theta_m < 1$). We set $\mu_e = 0.01$ to obtain a large viscosity ratio between the region with the temperature less than θ_m and that with θ greater than θ_m. The initial temperature of the dome is $\theta = 1$. We only show selected numerical results where the free surface evolution using the bi-viscosity model is structurally different from the previous results using the exponential viscosity model, keeping all other parameters the same. In Fig. 4.31 for spreading on a horizontal plane, the results with $Pe = 10^4$ gives a free surface profile with a much steeper flow front and an almost flat plateau region behind it (Fig. 4.31(a)) compared

to that with the exponential viscosity model (see Fig. 4.4(a) with the same Péclet number). This is due to the sharp increase in viscosity near the front's leading edge where $\theta \leq \theta_m = 0.5$ (Fig. 4.31(b)). The temperature profiles (Fig. 4.31(b)) are similar to the previous profile using the exponential viscosity model with the same Péclet number (see Fig. 4.4(a)). Increasing $\theta_m = 0.9$ (keeping all other parameters fixed as in

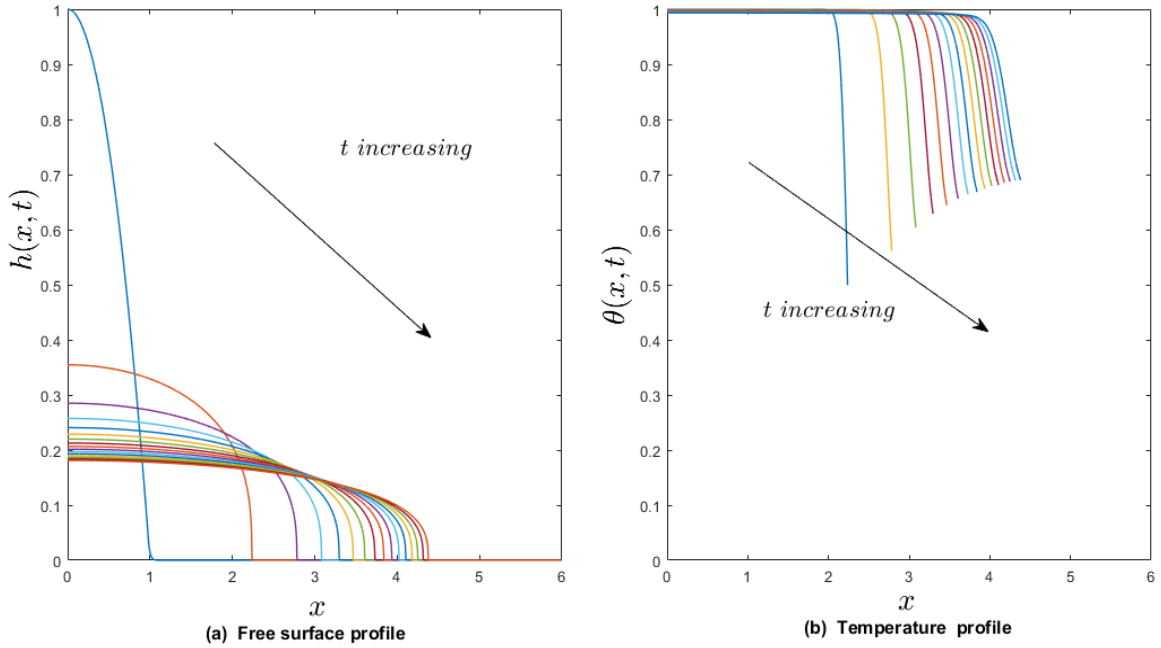

Figure 4.31: The evolution of (a) $h(x,t)$ and (b) $\theta(x,t)$ for t varying between $t = 0-30$ using the bi-viscosity model with $S = 0$, $Pe = 10^4$, $Q_{s_0} = 0$, $\theta_s = 0$, $a = 0.2$, $b = 0.3$, $\mu_a = 10^{-2}$ and $\theta_m = 0.5$.

the previous case), shows similar evolution of $h(x,t)$ but the spreading is considerably slower (compare Figs. 4.32(a) and 4.31(a)). The temperature profile (Fig. 4.32(b)) although shows less cooling near the leading edge of the front compared to the one above (see Fig. 4.31(b)), the viscosity is much higher there for $\theta < \theta_m = 0.9$ resulting in the slower spreading rate of the front, in this case. The next figure considers the evolution of $h(x,t)$ and $\theta(x,t)$ over a horizontal plane including the flowrate from the

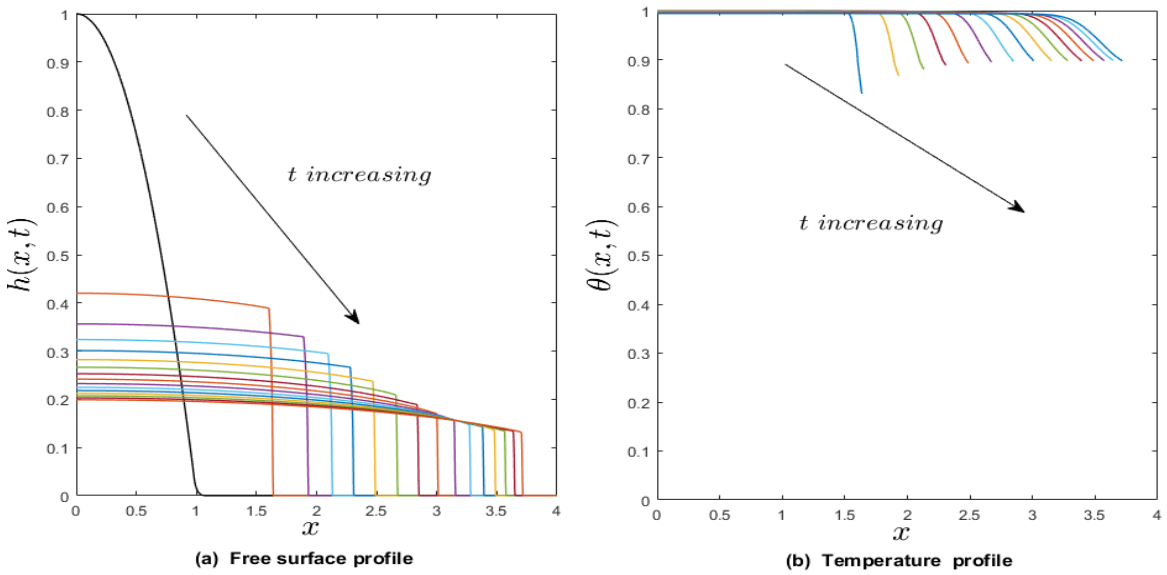

Figure 4.32: The evolution of (a) $h(x,t)$ and (b) $\theta(x,t)$ for t varying between $t = 0-30$ using the bi-viscosity model with $S = 0$, $Pe = 10^4$, $Q_{s_0} = 0$, $\theta_s = 0$, $a = 0.2$, $b = 0.3$, $\mu_a = 10^{-2}$ and $\theta_m = 0.9$.

source using the bi-viscosity model. Figure 4.33(a) shows enhanced spreading compared to the equivalent case using the exponential viscosity model (see, e.g., Fig 4.12(a) for $Pe = 10^4$). The leading edge of the front is also much steeper and the free surface much sharper. The temperature profile although similar to those using the exponential viscosity model (see, e.g., Fig 4.12(b) for $Pe = 10^4$), the viscosity near the leading edge is much lower there for $\theta < \theta_m = 0.5$ resulting in the enhanced spreading rate and the sharper feature, in this case. Figure 4.34(a, b) considers the evolution of $h(x,t)$ and $\theta(x,t)$ for spreading over an inclined plane, with $Pe = 10^4$, $\mu_e = 10^{-2}$ and $\theta_m = 0.5$. Fig. 4.34(a) shows the free surface profile with the development of the fluid hump only at much later times. This is in contrast to that shown previously in Fig. 4.21(a) where the fluid hump starts developing much earlier. This is explained from the temperature profile shown in Fig. 4.34(b). $\theta \geq \theta_m = 0.5$ for much of the early times, so the viscosity

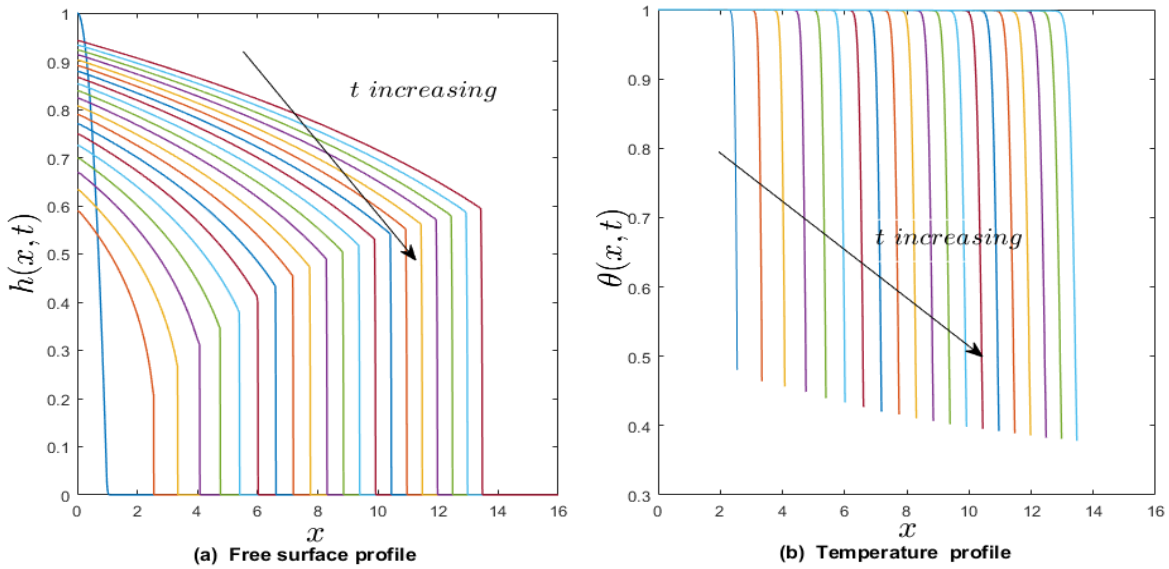

Figure 4.33: The evolution of (a) $h(x,t)$ and (b) $\theta(x,t)$ for t varying between $t = 0-30$ using the bi-viscosity model with $S = 0$, $Pe = 10^4$, $Q_{s_0} = 7$, $\theta_s = 0$, $a = 0.2$, $b = 0.3$, $\mu_a = 10^{-2}$ and $\theta_m = 0.5$.

is lower ($\mu = \mu_e = e^{-2}$) and the evolution is similar to the isothermal case of a spreading front with decreasing thickness. However, at later times $\theta < \theta_m = 0.5$ near the leading edge, so the viscosity now is much larger here ($\mu = \mu_a = 1$) compared to the bulk liquid. This temperature contrast then kick-starts the mechanism for the development of the hump as explained previously. Figure 4.35(a,b) considers the evolution of $h(x,t)$ and $\theta(x,t)$ for spreading over an inclined plane, with $Pe = 10^4$, $\mu_e = 0.2$ and $\theta_m = 0.5$. The increased viscosity for $\theta \geq \theta_m = 0.5$ results in less mobility of the hotter liquid, so the evolution is similar to the previous case but the development of the fluid hump is retarded compared to the free surface profile shown in Fig. 4.34(a). Figure 4.36(a,b) considers the evolution of $h(x,t)$ and $\theta(x,t)$ for spreading over an inclined plane, with $Pe = 10^4$, $\mu_e = 0.2$ and $\theta_m = 0.9$. The higher value of $\theta_m = 0.9$ allows the temperature contrast at the leading edge and the resulting viscosity contrast to be applicable in

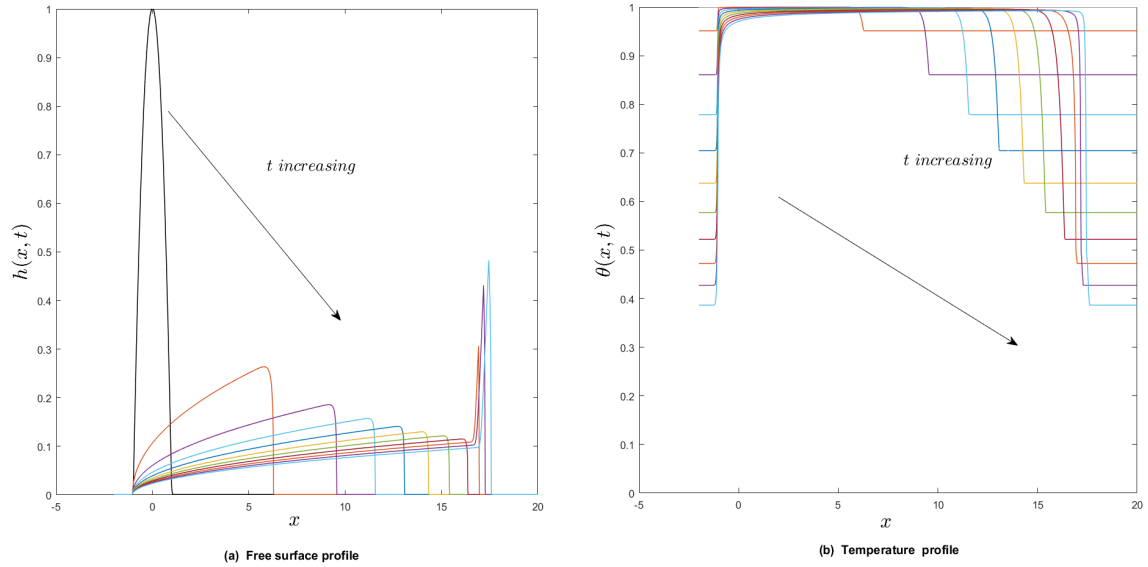

Figure 4.34: The evolution of (a) $h(x,t)$ and (b) $\theta(x,t)$ for t varying between $t = 0-30$ using the bi-viscosity model with $S = 1$, $Pe = 10^4$, $Q_{s_0} = 0$, $\theta_s = 0$, $a = 0.2$, $b = 0.3$, $\mu_a = 10^{-2}$ and $\theta_m = 0.5$.

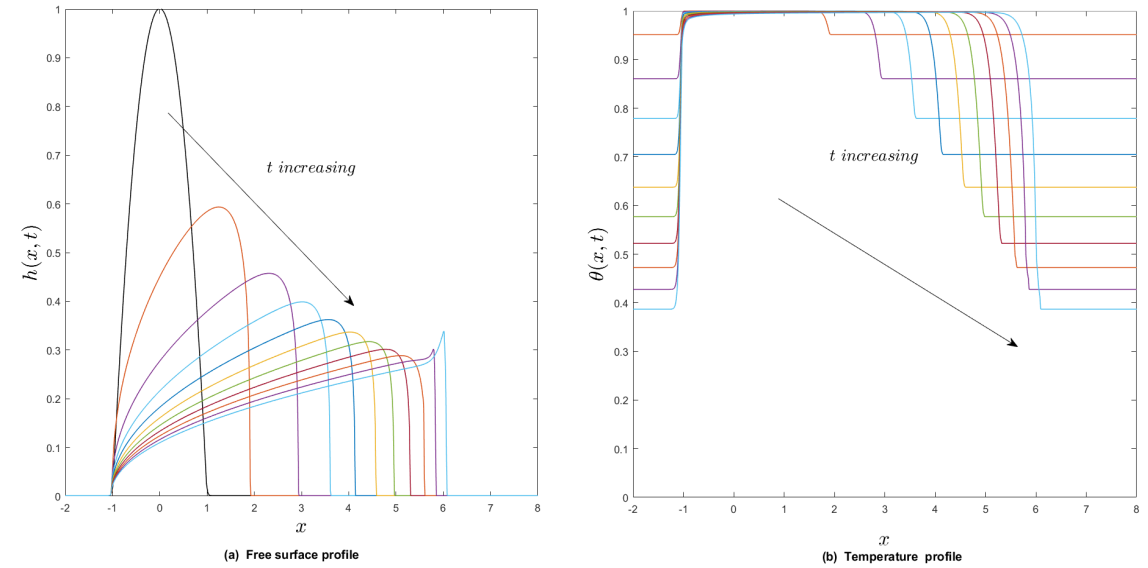

Figure 4.35: The evolution of (a) $h(x,t)$ and (b) $\theta(x,t)$ for t varying between $t = 0-30$ using the bi-viscosity model with $S = 1$, $Pe = 10^4$, $Q_{s_0} = 0$, $\theta_s = 0$, $a = 0.2$, $b = 0.3$, $\mu_a = 0.2$ and $\theta_m = 0.5$.

the development of the fluid hump at early times unlike the above two cases where $\theta_m = 0.5$. Figure 4.37(a, b) considers the evolution of $h(x,t)$ and $\theta(x,t)$ for spreading

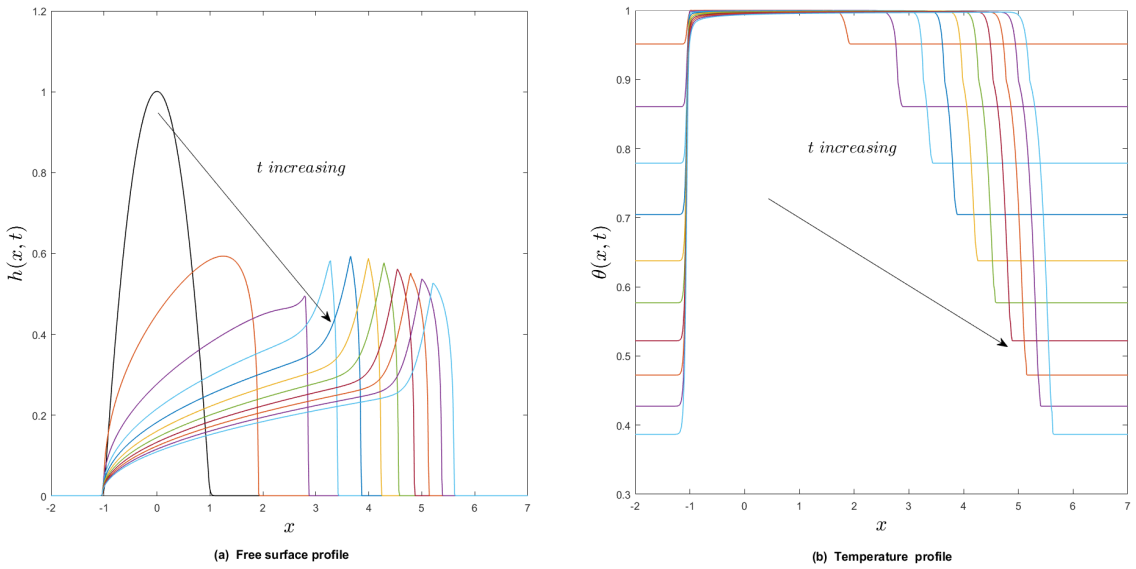

Figure 4.36: The evolution of (a) $h(x,t)$ and (b) $\theta(x,t)$ for t varying between $t = 0-30$ using the bi-viscosity model with $S = 1$, $Pe = 10^4$, $Q_{s_0} = 0$, $\theta_s = 0$, $a = 0.2$, $b = 0.3$, $\mu_a = 0.2$ and $\theta_m = 0.9$.

over an inclined plane with a flowrate from a source, with $Pe = 10^2$, $Q_{s_0} = 7$, $\mu_e = 10^{-2}$ and $\theta_m = 0.5$. The evolution of both $h(x,t)$ and $\theta(x,t)$ are similar to that using the exponential model for a similar Péclet number shown in Fig. 4.28(a, b). The main differences are that the fluid hump develops much earlier and is much bigger (Fig. 4.37(a)) than the one with the exponential viscosity model. Again this is due to the enhanced mobility of the bulk liquid due to its lower viscosity in the bi-viscosity model compared with the exponential viscosity model. The temperature profiles look very much similar in both except we observe a local maximum in the temperature near the leading edge of the front (Fig. 4.37(b)) which is not observed in the exponential viscosity model (see Fig. 4.20(b)). This local maximum in temperature coincides with

the maximum in the fluid hump where the heat loss is less than that around it (note the rate of heat loss is inversely proportional to the h). We observe that this local peak gets bigger as the peak in fluid hump region gets bigger.

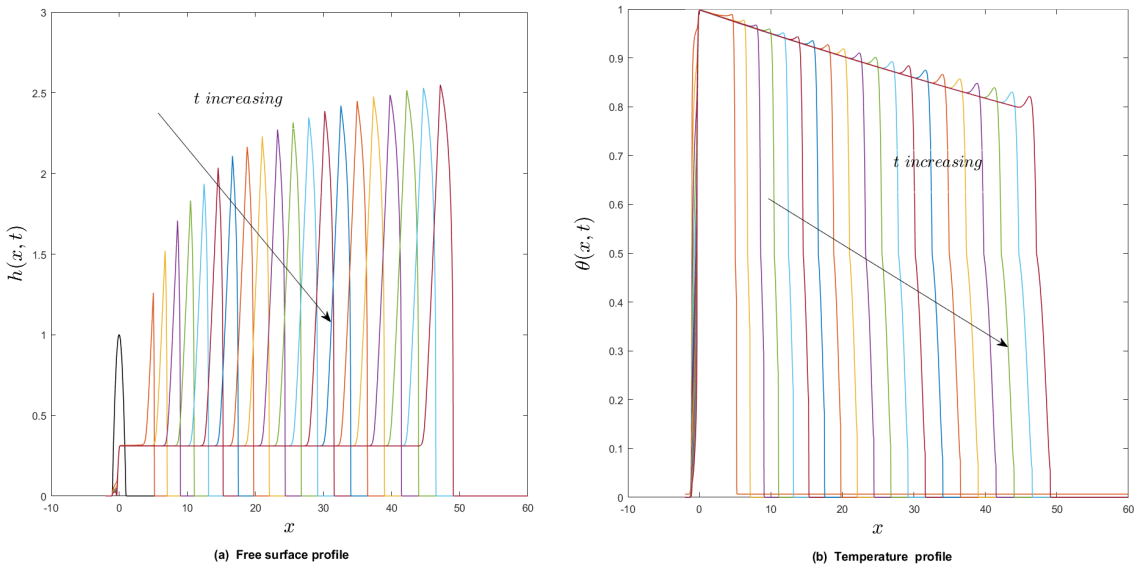

Figure 4.37: The evolution of (a) $h(x,t)$ and (b) $\theta(x,t)$ for t varying between $t = 0-30$ using the bi-viscosity model with $S = 1$, $Pe = 10^2$, $Q_{s_0} = 7$, $\theta_s = 0$, $a = 0.2$, $b = 0.3$, $\mu_a = 0.2$ and $\theta_m = 0.5$.

4.4 Conclusions

In this chapter we use the thin-film flow equations coupled to a vertically isothermal theory for the temperature based on the asymptotic limit of $Pe_r \ll 1$ to investigate the spreading and cooling of a hot Newtonian liquid down an inclined plane. We consider non-isothermal conditions which include a temperature-dependent viscosity and heat loss due to cooling at the free surface and substrate. A very important feature during the spreading process is the localised cooling near the leading edge of

the dome's free surface where the rate of heat loss is maximum. An extensive study of the system parameters, particularly, the Péclet number, Pe, the decay constant in the exponential viscosity model, α, and the heat transfer coefficients, a and b, reveal their influence on this localised cooling. The magnitude of this localised cooling and the resulting temperature and viscosity contrast there results in a variety of free surface shape profiles.

For spreading on a horizontal substrate ($S = 0$), we recover the free surface shapes previously identified in the studies by Sansom *et al.* [76, 53, 77] and Balmforth *et al.* [7, 11]. These include,

(i) a dome-shaped profile with a steep front at its leading edge which thins and spreads as it evolves (see Figs. 4.1-4.4) for low values of α, and

(ii) a flattened region (or plateau) with a much steeper front at its leading edge, similar to a pancake-shaped profile, for larger values of α and Pe (see Figs. 4.6, 4.7). The spreading rate of these structures is also much higher than the dome-shaped ones.

If we take $a = b$ and survey the three-dimensional parameter space, $(Pe, a = b, \alpha)$, we expect that for low values of α we would only observe dome-shaped profiles; as α increases past a critical value, we would also see pancake-shaped profiles developing for intermediate values of Pe. This region of pancake-shaped profiles would gradually expand as α increases. We speculate that as α becomes larger this region will gradually shrink and eventually we will observe only dome-shaped profiles and the spreading will

be near isothermal. This visual representation in $(Pe, a = b, \alpha)$ parameter space is crucial to the stability analysis in Chapter 6.

The new results in this chapter are related to spreading down an inclined substrate (shown for $S = 1$, with approximately 6^o inclination angle). The localised cooling mechanism described above also holds here. In addition, the mobility of the dome is also enhanced due to the inclination (contribution from the horizontal component of gravity). Our parameter study reveals two distinct free surface shapes:

(i) a slumped dome-shaped profile with a steep front for either small or very large Pe (see Figs. 4.17-4.19), and

(ii) a slumped profile with a fluid hump overriding the steep front at its leading edge for intermediate values of Pe (see Figs. 4.20, 4.21).

We observe that as α increases (increased coupling between the viscosity and temperature) so does the height of the hump. The viscosity contrast between the cold liquid near the leading edge and the hot liquid in the interior is further enhanced as α increases resulting in the increased hump height. Including a constant flowrate liquid at the source or vent results in sustained increase in the hump-shaped profile. The bi-viscosity model shows free surface profiles which are much sharper and steeper than the corresponding profiles using the exponential viscosity model. The parameter survey in $(a = b, Pe)$ space (see Fig. 4.25) shows the regions with and without a humped profile for low values of α. We expect the humped profile region to expand as α increases, gradually getting smaller for larger values of α and then approaching isothermal be-

haviour. This visual representation will be useful in analysing the transverse instability in Chapter 6.

As mentioned previously, the large values of Pe considered here may violate the $Pe_r \ll 1$ asymptotic limit underpinning this vertically isothermal theory. We will show in Chapter 5, which considers $Pe_r = O(1)$, the range of validity of the asymptotic theory presented here.

Chapter 5

The non-isothermal and Newtonian spreading of a hot liquid dome down an inclined plane: $O(1)$ reduced Péclet number

5.1 Introduction

In Chapter 4 we investigated the asymptotic limit of the reduced Péclet number, $Pe_r = \epsilon^2 Pe \ll 1$, where the Péclet number, $Pe = O(1)$, the so-called vertical conduction (or diffusion) dominated scenario of heat transport (also referred to as the vertically isothermal or well-mixed scenario). This enabled the non-isothermal problem to be

reduced to a one-dimensional evolution equation for the temperature, $\theta(x,t)$, coupled with the evolution of the free surface, $h(x,t)$ via a temperature-dependent viscosity, $\mu(\theta(x,t))$. In this chapter we relax the conduction dominated limit to include $Pe_r = O(1)$ or greater in order to consider heat transport by both convection and conduction (or diffusion). This allows us to consider, for example, the convection dominated case for $Pe \gg 1$ where the fluid in the dome's interior is hot and insulated between a colder *skin* (or diffusive boundary layer) near the free surface and the substrate

5.2 Mathematical Formulation

The fluid flow and temperature problem are the same as that described in Chapter 2, §2.2 and Chapter 4, §4.2, respectively, of a liquid dome spreading under the influence of gravity down an inclined and pre-wetted substrate (see Fig. 2.1 for a schematic) with hot liquid at temperature, T_e and flowrate, $Q_s(t)$ coming through a vent at a specified location on the substrate. The liquid in the dome is assumed to be Newtonian with constant properties, except, the liquid viscosity is dependent on the temperature modelled by either the exponential viscosity or bi-viscosity model.

5.2.1 Governing Equations

The governing equations for the flow speed $(u^\star, w^\star)$ in the $x^\star$ and $z^\star$ directions, respectively, and pressure, $p^\star$, are given by the conservation of mass and momentum, Eqs.

(2.1). The boundary conditions for the flow problem at the free surface, $z^\star = h^\star(x^\star, t^\star)$, and substrate, $z^\star = 0$, are given by Eqs. (2.9,2.11) and Eq. (2.4), respectively. The governing equations for the heat energy measured by the temperature, $T^\star$, is given by Eq. (4.1) in a material with density, $\rho^\star$, specific heat, $c_p^\star$, thermal conductivity, $\kappa^\star$ and thermal diffusivity, $\kappa_d^\star = \kappa^\star/(\rho^\star c_p^\star)$. We neglect the contribution from viscous dissipation. The boundary conditions for the temperature at the free surface and substrate are given by Eqs. (4.3,4.5), respectively.

The nondimensionalisation of the flow variables and temperature are the same as in §2.2.3 in Chapter 2 and Chapter 4, respectively. We proceed in the same way as described in Chapter 2 in performing the lubrication approximation for the leading order flow problem in ϵ. We follow the same sequence of steps in solving the leading order flow problem until the expression for the leading order shear stress, $\tau_{xz_0}(x, z) = (S - h_{0_x})(h_0 - z)$. Using the Newtonian constitutive relationship between the stress and shear rate, we obtain the leading order relationship between the shear stress and the shear rate as $\tau_{xz_0} = \mu(\theta_0)u_{0_z}$. Using the expression for τ_{xz_0}, we obtain

$$\mu(\theta_0)u_{0_z} = (S - h_{0_x})(h_0 - z). \tag{5.1}$$

The leading order liquid flux through any cross-section, $Q_0(x, t)$ is given by

$$Q_0 = \int_{z=0}^{z=h_0(x,t)} u_{0_z}(h_0 - z)\, dz = (S - h_{0_x}) \int_{z=0}^{z=h_0(x,t)} \frac{(h_0 - z)^2}{\mu(\theta_0)}\, dz. \tag{5.2}$$

Proceeding in the same way as described in Chapter 4, we derive the evolution equation as (dropping the "0" subscript):

$$h_t + Q_x = w_s, \;\; Q = (S - h_x) \int_{z=0}^{z=h(x,t)} \frac{(h-z)^2}{\mu(\theta)} \, dz, \tag{5.3}$$

where

$$w_s = \frac{3}{4} Q_{s_0} Q_s(t) \left[1 - (x/x_0)^2\right] \mathcal{H}(x^2 - x_0^2), \tag{5.4}$$

Following Chapter 2, the two-dimensional temperature field, $\theta(x, z, t)$, and the boundary conditions at $z = 0$ and $z = h(x, t)$ can be written as:

$$Pe_r[\theta_t + u\theta_x + w\theta_z) = \left[\epsilon^2 \theta_{xx} + \theta_{zz}\right], \tag{5.5a}$$

$$u = (S - h_x) \int_0^z \frac{(h - \acute{z})}{\mu(\theta)} d\acute{z}, \;\; w = -\int_0^z u_x d\acute{z} + w_s, \tag{5.5b}$$

$$\theta_z = Pe_r(\theta - 1)w_s + \epsilon^2 b(\theta - \theta_s), \text{ at } z = 0, \tag{5.5c}$$

$$\theta_z = \epsilon^2 h_x \theta_x - \epsilon^2 a\theta\sqrt{1 + \epsilon^2 h_x^2}, \text{ at } z = h(x, t). \tag{5.5d}$$

Here the reduced Péclet number, $Pe_r = \epsilon^2 Pe = O(1)$, $Pe = (\rho^\star c_p^\star U^\star L^\star)/\kappa^\star = U^\star L^\star/\kappa_d^\star$, is the Péclet number (compares convective to diffusive heat transport; assumed to be $O(1)$), $a = a_m^\star H^\star/(\epsilon^2 \kappa^\star)$ and $b = b_s^\star H^\star/(\epsilon^2 \kappa^\star)$ are the heat transfer coefficients at the free surface and substrate, respectively, and $\theta_s = (T_s^\star - T_a^\star)/(T_e^\star - T_a^\star)$.

The left-hand side terms in Eq. (5.5a), apart from the time derivative, represent the convection terms, the right-hand side term is the diffusion term. For large Pe_r the

temperature evolution is dominated by convection, and for small Pe_r, the temperature evolution equation is dominated by diffusion. The evolution equations for $h(x,t)$ and $\theta(x,z,t)$ including the boundary conditions for θ at $z=0$ and $z=h(x,t)$ are:

$$h_t + Q_x = w_s, \tag{5.6a}$$

$$Q = (S - h_x)\int_{z=0}^{z=h(x,t)} \frac{(h-z)^2}{\mu(\theta)}\, dz, \quad w_s = \frac{3}{4} Q_{s_0} Q_s(t)\left[1-(x/x_0)^2\right]\mathcal{H}(x^2 - x_0^2), \tag{5.6b}$$

$$Pe_r[\theta_t + u\theta_x + w\theta_z) = \left[\epsilon^2\theta_{xx} + \theta_{zz}\right], \tag{5.6c}$$

$$u = (S-h_x)\int_0^z \frac{(h-\acute{z})}{\mu(\theta)} d\acute{z}, \quad w = -\int_0^z u_x d\acute{z} + w_s, \tag{5.6d}$$

$$\theta_z = Pe_r(\theta - 1)w_s + \epsilon^2 b(\theta - \theta_s), \text{ at } z = 0, \tag{5.6e}$$

$$\theta_z = \epsilon^2 h_x\theta_x - \epsilon^2 a\theta\sqrt{1+\epsilon^2 h_x^2}, \text{ at } z = h(x,t). \tag{5.6f}$$

The temperature field is coupled with the free surface evolution by applying a temperature-dependent viscosity law, $\mu(\theta)$. Similar to the previous chapters, the viscosity laws which we considered are the exponential and bi-viscosity models.

In order to solve the temperature evolution equation numerically, it is useful to map the temperature field, $\theta(x,z,t)$, onto a rectangular domain. We apply the following change of variables:

$$\bar{x} = x, \quad \bar{z} = \frac{z}{h(x,t)}, \quad \bar{t} = t. \tag{5.7}$$

The chain rule gives

$$\frac{\partial}{\partial x} = \frac{\partial}{\partial \bar{x}} - \frac{\bar{z} h_x}{h}\frac{\partial}{\partial \bar{z}},\ \frac{\partial}{\partial z} = \frac{1}{h}\frac{\partial}{\partial \bar{z}},\ \frac{\partial}{\partial t} = \frac{\partial}{\partial \bar{t}} - \frac{\bar{z} h_t}{h}\frac{\partial}{\partial \bar{z}}. \tag{5.8}$$

Applying the above change of variables, the new set of transformed evolution equations for $h(\bar{x}, \bar{t})$ and $\theta(\bar{x}, \bar{z}, \bar{t})$ can be written as:

$$h_{\bar{t}} + Q_{\bar{x}} = w_s, \tag{5.9a}$$

$$Q = h^3(S - h_{\bar{x}}) \int_{\bar{z}=0}^{\bar{z}=1} \frac{(1-\bar{z})^2}{\mu(\theta)}\, d\bar{z},\ \ w_s = \frac{3}{4} Q_{s_0} Q_s(t) \left[1 - (\bar{x}/x_0)^2\right] \mathcal{H}(\bar{x}^2 - x_0^2), \tag{5.9b}$$

$$\theta_{\bar{t}} + u\theta_{\bar{x}} + (w - \bar{z} u h_{\bar{x}} - \bar{z} h_{\bar{t}})\frac{1}{h}\theta_{\bar{z}} = \frac{1}{h^2 P_{er}}\theta_{\bar{z}\bar{z}}, \tag{5.9c}$$

$$\theta_{\bar{z}} = hPe_r(\theta - 1)w_s + bh(\theta - \theta_s),\ \ \text{at } \bar{z} = 0, \tag{5.9d}$$

$$\theta_{\bar{z}} = \frac{\epsilon^2 h h_{\bar{x}} \theta_{\bar{x}}}{1 + \epsilon^2 \bar{z} h_{\bar{x}}^2} - \frac{ah\theta}{1 + \epsilon^2 \bar{z} h_{\bar{x}}^2},\ \ \text{at } \bar{z} = 1. \tag{5.9e}$$

We need to determine the transformed velocity field, (u, w). In order to do this, the Eq. (5.1) is first transformed and solved for horizontal velocity component which implies

$$u_{\bar{z}} = h^2(S - h_{\bar{x}})\frac{(1-\bar{z})}{\mu(\theta)}. \tag{5.10}$$

Using the continuity equation in transformed variables gives

$$w_{\bar{z}} = \bar{z} h_{\bar{x}} u_{\bar{z}} - h u_{\bar{x}}. \tag{5.11}$$

Integrating Eq. (5.10) subject to $u = 0$ on $\bar{z} = 0$ gives

$$u(\bar{x}, \bar{z}, \bar{t}) = h^2(S - h_x) \int_0^{\bar{z}} \frac{(1 - \acute{z})}{\mu} d\acute{z}, \tag{5.12}$$

Substituting Eq. (5.10) and (5.12) into transformed continuity equation, we obtain

$$w_{\bar{z}} = h^2 h_{\bar{x}}(S - h_{\bar{x}}) \frac{\bar{z}(1 - \bar{z})}{\mu(\theta)} - h\partial\bar{x} \left(h^2(S - h_{\bar{x}}) \int_0^{\bar{z}} \frac{(1 - \acute{z})}{\mu(\theta)} d\acute{z} \right). \tag{5.13}$$

Integrating with respect to $\bar{z}$ and using the condition $w = 0$ on $\bar{z} = 0$ implies

$$w = h^2 h_{\bar{x}}(S - h_{\bar{x}}) \int_0^{\bar{z}} \frac{\acute{z}(1 - \acute{z})}{\mu(\theta)} - h\partial\bar{x} \left(h^2(S - h_{\bar{x}}) \int_0^{\acute{z}} \left(\int_0^{\acute{\acute{z}}} \frac{(1 - \acute{z})}{\mu(\theta)} d\acute{\acute{z}} \right) d\acute{z} \right) + w_s. \tag{5.14}$$

The above equation can be simplified by changing the order of the integration. An integral of the form

$$\int_0^{\acute{z}} \int_0^{\acute{\acute{z}}} f(x, z, t) d\acute{z} d\acute{\acute{z}}, \tag{5.15}$$

on interchanging the order of integration becomes

$$\int_0^{\acute{z}} \int_0^{\acute{\acute{z}}} f(x, z, t) d\acute{z} d\acute{\acute{z}} = \int_0^{\acute{z}} f(x, z, t)(z - \acute{z}) d\acute{z}. \tag{5.16}$$

Therefore Eq. (5.14) can be written as:

$$w(\bar{x}, \bar{z}, \bar{t}) = h^2 h_{\bar{x}}(S - h_{\bar{x}}) \int_0^{\bar{z}} \frac{\acute{z}(1 - \acute{z})}{\mu(\theta)} d\acute{z} - h\partial\bar{x} \left(h^2(S - h_{\bar{x}}) \int_0^{\bar{z}} \frac{(1 - \acute{z})(\bar{z} - \acute{z})}{\mu(\theta)} d\acute{z} \right) + w_s. \tag{5.17}$$

5.3 Numerical Results

Equations (5.9, 5.12, 5.17) are solved numerically along with the viscosity-temperature relationship, $\mu(\theta)$.

Eqs. (5.9a, 5.9b) for $h(x,t)$ are solved for $x \in [-L, L]$, where L is the length of the computational domain. We assume that the plane is pre-wetted with a precursor layer of thickness b_1. The boundary conditions specified are: $h = b_1$ at $x = \pm L$. The two-dimensional evolution equation for the temperature, $\theta(x, z, t)$, Eq. (5.9c), is solved for $(x, \bar{z}) \in [-L, L] \times [0, 1]$. The boundary conditions are given by Eqs. (5.9d,5.9e) at $\bar{z} = 0, 1$, respectively, and $\theta_x = 0$ at $x = \pm L$. The initial conditions for h and θ are chosen as:

$$h(x,0) = (1-x^2)H(1-x^2) + b_1, \quad \theta(x,0) = 1, \quad x \in \quad [-L, L]. \tag{5.18}$$

Our focus is in investigating the evolution of the dome height h and the temperature θ varying the key parameters related to the non-isothermal conditions: the reduced Péclet number, Pe_r, the heat transfer coefficients, a, b, at the free surface and substrate, respectively, the decay constant, α, in the exponential viscosity-temperature relationship and μ_a and μ_e in the bi-viscosity model. We consider variations in the above parameters for $S = 0$ (horizontal plane) and $S = 1$ (plane inclined at angle of approximately 6^o), and for constant volume or zero source flowrate ($Q_{s_0} = 0$) and constant flow rate. The length of the computational domains L is chosen sufficiently large

so that the boundary condition $h \to b_1$ and $\theta_x = 0$ as $x \to \infty$ is satisfied numerically.

Equations (5.9, 5.12, 5.17) are solved numerically using the Method of Lines [78, 61]. Equations 5.9a, 5.9b for the evolution of $h(x,t)$ are discretised using finite differences in the same way as described in §2.4 in Chapter 2. We use the trapezoidal rule to approximate the integral in the expression for $Q(x,t)$ in Eq. (5.9b). The two-dimensional convection-diffusion equation, Eq. (5.9c), is discretised on a rectangular grid using a finite difference scheme. We use a second order finite difference scheme to discretise the second order derivatives (the terms corresponding to diffusion) and an upwinding scheme for the first-order derivatives (the terms corresponding to convection). The boundary conditions at $\bar{z} = 0, 1$, Eqs. (5.9d,5.9e), are used to determine fictitious points, if required, to discretise the derivatives near these boundaries. The horizontal and vertical velocities, (u, w), respectively, in Eqs. (5.12, 5.17) are discretised as follows:

$$u_{ij} = -h_i^2 \left(S - \frac{h_i - h_{i-1}}{\Delta x} \right) IA_{ij}, \tag{5.19}$$

$$\begin{aligned} w_{ij} = &-h_i^2 \left[\left(\frac{h_i - h_{i-1}}{\Delta x} \right) \left(S - \frac{h_i - h_{i-1}}{\Delta x} \right) IB_{ij} \right] \\ &- \frac{h_i}{\Delta x} \left[IC_{i+\frac{1}{2}} h_{i+\frac{1}{2}}^2 \left(S - h_{\bar{x}i+\frac{1}{2}} \right) - IC_{i-\frac{1}{2}} h_{i-\frac{1}{2}}^2 \left(S - h_{\bar{x}i-\frac{1}{2}} \right) \right], \end{aligned} \tag{5.20}$$

where $IA = \int_0^{\bar{z}} \frac{(1-\acute{z})}{\mu(\theta)} d\acute{z}$, $IB = \int_0^{\bar{z}} \frac{\acute{z}(1-\acute{z})}{\mu(\theta)} d\acute{z}$ and $IC = \int_0^{\bar{z}} \frac{(1-\acute{z})(\bar{z}-\acute{z})}{\mu(\theta)} d\acute{z}$, and the integrals are approximated numerically using the trapezoidal rule.

We first consider the results for $S = 0$ (horizontal plane) and $Q_{s_0} = 0$ (constant volume

drop) using the exponential decay viscosity model. Figure 5.1) shows the evolution of $h(x,t)$ for $t = 0 - 30$ with $\alpha = 0$ ($\mu = 1$ or $\theta = 0$). We observe the characteristic

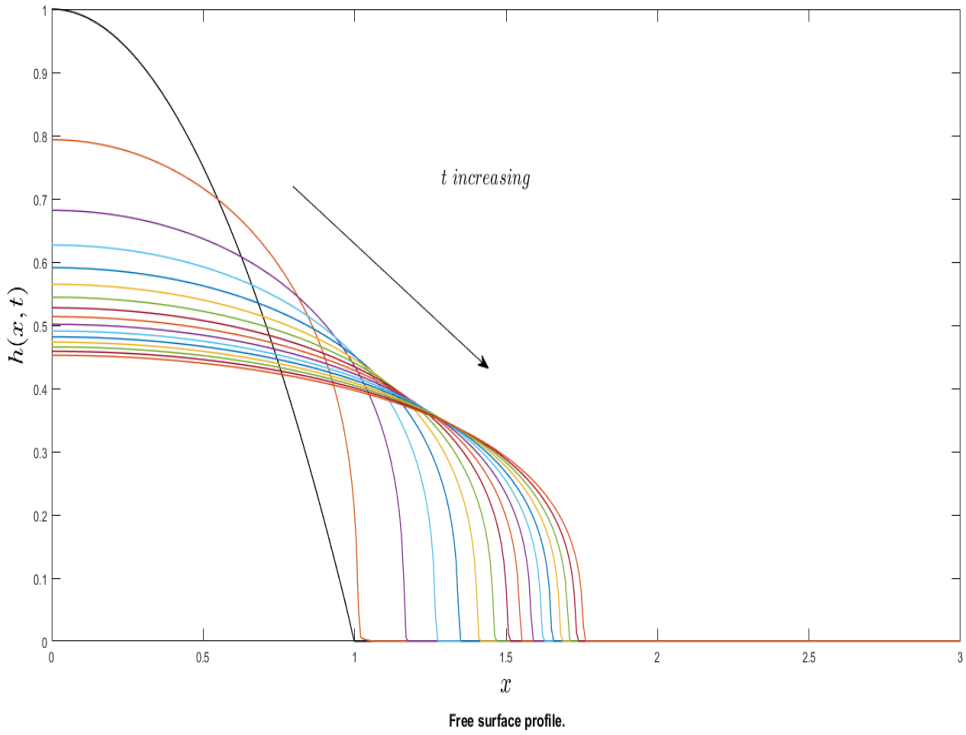

Figure 5.1: The evolution of $h(x,t)$ for t varying between $t = 0 - 30$ corresponding to the isothermal constant volume case with $\mu(\theta) = 1$. The parameter values are: $S = 0$, $\alpha = 0$, $Q_{s_0} = 0$ and $\theta_s = 0$.

dome-shaped (or lens-shaped) spreading with a steep front at its leading edge (see Fig. 5.1) as described in Fig. 4.1 in Chapter 4. Figure 5.2(a) shows $h(x,t)$ for t varying between $t = 0 - 30$ and the contour plot for $\theta(x,z,t)$ at times $t = 1$ (a), $t = 14$ (b) and $t = 30$ (c) with $\alpha = 2$, $Pe_r = 0.1$, $a = 0.02$ and $b = 0.03$. Note that these temperature profiles are superimposed on the corresponding free surface shape (shown by the thicker curves). The temperature quickly drops to zero over the entire dome

due to quick heat loss by vertical diffusion. The free surface profile shows little effect from the temperature field. The evolution of h is similar to the isothermal results in Fig. 5.1 and Fig. 4.2 in Chapter 4. Increasing to $Pe_r = 10^2$, Fig. 5.3(a) shows that the

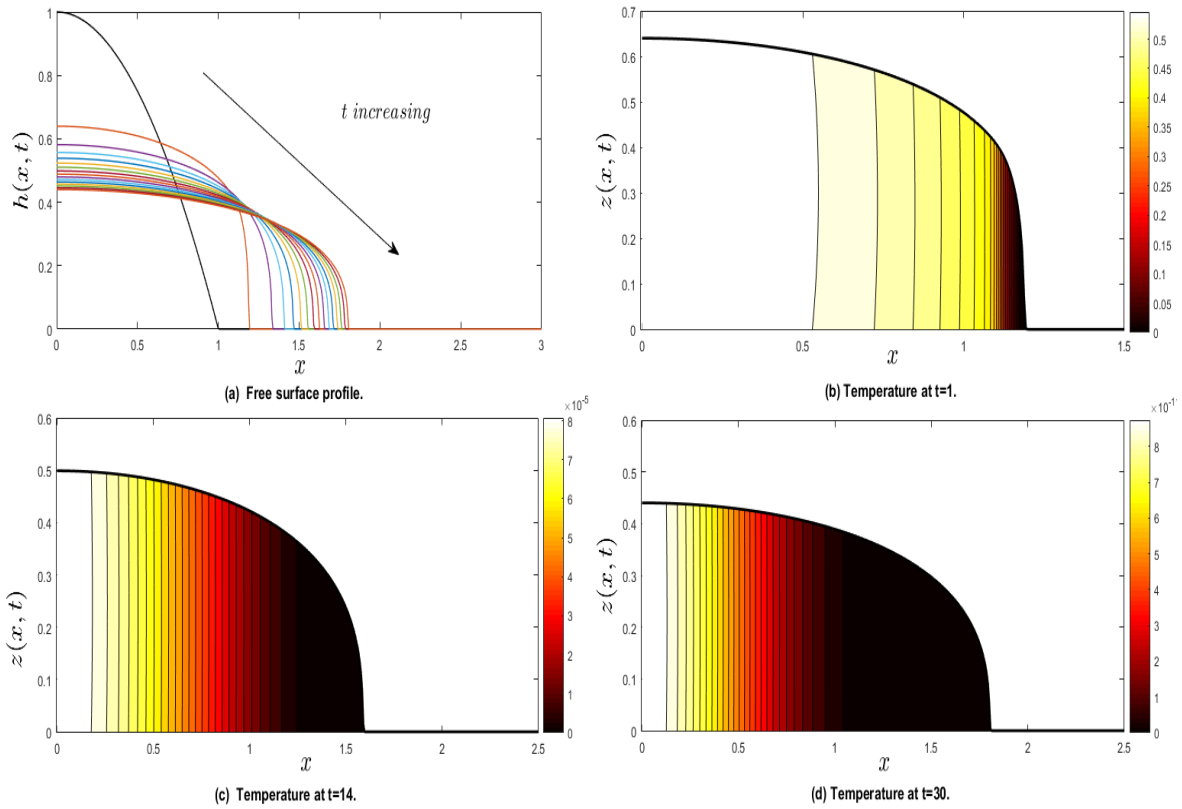

Figure 5.2: The evolution of (a) $h(x,t)$ for t varying between $t = 0-30$ and the contour plot for (b) $\theta(x,z,t=1)$, (c) $\theta(x,z,t=14)$, and (d) $\theta(x,z,t=30)$ (the temperature profiles are superimposed on the corresponding free surface shape h highlighted by thicker curves), with $Pe_r = 0.1$, $\alpha = 2$, $Q_{s_0} = 0$, $\theta_s = 0$, $a = 0.02$ and $b = 0.03$.

spreading dome develops a steep front at its leading edge due to cooling there and the resulting increase in viscosity. The temperature profiles in Fig. 5.3($b-d$) clearly show loss of a large amount heat and consequent cooling near the flow front with the bulk liquid in the dome remaining almost at uniform and higher temperature. Note that there is a thin diffusive boundary layer or skin near the free surface and the substrate

where cooling also occurs, but which is not fully resolved in the simulations shown. The evolution of h and θ is also consistent with that in Fig. 4.3 in Chapter 2 with $Pe = 10^2$. Increasing to $Pe_r = 10^4$, we observe from the contour plots shown in Fig.

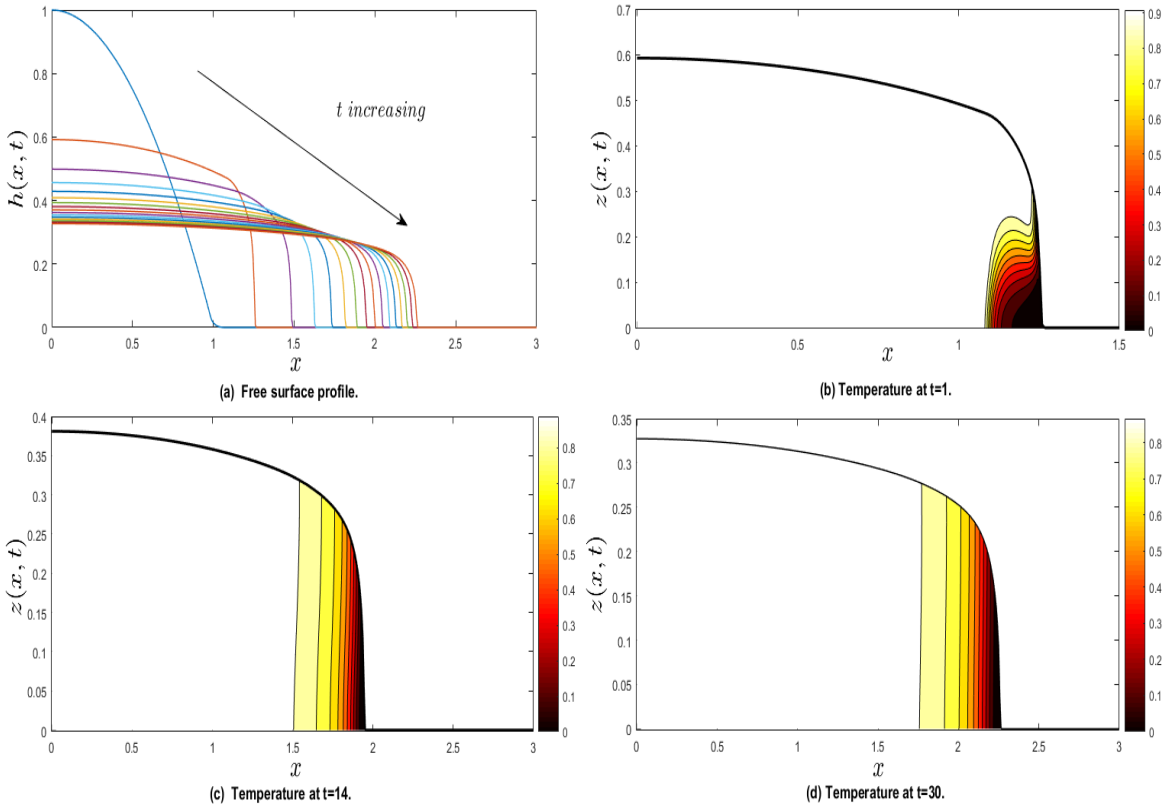

Figure 5.3: The evolution of (a) $h(x,t)$ for t varying between $t = 0-30$ and the contour plot for (b) $\theta(x,z,t=1)$, (c) $\theta(x,z,t=14)$, and (d) $\theta(x,z,t=30)$ (the temperature profiles are superimposed on the corresponding free surface shape h highlighted by thicker curves), with $Pe_r = 10^2$, $\alpha = 2$, $Q_{s_0} = 0$, $\theta_s = 0$, $a = 0.02$ and $b = 0.03$.

5.4$(b-d)$ for $\theta(x,z,t)$ that the cooling is now much more localised near the dome edge forming a collar of cooler liquid with the overlying hot bulk liquid in the dome is close to $\theta = 1$, the initial temperature. The collar of cooler liquid is formed due to advection of the cooler liquid at the surface being deposited to the dome edge. Increasing to $Pe_r = 10^6$ (Fig. 5.5) and $Pe_r = 10^8$ (Fig. 5.6), we observe from the contour plots

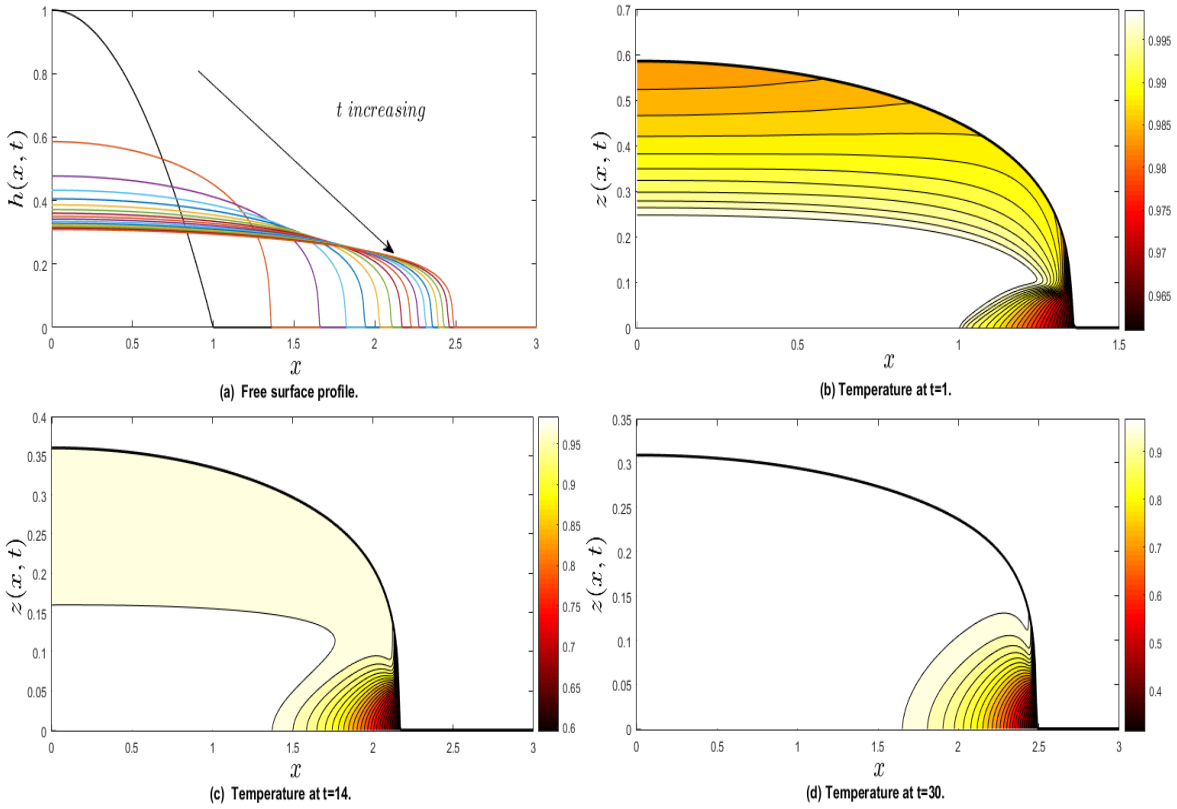

Figure 5.4: The evolution of (a) $h(x,t)$ for t varying between $t = 0-30$ and the contour plot for (b) $\theta(x,z,t=1)$, (c) $\theta(x,z,t=14)$, and (d) $\theta(x,z,t=30)$ (the temperature profiles are superimposed on the corresponding free surface shape h highlighted by thicker curves), with $Pe_r = 10^4$, $\alpha = 2$, $Q_{s_0} = 0$, $\theta_s = 0$, $a = 0.02$ and $b = 0.03$.

shown in Fig. 5.5$(b-d)$, 5.6$(b-d)$, respectively, for $\theta(x,z,t)$ that the collar of cold liquid is now even more localised near the drop edge due to re-heating by the overlying hot bulk liquid in the dome which is approximately at $\theta = 1$. The cooled skin at the free surface and substrate, and the collar of cold liquid are not resolved for $Pe_r = 10^8$. The evolution of $h(x,t)$ approaches that of the isothermal case (see Fig. 5.5(a), 5.6(a)).

In Fig. 5.7, we show the evolution of the location of the leading edge of the dome, x_N

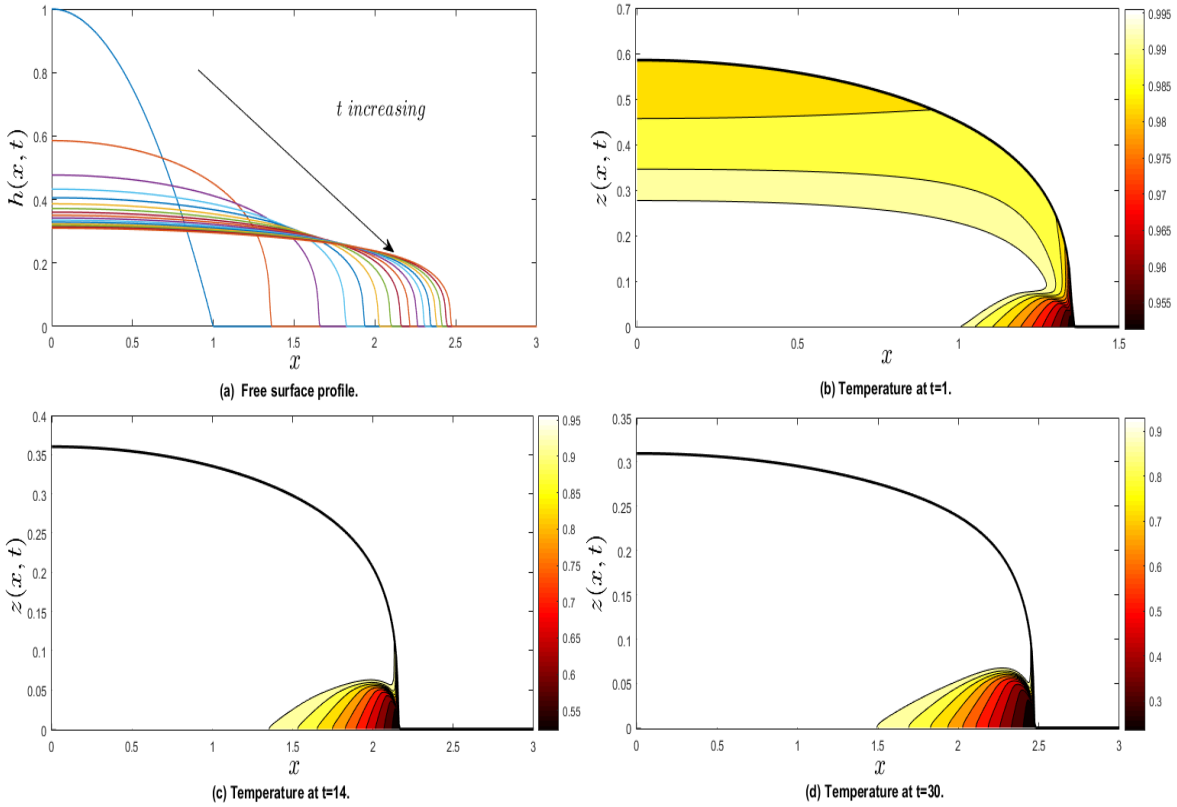

Figure 5.5: The evolution of (a) $h(x,t)$ for t varying between $t = 0-30$ and the contour plot for (b) $\theta(x,z,t=1)$, (c) $\theta(x,z,t=14)$, and (d) $\theta(x,z,t=30)$ (the temperature profiles are superimposed on the corresponding free surface shape h highlighted by thicker curves), with $Pe_r = 10^6$, $\alpha = 2$, $Q_{s_0} = 0$, $\theta_s = 0$, $a = 0.02$ and $b = 0.03$.

(Fig. 5.7(a)) and the dome height at its centre, $h_N = h(0,t)$ (Fig. 5.7(b)), for varying Péclet number Pe between $0.1 \leq Pe_r \leq 10^8$. We observe that the results are bounded

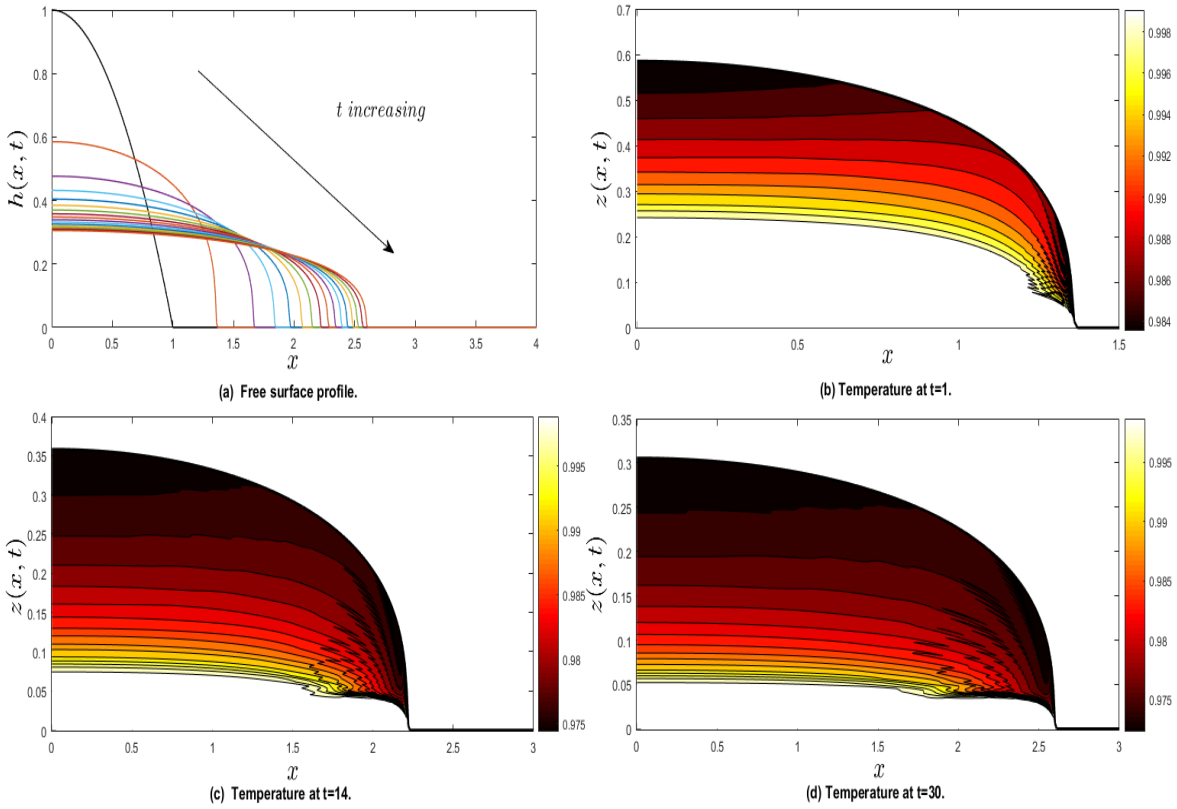

Figure 5.6: The evolution of (a) $h(x,t)$ for t varying between $t = 0-30$ and the contour plot for (b) $\theta(x,z,t=1)$, (c) $\theta(x,z,t=14)$, and (d) $\theta(x,z,t=30)$ (the temperature profiles are superimposed on the corresponding free surface shape h highlighted by thicker curves), with $Pe_r = 10^8$, $\alpha = 2$, $Q_{s_0} = 0$, $\theta_s = 0$, $a = 0.02$ and $b = 0.03$.

above and below by the two isothermal cases corresponding to $Pe_r \to \infty$ and $Pe_r \to 0$, respectively. For $Pe_r = 10^8$, we can confirm that $x_N \sim t^{1/5}$ and $h_N \sim t^{-1/5}$ which is in agreement with the spreading rates and similarity solution derived in Eq. (2.29) in §2.3 of Chapter 2. Figure 5.7(a) shows a non-monotonicity in x_N for larger Péclet

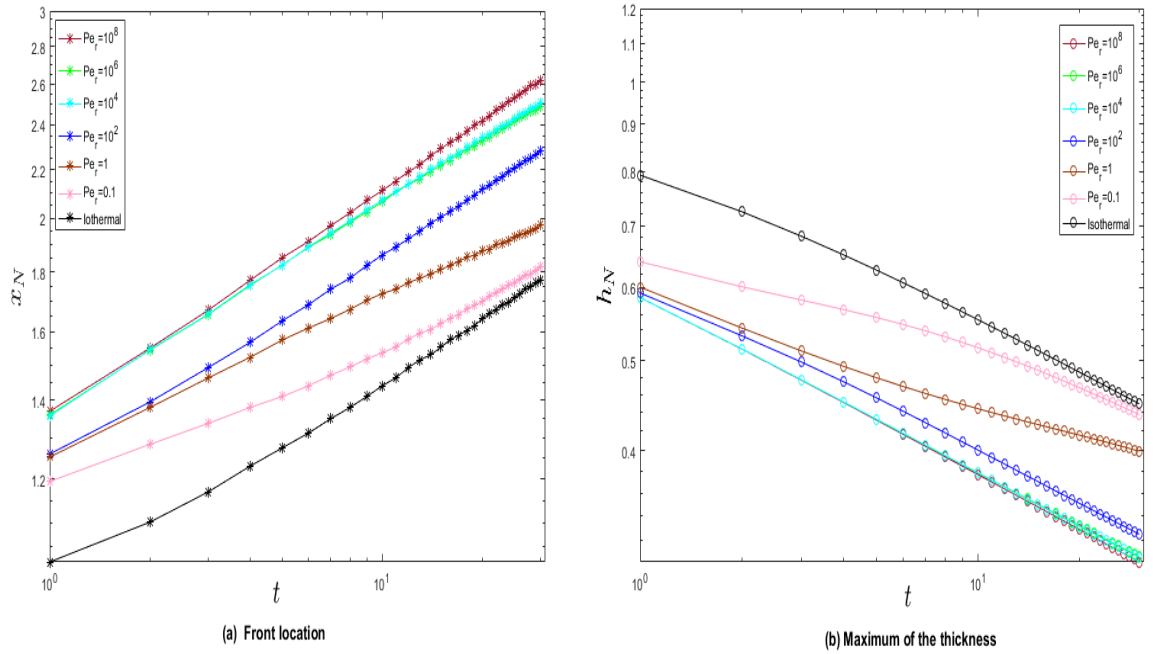

Figure 5.7: The (a) leading edge of the front, x_N, and (b) the maximum in h, $h_N = h(0,t)$, as a function of time, t, for various reduced Péclet number, Pe_r. The parameter values are: $\alpha = 2$, $Q_{s_0} = 0$, $\theta_s = 0$, $a = 0.02$ and $b = 0.03$.

numbers approximately in the range $10^5 \leq Pe_r \leq 10^6$. x_N is smaller for values of Pe_r in this range in comparison to $Pe_r \geq 10^6$. The lower x_N is due to the increased cooling near the front (see Fig. 5.5, compared to say Fig. 5.4) resulting in a larger viscosity and slowing down of the front. On the other hand, h_N, is monotonic as Pe_r increases, approaching the $Pe_r \to \infty$ limit.

By increasing α in the exponential viscosity relationship, the coupling between the

flow and temperature increases. Figure 5.8(a) shows $h(x,t)$ and the contour plot for $\theta(x,z,t)$ at times $t=1$ (a), $t=14$ (b) and $t=30$ (c) for $Pe_r=10^6$ and $\alpha=7$. We

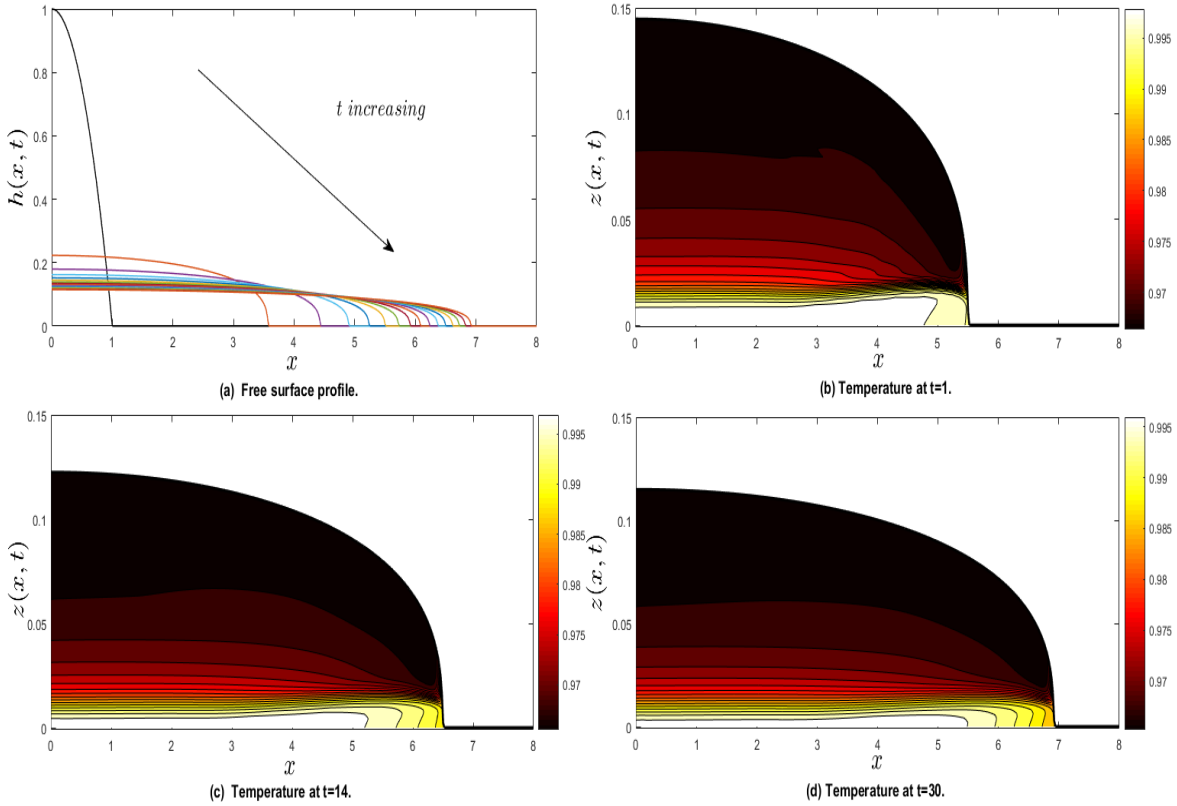

Figure 5.8: The evolution of (a) $h(x,t)$ for t varying between $t=0-30$ and the contour plot for (b) $\theta(x,z,t=1)$, (c) $\theta(x,z,t=14)$, and (d) $\theta(x,z,t=30)$ (the temperature profiles are superimposed on the corresponding free surface shape h highlighted by thicker curves), with $Pe_r=10^6$, $\alpha=7$, $Q_{s_0}=0$, $\theta_s=0$, $a=0.02$ and $b=0.03$.

observe that the spreading rate is much faster compared to the corresponding case with $\alpha=2$ (see Fig. 5.5). This is due to the cooling for this case now even more localised at the dome edge (note that the localised collar of cooled liquid is not resolved here) compared to the corresponding case with $\alpha=2$ (see Fig. $5.5(b-d)$). Figure 5.9(a) shows $h(x,t)$ and the contour plot for $\theta(x,z,t)$ at times $t=1$ (a), $t=14$ (b) and $t=30$ (c) for $Pe_r=10^4$ and $\alpha=7$. Figure 5.9(a) shows severe steepening of the

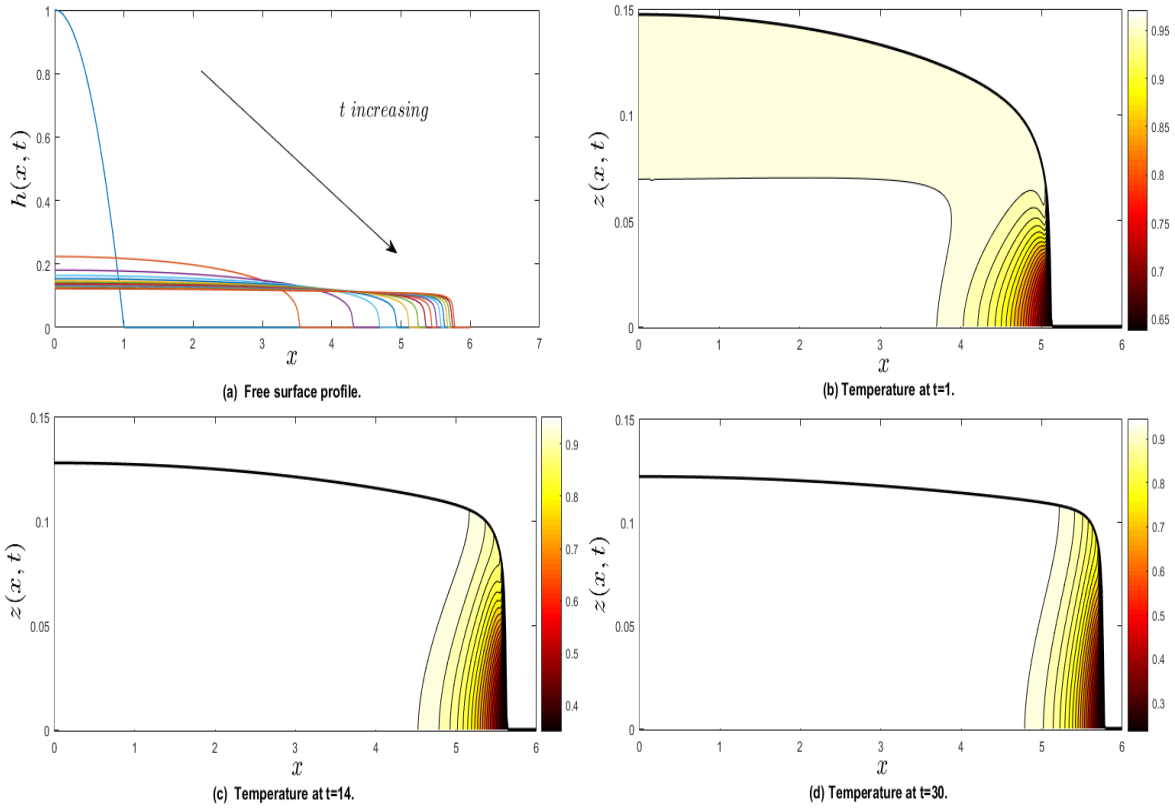

Figure 5.9: The evolution of (a) $h(x,t)$ for t varying between $t = 0-30$ and the contour plot for (b) $\theta(x,z,t=1)$, (c) $\theta(x,z,t=14)$, and (d) $\theta(x,z,t=30)$ (the temperature profiles are superimposed on the corresponding free surface shape h highlighted by thicker curves), with $Pe_r = 10^4$, $\alpha = 7$, $Q_{s_0} = 0$, $\theta_s = 0$, $a = 0.02$ and $b = 0.03$.

flow front in comparison to the corresponding case with $\alpha = 2$ (see Fig. 5.4(a), with a change in shape from that of a dome-shaped profile with a steep front (see Fig. 5.4(a) for $Pe = 10^4$ and $\alpha = 2$) to a pancake-type profile with a steep front and a long developing plateau behind it. The severe steepening of the flow front is due to build-up of very viscous fluid there causing the fluid to push this cooler region and develop the steep flow front. The cooler region is now more vertically spread across the front (Fig. 5.9(c, d)) compared to the more localised scenario for $\alpha = 2$ (see Fig. 5.4(c, d)). The results in Figs. 5.10 and 5.11 show the influence of increasing the heat transfer coefficients a and b with $Pe_r = 10^4$ and $\alpha = 2$. We clearly observe that increasing a and b slows down the spreading rate. This is due to enhanced cooling due to heat loss, hence increased viscosity, over the entire bulk liquid within the dome for larger a and b compared to smaller values, where the cooling is confined near the leading edge of the front and the rest of the bulk liquid is almost uniformly at a higher temperature, hence lower viscosity. We now consider the effects of an influx of liquid from a source or vent with flowrate, $Q_{s_0} = 5$. Figure 5.12(a) shows $h(x, t)$ for t varying between $t = 0 - 20$ and the contour plot for $\theta(x, z, t)$ at times $t = 1$ (b), $t = 12$ (c) and $t = 20$ (d) with $Q_{s_0} = 5$, $\alpha = 2$, $Pe_r = 10^2$, $a = 0.02$ and $b = 0.03$. The free surface profiles show an expanding and spreading dome (Fig. 5.12(a)). The temperature profiles show little heat loss near the flow front for early time (Fig. 5.12(b)). For later times, the heat loss is more noticeable resulting in an expanding layer of a very viscous fluid collar forming near the edge of the flow front and above the substrate causing the hotter fluid behind to *o*verhang over this cooler region. The degree of overhang may be strongly influenced

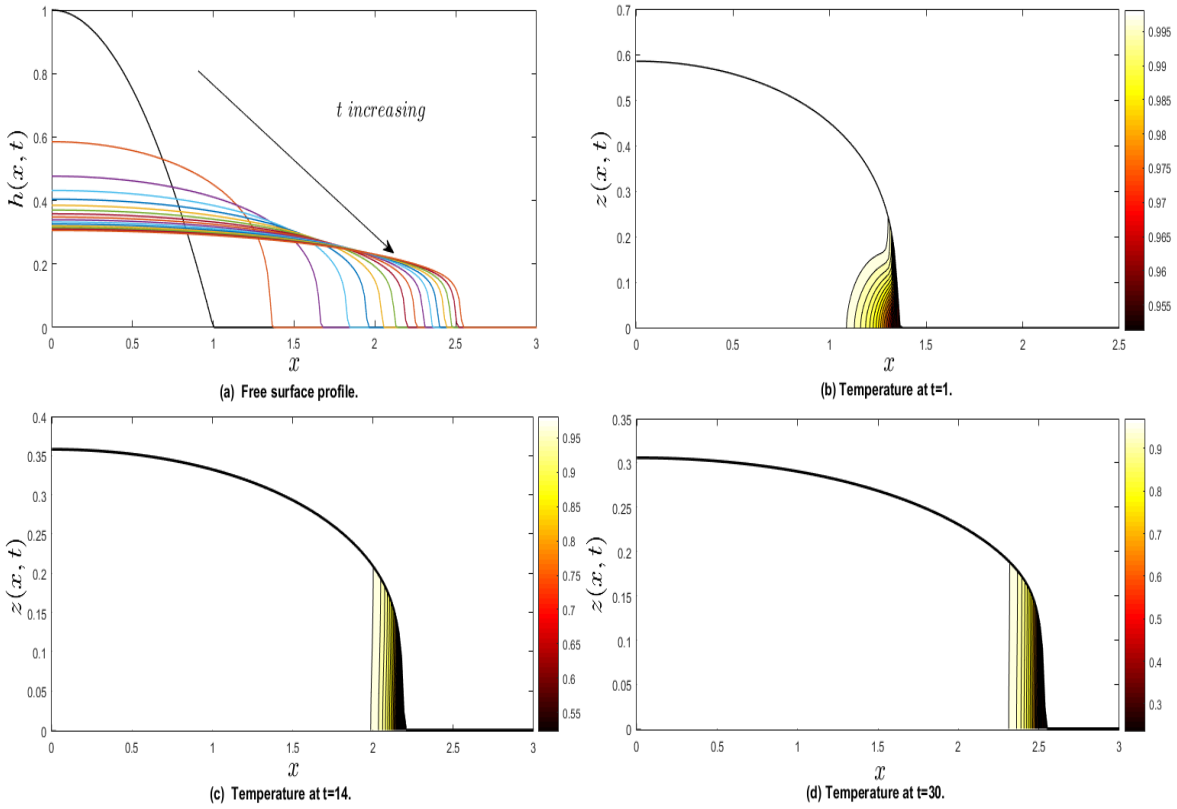

Figure 5.10: The evolution of (a) $h(x,t)$ for t varying between $t = 0-30$ and the contour plot for (b) $\theta(x,z,t=1)$, (c) $\theta(x,z,t=14)$, and (d) $\theta(x,z,t=30)$ (the temperature profiles are superimposed on the corresponding free surface shape h highlighted by thicker curves), with $Pe_r = 10^4$, $\alpha = 2$, $Q_{s_0} = 0$, $\theta_s = 0$, $a = 2\times10^{-4}$ and $b = 2\times10^{-4}$.

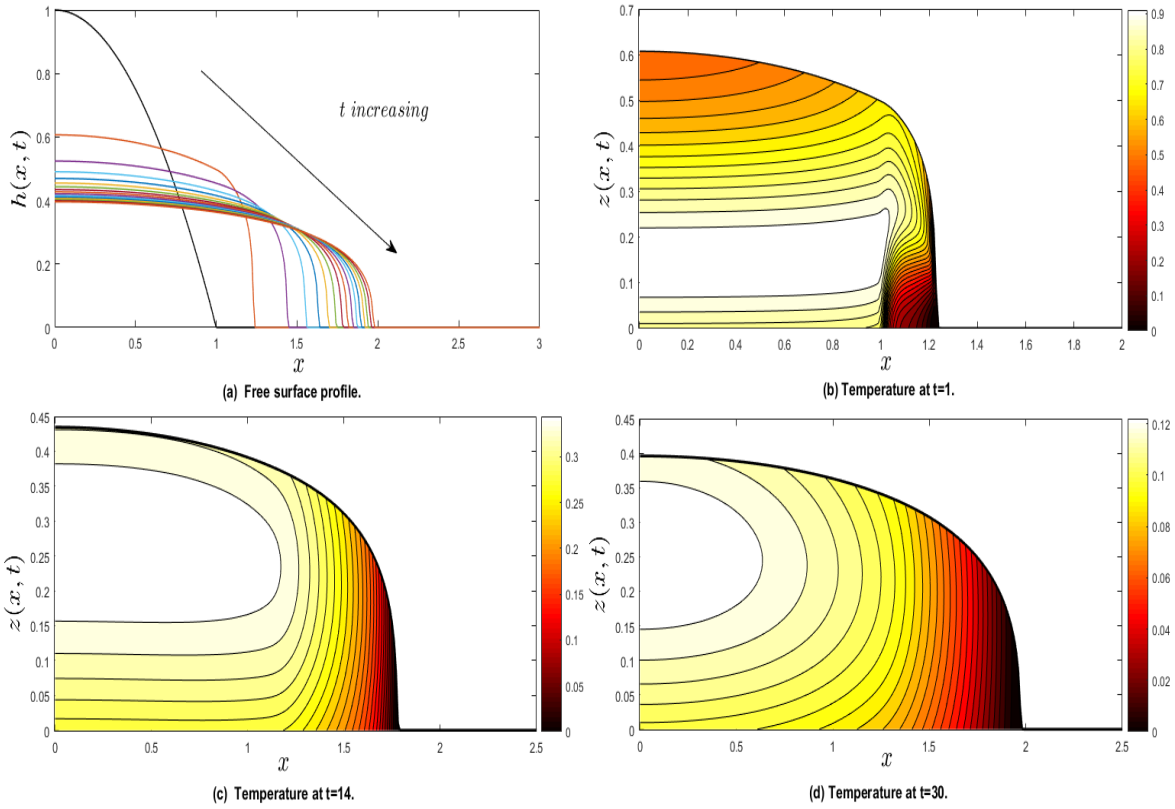

Figure 5.11: The evolution of (a) $h(x,t)$ for t varying between $t = 0-30$ and the contour plot for (b) $\theta(x,z,t=1)$, (c) $\theta(x,z,t=14)$, and (d) $\theta(x,z,t=30)$ (the temperature profiles are superimposed on the corresponding free surface shape h highlighted by thicker curves), with $Pe_r = 10^4$, $\alpha = 2$, $Q_{s_0} = 0$, $\theta_s = 0$, $a = 1$ and $b = 2$.

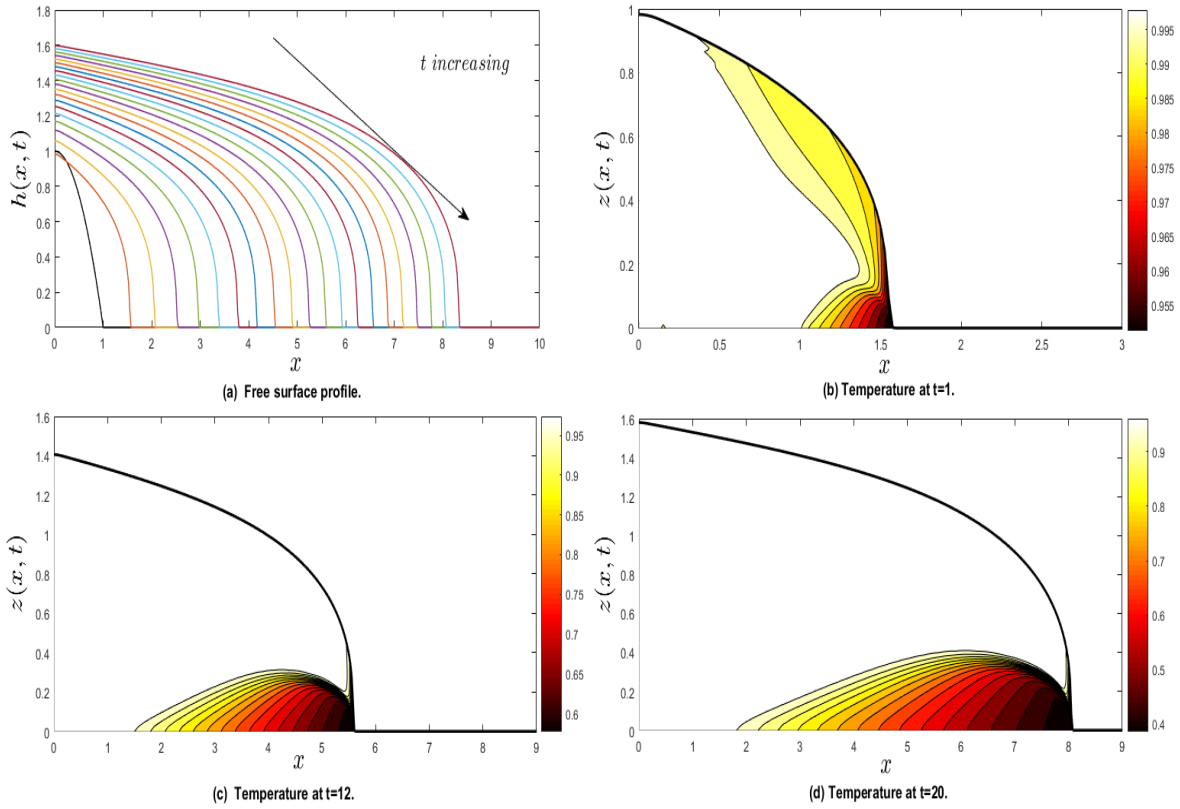

Figure 5.12: The evolution of (a) $h(x,t)$ for t varying between $t = 0-20$ and the contour plot for (b) $\theta(x,z,t=1)$, (c) $\theta(x,z,t=12)$, and (d) $\theta(x,z,t=20)$ (the temperature profiles are superimposed on the corresponding free surface shape h highlighted by thicker curves), with $Pe_r = 10^4$, $\alpha = 2$, $Q_{s_0} = 5$, $\theta_s = 0$, $a = 0.02$ and $b = 0.03$.

by the flowrate of the hot liquid feeding from the vent.

We next consider the results for $S = 1$ (plane inclined at angle of approximately 6^o) and $Q_{s_0} = 0$ (constant volume drop) using the exponential decay viscosity model. Figure 5.13 shows the evolution of $h(x,t)$ with $\alpha = 0$ corresponding to the isothermal case with $\mu(\theta) = 1$. This isothermal case is also obtained in the limit of $Pe \to 0$. The time

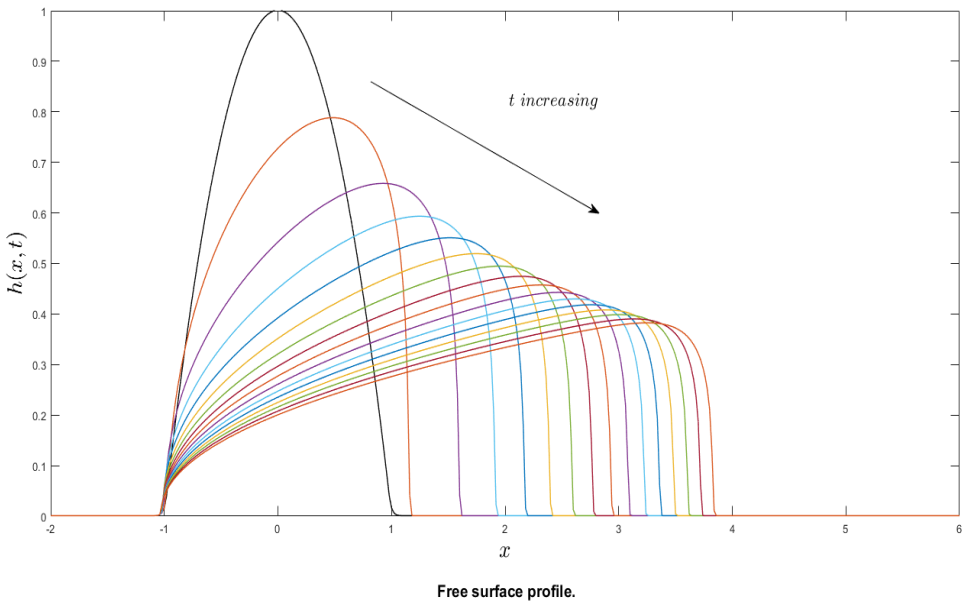

Figure 5.13: The evolution of $h(x,t)$ for t varying between $t = 0 - 30$ corresponding to the isothermal constant volume case with $\mu(\theta) = 1$. The parameter values are: $S = 1$ (approximately 6^o inclination), $\alpha = 0$, $Q_{s_0} = 0$ and $\theta_s = 0$.

range shown is for $0 \leq t \leq 30$. This case is equivalent to the fluid being at the ambient temperature $\theta = 0$. We observe that the spreading is non-symmetric about $x = 0$ and the dome slumps as it spreads with a steep front at its leading edge as described in Chapters 2, 4. Figure 5.14 shows $h(x,t)$ for t varying between $t = 0-30$ and the contour plot for $\theta(x,z,t)$ at times $t = 1$ (a), $t = 14$ (b) and $t = 30$ (c) with $S = 1$, $Q_{s_0} = 0$,

$\alpha = 2$, $Pe_r = 10^6$, $a = 0.02$ and $b = 0.03$. The evolution of $h(x,t)$ (Fig. 5.14)(a) is

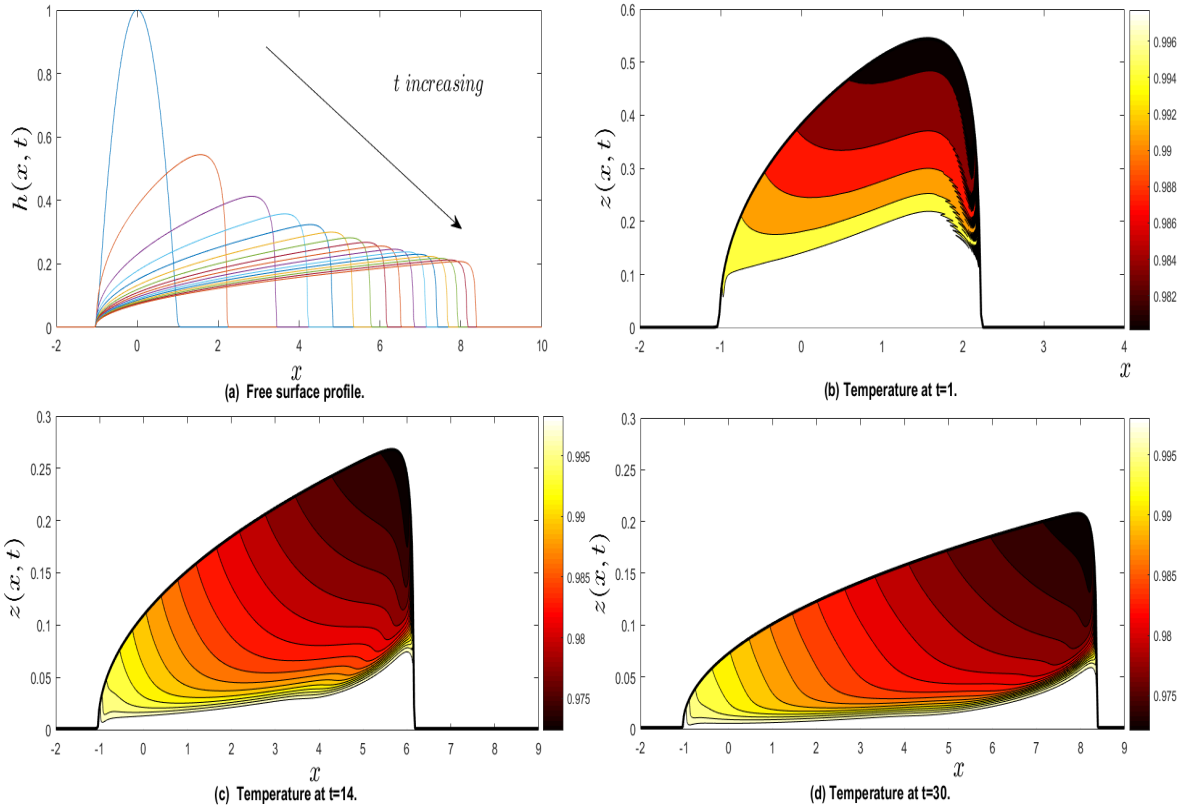

Figure 5.14: The evolution of (a) $h(x,t)$ for t varying between $t = 0-30$ and the contour plot for (b) $\theta(x,z,t=1)$, (c) $\theta(x,z,t=14)$, and (d) $\theta(x,z,t=30)$ (the temperature profiles are superimposed on the corresponding free surface shape h highlighted by thicker curves), with $S = 1$, $Pe_r = 10^6$, $\alpha = 2$, $Q_{s_0} = 0$, $\theta_s = 0$, $a = 0.02$ and $b = 0.03$.

similar to that for the isothermal case with $\mu = \mu_e = e^{-2}$ or as $Pe \to \infty$ (not shown here). The temperature appears almost uniform ($\theta \approx 1$) in the bulk liquid, except for cooling in a skin near the free surface and substrate (a diffusive boundary layer). The results with $Pe_r = 10^4$ are shown in Fig. 5.15(a) for h and $(b-d)$ for $\theta(x,z,t)$. We observe the formation of a collar of cooler liquid between the dome edge and the substrate. This slows down the spreading rate compared to the late-time results with $Pe_r = 10^6$. Decreasing the reduced Péclet number to $Pe_r = 10^2$, localises the cooling

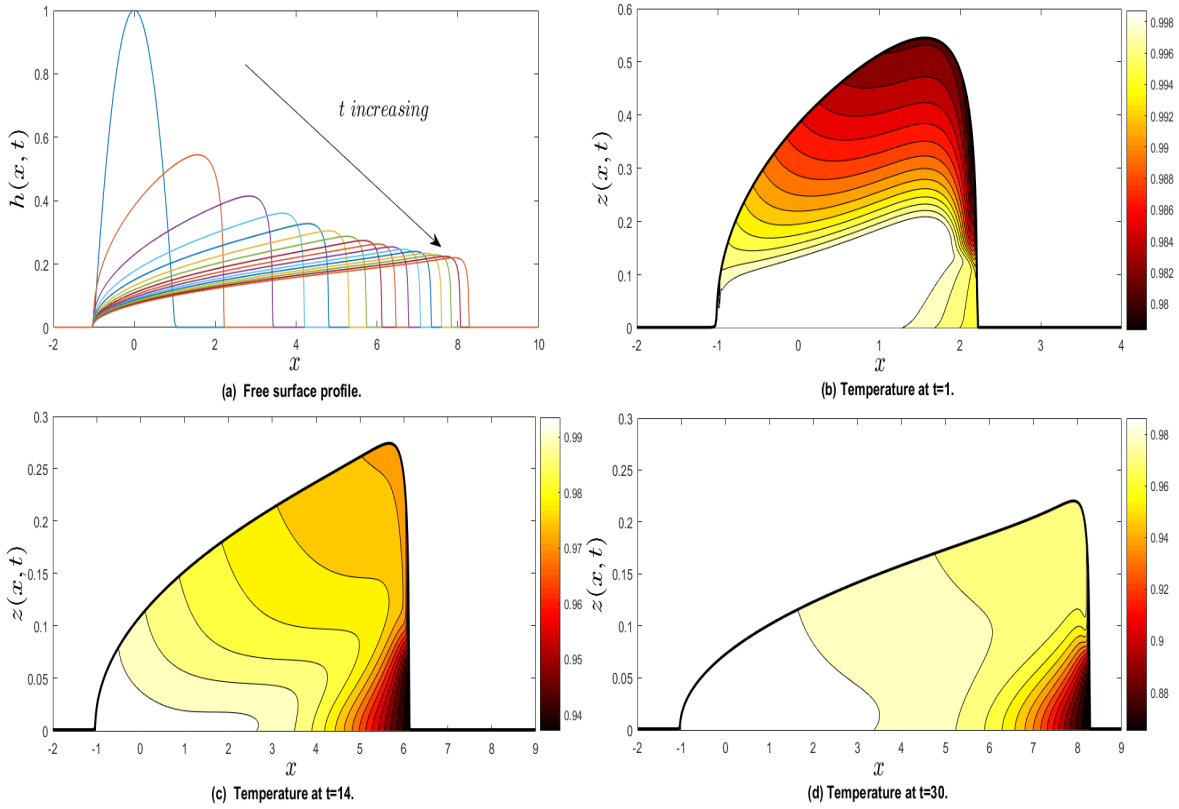

Figure 5.15: The evolution of (a) $h(x,t)$ for t varying between $t = 0-30$ and the contour plot for (b) $\theta(x,z,t=1)$, (c) $\theta(x,z,t=14)$, and (d) $\theta(x,z,t=30)$ (the temperature profiles are superimposed on the corresponding free surface shape h highlighted by thicker curves), with $S = 1$, $Pe_r = 10^4$, $\alpha = 2$, $Q_{s_0} = 0$, $\theta_s = 0$, $a = 0.02$ and $b = 0.03$.

to near the dome's edge and in the bulk of the drop the temperature is much higher (Fig. 5.16$(b-d)$). For later times, the temperature profiles show significant cooling

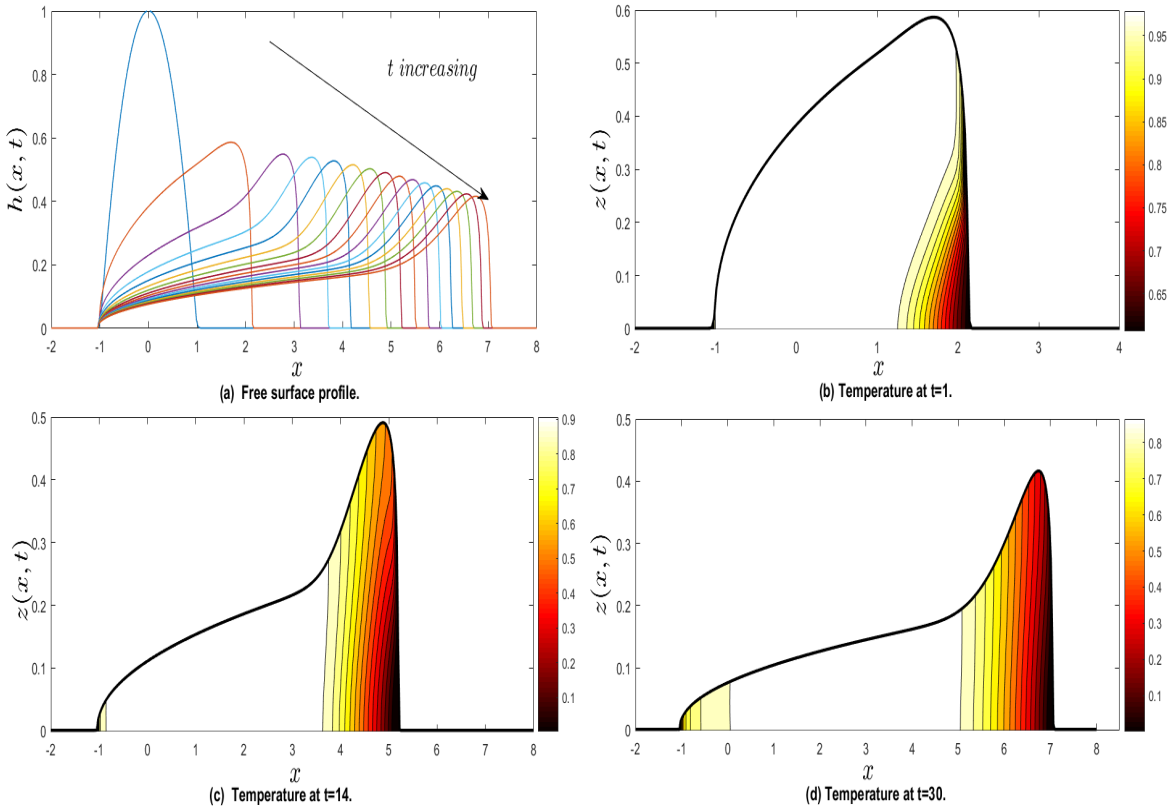

Figure 5.16: The evolution of (a) $h(x,t)$ for t varying between $t = 0-30$ and the contour plot for (b) $\theta(x,z,t=1)$, (c) $\theta(x,z,t=14)$, and (d) $\theta(x,z,t=30)$ (the temperature profiles are superimposed on the corresponding free surface shape h highlighted by thicker curves), with $S=1$, $Pe_r = 10^2$, $\alpha = 2$, $Q_{s_0} = 0$, $\theta_s = 0$, $a = 0.02$ and $b = 0.03$.

near the front with an almost vertically uniform temperature profile (Fig. 5.16$(b-d)$). This in turn increases the viscosity there resulting in slower spreading compared to the larger Pe_r cases. We start to see the formation of a characteristic fluid hump-like structure developing near the dome's leading edge (Fig. 5.16(a)). The temperature behind the leading edge is much higher than that ahead; the increase in mobility due to the reduced liquid viscosity results in the hotter liquid piling-up over the relatively

colder liquid ahead of it resulting in the development of the hump in the free surface shape near the leading edge. Figure 5.17 shows the results when $Pe_r = 1$. The cooling

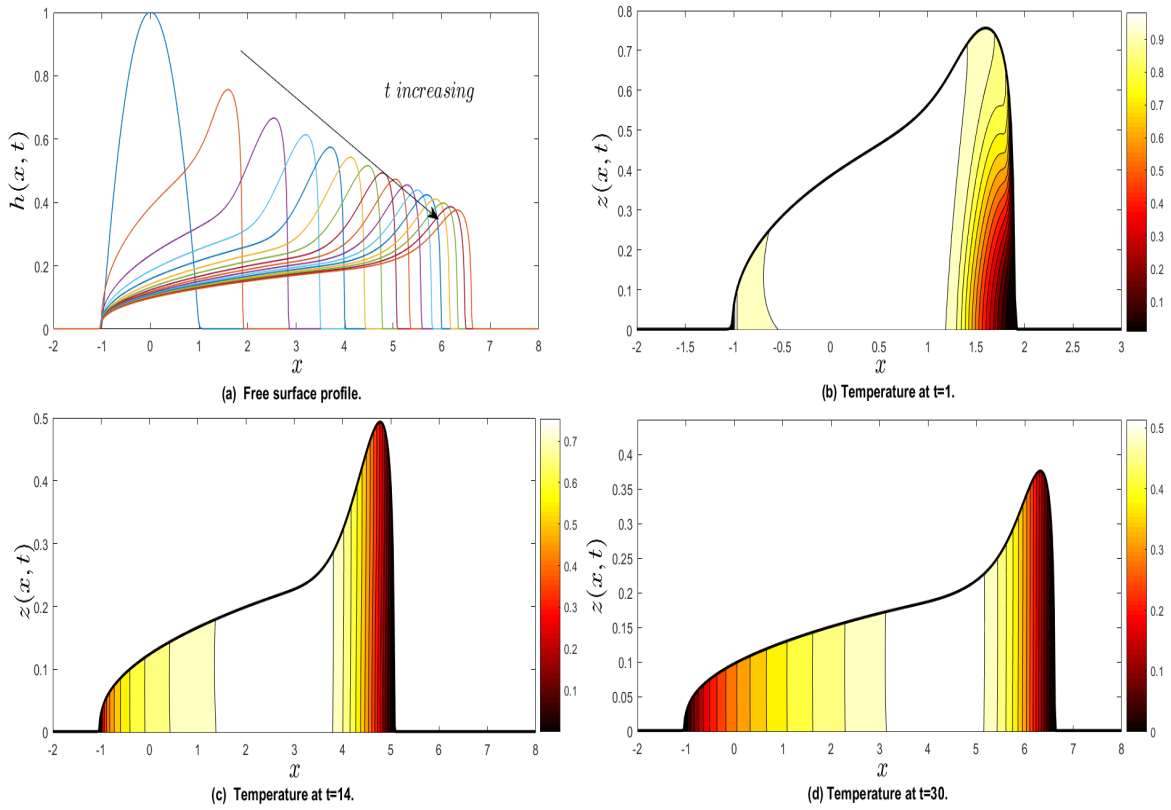

Figure 5.17: The evolution of (a) $h(x,t)$ for t varying between $t = 0-30$ and the contour plot for (b) $\theta(x,z,t=1)$, (c) $\theta(x,z,t=14)$, and (d) $\theta(x,z,t=30)$ (the temperature profiles are superimposed on the corresponding free surface shape h highlighted by thicker curves), with $S = 1$, $Pe_r = 10$, $\alpha = 2$, $Q_{s_0} = 0$, $\theta_s = 0$, $a = 0.02$ and $b = 0.03$.

is much more localised to near the leading edge of the front, while the bulk liquid behind is much hotter (Fig. $5.17(b-d)$). The formation of a fluid hump near the leading edge is also observed for this case (Fig. $5.17(a)$). It is much sharper and steeper than the earlier case with $Pe_r = 10^2$ due to the increased mobility of the fluid behind the front. Increasing to $\alpha = 3$, with $Pe_r = 10^2$ gives the results in Fig. 5.18.

A fluid hump still exists at the leading edge of the front (Fig. $5.18(a)$); the spreading is

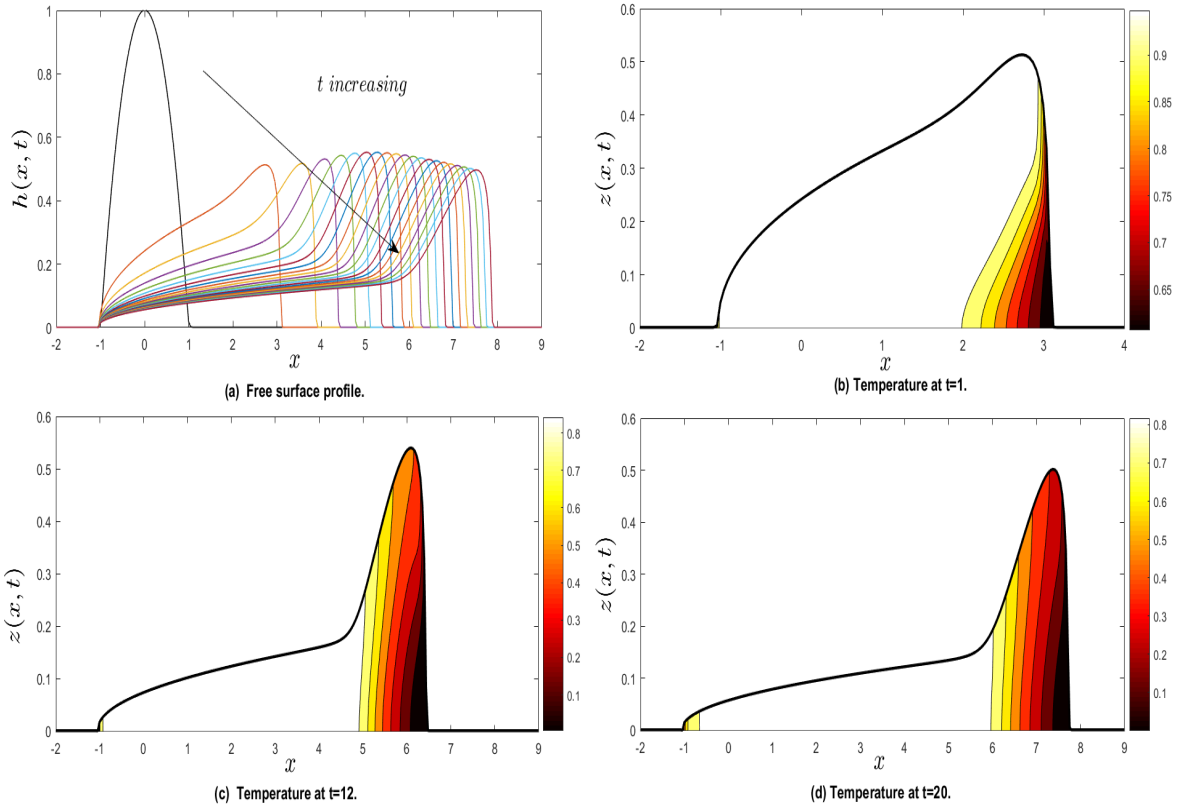

Figure 5.18: The evolution of (a) $h(x,t)$ for t varying between $t = 0-20$ and the contour plot for (b) $\theta(x,z,t=1)$, (c) $\theta(x,z,t=12)$, and (d) $\theta(x,z,t=20)$ (the temperature profiles are superimposed on the corresponding free surface shape h highlighted by thicker curves), with $S = 1$, $Pe_r = 10^2$, $\alpha = 3$, $Q_{s_0} = 0$, $\theta_s = 0$, $a = 0.02$ and $b = 0.03$.

faster than the corresponding case with $\alpha = 2$ (see Fig. 5.16(a)). The hump in this case is slightly bigger in height and sharper than that for $\alpha = 2$. The temperature profiles show that the maximum cooling is near the front causing the fluid humps to form, the mechanism identified in Chapter 4. Decreasing Pe_r to 0.1 with $\alpha = 3$, the free surface

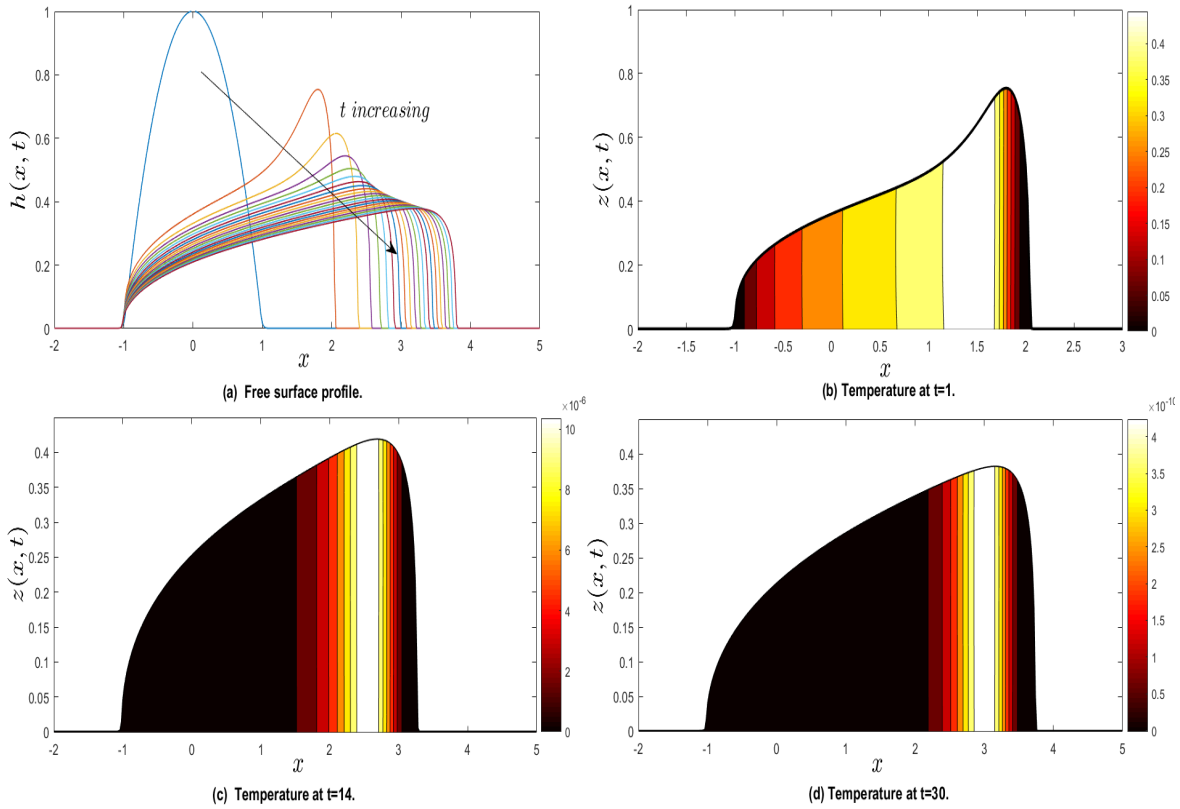

Figure 5.19: The evolution of (a) $h(x,t)$ for t varying between $t = 0-20$ and the contour plot for (b) $\theta(x,z,t=1)$, (c) $\theta(x,z,t=14)$, and (d) $\theta(x,z,t=30)$ (the temperature profiles are superimposed on the corresponding free surface shape h highlighted by thicker curves), with $S = 1$, $Pe_r = 0.1$, $\alpha = 3$, $Q_{s_0} = 0$, $\theta_s = 0$, $a = 0.02$ and $b = 0.03$.

profiles at later times to be similar to the isothermal case (Fig. 5.19(a)). However, at early time there exist fluid humps (Fig. 5.19(a)). The temperature difference between the front and the bulk liquid behind is still sufficiently strong (Fig. 5.19(b))) for the fluid behind to be more mobile than that ahead, resulting in the flow forming a fluid

hump. As time progresses, the cooling at the front progresses into the bulk liquid resulting in the temperature within the dome to be $\theta = 0$ (Fig. 5.19(c, d))). Fig. 5.20 shows $h(x, t = 20)$ for $\alpha = 3$, $a = 0.02$ and $b = 0.03$ and varying Péclet number, Pe.

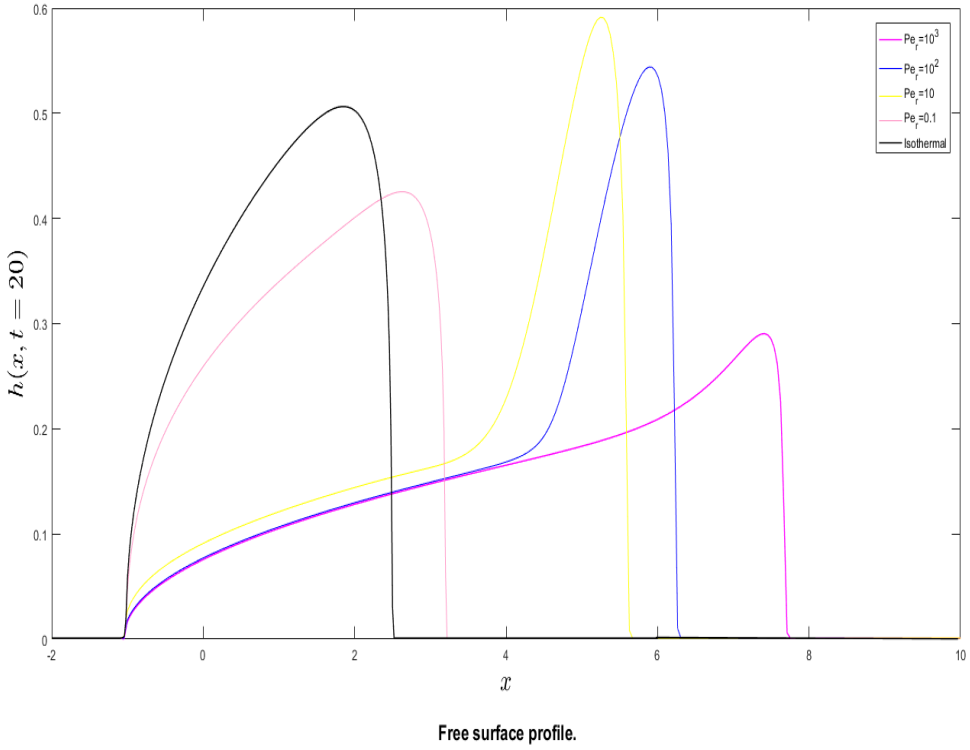

Figure 5.20: The dome height, $h(x, t = 20)$, for $\alpha = 3$ and varying Péclet number, Pe, $Q_{s_0} = 0$, $\theta_s = 0$, $a = 0.02$ and $b = 0.03$.

We observe two distinct types of profiles. A slumped dome-shaped profile with a fluid hump at it's leading edge is observed roughly for Péclet numbers roughly between $10 < Pe_r < 10^3$. For $Per > 10^3$ and $Pe_r < 10$, we observe the usual slumped dome-shaped profile with a steep front at it's leading edge but no fluid hump. The results in Figs. 5.21, 5.22 show the effects of varying the heat transfer coefficients a and b. They show that for low values of a, b, the cooling is localised near the front with the majority

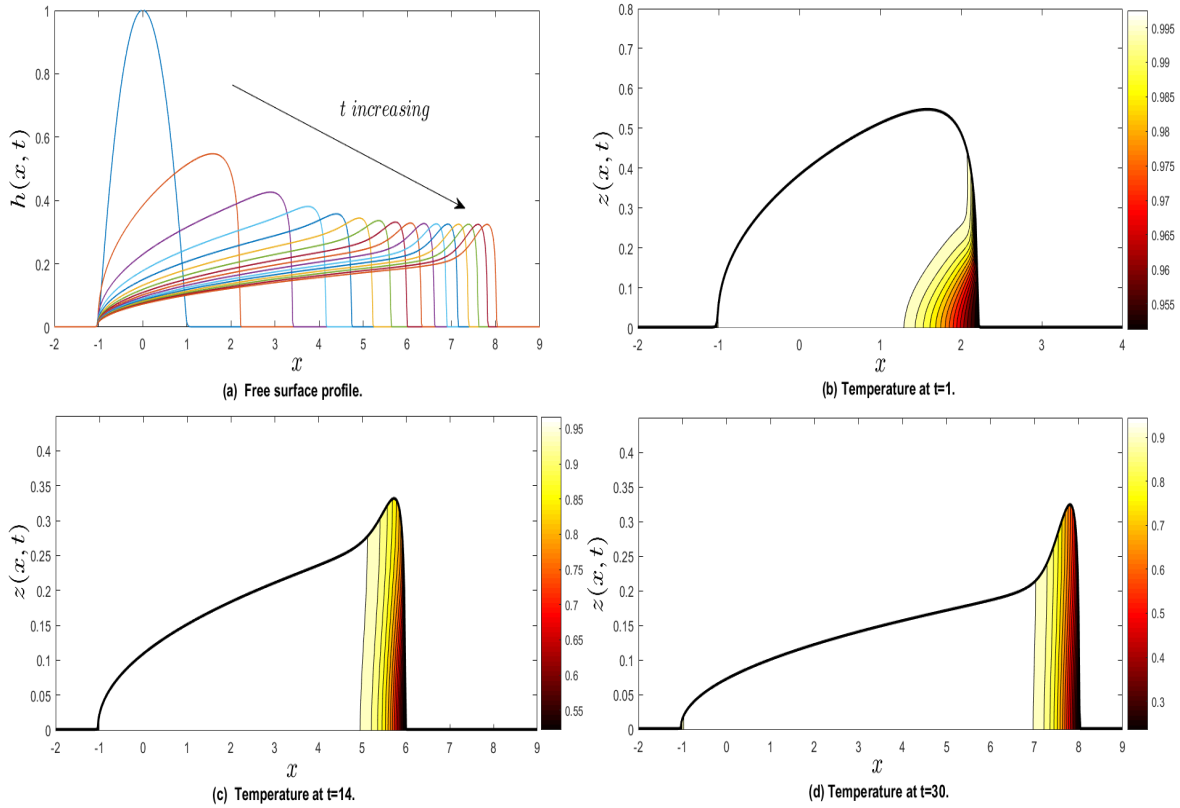

Figure 5.21: The evolution of (a) $h(x,t)$ for t varying between $t = 0-30$ and the contour plot for (b) $\theta(x,z,t=1)$, (c) $\theta(x,z,t=14)$, and (d) $\theta(x,z,t=30)$ (the temperature profiles are superimposed on the corresponding free surface shape h highlighted by thicker curves), with $S = 1$, $Pe_r = 10^2$, $\alpha = 2$, $Q_{s_0} = 0$, $\theta_s = 0$, $a = 2 \times 10^{-4}$ and $b = 3 \times 10^{-4}$.

of the bulk liquid being isothermal with temperature close to unity (Fig. $5.21b-d$). As a and b are increased, we observe that the cooling not only occurs near the front but also within the bulk, although not as high as that near the front (Fig. $5.22(b-d)$). The increased viscosity in this case slows down the spreading rate and the evolution is close to the isothermal case with $\theta \approx 0$. Fig. 5.23 is a parameter survey in $(a = b, Pe)$

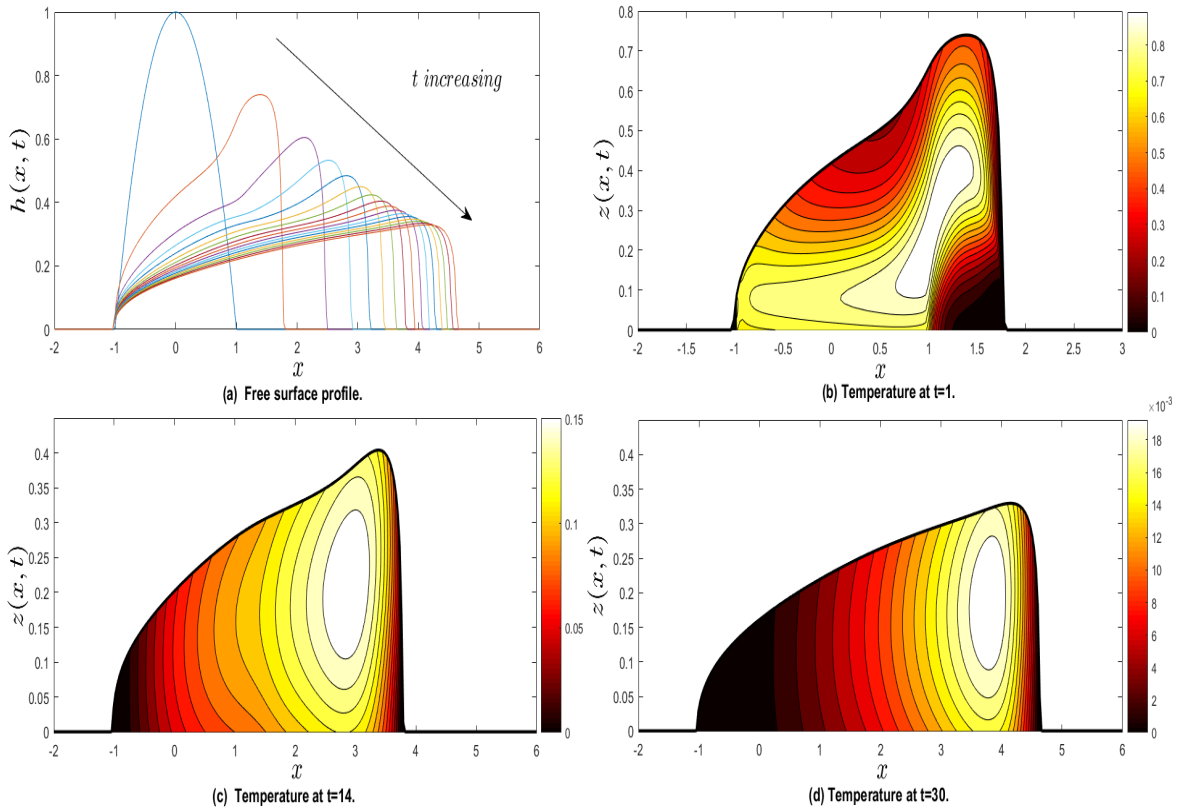

Figure 5.22: The evolution of (a) $h(x,t)$ for t varying between $t = 0-30$ and the contour plot for (b) $\theta(x,z,t=1)$, (c) $\theta(x,z,t=14)$, and (d) $\theta(x,z,t=30)$ (the temperature profiles are superimposed on the corresponding free surface shape h highlighted by thicker curves), with $S = 1$, $Pe_r = 10^2$, $\alpha = 2$, $Q_{s_0} = 0$, $\theta_s = 0$, $a = 2$ and $b = 3$.

space with $\alpha = 2$ and $S = 1$ (inclination angle approximately 6^o) to show the existence of free surface shapes, $h(x,t)$ with and without a fluid hump near the leading edge. If we were to extend the above investigation in two-dimensional $(Pe, a = b)$ space to

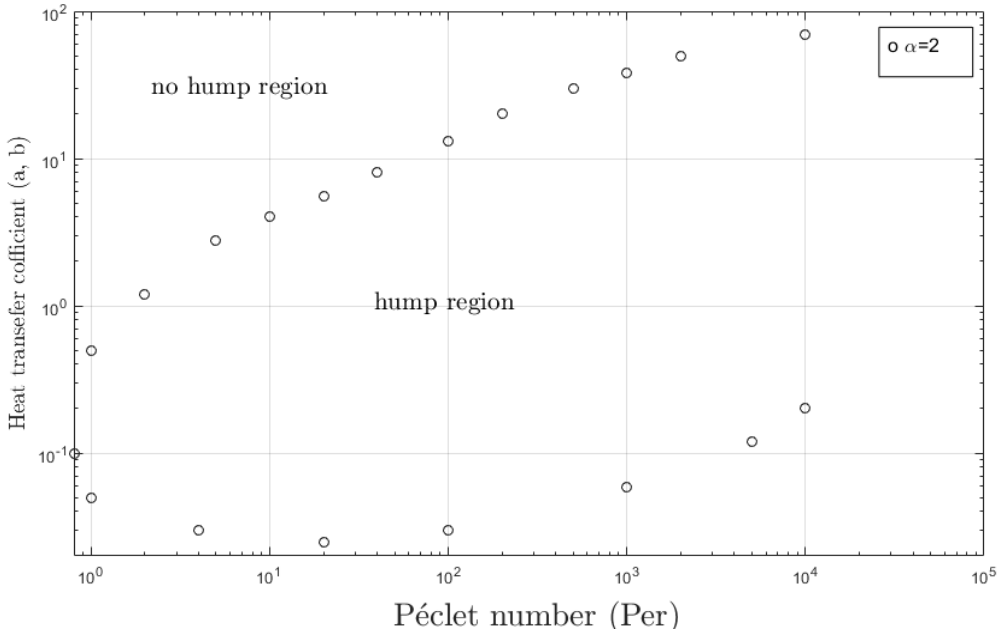

Figure 5.23: Parameter survey in $(Pe, a = b)$ space to show existence of free surface shapes, $h(x,t)$ with and without a fluid hump (or ridge). The parameter values are: $\alpha = 2$ and $S = 1$ (inclination angle approximately 6^o).

three-dimensional $(a = b, Pe, \alpha)$ space, we speculate that the regions of humps would expand as α increases. We also speculate that the height of the fluid hump would get bigger as α increases. This is due to the liquid viscosity difference between the hotter bulk liquid behind the front and the colder liquid at the front being even more enhanced for larger values of α. We now consider the effects of an influx of liquid from a source or vent with flowrate, $Q_{s_0} = 5$. Fig. 5.24 shows the influence of the flowrate with $Pe_r = 10^4$, $\alpha = 2$, $a = 0.02$ and $b = 0.03$. The free surface profiles (Fig. 5.24(a)) show that using a large reduced Péclet number leads to almost isothermal spreading with low viscosity. The temperature profiles (Fig. 5.24$(b-d)$) show minimum cooling within the bulk liquid with a cooler collar region forming around the edge of the front and the substrate. Decreasing the reduced Péclet number to $Pe_r = 10^2$, in Fig. 5.25,

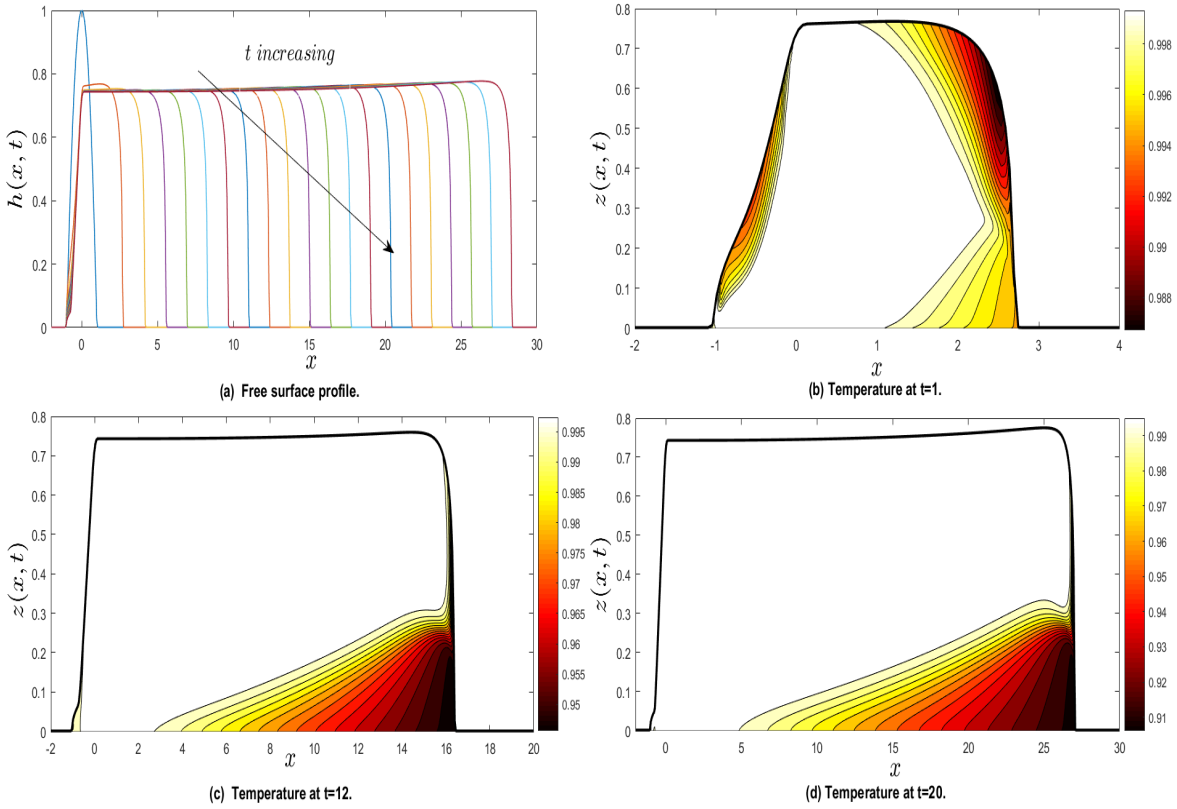

Figure 5.24: The evolution of (a) $h(x,t)$ for t varying between $t = 0-20$ and the contour plot for (b) $\theta(x,z,t=1)$, (c) $\theta(x,z,t=12)$, and (d) $\theta(x,z,t=20)$ (the temperature profiles are superimposed on the corresponding free surface shape h highlighted by thicker curves), with $S = 1$, $Pe_r = 10^4$, $\alpha = 2$, $Q_{s_0} = 5$, $\theta_s = 0$, $a = 0.02$ and $b = 0.03$.

the free surface profiles show a noticeable growing hump over the majority of the dome (Fig. 5.25(a)). The temperature profiles show maximum cooling near the flow front

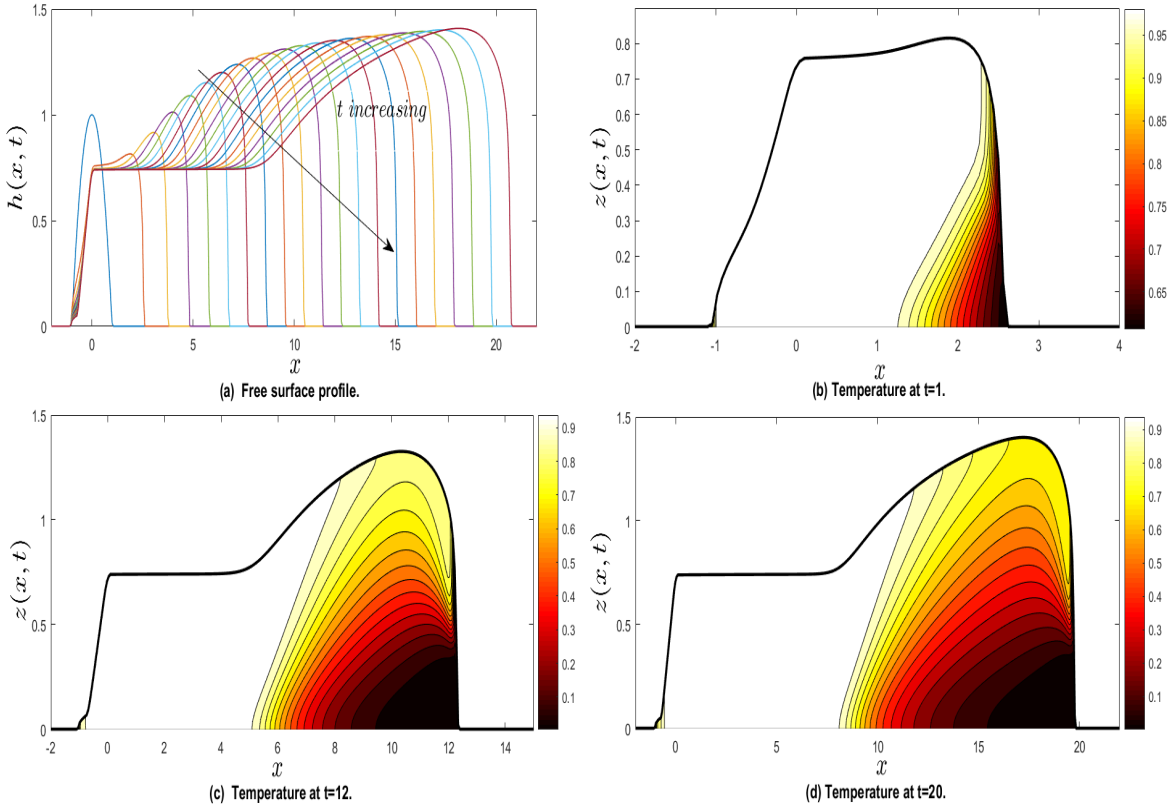

Figure 5.25: The evolution of (a) $h(x,t)$ for t varying between $t = 0-20$ and the contour plot for (b) $\theta(x,z,t=1)$, (c) $\theta(x,z,t=12)$, and (d) $\theta(x,z,t=20)$ (the temperature profiles are superimposed on the corresponding free surface shape h highlighted by thicker curves), with $S = 1$, $Pe_r = 10^2$, $\alpha = 2$, $Q_{s_0} = 5$, $\theta_s = 0$, $a = 0.02$ and $b = 0.03$.

causing build up a very viscous and cold fluid near the flow front. The hot interior fluid piles-up over this cooler region and develops a fluid hump. The mechanism is similar to the case of zero flowrate, except that the constant flowrate through the vent increases the volume of hot fluid piling-up into the fluid hump. The next set of results with flowrate, $Q_{s_0} = 0.5$ and $Pe_r = 10^4$, and varying the heat transfer coefficients are illustrated in Figs. 5.26 (for $h(x,t)$), 5.27 (for corresponding $\theta(x,z,t)$). The results

in Fig. 5.26 show the effects of increasing a and b superimposed on the free surface shape profiles. Figure 5.27 show that the temperature profiles quickly cool down for increasing a and b, where sufficiently large values of a and b lead to the free surface profile developing the growing hump. The temperature profiles show similar behaviour to the previous figures (Fig. 5.21-5.22).

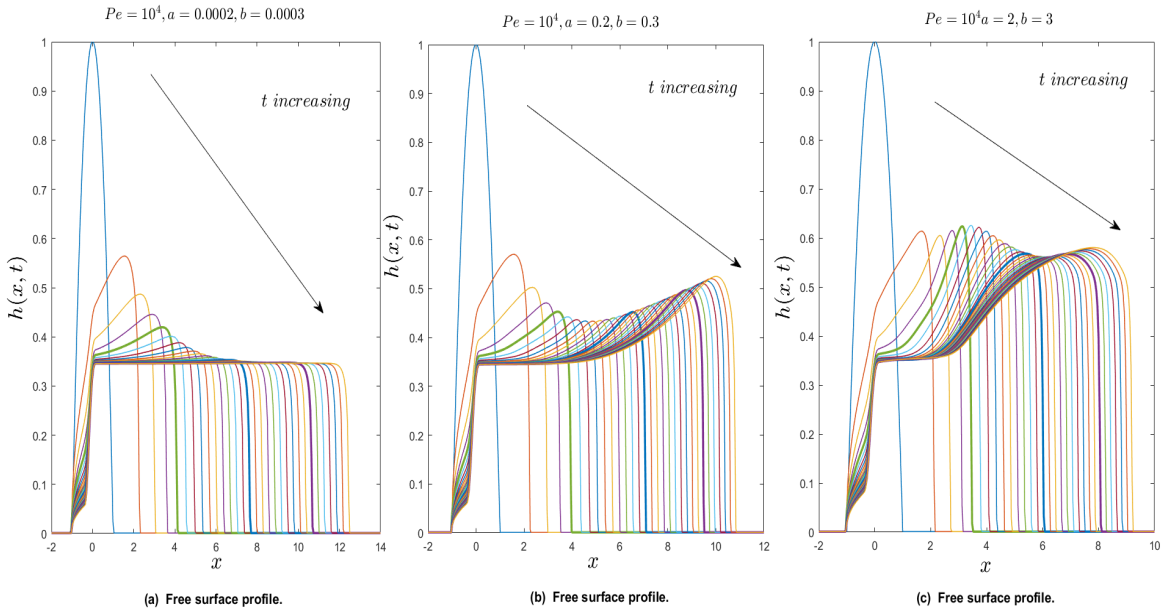

Figure 5.26: The evolution of $h(x,t)$ for t varying between $t = 0 - 30$ with $Pe_r = 10^4$, $a = 2 \times 10^{-4}$ and $b = 3 \times 10^{-4}$ (left panel), $Pe_r = 10^4$, $a = 0.2$ and $b = 0.3$ (middle panel) and $Pe_r = 10^4$, $a = 2$ and $b = 3$ (right panel). The other parameter values are: $S = 1$, $Q_{s_0} = 0.5$ and $\theta_s = 0$.

The next set of results consider the evolution of $h(x,t)$ and $\theta(x,z,t)$ using the bi-viscosity model (see Eq. (4.17b). We set μ_a=1, $\mu_e < \mu_a = 10^{-2}$ and $\theta_m = 0.5$ (note: $0 < \theta_m < 1$). We set $\mu_e = 0.01$ to obtain a large viscosity ratio between the region with the temperature less than θ_m and that with θ greater than θ_m. The initial temperature of the dome is $\theta = 1$. We only show selected numerical results where the free surface

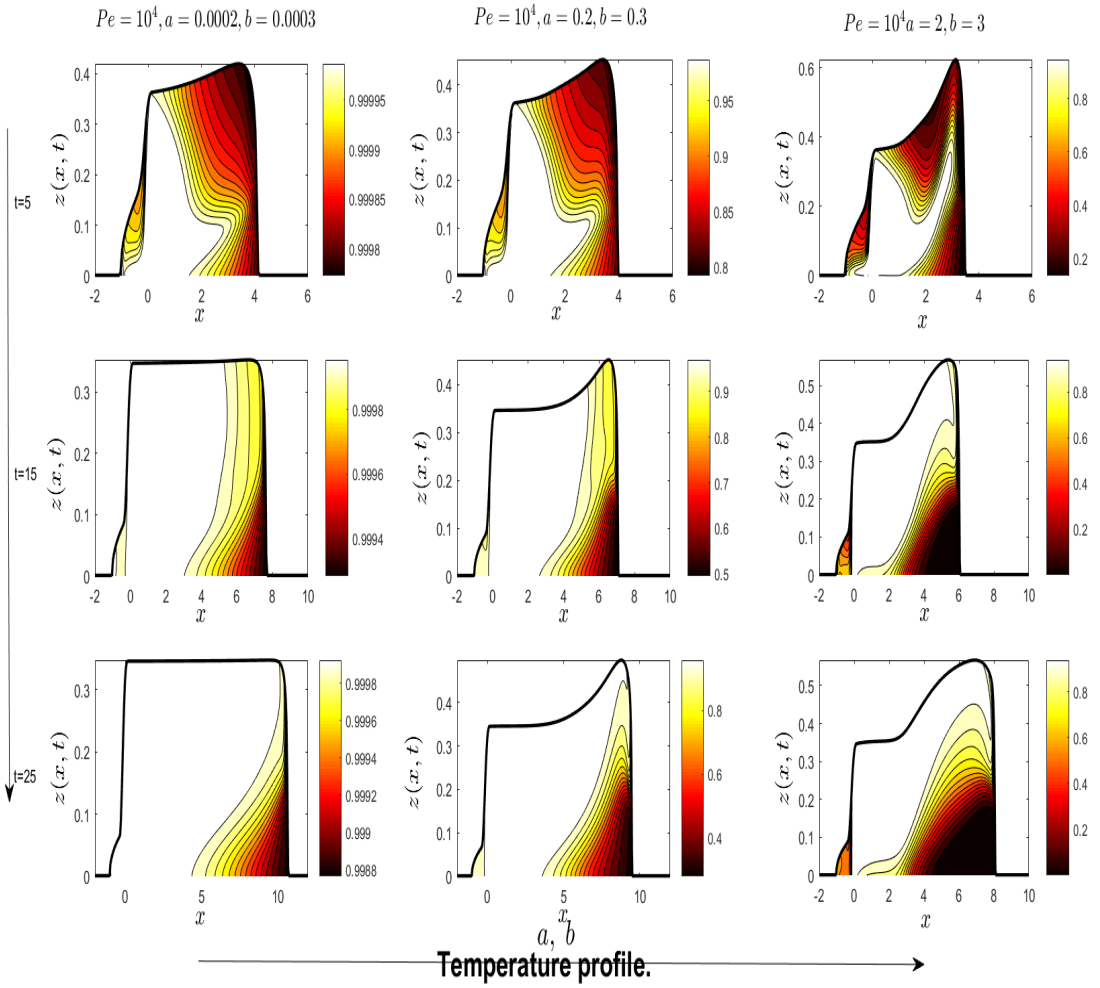

Figure 5.27: The contour plot for $\theta(x, z, t = 5, 15, 25)$ for $Pe_r = 10^4$, $a = 2 \times 10^{-4}$ and $b = 3 \times 10^{-4}$ (left panel), $Pe_r = 10^4$, $a = 0.2$ and $b = 0.3$ (middle panel) and $Pe_r = 10^4$, $a = 2$ and $b = 3$ (right panel). The temperature profiles are superimposed on the corresponding free surface shape h highlighted by thicker curves. The parameter values are: $S = 1$, $Q_{s_0} = 5$ and $\theta_s = 0$.

evolution using the bi-viscosity model is structurally different from the previous results using the exponential viscosity model, keeping all other parameters the same. Sitting $Pe_r = 10^2$, and $\mu_e = 0.01$, $\theta_m = 0.5$ gives results shown in Fig. 5.28. The jump in the

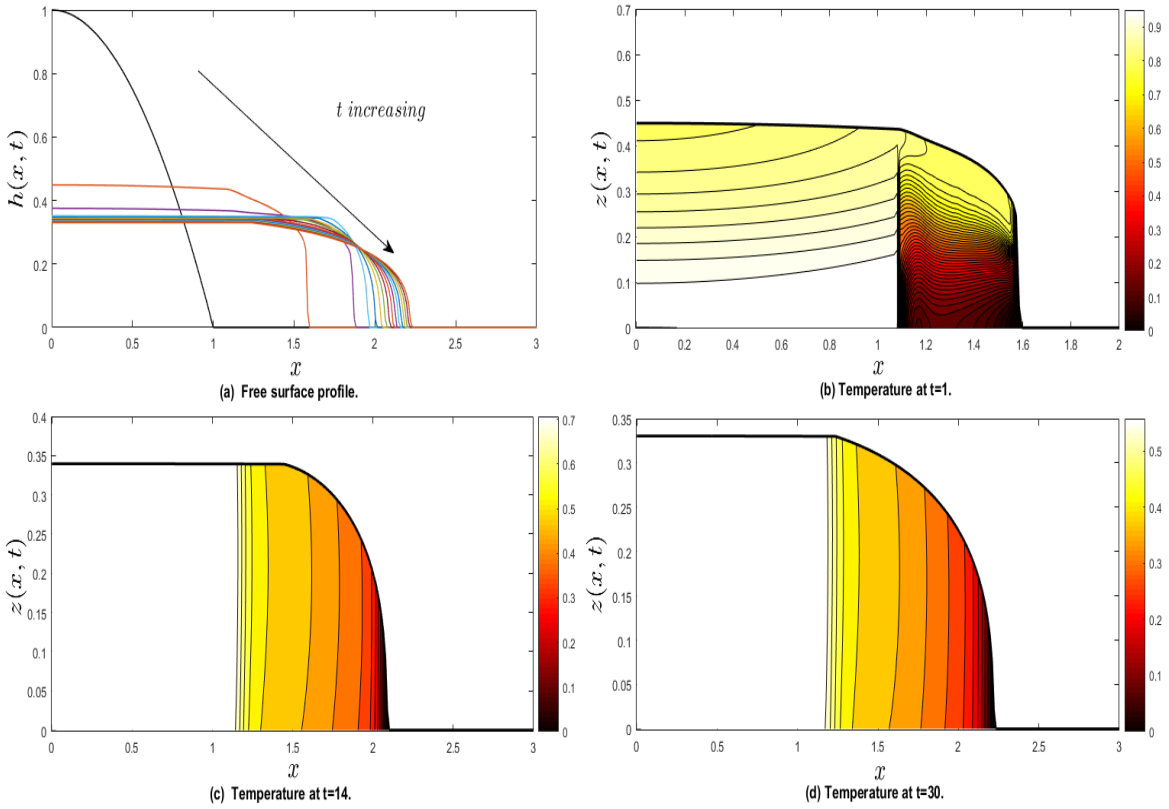

Figure 5.28: The evolution of (a) $h(x,t)$ for t varying between $t = 0-30$ and the contour plot for (b) $\theta(x,z,t=1)$, (c) $\theta(x,z,t=14)$, and (d) $\theta(x,z,t=30)$ (the temperature profiles are superimposed on the corresponding free surface shape h highlighted by thicker curves), with $S = 0$, $Pe_r = 10^2$, $Q_{s_0} = 0$, $\theta_s = 0$, $a = 0.2$ and $b = 0.3$, $\mu_e = 0.01$ and $\theta_m = 0.5$.

viscosity occurring where $\theta_m = 0.5$ affects the free surface profiles. The height profiles show a steep flow front at early time caused by the sharp increase in viscosity near the front as seen in Fig. 5.28(b). For later times the discontinuity is not noticeable and the temperature is almost everywhere less than θ_m producing a very viscous cold region.

Increasing $\theta_m = 0.9$, Fig. 5.29(a) shows the free surface profiles to be similar to the

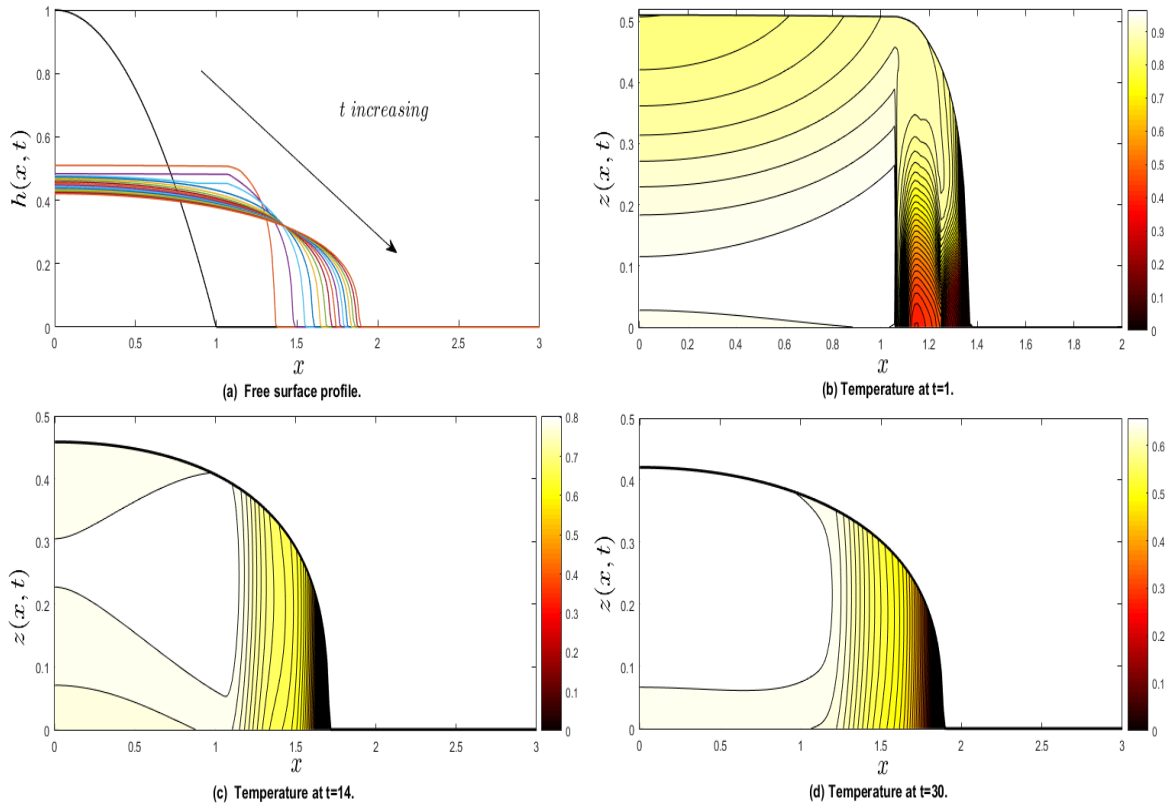

Figure 5.29: The evolution of (a) $h(x,t)$ for t varying between $t = 0-30$ and the contour plot for (b) $\theta(x,z,t=1)$, (c) $\theta(x,z,t=14)$, and (d) $\theta(x,z,t=30)$ (the temperature profiles are superimposed on the corresponding free surface shape h highlighted by thicker curves), with $S = 0$, $Pe_r = 10^2$, $Q_{s_0} = 0$, $\theta_s = 0$, $a = 0.2$ and $b = 0.3$, $\mu_e = 0.01$ and $\theta_m = 0.9$.

isothermal case where almost everywhere the temperature is less than θ_m. Increasing $\mu_m = 0.8$ which resulted in decrease of the viscosity contrast over the liquid. Fig. 5.30 shows the results for this case. It can be seen that the free surface profile spreads as in the isothermal case. In Fig. 5.31, the inclusion of the source flowrate with $Pe_r = 10^2$ and $Q_{s_0} = 0.5$ gives the results for free surface profile similar as in the $Q_{s_0} = 0$ case. The temperature profile shows that cooling is significant near the flow front causing

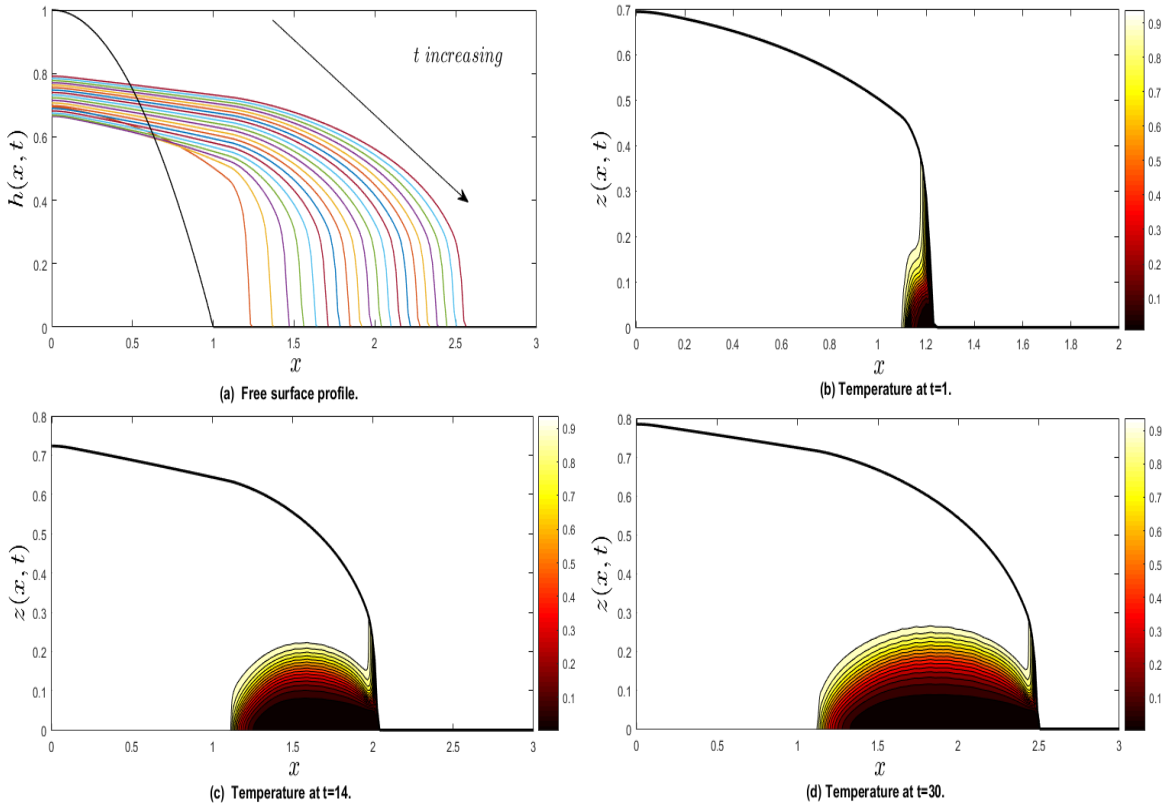

Figure 5.30: The evolution of (a) $h(x,t)$ for t varying between $t = 0-30$ and the contour plot for (b) $\theta(x,z,t=1)$, (c) $\theta(x,z,t=14)$, and (d) $\theta(x,z,t=30)$ (the temperature profiles are superimposed on the corresponding free surface shape h highlighted by thicker curves), with $S = 0$, $Pe_r = 10^2$, $Q_{s_0} = 0$, $\theta_s = 0$, $a = 0.2$ and $b = 0.3$, $\mu_e = 0.8$ and $\theta_m = 0.9$.

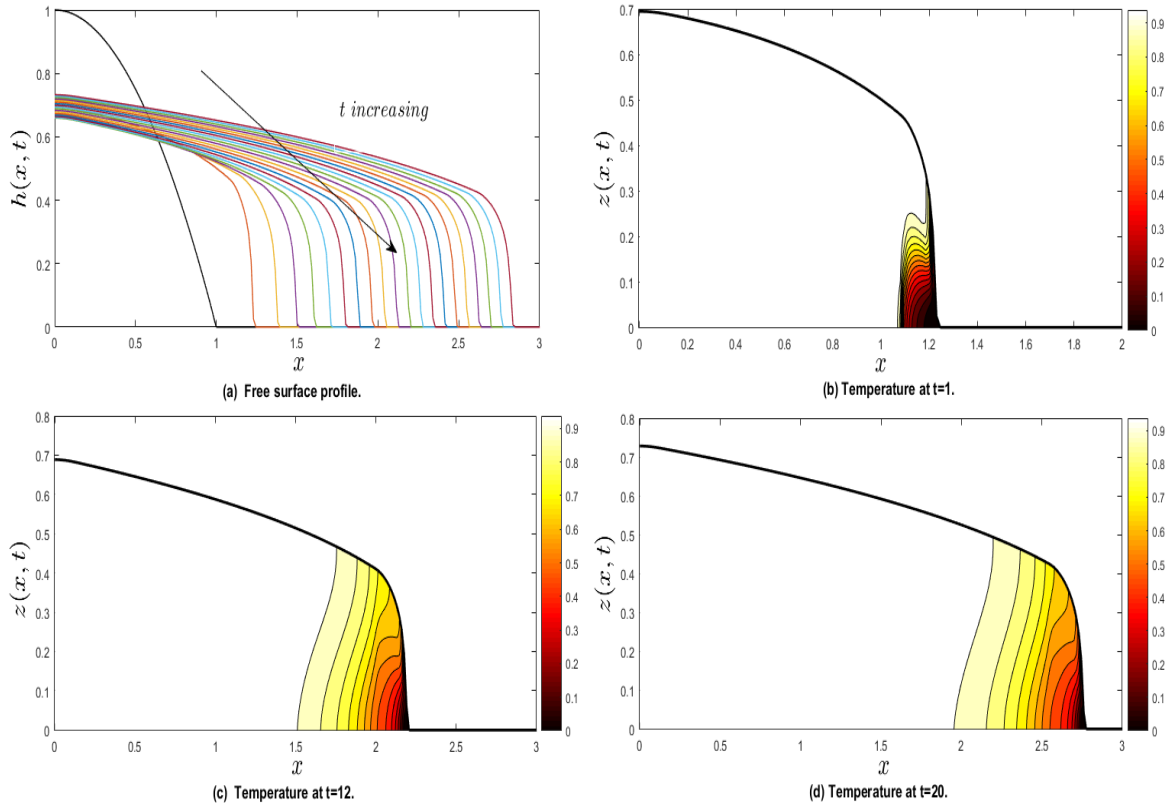

Figure 5.31: The evolution of (a) $h(x,t)$ for t varying between $t = 0-30$ and the contour plot for (b) $\theta(x,z,t=1)$, (c) $\theta(x,z,t=14)$, and (d) $\theta(x,z,t=30)$ (the temperature profiles are superimposed on the corresponding free surface shape h highlighted by thicker curves), with $S = 0$, $Pe_r = 10^2$, $Q_{s_0} = 5$, $\theta_s = 0$, $a = 0.2$ and $b = 0.3$, $\mu_e = 0.01$ and $\theta_m = 0.5$.

the leading edge to become steep. This is because the temperature of the liquid in the dome has $\theta < \theta_m$. Again increasing $\theta_m = 0.9$, Fig. 5.32 shows the results that are

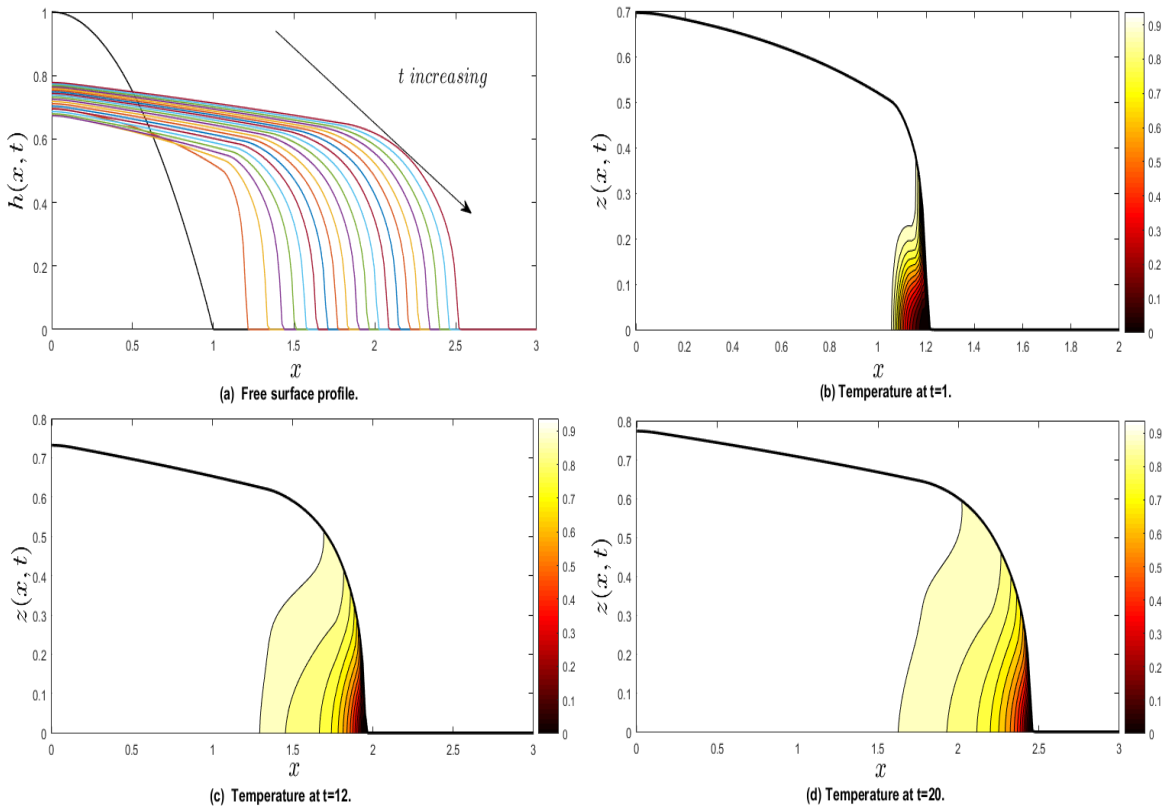

Figure 5.32: The evolution of (a) $h(x,t)$ for t varying between $t = 0-30$ and the contour plot for (b) $\theta(x,z,t=1)$, (c) $\theta(x,z,t=14)$, and (d) $\theta(x,z,t=30)$ (the temperature profiles are superimposed on the corresponding free surface shape h highlighted by thicker curves), with $S = 0$, $Pe_r = 10^2$, $Q_{s_0} = 5$, $\theta_s = 0$, $a = 0.2$ and $b = 0.3$, $\mu_e = 0.01$ and $\theta_m = 0.9$.

similar to the $\alpha = 2$ case with less spreading. In the following set of results, we consider the bi-viscosity model with spreading over an inclined plane with $S = 1$. First, sitting $\mu_e = 0.01$ and $\theta_m = 0.5$ gives again a large viscosity ratio between the region with the temperature less than or greater than θ_m. Figure 5.33 with $P_r = 1$ shows the results for the free surface profile with significant hump arising at a early time but decreases in

size as time progresses. The viscosity difference at $\theta_m = 0.5$ is shown to influence the

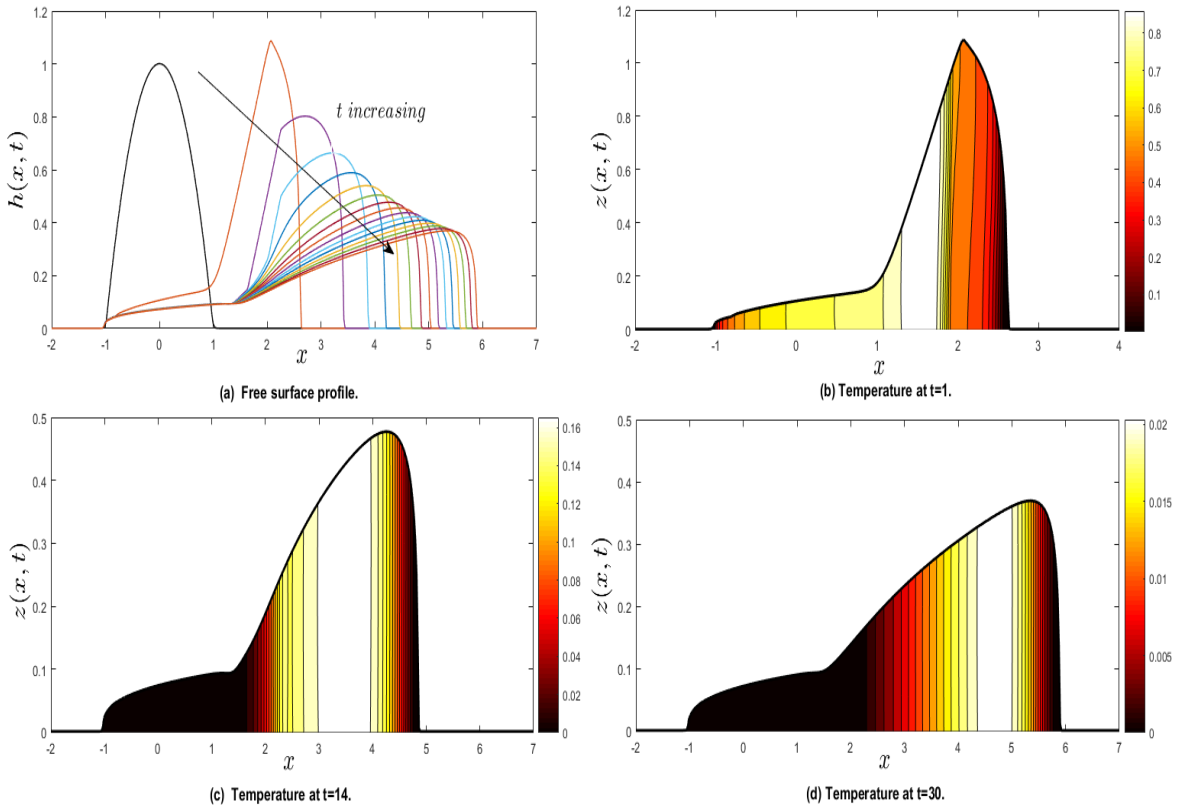

Figure 5.33: The evolution of (a) $h(x,t)$ for t varying between $t = 0-30$ and the contour plot for (b) $\theta(x,z,t=1)$, (c) $\theta(x,z,t=14)$, and (d) $\theta(x,z,t=30)$ (the temperature profiles are superimposed on the corresponding free surface shape h highlighted by thicker curves), with $S = 1$, $Pe_r = 1$, $Q_{s_0} = 0$, $\theta_s = 0$, $a = 0.02$ and $b = 0.03$, $\mu_e = 0.01$ and $\theta_m = 0.5$.

temperature at early time due to a cooler and hence more viscous region developing near the flow front and a hotter and less viscous region behind it (Fig. 5.33(b)). This results in the hotter mobile liquid flowing over the colder liquid ahead, hence forming a fluid hump (Fig. 5.33(a)) at early times. As time progresses, the temperature profile for later times is less than θ_m over the entire dome, hence $\mu(\theta) = 1$ holds everywhere. The final set of results shown in Fig. 5.34 considers the same parameters as the case

shown above, except increasing θ_m to $\theta_m = 0.9$. We clearly observe suppression of the fluid hump at early time. This is due to the temperature quickly dropping below $\theta_m = 0.9$, hence not enabling the full influence of the viscosity contrast in comparison to the previous case with $\theta_m = 0.5$ (Fig. 5.34(b)). As time progresses, the temperature is below θ_m (Fig. 5.34($c-d$)) and the spreading progresses with $\mu = 1$ and is similar to the isothermal case (Fig. 5.34(a)).

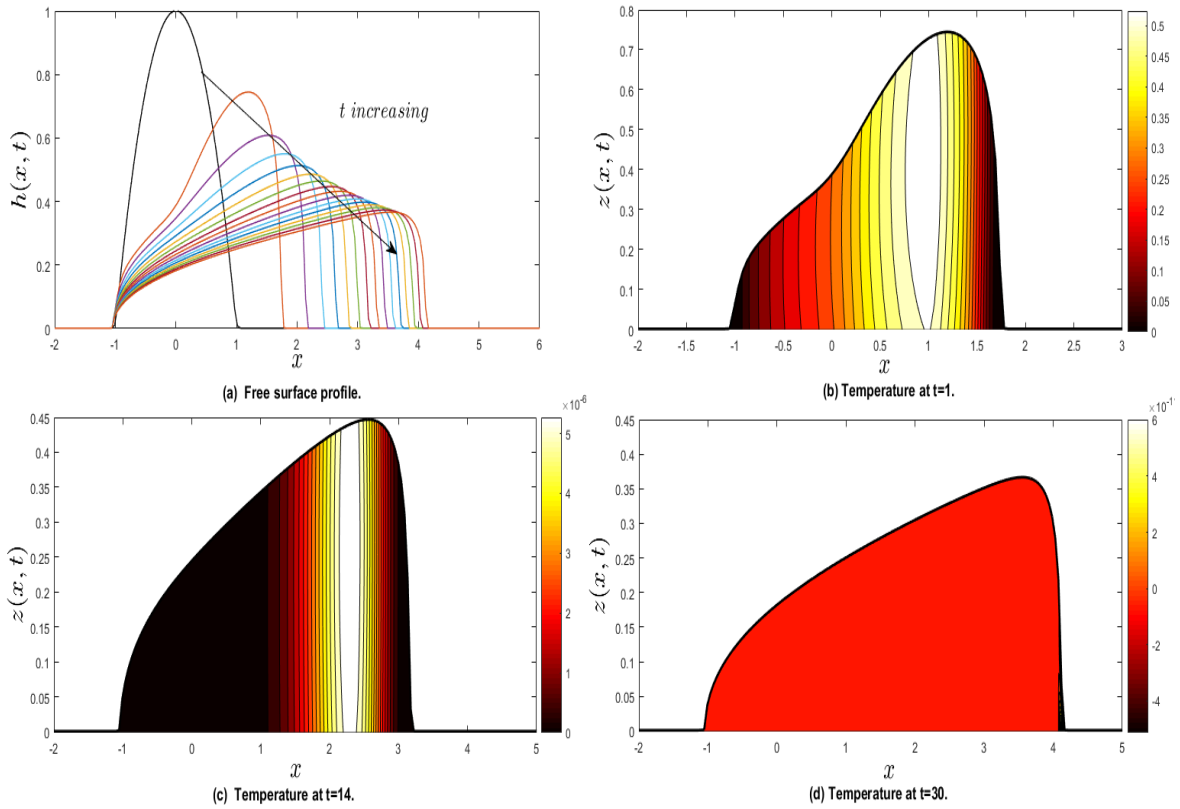

Figure 5.34: he evolution of (a) $h(x,t)$ for t varying between $t = 0-30$ and the contour plot for (b) $\theta(x,z,t=1)$, (c) $\theta(x,z,t=14)$, and (d) $\theta(x,z,t=30)$ (the temperature profiles are superimposed on the corresponding free surface shape h highlighted by thicker curves), with $S = 1$, $Pe_r = 1$, $Q_{s_0} = 0$, $\theta_s = 0$, $a = 0.02$ and $b = 0.03$, $\mu_e = 0.01$ and $\theta_m = 0.9$.

5.4 Conclusions

In this chapter we use the thin-film flow equations coupled to a two-dimensional advection-diffusion equation for the temperature to investigate the spreading and cooling of a hot Newtonian liquid down an inclined plane for the reduced Péclet number, $Pe_r = O(1)$. We consider non-isothermal conditions which include a temperature-dependent viscosity and heat loss due to cooling at the free surface and substrate. Our results highlight a very important feature during the spreading process which is the cooling near the dome's rim where the rate of heat loss is maximum. The extent of this cooling could range from a *collar* of colder liquid near the dome's rim to one where the temperature isotherms become almost vertical across the dome (Balmforth *et al.* [7, 11]). An extensive parameter study reveals the influence of the system parameters on this cooling, particularly, the Péclet number, Pe, the decay constant in the exponential viscosity model, α, and the heat transfer coefficients, a and b. The resulting temperature and viscosity contrast arising due to the cooling near the dome's edge results in a variety of free surface shape profiles.

For spreading on a horizontal substrate ($S = 0$), we recover the free surface shapes previously identified in the studies by Sansom *et al.* [76, 53, 77] and Balmforth *et al.* [7, 11]. These include,

(i) a dome-shaped profile with a steep front at its leading edge which thins and spreads as it evolves (see Figs. 5.1-5.6) for low values of α, and

(*ii*) a flattened middle or plateau region with a much steeper front at its leading edge, similar to a pancake-shaped profile, for larger values of α and Pe_r (see Figs. 5.9). The spreading rate of these structures is also much higher than the dome-shaped ones.

The new results in this chapter are related to spreading down an inclined substrate (shown for $S = 1$, with approximately 6^o inclination angle). The cooling mechanism described above also holds here. In addition, the mobility of the dome is also enhanced due to the inclination of the substrate. Our parameter study reveals two distinct free surface shapes (see Fig. 5.20):

(i) a slumped dome-shaped profile with a steep front for very large Pe_r (see Figs. 5.13-5.14 and possibly small Pe_r (results not shown here), and

(ii) a slumped profile with a fluid hump overriding the steep front at its leading edge for intermediate values of Pe_r (see Figs. 5.16-5.18).

We observe that the hump height increases as α increases. Including a constant flowrate liquid results in sustained increase in the hump-shaped profile (Fig. 5.25, 5.26).

The free surface profiles, particularly, the pancake and hump-shaped profiles, obtained in Chapter 4 using the approximate theory valid for $\epsilon^2 Pe_r \ll 1$ are also reproduced here for small and intermediate values of Pe_r and α. Although we have not made a direct comparison between both sets of results, based on the nearly vertical isotherms observed in the temperature profiles for this parameter range, we can be confident

about the validity of the approximate theory.

Encouraged by this, we will investigate the transverse stability of these one-dimensional free surface shapes using the small Pe_r reduced model for the temperature field coupled to the thin-film equation. This will be done in Chapter 6.

Chapter 6

The non-isothermal and Newtonian spreading of a hot liquid dome down an inclined plane: stability of transverse perturbations

6.1 Introduction

In this chapter we extend the non-isothermal problem from the previous two chapters to $2+1$ dimensions, (x, y), and the free surface, $z = h(x, y, t)$. Encouraged by the results using the small reduced Péclet number asymptotic limit in Chapter 4 and their validity shown in Chapter 5, we consider this asymptotic limit here for the temperature field

with $\theta(x, y, t)$. Our goal is to investigate the transverse stability of the one-dimensional solutions (the base state) for h and θ obtained in Chapter 4. The base state is usually represented by a steady-state (time-independent) solution of the system, however, Eqs. 6.33 do not have a steady state. One way to analyse the linear stability of such solutions is to assume that the basic state is slowly varying in time or quasi-steady. One can then *freeze* the basic state and superimpose the transverse perturbations on it. These perturbations are assumed to vary on a much faster timescale compared to the basic state. An alternative way is to perform a *transient analysis* (see, e.g., Matar *et al.* [27]. Our focus is in investigating the evolution of h, and temperature θ, particularly the growth rate and wavenumber of any transverse spatial instability that develops in time over the base state.

The outline of this chapter is as follows. In §6.1.1 we formulate the problem and state the governing equations and boundary conditions. Lubrication theory is used to simplify the equations to two coupled PDEs in $h(x, y, t)$ and $\theta(x, y, t)$. In §6.2, we perform a numerical stability analysis to determine the stability of transverse perturbations on a prescribed base state. In §6.3, we discuss the mechanism(s) underlying the fingering transverse instability observed in numerical simulations.

6.1.1 Governing Equations

The three-dimensional flow of a Newtonian liquid of constant density, $\rho^\star$, and variable viscosity, $\mu^\star$, are given by the conservation of mass and momentum which is written in

a Cartesian co-ordinate system, $(x^\star, y^\star, z^\star)$ as (see Acheson [1] and Ockendon [66]):

$$u^\star_{x^\star} + v^\star_{y^\star} + w^\star_{z^\star} = 0, \tag{6.1a}$$

$$u^\star_{t^\star} + u^\star u^\star_{x^\star} + v^\star u^\star_{y^\star} + w^\star u^\star_{z^\star} = -\frac{1}{\rho^\star} p^\star_{x^\star} + g^\star \sin\theta + \frac{1}{\rho^\star}[\partial^\star_x \tau^\star_{x^\star x^\star} + \partial^\star_y \tau^\star_{x^\star y^\star} + \partial^\star_z \tau^\star_{x^\star z^\star}], \tag{6.1b}$$

$$v^\star_{t^\star} + u^\star v^\star_{x^\star} + v^\star v^\star_{y^\star} + w^\star v^\star_{z^\star} = -\frac{1}{\rho^\star} p^\star_{y^\star} + \frac{1}{\rho^\star}[\partial^\star_x \tau^\star_{y^\star x^\star} + \partial^\star_y \tau^\star_{y^\star y^\star} + \partial^\star_z \tau^\star_{y^\star z^\star}], \tag{6.1c}$$

$$w^\star_{t^\star} + u^\star w^\star_{x^\star} + v^\star w^\star_{y^\star} + w^\star w^\star_{z^\star} = -\frac{1}{\rho^\star} p^\star_{z^\star} - g^\star \cos\theta + \frac{1}{\rho^\star}[\partial^\star_x \tau^\star_{z^\star x^\star} + \partial^\star_y \tau^\star_{z^\star y^\star} + \partial_{z^\star} \tau^\star_{z^\star z^\star}], \tag{6.1d}$$

where $(u^\star, v^\star, w^\star)$ are the flow speed in the $x^\star$, $y^\star$ and $z^\star$ directions, respectively, $\tau^\star_{ij}$ denote the liquid viscous stresses, $p^\star$ is the liquid pressure, $g^\star$ is the gravitational force and θ is the inclination angle of the substrate. The energy equation governing the temperature, T, is given by (see Carslaw & Jaeger [23]):

$$\rho^\star c^\star_p \left[T^\star_{t^\star} + u^\star T^\star_{x^\star} + v^\star T^\star_{y^\star} + w^\star T^\star_{z^\star}\right] = \kappa^\star \left[T^\star_{xx} + T^\star_{yy} + T^\star_{zz}\right], \tag{6.2}$$

where $c^\star_p$ is the specific heat of the liquid, $\kappa^\star$ is its thermal conductivity or alternatively the liquid's thermal diffusivity is $\kappa^\star_d = \kappa^\star/(\rho^\star c^\star_p)$. The constitutive relation between the liquid stress and its rate of strain for a Newtonian liquid is written as:

$$\boldsymbol{\tau}^\star = \mu^\star(T^\star)\dot{\boldsymbol{\gamma}}^\star, \tag{6.3}$$

where $\mu^\star$ is the liquid viscosity and $\dot{\boldsymbol{\gamma}}^\star$ is the rate of strain tensor given by The dimensionless strain rate tensor becomes

$$\dot{\boldsymbol{\gamma}}^\star = \begin{pmatrix} 2u^\star_{x^\star} & u^\star_{y^\star} + v^\star_{x^\star} & u^\star_{z^\star} + w^\star_{x^\star} \\ u^\star_{y^\star} + v^\star_{x^\star} & 2v^\star_{y^\star} & v^\star_{z^\star} + w^\star_{y^\star} \\ u^\star_{z^\star} + w^\star_{x^\star} & v^\star_{z^\star} + w^\star_{y^\star} & 2w^\star_{z^\star} \end{pmatrix}. \tag{6.4}$$

The viscosity is dependent on the temperature by a constitutive relationship. We use the exponential viscosity model throughout this chapter and is given by:

$$\mu^\star(T^\star) = \mu^\star_0 e^{-\alpha^\star(T^\star - T^\star_a)}, \tag{6.5}$$

where $T^\star_a$ is a reference temperature (e.g., the ambient temperature), $\mu^\star_0$ is the viscosity at the reference temperature and $\alpha^\star$ is the decay constant.

6.1.2 Boundary conditions

As discussed in Chapter 2, we impose the no-slip boundary condition for the velocity field at the surface of the plane $z^\star = 0$, with the flow speed from the source given by $w^\star_s(x^\star, y^\star, t^\star)$ taken as a vertical velocity. Therefore $u^\star = 0,\ w^\star = w^\star_s(x^\star, y^\star, t^\star)$ at $z^\star = 0$. Assuming Poiseuille flow through this vent (assumed rectangular between $|x^\star| \leq x^\star_0, |y^\star| \leq y^\star_0$, where $(x, y)^\star_0$ is the half-width of the source), with liquid flux, $Q^\star_s$,

$w_s^\star$ can be written as:

$$w_s^\star(x^\star, y^\star, t^\star) = \frac{9Q_s^\star(t^\star)}{16x_0^\star y_0^\star}\left[1-\left(\frac{x^\star}{x_0^\star}\right)^2\right]\left[1-\left(\frac{y^\star}{y_0^\star}\right)^2\right]\mathcal{H}(x_0^{\star 2}-x^{\star 2})\mathcal{H}(y_0^{\star 2}-y^{\star 2}), \quad (6.6)$$

where $\mathcal{H}(x^\star)$ is the Heaviside function. As discussed in Chapters 3, 4, the Newton's law of cooling is considered at the free surface, $z^\star = h^\star(x^\star, y^\star, t^\star)$ and the substrate, $z^\star = 0$. The form of the boundary condition for the substrate at $z^\star = 0$ is

$$\kappa^\star T_{z^\star}^\star = \rho^\star c_p^\star(T^\star(x^\star, y^\star, 0, t^\star) - T_e^\star)w_s^\star + b_s(T^\star(x^\star, y^\star, 0, t^\star) - T_s^\star), \quad (6.7)$$

where $T_e^\star$ and $T_s^\star$ are the eruption and substrate temperatures, respectively (assumed constant) and $b_s^\star$ is a heat transfer coefficient. Such a form of the flux function has been used by Balmforth *et al.* [5, 11]. On the free surface, $z^\star = h^\star(x^\star, y^\star, t^\star)$, we have

$$-\kappa^\star(\mathbf{n}^\star \cdot \nabla^\star T^\star) = F^\star[T^\star(x^\star, y^\star, h^\star, t^\star) = a_m^\star(T^\star(x^\star, y^\star, h^\star, t^\star) - T_a^\star), \quad (6.8)$$

where $a_m^\star$ is a heat transfer coefficient at the free surface and $T_a^\star$ is the ambient temperature. Such a form of the flux function has been used by Balmforth *et al.* [5, 11]. Taking the pressure of the liquid in the dome relative to the air pressure and neglecting surface tension, the normal stress at the air-liquid interface is written as:

$$(-p^\star \boldsymbol{I} + \boldsymbol{\tau}^\star)\cdot \mathbf{n}^\star = 0, \quad \text{at} \;\; z^\star = h^\star(x^\star, y^\star, t^\star), \quad (6.9)$$

where, $\mathbf{n}^\star$, the unit outward normal to the free surface $z^\star = h^\star(x^\star, y^\star, t^\star)$ is given by

$$\mathbf{n}^\star = \frac{\nabla^\star \left(z^\star - h^\star(x^\star, t^\star)\right)}{|\nabla^\star \left(z^\star - h^\star(x^\star, t^\star)\right)|} = \frac{1}{\sqrt{1 + h_{x^\star}^{\star 2} + h_{y^\star}^{\star 2}}} \left(-h_{x^\star}^\star, h_{y^\star}^\star, 1\right). \tag{6.10}$$

The corresponding tangent vectors to the free surface in the $x^\star$ and $y^\star$ directions are given by

$$\mathbf{n}^\star \cdot \mathbf{t}_x^\star = 0, \ \Rightarrow \ \mathbf{t}^{\star x} = \frac{1}{\sqrt{1+h_{x^\star}^{\star 2}+h_{y^\star}^{\star 2}}} \left(1, 0, h_{x^\star}^\star\right), \tag{6.11a}$$

$$\mathbf{n}^\star \cdot \mathbf{t}_y^\star = 0, \ \Rightarrow \ \mathbf{t}^{\star x} = \frac{1}{\sqrt{1+h_{x^\star}^{\star 2}+h_{y^\star}^{\star 2}}} \left(0, 1, h_{y^\star}^\star\right). \tag{6.11b}$$

We can write the normal and two tangential components of Eq. (6.9) as

$$\mathbf{n}^\star \cdot (-p^\star \boldsymbol{I} + \boldsymbol{\tau}^\star) \cdot \mathbf{n}^\star = 0, \ \Rightarrow$$

$$\frac{1}{\sqrt{1 + h_{x^\star}^{\star 2} + h_{y^\star}^{\star 2}}}[-2h_{x^\star}^\star \tau_{zx}^\star - 2h_{y^\star}^\star \tau_{yz}^\star + 2h_{x^\star}^\star h_{y^\star}^\star \tau_{xy}^\star + \tau_{zz}^\star + h_{x^\star}^{\star 2} \tau_{xx}^\star + h_{y^\star}^{\star 2} \tau_{yy}^\star] - p^\star = 0, \tag{6.12a}$$

$$\mathbf{t}_\mathbf{x}^\star \cdot (-p^\star \boldsymbol{I} + \boldsymbol{\tau}^\star) \cdot \mathbf{n}^\star = 0, \ \Rightarrow$$

$$h_{x^\star}^\star(\tau_{zz}^\star - \tau_{xx}^\star) + \tau_{xz}^\star(1 - h_{x^\star}^{\star 2}) - h_{x^\star}^\star h_{y^\star}^\star \tau_{yz}^\star - h_{y^\star}^\star \tau_{xy}^\star = 0, \tag{6.12b}$$

$$\mathbf{t}_\mathbf{y}^\star \cdot (-p^\star \boldsymbol{I} + \boldsymbol{\tau}^\star) \cdot \mathbf{n}^\star = 0, \ \Rightarrow$$

$$h_{y^\star}^\star(\tau_{zz}^\star - \tau_{yy}^\star) + \tau_{yz}^\star(1 - h_{y^\star}^{\star 2}) - h_{x^\star}^\star h_{y^\star}^\star \tau_{xz}^\star - h_{x^\star}^\star \tau_{xy}^\star = 0. \tag{6.12c}$$

The kinematic condition at the free surface $z^\star = h^\star(x^\star, y^\star, t^\star)$ is based on this being a material surface so that fluid particles which lie on the surface must always remain on

the surface. This implies that $\frac{D}{Dt}[z^\star - h^\star(x^\star, y^\star, t^\star)] = 0$. This can be written as:

$$h^\star_{t^\star} + u^\star h^\star_{x^\star} + v^\star h^\star_{y^\star} = w^\star. \tag{6.13}$$

6.1.3 Nondimensionalisation and the lubrication approximation

We define an aspect ratio $\epsilon = H^\star/L^\star$, where $L^\star$, is a typical length scale in the flow direction and $H^\star$, is a characteristic dome height. Also, $U^\star$, is a typical flow speed in the $x^\star$ and $y^\star-$direction which is determined below, $\mu^\star_R$, is a reference viscosity, the pressure is measured using a characteristic scale $P^\star = \rho^\star g^\star H^\star \cos\theta$ (the hydrostatic pressure). The equations are nondimensionlised by introducing the following:

$$(x^\star, y^\star) = L^\star(\tilde{x}, \tilde{y}), \;\; (z^\star, h^\star) = H^\star(\tilde{z}, \tilde{h}), \;\; (u^\star, v^\star, w^\star) = (U^\star, \epsilon U^\star)(\tilde{u}, \tilde{v}, \tilde{w}), \;\; p^\star = P^\star \tilde{p},$$

$$\tau^\star = \mu^\star \left(\frac{U^\star}{H^\star}\right)\tilde{\tau}, \;\; \dot{\gamma}^\star = \left(\frac{U^\star}{H^\star}\right)\tilde{\dot{\gamma}}, \;\; \mu^\star = \mu^\star_R \tilde{\mu}, \;\; \theta^\star = \frac{(T^\star - T^\star_e)}{\Delta T^\star}, \;\; t^\star = (L^\star/\tilde{U}^\star)\tilde{t}. \tag{6.14}$$

The characteristic speed $U^\star$ is chosen to balance the horizontal liquid pressure gradient and the liquid shear stress. This gives $U^\star = (\rho^\star g^\star {H^\star}^3)/(\mu^\star L^\star)\cos\theta$.

Dropping the tilde notation, the dimensionless equations for the flow and energy can

be written as:

$$u_x + v_y + w_z = 0, \tag{6.15a}$$

$$\epsilon^2 R_e \left[u_t + uu_x + vu_y + wu_z\right] = -p_x + S + \epsilon\partial_x\tau_{xx} + \epsilon\partial_y\tau_{xy} + \partial_z\tau_{xz}, \tag{6.15b}$$

$$\epsilon^2 R_e \left[v_t + uv_x + vv_y + wv_z\right] = -p_y + \epsilon\partial_x\tau_{yx} + \epsilon\partial_y\tau_{yy} + \partial_z\tau_{yz}, \tag{6.15c}$$

$$\epsilon^4 R_e \left[w_t + uw_x + vw_y + ww_z\right] = -p_z - 1 + \partial_x\epsilon^2\tau_{zx} + \epsilon^2\partial_y\tau_{zy} + \epsilon\partial_z\tau_{zz}, \tag{6.15d}$$

$$\epsilon^2 Pe \left[\theta_t + u\theta_x + v\theta_y + w\theta_z\right] = \left[\epsilon^2\theta_{xx} + \epsilon^2\theta_{yy} + \theta_{zz}\right], \tag{6.15e}$$

The nondimensionalised constitutive relation between the liquid stress and its rate of strain for a Newtonian liquid is written as:

$$\boldsymbol{\tau} = \mu(\theta)\dot{\boldsymbol{\gamma}}. \tag{6.16}$$

The viscosity is dependent on the temperature by a constitutive relationship. We use the exponential viscosity model which in dimensionless form is written as:

$$\mu(\theta) = e^{-\alpha\theta}, \tag{6.17}$$

The dimensionless strain rate tensor becomes

$$\dot{\boldsymbol{\gamma}} = \begin{pmatrix} 2\epsilon u_x & \epsilon(u_y + v_x) & u_z + \epsilon^2 w_x \\ \epsilon(u_y + v_x) & 2\epsilon v_y & v_z + \epsilon^2 w_y \\ u_z + \epsilon^2 w_x & v_z + \epsilon^2 w_y & 2\epsilon w_z \end{pmatrix}. \tag{6.18}$$

The nondimensional boundary conditions at $z = 0$ can be written as:

$$u = 0, \quad w = w_s(x, y, t), \quad \text{at} \quad z = 0, \tag{6.19a}$$

$$\theta_z = P_e\epsilon^2(\theta - 1)w_s + b\epsilon^2(\theta - \theta_s), \quad \text{at} \quad z = 0. \tag{6.19b}$$

The nondimensional boundary conditions at $z = h(x, y, t)$ are given by

$$h_t + uh_x + vh_y = w, \tag{6.20a}$$

$$p = \frac{\epsilon}{[1 + \epsilon^2(h_x^2 + h_y^2)]}(\tau_{zz} + \epsilon^2 h_x^2\tau_{xx} + \epsilon^2 h_y^2\tau_{yy} - 2\epsilon h_x\tau_{xz} - 2\epsilon h_y\tau_{yz} + 2\epsilon^2 h_x h_y\tau_{xy}), \tag{6.20b}$$

$$\tau_{yz}(1 - \epsilon^2 h_y^2) + \epsilon h_y(\tau_{zz} - \tau_{yy}) - \epsilon h_x\tau_{xy} - \epsilon^2 h_x h_y\tau_{xz} = 0, \tag{6.20c}$$

$$\theta_z = \epsilon^2 h_x\theta_x + \epsilon^2 h_y\theta_y - \epsilon^2 a\theta\sqrt{1 + \epsilon^2 h_x^2 + \epsilon^2 h_y^2}. \tag{6.20d}$$

In the above, $w_s(x, t) = [(9Q_{s_0}Q_s(t))/16]\,[1 - (x/x_0)^2]\,[1 - (y/y_0)^2]\,\mathcal{H}(x_0^2 - x^2)\mathcal{H}(y_0^2 - y^2)$, where Q_{s_0} is a dimensionless parameter, $Q_{s_0} = Q^\star_{s_0}/(x_0^\star y_0^\star \epsilon U)$ and $Q^\star_{s_0}$ is a characteristic source flow rate. The dimensionless vent width is $(x_0, y_0) = (x_0^\star, y_0^\star)/L^\star$. The dimensionless parameters are: $S = \tan\theta/\epsilon$, is a measure of the downslope, the Reynold's number, $Re = U^\star L^\star/\mu_R^\star \equiv (g^\star {H^\star}^3/{\mu_R^\star}^2)\cos\theta$, compares inertial and viscous effects and is assumed to be $O(1)$, the Peclet number, $Pe = (\rho^\star c_p^\star U^\star L^\star)/\kappa^\star$, compares convective and diffusive heat transport, the heat transfer coefficients at the free surface and substrate, $b = (b_s H^\star)/(\epsilon^2\kappa^\star)$ and $a = (a_m H^\star)/(\epsilon^2\kappa^\star)$, respectively, and $\alpha = \alpha^\star(T_e^\star - T_a^\star)$, is the decay constant in the exponential viscosity model.

Assuming $\epsilon^2 \ll 1$, the leading order equations governing the flow can be written as, using the lubrication approximation:

$$u_x + v_y + w_z = 0, \tag{6.21a}$$

$$-p_x + \partial_z \tau_{xz} + S = 0, \tag{6.21b}$$

$$-p_y + \partial_z \tau_{yz} = 0, \tag{6.21c}$$

$$-p_z - 1 = 0, \tag{6.21d}$$

$$\tau_{xz} = p = 0,\ h_t + u h_x + v h_y = w, \quad \text{at} \quad z = h(x,t), \tag{6.21e}$$

$$u = 0,\ v = 0,\ w = w_s(x,t), \quad \text{at} \quad z = 0. \tag{6.21f}$$

Integrating Eq. (6.21d) and using the boundary condition for p in Eq. (6.21e) gives $p = h(x,t) - z$. Integrating Eq. (6.21b) and using the boundary condition for τ_{xz} in Eq. (6.21e) and p above gives $\tau_{xz}(x,z) = (S - h_x)(h - z)$,using the same way gives $\tau_{yz}(x,z) = (-h_y)(h-z)$ Using the shear stress τ_{xz}, and τ_{yz}, we obtain the leading order shear rate,

$$u_z = (S - h_x)\frac{(h-z)}{\mu(\theta)}, \quad v_z = (-h_y)\frac{(h-z)}{\mu(\theta)}. \tag{6.22}$$

Now, the leading order liquid flux through a cross-section can be written as:

$$Q^{(x)}(x,y,t) = \int_0^h (h-z)u_z dz, \quad Q^{(y)}(x,y,t) = \int_0^h (h-z)v_z dz. \tag{6.23}$$

Using the expression for u_z, and v_z above and the boundary condition for u, v in Eq. (6.21f), we obtain

$$Q^{(x)}(x,y,t) = (S - h_x)\int_0^h \frac{(h-z)^2}{\mu(\theta)}dz, \quad Q^{(y)}(x,t) = (-h_y)\int_0^h \frac{(h-z)^2}{\mu(\theta)}dz. \tag{6.24}$$

Integrating the continuity equation Eq. (6.21a) using the boundary conditions in Eq. (6.21f) and substituting into the kinematic boundary condition in Eq. (6.21e), one obtains the evolution equation for h:

$$h_t + Q_x^{(x)} + Q_y^{(y)} = w_s. \tag{6.25}$$

Using the expressions for $Q^{(x)}$, $Q^{(y)}$ and w_s from above, we can write the evolution equation for h as:

$$h_t + \left[(S - h_x)\int_0^h \frac{(h-z)^2}{\mu(\theta)}dz\right]_x + \left[(-h_y)\int_0^h \frac{(h-z)^2}{\mu(\theta)}dz\right]_y = w_s, \tag{6.26}$$

where $w_s(x,t) = [(9Q_{s_0}Q_s(t))/16]\,[1-(x/x_0)^2]\,[1-(y/y_0)^2]\,\mathcal{H}(x_0^2-x^2)\mathcal{H}(y_0^2-y^2)$. The flow is coupled with the temperature field via the viscosity relationship $\mu(\theta)$. The nondimensionalised governing equation and boundary conditions for the temperature

field are given by:

$$[\theta_t + u\theta_x + v\theta_y + w\theta_z] = \frac{1}{\epsilon^2 P_e}\left[\epsilon^2\theta_{xx} + \epsilon^2\theta_{yy} + \theta_{zz}\right], \tag{6.27a}$$

$$\theta_z = P_e\epsilon^2(\theta - 1)w_s + b\epsilon^2(\theta - \theta_s), \text{ at } z = 0, \tag{6.27b}$$

$$\theta_z = \epsilon^2 h_x\theta_x + \epsilon^2 h_y\theta_y - \epsilon^2 a\theta\sqrt{1 + \epsilon^2 h_x^2 + \epsilon^2 h_y^2}, \text{ at } z = h(x, y, t). \tag{6.27c}$$

We consider the asymptotic limit similar to Chapter 4, where the Péclet number, $Pe = O(1)$, so that the reduced Péclet number, $Pe_r = \epsilon^2 Pe \ll 1$. This is called the conduction-dominated scenario. The heat transfer coefficients, a, $b = O(1)$. Let $\theta \simeq \theta_0(x, y, z, t) + \epsilon^2\theta_2(x, y, z, t) + \ldots$ Substituting into Eq. (6.27) gives to leading order:

$$\frac{\partial^2\theta_0}{\partial z^2} = 0, \quad \theta_{0_z} = 0 \text{ at } z = 0 \text{ and } z = h_0(x, y, t). \tag{6.28}$$

This implies $\theta_0 = \theta_0(x, y, t)$. Hence, $\theta \simeq \theta_0(x, y, t) + \epsilon^2\theta_2(x, y, z, t) + \ldots$. Substituting this in Eq. (6.27) gives

$$\theta_{0t} + u\theta_{0x} + v\theta_{0y} = \frac{1}{P_e}\left[\theta_{2zz} + \theta_{0xx} + \theta_{0yy}\right], \tag{6.29a}$$

$$\theta_{2z} = h_{0x}\theta_{0x} + h_{0y}\theta_{0y} - a\theta_0, \text{ at } z = 0, \tag{6.29b}$$

$$\theta_{2z} = P_e(\theta_0 - 1)w_s + b(\theta_0 - \theta_{0s}), \text{ at } z = h_0(x, y, t). \tag{6.29c}$$

Integrating Eq. (6.29a) from $z = 0$ to $h_0(x, y, t)$ and using the boundary conditions

Eqs. (6.29b), (6.29c), we obtain

$$h_{0x}\theta_{0x} + h_{0y}\theta_{0y} - a\theta - [Pe(\theta_0 - 1)w_s + b(\theta_0 - \theta_{0s})] = Pe(h_0\theta_{0t} + \theta_{0x}\int_0^{h_0} u\ dz + \theta_{0y}\int_0^{h_0} v\ dz) - h_0\theta_{0xx} - h_0\theta_{0yy}. \tag{6.30}$$

Dropping the subscripts, the leading order temperature field is thus gives by

$$\theta_t + [\frac{Q^{(x)}}{h} - \frac{h_x}{hPe}]\theta_x + [\frac{Q^{(y)}}{h} - \frac{h_y}{hPe}]\theta_y = \frac{1}{Pe}[\theta_{xx} + \theta_{yy}] - \frac{1}{hPe}[a\theta + b(\theta - \theta_s)] - \frac{w_s}{h}(\theta - 1), \tag{6.31}$$

where

$$Q^{(x)} = \frac{1}{3}\frac{h^3}{\mu(\theta)}(S - h_x), \quad Q^{(y)} = \frac{1}{3}\frac{h^3}{\mu(\theta)}(-h_y). \tag{6.32}$$

Thus, the evolution equation for the free surface and the temperature field are given by:

$$h_t + Q_x^{(x)} + Q_y^{(y)} = w_s, \tag{6.33a}$$

$$\theta_t + [\frac{Q^{(x)}}{h} - \frac{h_x}{hP_e}]\theta_x + [\frac{Q^{(y)}}{h} - \frac{h_y}{hP_e}]\theta_y = \frac{1}{Pe}[\theta_{xx} + \theta_{yy}] - \frac{1}{hP_e}[a\theta + b(\theta - \theta_s)] - \frac{w_s}{h}(\theta - 1), \tag{6.33b}$$

$$Q^{(x)} = \frac{1}{3}\frac{h^3}{\mu(\theta)}(S - h_x), \quad Q^{(y)} = \frac{1}{3}\frac{h^3}{\mu(\theta)}(-h_y), \quad \mu(\theta) = e^{-\alpha\theta}, \tag{6.33c}$$

$$w_s(x,t) = \left[\frac{9Q_{s_0}Q_s(t)}{16}\right]\left[1 - \left(\frac{x}{x_0}\right)^2\right]\left[1 - \left(\frac{y}{y_0}\right)^2\right]\mathcal{H}(x_0^2 - x^2)\mathcal{H}(y_0^2 - y^2). \tag{6.33d}$$

Eq. (6.33a) shows the contribution to the evolution of h from the fluxes $Q^{(x)}$ and $Q^{(y)}$

in the x and y directions, respectively, due to the horizontal and vertical component of gravity. The evolution of the temperature, θ, given in Eq. (6.33b) shows the contribution to the heat transport due to: convection by the flow (second and third terms on the left-hand-side), diffusion or conduction (first and second term on the right-hand-side), het loss or cooling to the colder surrounding air and substrate and the gain in heat coming from the source (last term on the right-hand-side).

6.2 Numerical results

In this section, we examine the nonlinear stability of Eqs. 6.33 to small-amplitude transverse perturbations superimposed on a base state flow and temperature field using two-dimensional numerical simulations. The base state flow and temperature are represented by one-dimensional (y-independent) solutions that have been computed in Chapter 4. We seek 2π-periodic solutions in y of Eqs. 6.33a and 6.33b for $-L_1 \leq x \leq L_2$ and $0 \leq y \leq 2\pi$, where L_1 and L_2 are arbitrary lengths of the computational domain in the x direction. Eq. 6.33a and 6.33b are supplemented by two boundary conditions at $x = -L_1, L_2 \; \forall \; 0 \leq y \leq 2\pi$, which are given by $h = b_1$ and $\theta_x = 0$. We assume that the plane is pre-wetted with a precursor film of thickness b_1 as in the previous chapters. These boundary conditions characterise a flat precursor and zero temperature gradient far ahead and behind of the spreading dome. We impose periodic boundary conditions at the transverse y boundaries, $y = 0, 2\pi$.

We start our simulations from two types of initial conditions for h and θ which represent the y-independent base state solutions. These are:

(i) a parabolic dome shape, $h(x,0) = (1-x^2)\mathcal{H}(1-x^2) + b_1$ ($\mathcal{H}$ is the Heaviside function) and uniform temperature, $\theta(x,0) = 1$, for all $-L_1 \leq x \leq L_2$, used in the one dimensional simulations in Chapters 4, 5, and 6,

(ii) the quasi-steady solutions for $h(x)$ and $\theta(x)$ at specific times obtained numerically in Chapter 4. These quasi-steady solutions are chosen based on characteristic features of the free surface shapes of h observed during their evolution while varying key parameters such as the Péclet number, Pe, the heat transfer coefficients, a and b, linked to the rate of cooling, and the decay constant, α, in the exponential viscosity model. For $S = 0$, i.e., spreading over a horizontal plane, two characteristic free surface shapes are observed; a spreading dome-shaped profile and a *pancake*-type profile (a flattened plateau region with a steep front at its leading edge). For spreading over an inclined surface, we always observe a tilted dome-shaped profile with a steep front at its leading edge, with or without a fluid hump (or ridge) overriding the front. We choose the initial conditions for this case based on Fig. 6.1 which is a parameter survey in $(a = b, Pe)$ space with $\alpha = 2$ and $S = 1$ (inclination angle approximately 6^o) to show the existence of free surface shapes, $h(x,t)$ with and without a fluid hump near the leading edge. The parameter value pairs marked on Fig. 6.1 are the parameter values of Pe and $a = b$, respectively, for which the corresponding free surface profile at some

prescribed time is chosen as the initial condition to represent the base state for the two-dimensional stability simulations.

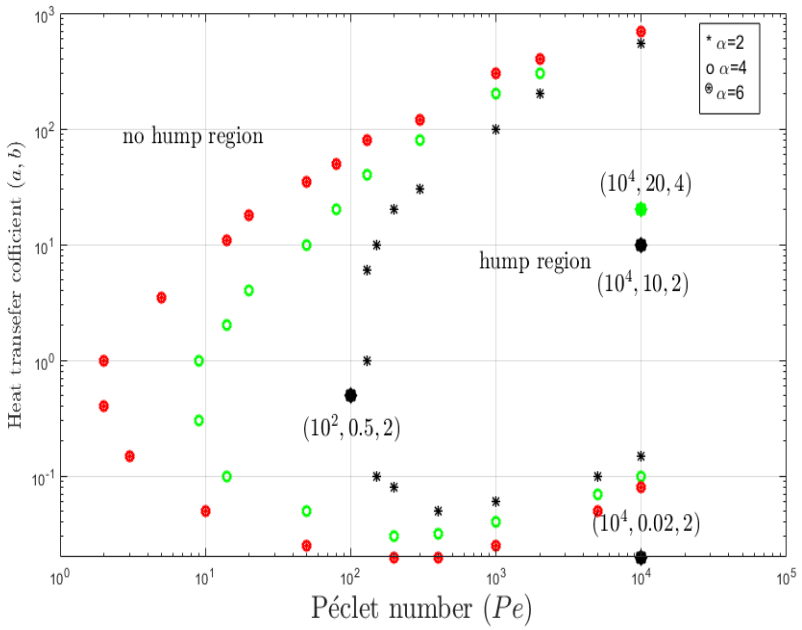

Figure 6.1: Parameter survey in $(Pe, a = b, \alpha)$ space to show existence of free surface shapes, $h(x,t)$ with and without a fluid hump (or ridge). The parameter values are: $\alpha = 2, 4, 6$ and $S = 1$ (inclination angle approximately 6^o). The parameter value pairs shown are the parameter values investigated in the two-dimensional stability simulations.

We introduce localised periodic transverse perturbations (localised around the leading edge of the dome) of a given wavenumber to the above initial conditions of the form:

$$[h(x,y,t), \theta(x,y,t)] = [h_b(x), \theta_b(x)] + A\cos(k\pi y)e^{[-K(x-x_N)^2]}, \quad (x,y) \in [-L_1, L_2] \times [0,2], \tag{6.34}$$

where $h_b(x)$ and $\theta_b(x)$ are the initial conditions for h and θ, respectively, k is the wavenumber and A is the amplitude of the 2-periodic transverse mode, K controls the width of the localised perturbation which is applied at $x = x_N$, the location of the

leading edge of the dome or front.

We are interested in investigating and simulating the existence of a fingering instability when the dome spreads to a much longer distance (simulation type (ii) above). In this scenario, the order of a wavelength in the transverse y direction is much smaller than the spreading length. We do, however, consider evolution of transverse perturbations of the order of a wavelength superimposed on the initial dome shape (simulation type (i) above) with the caution that the dome curvature would be important for the longer wavelengths. We speculate that the instability, if it exists, would develop when the initial dome shape spreads to a longer distance, which we can check by considering this scenario.

The evolution equation for $h(x, y, t)$ and $\theta(x, y, t)$ given by Eqs. (6.33a), (6.33b are solved numerically using the Method of lines [78, 61]. This is done as follows. We discretise the domain, $[-L_1, L_2]$ for x, into $N+1$ points and $[0, 2]$ for y, into $M+1$ points. Hence, $x_i = -L_1 + (i-1)\Delta x,\ i = 1, \ldots, N+1$, and $y_i = (j-1)\Delta y,\ j = 1, \ldots, M+1$, where $\Delta x = (L_2 + L_1)/N$, and $\Delta y = 2/M$. For $S = 0$ (horizontal plane), we use symmetry about $x = 0$ to only consider the domain $[0, L_1]$. We define a forward and backward finite difference for the spatial derivative as:

$$h_{x,ij} = \frac{h_{i+1j} - h_{ij}}{\Delta x}, \quad h_{\bar{x},ij} = \frac{h_{ij} - h_{i-1j}}{\Delta x}, \tag{6.35a}$$

$$h_{y,ij} = \frac{h_{ij+1} - h_{ij}}{\Delta y}, \quad h_{\bar{y},ij} = \frac{h_{ij} - h_{ij-1}}{\Delta y}, \tag{6.35b}$$

where $h_{,ij}$ represents a quantity evaluated at (x_i, y_j). The spatial derivatives in Eq. (6.33a) are then discretised as follows:

$$\left[(\frac{h^3}{\mu})_{ij}(S - h_{\tilde{x},ij})\right]_x = \frac{1}{\Delta x}\Big[(\frac{h^3}{\mu})_{i+\frac{1}{2}j}(S - h_{x,i+\frac{1}{2}j}) - (\frac{h^3}{\mu})_{i-\frac{1}{2}}(S - h_{x,i-\frac{1}{2}j})\Big], \quad (6.36a)$$

$$\left[(\frac{h^3}{\mu})_{ij}(-h_{\tilde{y},ij})\right]_y = \frac{1}{\Delta y}\Big[(\frac{h^3}{\mu})_{ij+\frac{1}{2}}(-h_{y,ij+\frac{1}{2}}) - (\frac{h^3}{\mu})_{ij-\frac{1}{2}}(-h_{y,ij-\frac{1}{2}})\Big], \quad (6.36b)$$

where $(\frac{h^3}{\mu})_{i+\frac{1}{2}j} = \frac{(h^3/\mu)_{i+1j}+(h^3/\mu)_{ij}}{2}$, $(\frac{h^3}{\mu})_{i-\frac{1}{2}j} = \frac{(h^3/\mu)_{ij}+(h^3/\mu)_{i-1j}}{2}$,

$h_{x,i+\frac{1}{2}j} = \frac{h_{i+1j}-h_{ij}}{\Delta x}$, $h_{x,i-\frac{1}{2}j} = \frac{h_{ij}-h_{i-1j}}{\Delta x}$, and $h_{y,ij+\frac{1}{2}} = \frac{h_{ij+1}-h_{ij}}{\Delta y}$, $h_{y,ij-\frac{1}{2}} = \frac{h_{ij}-h_{ij-1}}{\Delta y}$. Using this, the discretised form of Eq. (6.33a), keeping the time derivative continuous, can be written as:

$$h_{t,ij} + \frac{1}{3\Delta x}\Big[(\frac{h^3}{\mu})_{i+\frac{1}{2}j}(S - h_{x,i+\frac{1}{2}j}) - (\frac{h^3}{\mu})_{i-\frac{1}{2}}(S - h_{x,i-\frac{1}{2}j})\Big]$$
$$+ \frac{1}{3\Delta y}\Big[(\frac{h^3}{\mu})_{ij+\frac{1}{2}}(-h_{y,ij+\frac{1}{2}}) - (\frac{h^3}{\mu})_{ij-\frac{1}{2}}(-h_{y,ij-\frac{1}{2}})\Big] = w_{s,ij}, \;\; i = 2, \ldots, N, \; j = 2, \ldots, M. \quad (6.37)$$

The prescribed boundary conditions, $h(-L_1, y) = h(L_2, y) = b_1$, give $h_{1j} = h_{N+1j} = b_1$. Periodicity is applied to h at the y boundaries.

In the same way we discritize the temperature evolution equation, Eq. (6.33b), using

an up-winding discretisation scheme for the convection term in x, as follows:

$$\theta_{t,i} + (a_x)_{ij}\left[\frac{(\theta_{ij} - \theta_{i-1j})}{\Delta x}\right] + (a_y)_{ij}\left[\frac{(\theta_{ij+1} - \theta_{ij-1})}{2\Delta y}\right]$$
$$= \frac{1}{Pe}\left[\frac{(\theta_{i+1j} - 2\theta_{ij} + \theta_{i-1j})}{\Delta x^2} + \frac{(\theta_{ij+1} - 2\theta_{ij} + \theta_{ij-1})}{\Delta y^2}\right] + c_{ij}\theta_{ij}, \quad i = 2, \ldots, N, \; j = 2, \ldots, M \tag{6.38}$$

where $(a_x)_{ij} = \frac{h_{ij}^3}{3\mu_{ij}h_{ij}}(S - h_{x,i-\frac{1}{2}j}) - \frac{h_{x,i-\frac{1}{2}j}}{h_{ij}Pe}$, $(a_y)_{ij} = \frac{h_{ij}^3}{3\mu_{ij}h_{ij}}(S - h_{y,ij-\frac{1}{2}}) - \frac{h_{y,ij-\frac{1}{2}}}{h_{ij}Pe}$ and $c_{ij} = \frac{a\theta + b(\theta - \theta_s)}{h_{ij}Pe} + \frac{w_s(\theta - 1)}{h_{ij}}$. The boundary condition $\theta_x(x = -L_1, L_2, y) = 0$ is used to determine the fictitious points for the evolution equation of $\theta_{t,1j}$ and $\theta_{t,N+1j}$ using the above scheme. Periodicity is applied to θ at the y boundaries.

The growth rate and wavenumber of the dominant instability modes are investigated for variations in key parameters: the Péclet number (compares convective to vertically diffusive heat transport), Pe, the heat transfer coefficients, a and b (linked to the rate of cooling) and the decay constant, α (controls the change in viscosity with temperature) in the exponential viscosity model. In all the results shown below, we fix the source flow rate $Q_{s_0} = 0$ (constant volume spreading), the precursor thickness, $b_1 = 10^{-5}$ for simulations with $S = 0$ (horizontal plane) and $b_1 = 10^{-3}$ with $S = 1$ (inclined plane at an angle of approximately 6^o) and the length of the computational domains L is chosen sufficiently large so that the boundary condition $h \to b_1$ as $x \to \infty$ is satisfied numerically. We have tested the accuracy and convergence of our numerical scheme by reproducing the y-independent solutions shown in Chapter 4 for a variety of parameter values. Next, we investigate the transverse stability of these solutions using the initial

condition given in Eq. (6.34).

We first consider spreading over a horizontal plane ($S = 0$). Figure 6.2 shows the evolution of $h(x, y, t)$ $(a - c)$ and $\theta(x, y, t)$ $(d - f)$ for times, $t = 0$ (initial condition), $t = 10$ and $t = 30$ with $Pe = 10^6$, $\alpha = 2$, $a = 0.2$ and $b = 0.2$. The base states for this

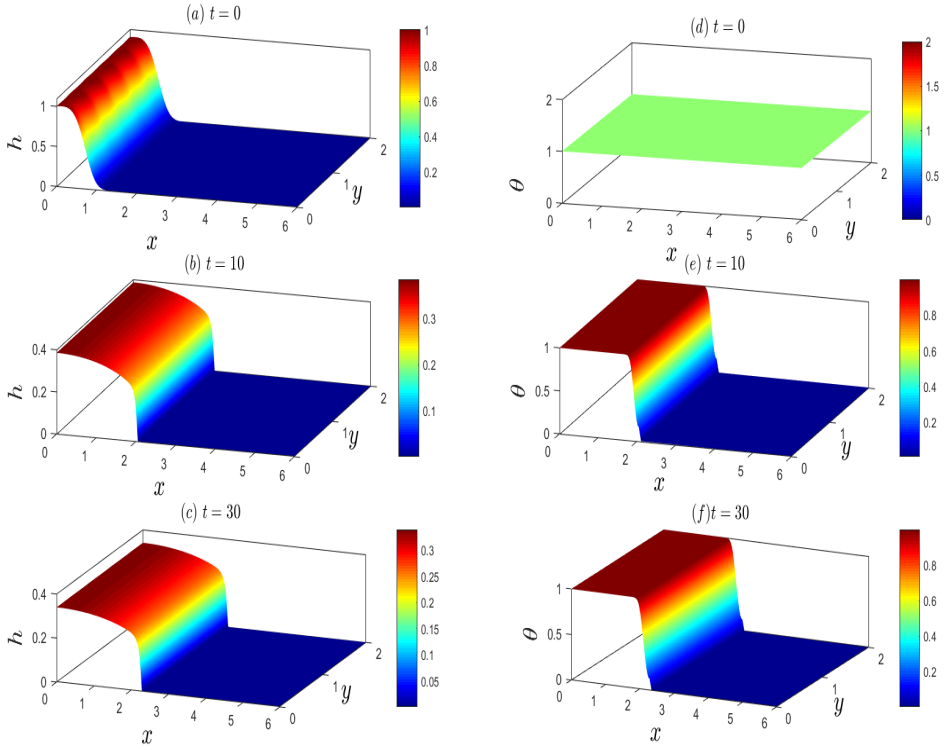

Figure 6.2: Evolution of $h(x, y, t)$ $(a - c)$ and $\theta(x, y, t)$ $(d - f)$ for time, $t = 0$ (a, d), $t = 10$ (b, e) and $t = 30$ (c, f) with $S = 0$, $Pe = 10^6$, $\alpha = 2$, $a = 0.2$, $b = 0.2$, $k = 6$, $A = 0.02$, $h_b(x) = (1 - x^2)\mathcal{H}(1 - x^2) + b_1$ ($\mathcal{H}$ is the Heaviside function) and $\theta_b(x) = 1$.

case are $h_b(x) = (1-x^2)\mathcal{H}(1-x^2)+b_1$ ($\mathcal{H}$ is the Heaviside function) and $\theta_b(x) = 1$. We impose a transverse perturbation with wavenumber $k = 6$ and amplitude $A = 0.02$ only on $h_b(x)$ (see Fig. 6.2(a)). We observe that the perturbations quickly decay to zero and the one-dimensional evolution is the same as that shown in Fig. **??** in Chapter 4. The

same behaviour is also observed for any other value of k (results not shown here). We have also investigated varying Pe ($Pe = 10^{-1} - 10^{6}$) with all other parameters fixed as above and the perturbations are observed to decay to zero for all wavenumbers k and the corresponding one-dimensional evolution is the same as that shown in Figs. 4.1 - **??** in Chapter 4. Figure 6.3 shows the evolution of $h(x, y, t)$ $(a-c)$ and $\theta(x, y, t)$ $(d-f)$ for times, $t = 0$ (initial condition), $t = 10$ and $t = 30$ with $Pe = 10^{3}$, $\alpha = 10$, $a = 0.2$ and $b = 0.2$. The base states for this case, $h_b(x)$ and $\theta_b(x)$ are obtained by running the one-dimensional simulations until $t = 4$; $h_b(x)$ has a pancake-shaped profile. We impose a transverse perturbation with wavenumber $k = 3$ and amplitude $A = 0.02$ on both $h_b(x)$ and $\theta_b(x)$ (see Fig. $6.3(a, d)$). We observe that the perturbations in h and θ increase in wavenumber from $k = 3$ at $t = 0$ to $k = 6$. The h perturbations appear to grow with a small growth rate while the θ perturbations grow quite dramatically as time progresses (Fig. $6.3(e, f)$). We observe the initial perturbation in θ growing into lengthening finger-like protrusions with a higher temperature at the tip compared to the ends. This temperature contrast leads to a viscosity difference (lower at the tip than at the ends) resulting in growth of perturbations in h, although quite small for the case shown here. We have not continued for longer time but speculate that the perturbations in h will lengthen with time keeping the same wavenumber $k = 6$.

Next, we consider the case of an inclined plane with $S = 1$ (inclination angle approximately 6^{o}). Figure 6.4 shows the evolution of $h(x, y, t)$ $(a - c)$ and $\theta(x, y, t)$ $(d - f)$ for times, $t = 0$ (initial condition), $t = 10$ and $t = 30$ with $Pe = 10^{2}$, $\alpha = 2$, $a = 0.5$

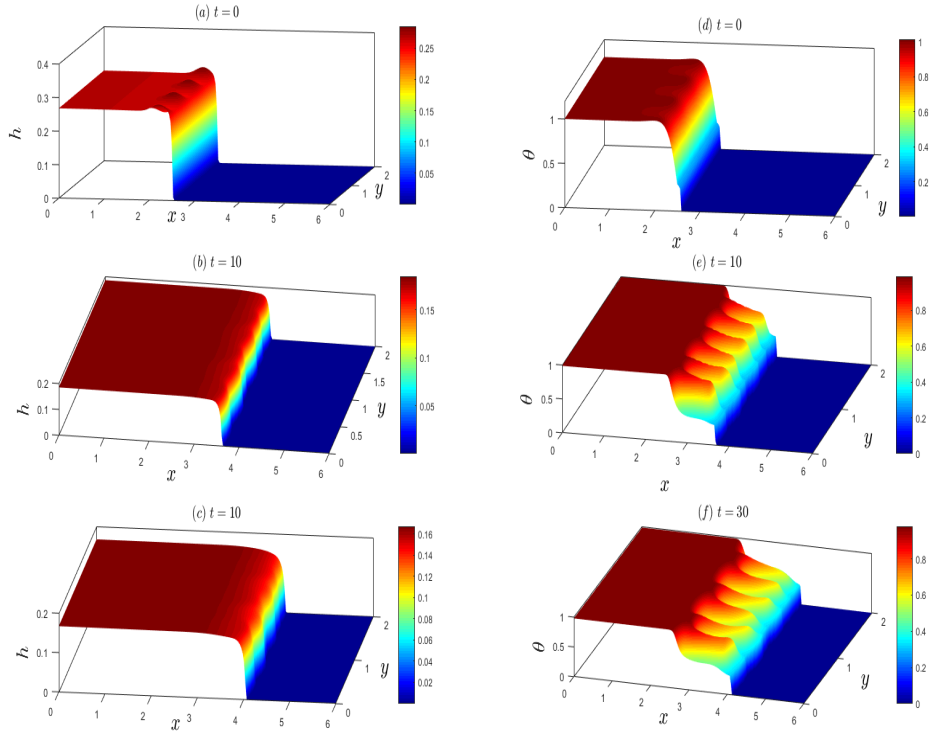

Figure 6.3: Evolution of $h(x, y, t)$ $(a - c)$ and $\theta(x, y, t)$ $(d - f)$ for time, $t = 0$ (a, d), $t = 10$ (b, e) and $t = 30$ (c, f) with $S = 0$, $Pe = 10^3$, $\alpha = 10$, $a = 0.2$, $b = 0.2$, $k = 3$ and $A = 0.02$.

and $b = 0.5$ (marked on Fig. 6.1). The base states for this case, $h_b(x)$ and $\theta_b(x)$ are

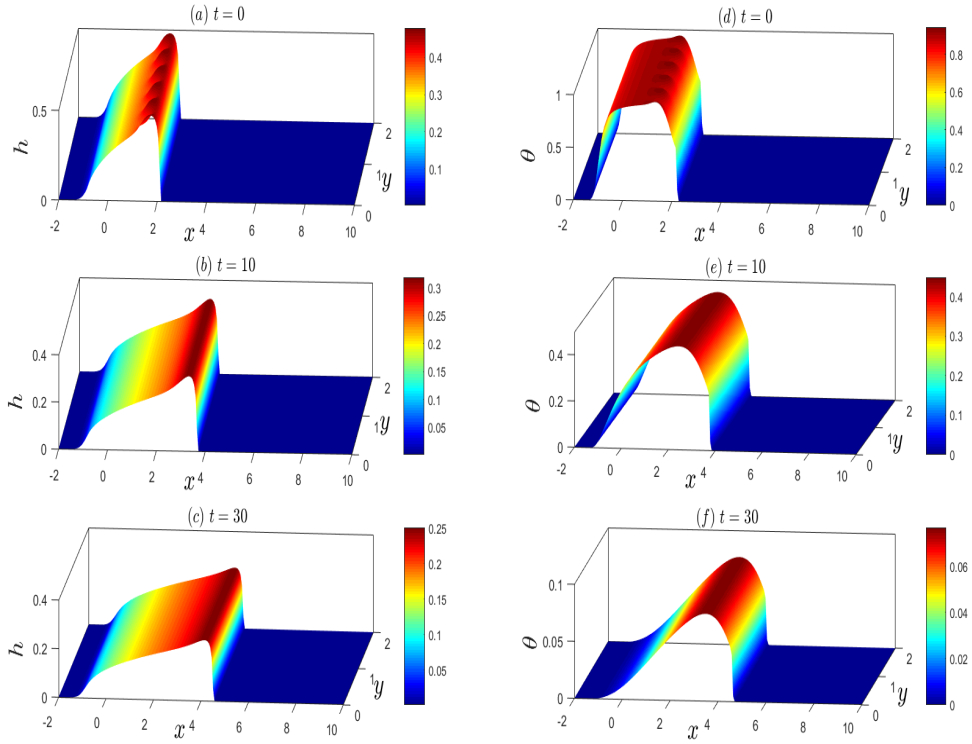

Figure 6.4: Evolution of $h(x, y, t)$ $(a - c)$ and $\theta(x, y, t)$ $(d - f)$ for time, $t = 0$ (a, d), $t = 10$ (b, e) and $t = 30$ (c, f) with $S = 1$ (inclination angle approximately 6^o), $Pe = 10^2$, $\alpha = 2$, $a = 0.5$, $b = 0.5$, $k = 3$ and $A = 0.02$.

obtained by running the one-dimensional simulations until $t = 2$; $h_b(x)$ has a slumped dome-shaped profile with a steep front at its leading edge, without a fluid hump. We impose a transverse perturbation with wavenumber $k = 3$ and amplitude $A = 0.02$ on both $h_b(x)$ and $\theta_b(x)$ (see Fig. 6.4(a, d)). We observe that the perturbations quickly decay to zero and the evolution of h and θ is one-dimensional. The same behaviour is also observed for any other value of k (results not shown here). Figure 6.5 shows the evolution of $h(x, y, t)$ $(a - c)$ and $\theta(x, y, t)$ $(d - f)$ for times, $t = 0$ (initial con-

dition), $t = 10$ and $t = 30$ with $Pe = 10^4$, $\alpha = 2$, $a = 0.02$ and $b = 0.02$ (marked on Fig. 6.1). The base states for this case, $h_b(x)$ and $\theta_b(x)$ are obtained by running the one-dimensional simulations until $t = 5$; $h_b(x)$ has a slumped dome-shaped profile with a steep front at its leading edge, without a fluid hump. We impose a transverse perturbation with wavenumber $k = 3$ and amplitude $A = 0.02$ on both $h_b(x)$ and $\theta_b(x)$ (see Fig. 6.5(a, d)). We observe that the perturbations quickly decay to zero and the evolution of h and θ is one-dimensional. The same behaviour is also observed for any other value of k (results not shown here). The results for increasing $a = b = 10$ with

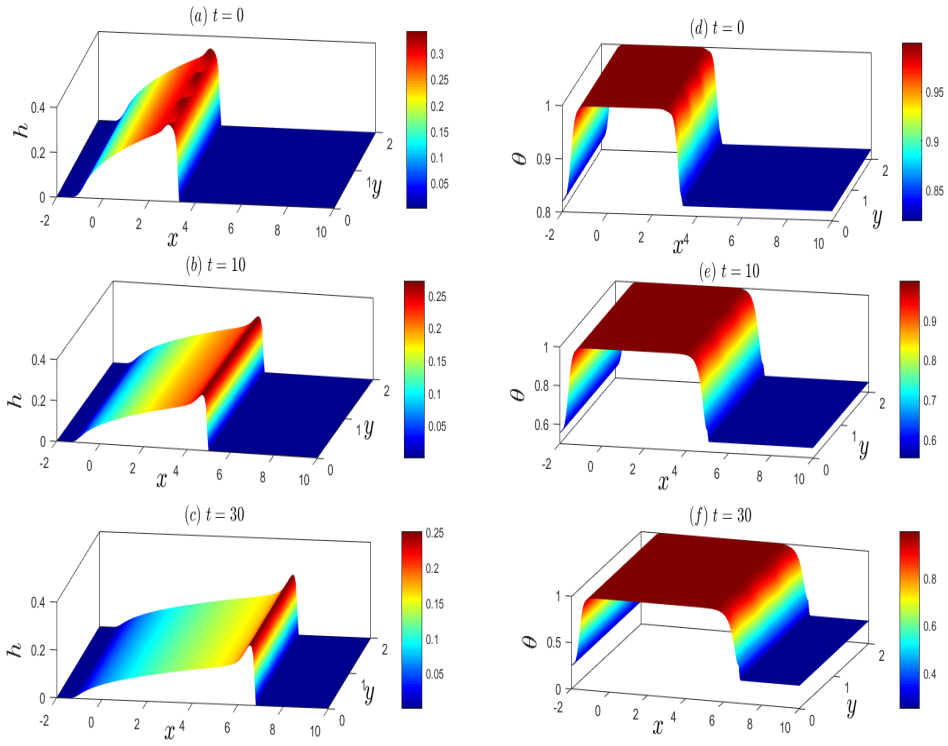

Figure 6.5: Evolution of $h(x, y, t)$ $(a - c)$ and $\theta(x, y, t)$ $(d - f)$ for time, $t = 0$ (a, d), $t = 10$ (b, e) and $t = 30$ (c, f) with $S = 1$ (inclination angle approximately 6^o), $Pe = 10^4$, $\alpha = 2$, $a = 0.02$, $b = 0.02$, $k = 3$ and $A = 0.02$.

all other parameters fixed (marked on Fig. 6.1) as in Fig. 6.5, are shown in Fig. 6.6 for $h(x, y, t)$ $(a - c)$ and $\theta(x, y, t)$ $(d - f)$ for times, $t = 0$ (initial condition), $t = 10$ and $t = 30$. The base states for this case, $h_b(x)$ and $\theta_b(x)$ are obtained by running the one-dimensional simulations until $t = 2$; $h_b(x)$ has a slumped dome-shaped profile with a steep front at its leading edge, with a fluid hump. We impose a transverse

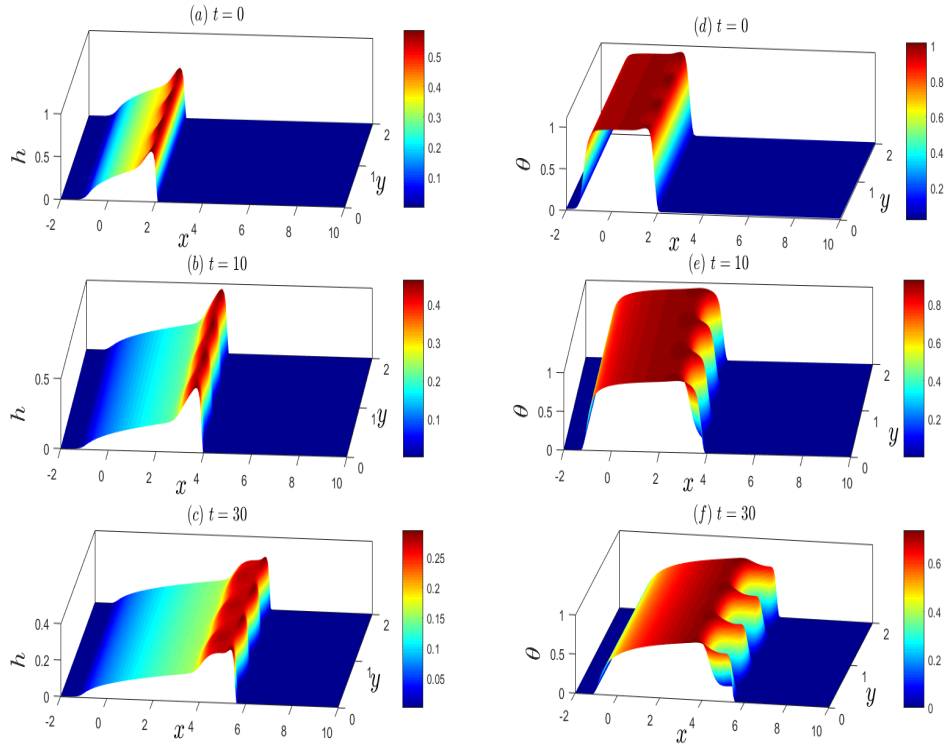

Figure 6.6: Evolution of $h(x, y, t)$ $(a - c)$ and $\theta(x, y, t)$ $(d - f)$ for time, $t = 0$ (a, d), $t = 10$ (b, e) and $t = 30$ (c, f) with $S = 1$ (inclination angle approximately 6^o), $Pe = 10^4$, $\alpha = 2$, $a = 10$, $b = 10$, $k = 3$ and $A = 0.02$.

perturbation with wavenumber $k = 3$ and amplitude $A = 0.02$ on both $h_b(x)$ and $\theta_b(x)$ (see Fig. 6.6(a, d)). We observe clearly in this case that the both the base states lose their stability to a fingering instability. The fingering instability is more dramatic in

the temperature field. The mechanism is the same as described for the earlier case but much more dramatic. Along a finger protrusion in the temperature field, θ is maximum at the tip compared to its ends, so the fluid viscosity at the tip is then greater than that at the ends. This results in fluid moving faster near the tip than at the ends which leads to the lengthening of the finger in h. Conversely, since the rate of cooling is inversely proportional to h (Eq. 6.33b), along a finger h is higher at the tip compared to the ends, so the tip will cool at a slower rate than the ends which would then maintain the temperature difference necessary to sustain the finger in θ. In addition, the enhanced advection at the tip compared to the ends would result in lengthening of the temperature finger protrusions, completing the cycle. The same fingering behaviour is also observed for $k = 1, 2, 4, 5$ but the growth rate of the fingers is less than that shown for $k = 3$ (results not shown here). Any perturbations with wavenumber $k \geq 10$ are observed to be damped out (not shown here), suggesting a cutoff wavenumber of $k \approx 10$ for this case. Figure 6.7 shows the evolution of $h(x, y, t)$ $(a - c)$ and $\theta(x, y, t)$ $(d - f)$ for times, $t = 0$ (initial condition), $t = 10$ and $t = 30$ with $Pe = 10^6$, $\alpha = 2$, $a = 2$ and $b = 2$ (marked on Fig. 6.1). The base states for this case, $h_b(x)$ and $\theta_b(x)$ are obtained by running the one-dimensional simulations until $t = 5$; $h_b(x)$ has a slumped dome-shaped profile with a steep front at its leading edge, without a fluid hump. We impose a transverse perturbation with wavenumber $k = 3$ and amplitude $A = 0.02$ on both $h_b(x)$ and $\theta_b(x)$ (see Fig. 6.7(a, d)). We observe that the perturbations in h decay to zero while those in θ are much slower to be damped out. The same behaviour is also observed for any other value of k (results not shown

here). The results for increasing $a = b = 200$ with all other parameters fixed (marked

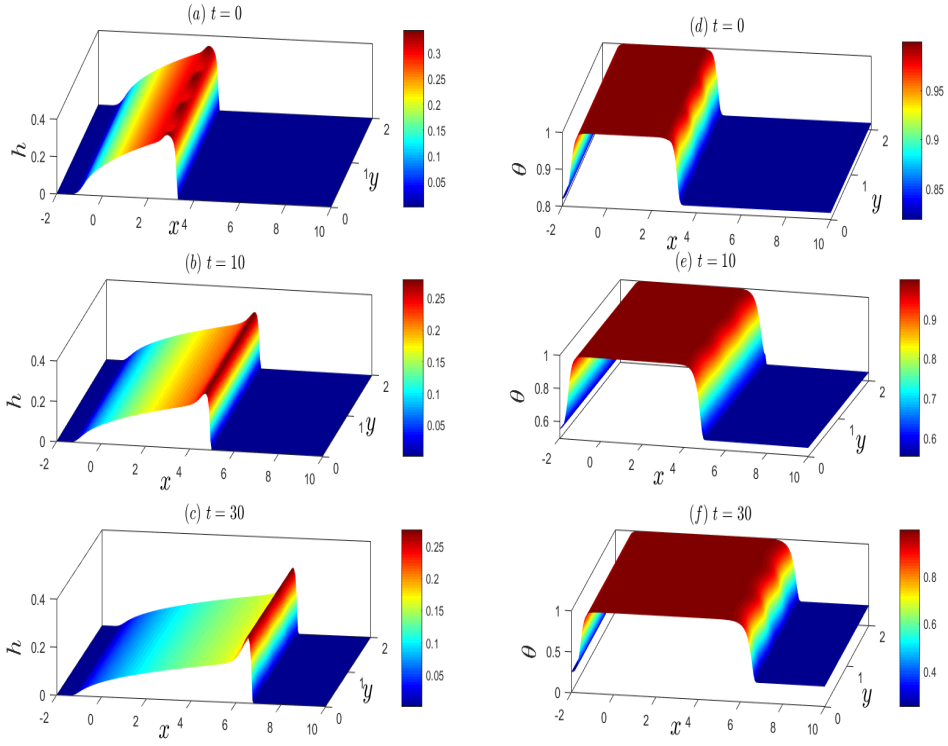

Figure 6.7: Evolution of $h(x, y, t)$ $(a - c)$ and $\theta(x, y, t)$ $(d - f)$ for time, $t = 0$ (a, d), $t = 10$ (b, e) and $t = 30$ (c, f) with $S = 1$ (inclination angle approximately 6^o), $Pe = 10^6$, $\alpha = 2$, $a = 2$, $b = 2$, $k = 3$ and $A = 0.02$.

on Fig. 6.1) as in Fig. 6.7, are shown in Fig. 6.8 for $h(x, y, t)$ $(a - c)$ and $\theta(x, y, t)$ $(d - f)$ for times, $t = 0$ (initial condition), $t = 10$ and $t = 30$. The base states for this case, $h_b(x)$ and $\theta_b(x)$ are obtained by running the one-dimensional simulations until $t = 4$; $h_b(x)$ has a slumped dome-shaped profile with a steep front at its leading edge, with a fluid hump. We impose a transverse perturbation with wavenumber $k = 3$ and amplitude $A = 0.02$ on both $h_b(x)$ and $\theta_b(x)$ (see Fig. 6.8(a, d)). We observe that the both the base states lose their stability to a fingering instability. The character-

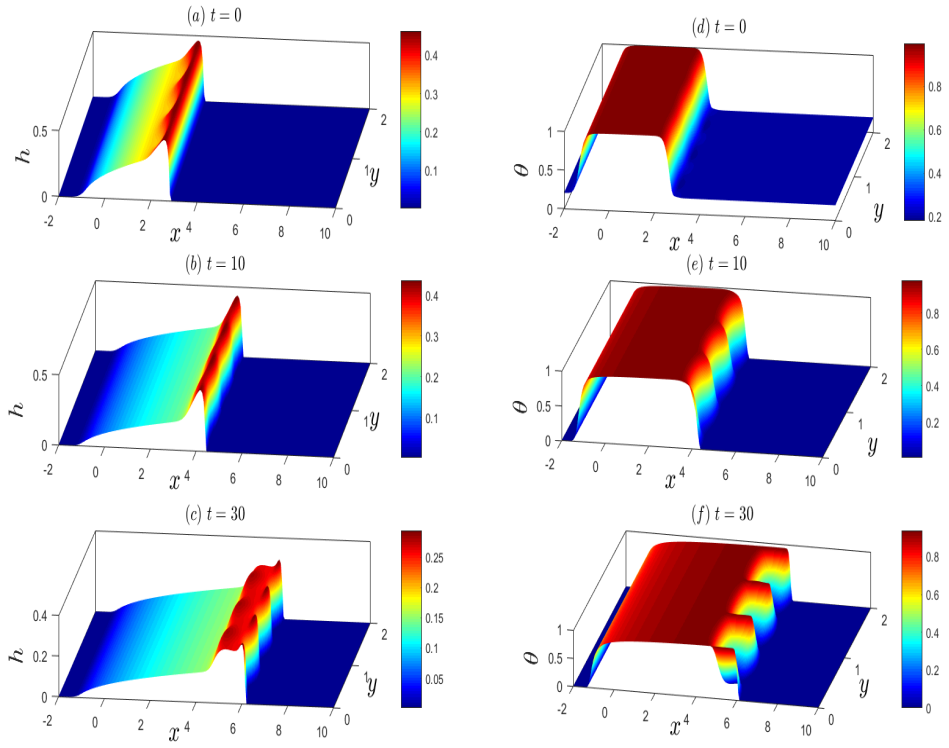

Figure 6.8: Evolution of $h(x, y, t)$ $(a - c)$ and $\theta(x, y, t)$ $(d - f)$ for time, $t = 0$ (a, d), $t = 10$ (b, e) and $t = 30$ (c, f) with $S = 1$ (inclination angle approximately 6^o), $Pe = 10^6$, $\alpha = 2$, $a = 200$, $b = 200$, $k = 3$ and $A = 0.02$.

istics of this instability are similar to the previous cases and the mechanism is also the same. Figures 6.9, 6.10 show the results using the same parameter values as in Fig. 6.8, except the wavenumbers are $k = 2$ and $k = 5$, respectively. The evolution of the fingering instability is very similar and they appear to have similar growth rates, atleast by inspection. The cutoff wavenumber for this case was observed to be $k \approx 10$.

We now consider the influence of increasing α. Figure 6.11 shows the evolution of

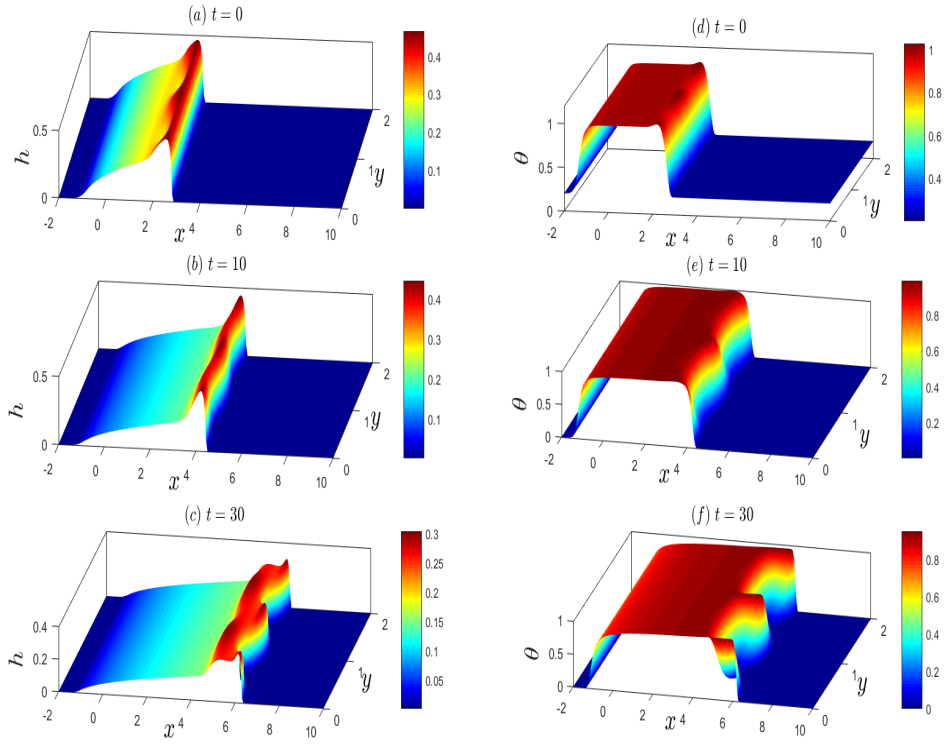

Figure 6.9: Evolution of $h(x, y, t)$ $(a - c)$ and $\theta(x, y, t)$ $(d - f)$ for time, $t = 0$ (a, d), $t = 10$ (b, e) and $t = 30$ (c, f) with $S = 1$ (inclination angle approximately 6^o), $Pe = 10^6$, $\alpha = 2$, $a = 200$, $b = 200$, $k = 2$ and $A = 0.02$.

$h(x, y, t)$ $(a - c)$ and $\theta(x, y, t)$ $(d - f)$ for times, $t = 0$ (initial condition), $t = 10$ and $t = 30$ with $Pe = 10^4$, $\alpha = 4$, $a = 20$ and $b = 20$. The base states for this case, $h_b(x)$

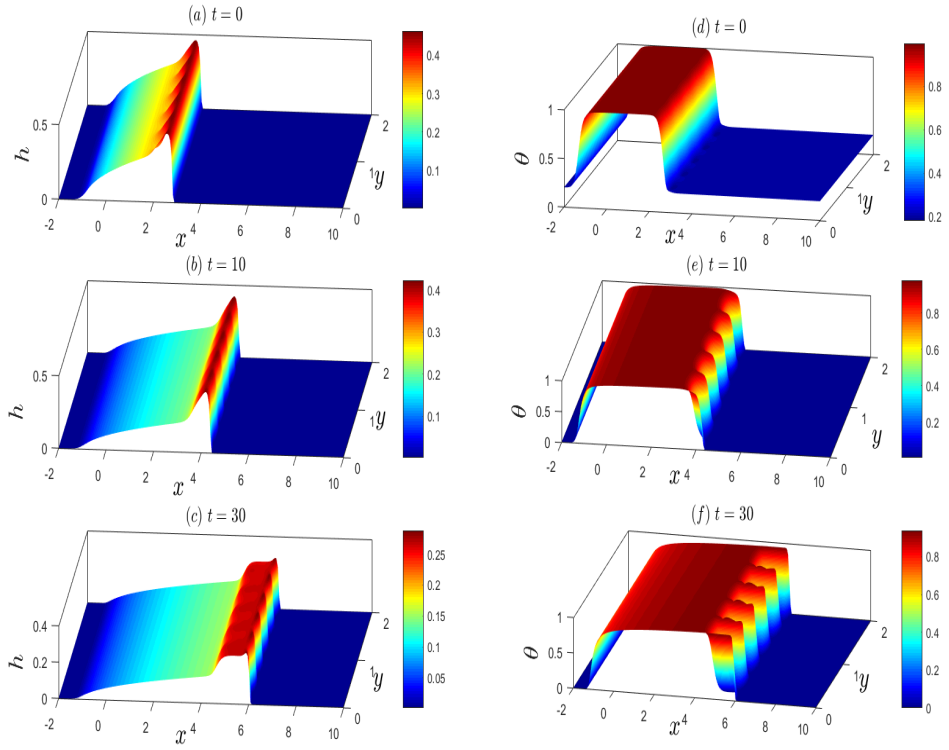

Figure 6.10: Evolution of $h(x, y, t)$ $(a - c)$ and $\theta(x, y, t)$ $(d - f)$ for time, $t = 0$ (a, d), $t = 10$ (b, e) and $t = 30$ (c, f) with $S = 1$ (inclination angle approximately 6^o), $Pe = 10^6$, $\alpha = 2$, $a = 200$, $b = 200$, $k = 5$ and $A = 0.02$.

and $\theta_b(x)$ are obtained by running the one-dimensional simulations until $t = 4$; $h_b(x)$ has a slumped dome-shaped profile with a steep front at its leading edge, with a fluid hump. We impose a transverse perturbation with wavenumber $k = 3$ and amplitude $A = 0.02$ on both $h_b(x)$ and $\theta_b(x)$ (see Fig. 6.11(a, d)). We observe that the both the base states lose their stability to a fingering instability with similar characteristics as the previous cases. The cutoff wavenumber for this case is also $k \approx 15$. The growth rate in this case is much higher than the case shown in Fig. 6.6 with a lower value of $\alpha = 2$. Figure 6.12 shows the evolution of $h(x, y, t)$ $(a - c)$ and $\theta(x, y, t)$ $(d - f)$ for

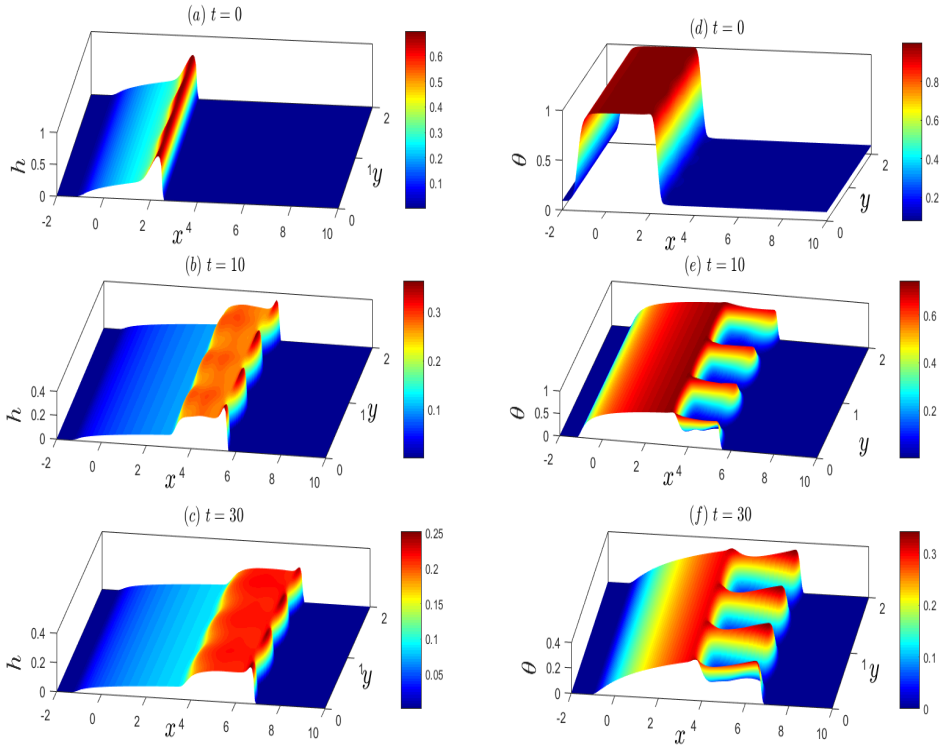

Figure 6.11: Evolution of $h(x, y, t)$ $(a - c)$ and $\theta(x, y, t)$ $(d - f)$ for time, $t = 0$ (a, d), $t = 10$ (b, e) and $t = 30$ (c, f) with $S = 1$ (inclination angle approximately 6^o), $Pe = 10^4$, $\alpha = 4$, $a = 20$, $b = 20$, $k = 3$ and $A = 0.02$.

times, $t = 0$ (initial condition), $t = 10$ and $t = 30$ with $Pe = 10^6$, $\alpha = 4$, $a = 300$ and $b = 300$. The base states for this case, $h_b(x)$ and $\theta_b(x)$ are obtained by running the one-dimensional simulations until $t = 4$; $h_b(x)$ has a slumped dome-shaped profile with a steep front at its leading edge, with a fluid hump. We impose a transverse perturbation with wavenumber $k = 3$ and amplitude $A = 0.02$ on both $h_b(x)$ and $\theta_b(x)$ (see Fig. 6.12(a, d)). We observe that the both the base states lose their stability to a fingering instability. The cutoff wavenumber is $k \approx 15$ for this case. The growth rate is much higher than the case shown in Fig. 6.8 with a lower value of $\alpha = 2$.

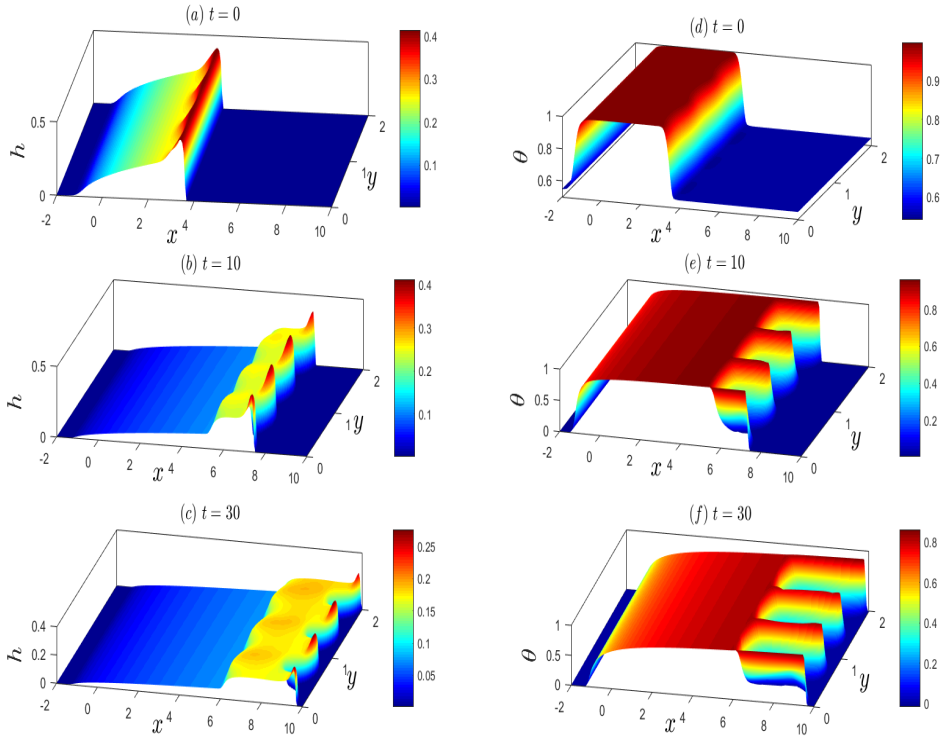

Figure 6.12: Evolution of $h(x, y, t)$ $(a - c)$ and $\theta(x, y, t)$ $(d - f)$ for time, $t = 0$ (a, d), $t = 10$ (b, e) and $t = 30$ (c, f) with $S = 1$ (inclination angle approximately 6^o), $Pe = 10^6$, $\alpha = 4$, $a = 300$, $b = 300$, $k = 3$ and $A = 0.02$.

6.3 Conclusions

In this chapter, we have investigated numerically the transverse linear stability of the one-dimensional solutions (the base states) for h and θ obtained in Chapter 4. We have successfully shown the existence of a new fingering instability in h and θ in Pe, a, b and α parameter space.

We have identified the mechanism underlying this fingering instability, based on a *thermo-viscous* mechanism. This involves a delicate coupling between the thermal and flow fields. A temperature difference across the length of a finger results in a viscosity contrast there. This leads to a difference in mobility across the finger, resulting in lengthening of the finger. h is also higher at the tip compared to the end of the finger which results in the rate of cooling to be less at the tip compared to the ends. This maintains the temperature difference across the finger which sustains the growth of the finger. Our results show that the increased mobility for $S > 0$ due to horizontal gravity enhances this fingering instability. Previous stability studies by Sansom *et al.* [76, 53, 77] and Balmforth *et al.* [7, 11] have attempted to simulate this instability for spreading on a horizontal plane ($S = 0$) but could only identify a transient instability.

Based on this thermo-viscous mechanism we obtain a band of unstable wavenumbers; the much higher wavenumbers are damped out by diffusion in h and θ. The band of unstable wavenumbers and their growth rates depend on the parameter values of Pe, a, b and α through the corresponding base state. We have shown that a necessary condition for instability to occur is based on the characteristic shape of the base state.

Pancake-shaped profiles (for $S = 0$) and slumped dome-shaped profiles with a hump (for $S > 0$) are shown to become linearly unstable while dome shapes (for $S = 0$) and slumped domes without a hump (for $S > 0$) are shown to be linearly stable. It is uncertain what might happen near the boundaries between the two different shapes. It is worth noting that a similar fluid hump profile is observed in drops spreading down an inclined surface under isothermal conditions and has been shown to be a necessary condition for linear instability (see Bertozzi & Brenner [17]). Surface tension and surface tension gradients are important in such flow scenarios. We observe that the growth rates and the band of unstable wavenumbers increase with α. Increasing α, enhances the coupling between the thermal and the flow fields and we expect a more dramatic fingering instability. We would need to determine numerical dispersion relationships between the growth rate and the wavenumber to better understand the dependence on the parameters.

In conclusion, we have clearly identified a thermo-viscous fingering instability for non-isothermal spreading down an inclined substrate. While previous studies by Sansom *et al.* [76, 53, 77] and Balmforth *et al.* [7, 11] have attempted to show their existence, ours is the first study to successfully simulate the fingering instability. Additional analysis is required to fully characterise this instability. This will be reported in a paper which is being currently compiled for submission to the Journal of Fluid Mechanics.

Chapter 7

Conclusions and future work

In this thesis we have theoretically modelled the spreading of a hot liquid dome undergoing cooling as it flows down an inclined substrate due to gravity. This model incorporates non-Newtonian and viscoplastic behaviour, a temperature-dependent viscosity and heat transfer boundary conditions at the dome's free surface and the underlying substrate. These key ingredients are essential to capture the strong coupling between the flow and cooling inherent in these flows. We have combined numerical simulations and similarity solutions to perform an extensive parameter study on the influence of key parameters on the evolution of the dome's free surface and spreading behaviour, such as the apparent viscosity, yield stress, Péclet number, temperature-viscosity coupling constant and the surface and substrate heat transfer coefficients.

The influence of non-Newtonian and viscoplastic effects in the context of this problem under isothermal conditions have been well studied (Balmforth *et al.* [5, 9]). Our

contribution has been in identifying new similarity solutions for general volume constraints and these are validated against numerical experiments. We have shown that for a constant flowrate from a source or vent, there exists a critical value of the source flowrate beyond which the dome will grow in height significantly. This prediction could be linked to catastrophic events related to dome collapse.

Our results for the non-isothermal spreading down an inclined plane provide new insights into some important physical mechanisms that were not accessible from previous studies (Sansom *et al.* [76, 53, 77] and Balmforth *et al.* [7, 11]). Previous studies have only considered spreading over a horizontal plane. We have shown that enhanced mobility due to the inclination of the substrate leads to the existence of a fluid hump overriding the steep front at the leading edge of the dome. We have also been able to characterise the variety of one-dimensional free surface shapes in parameter space. This was useful when we considered their stability to transverse perturbations. The main highlight of this thesis is in identifying a new fingering instability and the underlying thermo-viscous mechanism. While previous studies by Sansom *et al.* [76, 53, 77] and Balmforth *et al.* [7, 11] have attempted to show their existence, ours is the first study to successfully simulate the fingering instability. The preliminary work undertaken here provides the basis for doing a thorough theoretical analysis of the instability and for exploring the nonlinear stability of the flow.

There are limitations to this study. Our non-Newtonian and viscoplastic study is under isothermal conditions. In reality, the yield stress (and to some extent the power law

index) strongly depend on temperature. Balmforth *et al.* [7, 11] have considered this temperature dependence on spreading over a horizontal plane. The interaction between the pseudo-plug region (which starts forming from the surface) and surface cooling is important when the cooling boundary layer at the surface advances into the plug region, otherwise the plug *shields* the dome from cooling. As part of future work, we would need to extend our model of spreading down an inclined plane to include temperature-dependent non-Newtonian effects and their influence on cooling. Probably more than temperature-dependent non-Newtonian effects, a key ingredient missing in this work is phase transition due to solidification. It is likely that the results reported here might not be applicable when solidification by the formation of a surface crust is taken into account. We would need to include solidification effects into any future extensions of our model. The lubrication approximation is not valid where there are steep changes in the fluid height. We see that at the leading edge of the spreading front there are large gradients, in particular, in the cases where the leading edge develops a fluid hump. In addition, we observe in Figs. 5.25, 5.26, 5.27 and 5.33 for the cases where the flux through the vent is large or the bi-viscosity model is used with a large viscosity contrast, that the vertical length scale of the fluid hump is comparable to the horizontal length scale which question the validity of the lubrication model in these scenarios. To test the validity of our results full numerical simulations of the Navier-Stokes equations and boundary conditions would need to be undertaken using, for example, boundary element or finite element methods.

In conclusion, the work presented in this thesis provides new theoretical insight into the flow-cooling coupling mechanism that is inherent in spreading of hot flows undergoing cooling. This insight would form the basis for future developments of this model to incorporate additional effects mentioned above and to transfer knowledge to experimentalists and geophysicists interested in characterising such flows.

Bibliography

[1] D.J. Acheson. *Elementary fluid dynamics*. Oxford University Press, 1990.

[2] V.S. Ajaev and D.A. Willis. Thermocapillary flow and rupture in films of molten metal on a substrate. *Phys. Fluids*, 15(10):3144–3150, 2003.

[3] C. Ancey. Plasticity and geophysical flows: A review. *J. Non-Newtonian Fluid Mech.*, 142:4–35, 2007.

[4] N. Bagdassarov and H. Pinkerton. Transient phenomena in vesicular lava flows based on laboratory experiments with analogue materials. *Journal of Volcanology and Geothermal Research*, 132:115–136, 2004.

[5] N.J. Balmforth, A.S. Buridge, R.V. Craster, J. Salzig, and A. Shen. Visco-plastic models of isothermal lava domes. *J. Fluid Mech.*, 403(37-65), 2000.

[6] N.J. Balmforth and R.V. Craster. A consistent thin-layer theory for Bingham Plastics. *J. Non-Newtonian Fluid Mech.*, 84:65–81, 1999.

[7] N.J. Balmforth and R.V. Craster. Dynamics of cooling domes of viscoplastic fluid. *J. Fluid Mech.*, 422:225–248, 2000.

[8] N.J. Balmforth and R.V. Craster. *Geomorphological Fluid Mechanics*, volume 582, chapter 2, pages 34–51. Springer - Verlag Berlin Heidelberg, 2001.

[9] N.J. Balmforth, R.V. Craster, A.C. Rust, and R. Sassi. Viscoplastic flow over an inclined surface. *J. Non- Newtonian Fluid Mech.*, 139:103–127, 2006.

[10] N.J. Balmforth, R.V. Craster, and R. Sassi. Shallow viscoplastic flow on an inclined plane. *J. Fluid Mech.*, 470:1–29, 2002.

[11] N.J. Balmforth, R.V. Craster, and R. Sassi. Dynamics of cooling viscoplastic domes. *J. Fluid Mech.*, 499:149–182, 2004.

[12] N.J. Balmforth, I.A. Frigaard, and G. Ovarlez. Yielding to stress: Recent developments in viscoplastic fluid mechanics. *J. Non-Newtonian Fluid Mech.*, 46:4–35, 2014.

[13] D. Bercovici. A theoretical model of cooling viscous gravity currents with temperature-dependent viscosity. *Geophys. Res. Lett.*, 21:1177–1180, 1994.

[14] D. Bercovici and J. Lin. A gravity current model of cooling mantle plume heads with temerature-dependent bouyancy and viscosity. *J. Geophys. Res.*, 101(0):3291–3309, 1996.

[15] N. Bernabeu, P. Saramito, and C. Smutek. A new shallow approximation for tridimenesional non- isothermal viscoplastic lava flows. unpublished, August 2014.

[16] N. Bernabeu, P. Saramito, and C. Smutek. Numerical modeling of non- Newtonian

viscoplastic flows: Part II. Viscoplastic fluids and general tridimenesional topographies. *International Journal of Numerical Analysis and Modeling*, 11(1):213–228, 2014.

[17] A. Bertozzi and M. Brenner. Linear stability and transient growth in driven contact lines. *Phys. Fluids*, 9:530539, 1997.

[18] R. B. Bird, C. F. Curtiss, R. C. Armstrong, and O. Hassager. *Dynamics of Polymeric Liquids*, volume Volume 2: Kinetic Theory. John Wiley and Sons Inc., 2 edition, 1987.

[19] S. Blake. *Viscoplastic Models of Lava Domes*, pages 88–126. Springer Berlin Heidelberg, Berlin, Heidelberg, 1990.

[20] S. Blake and B.C. Bruno. Modelling the emplacement of compound lava flows. *Earth and Planetary Science Letters*, 184:181–197, 2000.

[21] L. Bourgouin, H-B. Muhlhaus, A.J. Hale, and A. Arsac. Studying the influence of a solid shell on lava dome growth and evolution using the level set method. *Geophysical Journal International*, 170:1431–1438, 2007.

[22] M. Bunk and J.R. King. Spreading melts with basal solidification. *Z. Angew. Math. Mech.*, 83(12):820–843, 2003.

[23] H.S. Carslaw and J.C. Jaeger. *Conduction of heat in solids*. Oxford University Press, 1980.

[24] K. V. Cashman, H. Pinkerton, and P. J. Stephenson. Long lava flows. *J. Geophys. Res.*, 103:27281–27289, 1998.

[25] R.P. Chhabra and J.F. Richardson. *Non- Newtonian Flow and Applied Rheology: Engineering Applications*. Elsevier Ltd., 2nd edition, 2008.

[26] P. Coussot. Mudflow rheology and dynamics. In *IAHR Monograph Series*. Balkema, 1997.

[27] R.V. Craster and O.K. Matar. Dynamics and stability of thin liquid films. *Rev. Mod. Phys.*, 81:1131–1198, 2009.

[28] T.R.H Davies. Large debris flows: a macro-viscous phenomenon. *Acta Mechanica*, 63:161–178, 1986.

[29] S. Diniega, S.E. Smrekar, S. Anderson, and E Stofan. The influence of temperature-dependent viscosity on lava flow dynamics. *J. Geophys. Res. Earth Surf*, 118:1516–1532, 2013.

[30] M. Dragoni. Physical modelling of lava flows. *Annali Di Geofisica*, 15(5):1179–1187, 1997.

[31] N. Dubash, N.J. Balmforth, A.C. Slim, and S. Cochard. What is the final shape of a viscoelastic slump? *J. Non-Newtonian Fluid Mech.*, 158:91–100, 2009.

[32] P. Ehrhard and S.H. Davis. Non-isothermal spreading of liquid drops on horizontal plates. *J. Fluid Mech.*, 229(0):365–388, 1991.

[33] G. Engel, G. Fieg, H. Massier, U. Stegmaier, and W. Schutz. Kats experiments to simulate corium spreading in the epr core catcher concept. In H. Alsmeyer, editor, *Proceedings of the OECD Workshop on Ex-Vessel Debris Coolability*, pages 148–155. Forschungszentrum Karlsruhe, 2000.

[34] J.H. Fink and R.W. Griffiths. Radial spreading of viscous-gravity currents with solidifying crust. *J. Fluid Mech.*, 221:485–509, 1990.

[35] J.H. Fink and R.W. Griffiths. Morphology eruption rates, and rheology of lava domes: Insights from laboratory models. *J. Fluid Mech.*, 84:125–143, 1998.

[36] A.C. Fowler. A mathematical analysis of glacier surges. *SIAM J. Appl. Maths.*, 49:246–263, 1989.

[37] A.C. Fowler. Modelling ice sheet dynamics. *Geophys. Astrophys. Fluid Dyn.*, 63:29–65, 1989.

[38] F. Garel, E. Kaminski, S. Tait, and A. Limare. Analogue study of the influence of solidification on the advance and surface thermal signature of lava flows. *Earth and Planetary Science Letters*, 396:46–55, 2014.

[39] R. W. Griffiths and K.C. Kerr. Coupling of cooling, solidification and gravity-driven flow. In *Procedia IUTAM*, volume 15, pages 165–171. Elsevier, 2015. IUTAM Symposium on Multiphase flows with phase change: challenges and opportunities, Hyderabad, India (December 08 December 11, 2014).

[40] R.W. Griffiths. The dynamics of lava flows. *Annu. Rev. Fluid Mech.*, 32:477–518, 2000.

[41] R.W. Griffiths, R.C. Kerr, and K.V. Cashman. Patterns of solidification in channel flows with surface cooling. *J. Fluid Mech.*, 496:33–62, 2003.

[42] A.J. Hale. Lava dome growth and evolution with an independently deformable talus. *Geophysical Journal International*, 174(1):391–417, 2008.

[43] D.R. Hewitt and N.J. Balmforth. Thixotropic gravity currents. *J. Fluid Mech.*, 727:56–82, 2013.

[44] X. Huang and M.H. Garcia. A Herschel-Bulkley model for mud flow down a slope. *J. Fluid Mech.*, 374:305–333, 1998.

[45] G. Hulme. The interpretation of lava flow morphology. *Geophys. J. R. Astron. Soc.*, 39:361–383, 1974.

[46] H.E. Huppert. Flow and instability of a viscous gravity current down a slope. *Nature*, 300(2), December 1982.

[47] H.E. Huppert. The propagation of two-dimensional and axisymmetric viscous gravity currents over a rigid horizontal surface. *J. Fluid Mech.*, 121:43–58, 1982.

[48] H.E. Huppert. The intrusion of fluid mechanics into geology. *J. Fluid Mech.*, 173:557–594, 1986.

[49] H.E. Huppert. Gravity currents: a personal perspective. *J. Fluid Mech.*, 554:299–322, 2006.

[50] R.M. Iverson. Lava domes modeled as brittle shells that enclose pressurized magma. In J.H. Fink, editor, *Lava Flows and Domes: Emplacement Mechanisms and Hazard Implications*, volume 2, pages 47–69. Springer, 1990.

[51] A.M. Johnson. *Physical Processes in Geology.* Freeman, San Francisco, 1970.

[52] J. P. Kauahikaua, K. V. Cashman, T. N. Mattox, K. Hon, C. C. Heliker, M. T. Mangan, and C. R. Thornber. Observations on basaltic lava streams in tubes from kilauea volcano, Hawaii. *J. Geophys. Res.*, 103:27303–27324, .

[53] J.R. King, D.S. Riley, and A. Sansom. Gravity currents with temperature-dependent viscosity. *Comput. Assist. Mech. Eng. Scl.*, 7(1):251–277, 2000.

[54] J.R. Lister. Viscous flows down an inclined plane from point and line sources. *J. Fluid Mech.*, 242:631–653, 1992.

[55] K.F. Liu and C.C. Mei. Slow spreading of a sheet of Bingham fluid on an inclined plane. *J. Fluid Mech.*, 207:505–529, 1989.

[56] K.F. Liu and C.C. Mei. Approximate equations for the slow spreading of a thin sheet of Bingham plastic fluid. *Phys. Fluids A*, 2:30–36, 1990.

[57] A. W Lyman and R.W. Kerr. Effect of surface solidification on the emplacement of lava flows on a slope. *J. Geophys. Res.*, 111:B05206, 2006.

[58] A. W Lyman, R.W. Kerr, and R.W. Griffiths. The effects of internal rheology and surface cooling on the emplacement of lava flows. *J. Geophys. Res.*, 110:B08207, 2005.

[59] A. W Lyman, E. Koenig, and J.H. Fink. Predicting yield strengths and effusion rates of lava domes from morphology and underlying topography. *J. Volcanol. Geotherm. Res.*, 129:125–138, 2004.

[60] F.A. Morrison. *Understanding rheology*. Oxford University Press, USA, 2001.

[61] K. W. Morton and D.F. Mayers. Numerical Solution of Partial Differential Equations. Cambridge University, 1994.

[62] T. G. Myers. Surface tension driven thin film flows. In *The Mechanics of Thin Film Coatings*. Wiley, 1996.

[63] T.G. Myers. Application of non-Newtonian models to thin film flow. *Phy. Rev. E*, 72:066302, 2005.

[64] T.G. Myers, J. Charpin, and S. J. Chapman. The flow and solidifiction of a thin fluid film on an arbitrary three-dimensional surface. *Phys. Fluids*, 14:2788–2803, 2002.

[65] J.F. Nye. Mechanics of glacier flow. *J. Glaciol.*, 2:82–93, 1952.

[66] H. Ockendon and J.R. Ockendon. *Viscous flows*. Cambridge University Press, August 1995.

[67] A. Oron, S. H. Davis, and S. G. Bankoff. Long-scale evolution of thin liquid films. *Rev. Mod. Phy.*, 69:931–980, 1997.

[68] A.A. Osiptsov. Steady film flow of a highly viscous heavy fluid with mass supply. *Fluid Dynamics*, 39:47–60, 2003.

[69] A.A. Osiptsov. A self-similar solution to the problem of lava dome growth on an arbitrary conical surface. *Fluid Dynamics*, 38:846–853, 2004.

[70] D.I. Osmond and R.W. Griffiths. The static shape of yield strength fluids slowly emplaced on slopes. *J. Geophys. Res.*, 106(16):241–250, 2001.

[71] M.F. Perutz. Glaciology - the flow of glaciers. *The Observatory*, 70:64–65, 1950.

[72] H. Pinkerton and G. Norton. Rheological properties of basaltic lava at sub- liquidus temperatures: Laboratory and field mesurements on lavas from Mount Etna. *J. Volcan. Geotherm. Res.*, 1995.

[73] D. Pritchard, B.R. Duffy, and S. Wilson. Shallow flows of generalised Newtonian fluids on an inclined plane. *J. Eng. Maths.*, 94(1):115–133, 2014.

[74] J.C. Robertson and R.W. Kerr. Solidification dynamics in channeled viscoplastic lava flows. *J. Geophys. Res.*, 117:B07206, 2012.

[75] S.E.H. Sakimoto and M.T. Zuber. The spreading of variable-viscosity axisymmetric radial gravity currents: applications to the emplacement of Venusian "pancake" domes. *J. Fluid Mech.*, 301:65–77, 1995.

[76] A. Sansom. *Spreading gravity currents with temperature-dependent viscosity.* PhD thesis, University of Nottingham, 2000.

[77] A. Sansom, J.R. King, and D.S. Riley. Degenerate-diffusion models for the spreading of thin non-isothermal gravity currents. *J. Eng. Maths*, 48(1):43–68, 2004.

[78] G. D. Smith. Numerical Solution of Partial Differential Equations: Finite Difference Methods. Macmillan, third edition edition, 1985.

[79] E.A. Vedeneeva. Lava spreading during volcanic eruptions on the condition of partial slip along the underlying surface. *Fluid Dynamics*, 50(2):203–214, 2015.

[80] M. V.Stasiuk, C. Jaupart, and R. S. J. Sparks. Influence of cooling on lava-flow dynamics. *J. Geol.*, 21(0):335–338, 1993.

[81] D.P. Wall and S.K. Wilson. The linear stability of channel flow of fluid with temperature-dependent viscosity. *J. Fluid Mech.*, 323:107–132, 1996.

[82] S.K. Wilson and B. R. Duffy. On the gravity-driven draining of a rivulet of fluid with temperature-dependent viscosity down a uniformly heated or cooled substrate. *J. Eng. Math.*, 42:349–372, 2002.

[83] S.K. Wilson and B. R. Duffy. Strong temperature-dependent-viscosity effects on a rivulet draining down a uniformly heated or cooled slowly varying substrate. *Phys. Fluids*, 15:827–840, 2003.

[84] J.J. Wylie and J.R. Lister. The effect of temperature-dependent viscosity on flow

in a cooled channel with application to basaltic fissure eruptions. *J. Fluid Mech.*, 305:239–261, 1995.

[85] A. Zadrazil, F. Stepanek, and O.K. Matar. Droplet spreading, imbibition and solidification on porous media. *J. Fluid Mech.*, 562:1–33, 2006.

Appendix 1

In order to solver Eq. (2.34b) numerically, we need to determine a solution of Eq. (2.34b) in the neighborhood of the point $z = 1$ using Frobenius method. consider Eq. (2.34b)which can be written as:

$$3\tilde{\phi}^2\tilde{\phi}_z^2 + \tilde{\phi}^3\tilde{\phi}_{zz}^2 + \frac{1}{5}(3\alpha+1)z\tilde{\phi}_z - \frac{1}{5}(2\alpha-1)\tilde{\phi} = 0. \tag{7.1}$$

Consider Frobenius method

$$\tilde{\phi} = \sum_{k=0}^{\infty} a_k(1-z)^{k+r} = a_0(1-z)^r + a_1(1-z)^{1+r} + ..., \tag{7.2}$$

where k, r are constant. Substituting in Eq. (7.1) and ignoring high order terms, we obtain

$$\begin{aligned}
&3\left[a_0^2(1-z)^{2r} + 2a_0a_1(1-z)^{2r+1}\right]\left[a_0^2r^2(1-z)^{2r-2} + 2a_0a_1(1-z)^{2r-1}\right] + \\
&\left[a_0^3(1-z)^{34} + 3a_0^3a_1(1-z)\right]\left[a_0r(r-1)(1-z)^{r-2} + a_1r(r+1)(1-z)^{r-1}\right] - \\
&\frac{1}{5}(3\alpha+1)z\left[a_0r(1-z)^{r-1} + a_1(r+1)(1-z)^r\right] - \\
&\frac{1}{5}(2\alpha-1)\left[a_0(1-z)^r + a_1(r+1)\right] = 0.
\end{aligned} \tag{7.3}$$

Assuming $(1-z)^{r-1} \sim (1-z)^{r-1}$ implies $r = 1/3$, substituting in Eq. (7.3), and solvrd

for a_0 we obtain

$$a_0 = \left(\frac{3}{5}(3\alpha+1)\right)^{1/3}, \tag{7.4}$$

in the same way we obtain

$$a_1 = \frac{3a_0(2\alpha-1)}{24(3\alpha+1)}. \tag{7.5}$$

Substituting Eqs. (7.4) and (7.5)into Eq. (7.2), we obtain

$$\tilde{\phi}(z) = \left(\frac{3}{5}(3\alpha+1)\right)^{1/3}(1-z)^{1/3}\left[1 - \frac{3(2\alpha-1)}{24(3\alpha+1)}(1-z) + O(1-z)^2\right]. \tag{7.6}$$

Appendix 2

Consider Eq. (3.49a)

$$\left[\frac{n(\alpha-1)}{2n+1}\phi - \frac{\alpha(n+1)+n}{2n+1}\xi\phi_\xi\right] = \left[S^{\frac{1}{n}}\phi^{\frac{1}{n}+2}\right]_\xi. \tag{7.7}$$

Integrating with respect to ξ and using Eq. (3.49b) for $\xi_N T = 0$ gives

$$\frac{\alpha(n+1)+n}{2n+1}\xi_N\phi_N - \alpha = S^{\frac{1}{n}}\left(\phi_N^{\frac{1}{n}+2} - \phi_0^{\frac{1}{n}+2}\right). \tag{7.8}$$

If $S^{\frac{1}{n}}\phi_0^{\frac{1}{n}+2} = \alpha$, this implies

$$\phi_0 = \left(\frac{\alpha}{S^{1/n}}\right)^{\frac{n}{2n+1}}, \tag{7.9}$$

and if $\frac{\alpha(n+1)+n}{2n+1}\xi_N\phi_N = S^{\frac{1}{n}}\phi_N^{\frac{1}{n}+2}$, implies

$$\phi_N = \left(\frac{\xi_N}{S^{1/n}}\right)\left(\frac{\alpha(n+1)+n}{2n+1}\right)^{\frac{n}{n+1}}. \tag{7.10}$$

Now, from Eq. (3.51) for $\xi_T = 0$, we have

$$\xi = \left(\frac{2n+1}{n}\right) S^{1/n}\left(\phi_N^{\frac{(n+1)}{n}} - \phi_0^{\frac{(2n+1)}{(1-\alpha)n}}\phi_N^{\frac{-\alpha(n+1)-n}{(1-\alpha)n}}\right). \tag{7.11}$$

Substituting Eq (7.10) into the above equation, we obtain

$$\xi_N = \left(\frac{\alpha(n+1)+n}{(2n+1)S^{1/n}}\right)\xi_N - \phi_0^{\frac{2n+1}{(1-\alpha)n}}\left[\left(\frac{\xi_N}{S^{1/n}}\right)^{\frac{n}{n+1}}\left(\frac{\alpha(n+1)+n}{2n+1}\right)^{\frac{n}{n+1}}\right]^{\frac{-(\alpha(n+1)+n)}{(1-\alpha)n}}. \tag{7.12}$$

To simplify this equation, we set $B = \left(\frac{\alpha(n+1)+n}{(2n+1)S^{1/n}}\right)$, $A = \phi_0^{\frac{2n+1}{(1-\alpha)n}}\left[\left(\frac{1}{S^{1/n}}\right)^{\frac{n}{n+1}}\left(\frac{\alpha(n+1)+n}{2n+1}\right)^{\frac{n}{n+1}}\right]$, and $C = \frac{1}{(\frac{2n+1}{n})S^{1/n}}$, then Eq. (7.12) can be written as:

$$C\xi_N = B\xi_N - A\xi_N^{\frac{\alpha(n+1)+n}{(n+1)(\alpha-1)}}, \tag{7.13}$$

which implies

$$\xi_N = \left(\frac{B-C}{A}\right)^{\frac{\alpha(n+1)+n}{(n+1)(\alpha-1)}}. \tag{7.14}$$

Hence,

$$\xi_N = \frac{(2n+1)}{(n+1)\phi_0}\left(\frac{\alpha(n+1)}{\alpha(n+1)+n}\right)^{\frac{\alpha(n+1)+n}{(2n+1)}}. \tag{7.15}$$

Now, substituting above Eq. into (7.10), we obtain

$$\phi_N = \left(\frac{\alpha(n+1)+n}{\alpha(n+1)}\right)^{\frac{n(1-\alpha)}{(2n+1)}} \phi_0. \tag{7.16}$$